8-18-2014

Modeling Landslides by using the DDA and a New Combined Hydrology and Stability Model

Seyed Amirreza Beyabanaki
a.beyabanaki@gmail.com

Modeling Landslides by using the DDA and a New Combined Hydrology and Stability Model

Seyed Amirreza Beyabanaki, PhD

University of Connecticut, 2014

Landslides are one of the major geological hazards in the world due to the resulting loss of life and overwhelming costs to the neighboring communities and damage to the environment. The main triggering events for landslides are earthquakes and rainfall events. In this dissertation, the disk-based Discontinuous Deformation Analysis (DDA) method is used to model landslides triggered by earthquakes. The DDA method is applied to model particulate media with the application to landslide behavior. For this purpose, stiffness and force matrices due to body forces, point loading, inertia forces, and displacement and directional constraints are derived in detail for disk blocks. Next, an efficient model for particle contacts is presented. Normal and shear contact forces as well as friction forces for all contact types are derived by vector analysis. Furthermore, the validity and capability of the model are demonstrated by numerical results obtained for several illustrative examples. Moreover, to investigate the applicability of disk-based DDA to dynamic problems (like earthquake-triggered landslides) the accuracy of the method under dynamic conditions is evaluated by a comprehensive sensitivity analysis and comparison of results with existing analytical solutions. Also, for the first time, the disk-based DDA method is applied to simulate a real landslide triggered by an

earthquake. For this purpose, the kinematic behavior of the Donghekou landslide triggered by the Wenchuan earthquake is simulated and results obtained using disk-based DDA are compared favorably with actual data. This study shows that disk-based DDA, as a practical numerical tool, can be used to simulate the post-failure behavior of landslides triggered by an earthquake. Finally, a new combined hydrology and slope stability method is developed to model landslides triggered by rainfall and earthquake events. In order to verify the method, two case studies are considered and the results obtained by the developed model are compared successfully with actual data. Moreover, this model is used to study the impact of rainfall and several soil and slope parameters on instability of landslides triggered by earthquakes.

Modeling Landslides by using the DDA and a New Combined Hydrology and Stability Model

Seyed Amirreza Beyabanaki

B.S., Isfahan University of Technology, 2000

M.S., University of Tehran, 2003

A Dissertation

Submitted in Partial Fulfillment of the

Requirements for the Degree of

Doctor of Philosophy

At the

University of Connecticut

2014

APPROVAL PAGE

Doctor of Philosophy Dissertation

Modeling Landslides by using the DDA and a New Combined Hydrology and Stability Model

Presented by

S. Amirreza Beyabanaki, B.Sc., M.Sc.

Major advisor_____

Amvrossios C. Bagtzoglou

Associate advisor_____

Emmanouil N. Anagnostou

Associate advisor_____

Lanbo Liu

Associate advisor_____

Ramesh B. Malla

Associate advisor_____

Jafar Razmi

University of Connecticut

2014

Acknowledgements

First and foremost, I would like to express my warmest thanks and appreciation to my advisor, Prof. Amvrossios Bagtzoglou, for his endless support and advice. He is not only an excellent mentor but also is a great person.

My thanks are extended to my advisory committee members, Prof. Emmanouil Anagnostou, Prof. Lanbo Liu, Prof. Ramesh Malla and Prof. Jafar Razmi, for their comments and advice.

I cannot thank my family enough for all their encouragement and support. Without their support, I would never find the courage to overcome the difficulties during my studies at UConn.

My deepest gratitude and love goes to my wife, Bahareh Arabzadeh. Without her, I have nothing and with her I have everything.

I would also like to thank all my good friends at UConn for all the unforgettable and joyful times.

Table of Contents

List of Figures

List of Tables

Chapter 1: Background

1.1. Introduction

A landslide is a geological phenomenon that includes a wide range of ground movement, such as rock falls, deep failure of slopes and shallow debris flows, which can occur in offshore, coastal and onshore environments (Crosta and Frattini, 2008). Not only landslides kill people, but also they destroy the environment. Slope saturation by water and earthquakes are primary causes of landslides (Anderson and Sitar, 1995). Slope saturation can occur in the form of intense rainfall, snowmelt, changes in ground-water levels, and water level changes along coastlines, earth dams, and the banks of lakes, reservoirs, canals, and rivers (Crosta et al., 2003).

Numerical methods, such as Finite Element Method (FEM), Discrete Element Method (DEM), and Discontinuous Deformation Analysis (DDA) and Limit Equilibrium (LE) methods are typically used to analyze slope stability (Cheng and Lau, 2008). To simulate large movements, the discrete element method (DEM) and discontinuous deformation analysis (DDA) are employed.

DEM is presented by Cundall and Strack (1979). The development and applications of the DEM for micro-mechanics of granular materials are presented in a series of conference and symposia proceedings (Jenkins and Satake, 1983; Satake and Jenkins, 1988; Mustoe et al., 1989; Williams and Mustoe, 1993; Benjamin and Richard, 2002; Cleary, 2007; and Munjiza, 2010). A comprehensive review of DEM work can be found in Radjai and Dubois (2011). The PFC (Particle Flow Code) (Itasca, 2001) is the most renowned and widely used numerical code in this field.

The DDA technique was introduced by Shi (1988, 1993) to analyze the mechanical response of discrete blocks. An implicit approach is used by the DDA to solve for displacement unknowns at discrete time intervals. A penalty method is used to model the block interactions by springs. The DDA method has four main advantages over the DEM (Jing and Hudson, 2002; Jing, 2003; Bobet et al., 2009; Koyama et al., 2011; MacLaughlin and Doolin, 2006): (1) The DDA is unconditionally stable due to its implicit time integration and can use significantly larger time steps. (2) The DDA method does not require an artificial damping term to dissipate energy by using an energy approach. (3) In the DEM, dashpot is used to prevent the oscillation during the analysis, whereas in the DDA, only penalty springs are used for contact mechanics. (4) In the DDA method, closed-form integrations for the stiffness matrices of blocks can be derived without the need for Gaussian quadrature techniques.

Simulation of dynamic movement of landslides triggered by earthquakes, and investigation of the effect of rainfall on landslides are critically important since they help us to find unsafe regions and stabilize them before they result in the loss of life and costly damage to the environment.

The goal of this research is to model landslides triggered by earthquakes using the DDA method. Moreover, a new combined hydrology and slope stability model is developed to simulate landslides triggered by earthquakes under rainfall. In the first part, the DDA method is employed to model particulate media with the application targeting granular soils and landslide behavior. For this purpose, stiffness and force matrices due to body forces, point loading, inertia forces, and displacement and directional constraints are derived in detail for disk blocks. Next, an efficient model for particle contacts is presented. Normal and shear contact forces as well as friction forces for all contact types

are derived by vector analysis. Furthermore, the validity and capability of the model is demonstrated by numerical results obtained for several illustrative examples. Then, in order to model the earthquake effects on landslides using the DDA method, the accuracy of disk-based DDA under dynamic conditions by a comprehensive sensitivity analysis is studied and comparison of results with existing analytical solutions is performed. Finally, to show the ability of the DDA developed, a real landslide triggered by an earthquake is simulated and the results obtained are compared with actual data.

The second part of the dissertation focuses on developing a new combined hydrology and stability model. In order to verify the model, two case studies are modeled and the results obtained are compared with actual data. Moreover, in order to provide a better understanding of the conditions leading to catastrophic landslides, the effects of groundwater table position, soil strength properties and rainfall intensity on instability of a homogenous soil slopes under different earthquake conditions are investigated through a series of sensitivity analyses by using the developed combined model.

This dissertation includes six chapters other than the introduction and conclusion sections. The first chapter is presenting a new contact model in disk-based DDA. The second chapter is showcasing a three-dimensional discontinuous deformation analysis (3-D DDA) method for particulate media applications. The third chapter presents details for sphere-boundary edge and sphere-boundary corner contacts in DDA for simulating particulate media in 3-D. The fourth chapter investigates the accuracy of dynamic disk-based DDA. The fifth chapter applies the disk-based DDA to simulate the Donghekou landslide triggered by the Wenchuan earthquake. The sixth chapter presents a study on the effects of groundwater table position, soil Strength properties and rainfall intensity on instability of earthquake-triggered landslides.

1.2. Previous studies

1.2.1. The DDA method

Discontinuous Deformation analysis (DDA) is a displacement-based method that was introduced by Shi (1988, 1999). This method provides a useful tool to analyze the mechanical response of discrete blocks. The DDA has attracted the attention of researchers and geotechnical engineers worldwide and has been widely used in geotechnical engineering due to its advantages. In the past two decades, a lot of studies have been done on the DDA to validate this approach and improve its performance.

MacLaughlin and Doolin (2006) provided a review of more than 100 validation studies on the 2-D DDA approach. Several works has been done on dynamic DDA (e.g., Liu et al., 1996; Hatzor, and Feintuch, 2001; Yagoda-Biran and Hatzor, 2010; Bao et al. 2012; Bakun-Mazor et al., 2012, 2013). Applications of the DDA in rock mechanics and rock engineering are reviewed by Jing and Hudson (2002), Jing (2003), Ohnishi and Nishiyama (2007). Furthermore, Shi (2007) presented applications of the DDA to rock stability analysis. Applications of the DDA to model slopes and underground openings are reviewed by Hatzor and Bakon-Mazor (2011).

However, relatively little work on DDA development in 3-D has been published. Basic formulations of matrices for different potential terms in details are presented by Shi (2001) and Wu et al. (2005a). Applications of 3-D DDA were demonstrated by Liu et al. (2004) and Yeung et al. (2003, 2004). A point-to-face model for contacts between polyhedral blocks in 3-D DDA was presented by Jiang and Yeung (2004). Wu et al. (2005b) developed a new contact searching algorithm for frictionless vertex-to-face contact problems. Yeung et al. (2007) and Wu (2008) presented different algorithms for

edge-to-edge contacts were presented by. A new algorithm to search and calculate geometrical contacts in 3-D was presented by Beyabanaki et al. (2008). Beyabanaki et al. (2009a, 2009b) implemented 8-node and 20-node hexahedral isoparametric finite elements into 3-D DDA to improve deformability of blocks. As an alternative method to improve block deformability in 3-D DDA, high-order displacement functions were used by Beyabanaki et al. (2009c, 2010). Beyabanaki et al. (2009d) presented a new point-to-face contact algorithm for contacts between two polyhedral blocks with planar faces in 3-D DDA. Beyabanaki et al. (2009e) compared 3-D DDA solution for dynamic block displacement with analytical solution to study the validity of the method. Ahn and Song (2011) presented a new contact definition algorithm for 3-D DDA. Bakun-Mazor et al. (2012) validated 3-D DDA by comparing the numerical results obtained for modeling dynamic, single and double face sliding of a block with their proposed analytical solution. Validation and application of 3-D DDA with tetrahedron finite element meshed block was presented by Liu et al. (2012).

Although a lot of work has been done on DDA to date, the development of the DDA for particulate media applications is still at an early stage. Disk-based DDA in 2-D to model particulate media was presented by Ke and Bray (1995). Rein and Andrés (2001) used the method to model granular transport in vibrating feeders. The ability of the DDA to model the response of systems of disks was presented by Thomas and Bray (1999), Thomas (1999), and Koyama et al. (2011).

1.2.2. Combination of hydrology and slope stability methods

To study the effect of rainfall on the stability of slopes, a method that combines hydrological information and slope stability analysis is required. One-dimensional infinite slope stability method is widely used in available combined models (e.g., Dietrich et al., 1995; Wu and Sidle, 1995; Baum et al., 2002, 2008; Iverson, 2000; Lu and Godt, 2008; Godt et al., 2009; Ren et al., 2009, Liao et al., 2012) to study the effect of rainfall on the stability of soil slopes.

By using these models, the effect of water infiltration on soil strength and slope stability, both in saturated and unsaturated conditions, is studied (Eigenbrod, 1993; Rahardjo et al., 1995; Ng and Chiu, 2001). Also, the processes that control surface and sub-surface storm-flow at the hillslope and catchment scale are studied (Uchida et al., 2001; Freer et al., 2002; Seibert et al. 2003). Geomorphologists have contributed to the quantification of the topographic controls on hydrological processes in landslides (Western et al., 1999; Sidle et al., 2001; Pellenq et al., 2003; Hjerdt et al., 2004; McGuire et al., 2005). In the last decades, contributions made possible the development of new theories and new models for rainfall induced landslides and debris flows (e.g., Van, 2005; Wen and Aydin, 2005). Recently, GIS systems (e.g., Frattini et al., 2004; Haneberg, 2004; Ko et al., 2005; Wang et al., 2006; Nandia and Shakoorb, 2010; Xu et al., 2012; Gao and Yin, 2014) and satellite remote sensing data (e.g., Hong et al., 2007; Joyce et al., 2009; Geib and Taubenbock, 2013; Tofani et al., 2014) are used to study landslides.

A combined model named CHASM (Combined Hydrology and Stability Model) was presented by Wilkinson et al. (2000). In this method, a 2-D finite slope stability method is used. This model was developed as commercial software (Wilkinson et al., 2002a). This

model has been used for various environmental conditions in different countries, for example, in Hong Kong (Wilkinson et al. 2002b), Malaysia (Wilkinson et al. 2000; Wilkinson et al. 2002a; Lateh et al. 2008), Greece (Ferentinou et al. 2006; Sakellariou et al. 2006), the Caribbean (Anderson et al. 2008; Holcombe et al., 2012), and Germany (Thiebes et al. 2014). Recently, this model is integrated into a web-based GIS (Thiebes et al. 2013).

1.3. Summary of chapters

1.3.1. Chapter 2: A new contact model in disk-based DDA

In this chapter, a new disk-based DDA formulation is presented. In the original disk-based DDA, disks are considered to be rigid and the penalty method is used to enforce disk contact constraints. In order to improve the accuracy of the disk-based DDA, new formulations of stiffness and force matrices for non-rigid disks using a new efficient contact model are presented in this chapter. Blocks are considered deformable without need to do more computations for contact detection. In the proposed contact model, disk-disk and disk-boundary contacts are transformed into the form of point-to-line contacts and normal spring, shear spring and frictional force sub-matrices are derived by vector analysis. The penalty method is quite simple to implement, but has some major disadvantages. In the presented contact model, not only the simplicity of the penalty method is retained but also the limitations are overcome by using the augmented Lagrangian method. Moreover, unlike the contact model used in the original disk-based DDA, reference line can be obtained directly by using only coordinates of disk centers

and their radii, and no more computations are needed. The validity and capability of the new disk-based DDA formulation are demonstrated by several illustrative examples.

1.3.2. Chapter 3: 3-D DDA Method for Particulate Media Applications

This chapter presents a new numerical model for simulation of granular materials consisting of 3-D spheres bounded by rigid boundaries. The proposed model is based on Three-Dimensional Discontinuous Deformation Analysis (3-D DDA), a numerical method recently developed for simulation of particles in motion. Stiffness and force matrices due to body forces, point loading, inertia forces, and displacement and directional constraints are derived in detail. Moreover, an efficient model for particle contacts in 3-D is presented. In this model, sphere-sphere and sphere-boundary contacts are simply transformed into the form of point-to-plane contacts. Normal and shear contact forces as well as friction force for both sphere-sphere and sphere-plane contact types are derived by vector analysis and the penalty method. The numerical model developed herein is a simple and efficient method that can be easily coded into a computer program. The validity and capability of the model are demonstrated by numerical results obtained for several illustrative examples. Furthermore, some examples are presented and discussed to illustrate the application of the 3-D DDA to particulate media.

1.3.3. Chapter 4: Sphere-boundary edge and sphere-boundary corner contacts model in DDA for simulating particulate media in 3-D

In modeling particulate media, such as soils, using 3-D DDA, there are four types of contacts: sphere to sphere, sphere to boundary face, sphere to boundary edge, and sphere to boundary corner contacts. The first two were studied in the previous chapter. In this chapter, a new contact model for sphere-boundary edge and sphere-boundary corner contacts in sphere-based 3-D DDA is presented. The model includes a new algorithm to search for contacts, detect the contact types and calculate contact points. Moreover, formulas for contact sub-matrices are derived. The proposed contact model has been implemented into a sphere-based 3-D DDA program and three test cases are studied in order to verify the workability of the new contact model. The numerical results obtained demonstrate the capability of the model to deal with sphere-boundary interaction in particulate media.

1.3.4. Chapter 5: Accuracy of dynamic disk-based DDA

Investigating the behavior of dynamic disk-based DDA is very important to evaluate the applicability of disk-based DDA to dynamic problems in geomechanics. In this chapter, the accuracy of disk-based DDA under dynamic conditions is studied by a comprehensive sensitivity analysis. The results obtained by disk-based DDA are compared with the analytical solutions of a disk cluster on an incline subjected to gravitational force only, and three different accelerations of increasing complexity with sinusoidal input functions as well as gravitational load. In this research, the effect of time step size and interface friction angles on the results are studied. Overall, most of error for both velocity and displacement occurs at the beginning of the solution. With

increasing friction angle, the initial perturbation of the solution increases in the case of sliding under gravitational force only, and decreases in the case of sliding under dynamic loads. This study shows that disk-based DDA predicts accurately the velocities and displacements derived with respect to the frictional resistance offered by the inclines.

1.3.5. Chapter 6: Applying disk-based DDA to simulate the Donghekou landslide

In this chapter, for the first time, disk-based discontinuous deformation analysis (DDA) is applied to simulate a landslide triggered by an earthquake. For this purpose, the kinematic behavior of the Donghekou landslide triggered by the Wenchuan earthquake is simulated and the results obtained using disk-based DDA are compared with actual data. The comparisons show that there is an acceptable agreement between the results obtained using disk-based DDA and actual data. The simulation results provided an understanding of the failure behavior of the landslide. This study shows that disk-based DDA, as a practical numerical tool, can be used to simulate the post-failure behavior of landslides triggered by an earthquake.

1.3.6. Chapter 7: Effects of groundwater table position, soil strength properties and rainfall on instability of earthquake-triggered landslides

Although earthquake-triggered landslides are widely studied, less attention has been focused on the effects of groundwater table position, soil strength properties and rainfall intensity on the instability of landslides triggered by earthquakes during rainfall events. In

this study, in order to provide a better understanding of the conditions leading to catastrophic landslides, the effects of these factors on the instability of a homogeneous soil slope under different earthquake conditions are investigated through a series of sensitivity analyses by using a newly developed combined hydrology and slope stability model. The results show that groundwater table position, soil friction, soil cohesion, rainfall intensity and rainfall duration have significant effects on the instability of landslides. Groundwater table position and soil strength properties are found to be the primary factors controlling the instability of landslides, while rainfall intensity plays a secondary role. On the other hand it is shown that increasing soil saturation, which is a direct effect of rainfall accumulation, decreases the factor of safety. The results also show the combined effect of rainfall duration and earthquake acceleration on the landslide instability. Specifically, for a given rainfall duration, there exists a threshold earthquake acceleration coefficient that would trigger a landslide; for higher rainfall durations, landslides can be triggered by earthquakes with smaller acceleration coefficients.

1.4. References

Ahn TY, Song JJ. 2011. New Contact-Definition Algorithm using Inscribed Spheres for 3D Discontinuous Deformation, International Journal of Computational Methods, 8(2): 171–191.

Anderson SA, Sitar N. 1995. Analysis of rainfall-induced debris flows. Journal of Geotechnical Engineering-ASCE 121(7): 544–552.

Anderson M, Holcombe L, Flory R, Renaud J-P. 2008. Implementing low-cost landslide risk reduction: a pilot study in unplanned housing areas of the Caribbean. Nat Hazard 47:297–315.

Bakun-Mazor D, Hatzor YH, Glaser SD. 2012. Dynamic sliding of tetrahedral wedge: The role of interface friction. International Journal for Numerical and Analytical Methods in Geomechanics, 36(3): 327–343.

Bakun-Mazor D, Hatzor YH, Glaser SD, Santamarina JC. 2013. Thermally vs. seismically induced block displacements in Masada rock slopes, International Journal of Rock Mechanics & Mining Sciences, 61:196–211.

Bao H, Hatzor YH, Huang X. 2012. A New Viscous Boundary Condition in the Two-Dimensional Discontinuous Deformation Analysis Method for Wave Propagation Problems, Rock Mech Rock Eng, 45:919–928.

Baum RL, Savage WZ, Godt JW. 2002. TRIGR—a Fortran program for transient rainfall infiltration and grid-based regional slope-stability analysis. U.S. Geological Survey Open File Report.

Baum RL, Savage WZ, Godt JW. 2008. TRIGRS—a Fortran program for transient rainfall infiltration and grid-based regional slope-stability analysis, version 2.0: US Geological Survey Open-File Report, 75 p.

Benjamin K. Cook, Richard P. Jensen, editors. 2002. Proceedings of the Third International Conference on Discrete Element Methods. ASCE, Santa Fe, New Mexico, USA.

Beyabanaki SAR, Grayeli R, Hatami K. 2008. Three-dimensional discontinuous deformation analysis (3-D DDA) using a new contact resolution algorithm. Computers and Geotechnics, 35:346-356.

Beyabanaki SAR, Jafari A, Biabanaki SO, Yeung MR. 2009a. A Coupling Model of 3-D Discontinous Deformation Analysis (3-D DDA) and Finite Element Method, AJSE, 34:2B:107-119.

Beyabanaki SAR, 2009b. Jafari A, Biabanaki SO, and Yeung MR. Nodal-based Three-Dimensional Discontinuous Deformation Analysis (3-D DDA), Computers and Geotechnics, 36:359-372.

Beyabanaki SAR, Jafari A, Yeung MR. 2009c. Second-Order Displacement Functions for Three-Dimensional Discontinuous Deformation Analysis (3-D DDA), International Journal of Science and Technology, 16(3):216-225.

Beyabanaki SAR, Mikola GR, Biabanaki SO, Mohammadi S. 2009d. New Point-to-Face Contact Algorithm for 3-D Contact Problems using the Augmented Lagrangian Method, Geomechanics and Geoengineering: An International Journal, Taylor & Francis, 4 (3):221-236.

Beyabanaki SAR, Ferdosi B, Mohammadi S. 2009e. Validation of dynamic block displacement analysis and modification of edge-to-edge contact constraints in 3-D DDA, International Journal of Rock Mechanics and Mining Sciences, Elsevier, 46:1223-1234.

Beyabanaki SAR, Jafari A, and Yeung MR. 2010. High - order three - dimensional discontinuous deformation analysis (3-D DDA), International Journal for Numerical Methods in Biomedical Engineering, 26 (12):1522–1547.

Beyabanaki SAR and Bagtzoglou AC. 2012. Three-dimensional discontinuous deformation analysis (3-D DDA) method for particulate media applications, Geomechanics and Geoengineering: An International Journal 7(4):239-253.

Beyabanaki SAR and Bagtzoglou AC, 2013. Non-rigid disk-based DDA with a new contact model, Computers and Geotechnics 49:25–35.

Beyabanaki SAR and Bagtzoglou AC, 2014a. Sphere-boundary edge and sphere-boundary corner contacts model in DDA for simulating particulate media in 3-D, Geomechanics and Geoengineering: An International Journal, DOI 10.1080/17486025.2014.933892, in press.

Beyabanaki SAR and Bagtzoglou AC, 2014b. Accuracy of Dynamic Disk-Based DDA with Respect to a Single Sliding Disk Cluster, Geomechanics and Geoengineering: An International Journal, 9(3): 231-240.

Bobet A, Fakhimi A, Johnson S, Morris J, Tonon F, Yeung MR. 2009. Numerical Models in Discontinuous Media: Review of Advances for Rock Mechanics Applications, Journal of Geotechnical and Geoenvironmental Engineering, 135 (11): 1547-1561.

Cheng YM; Lau CK. 2008. Slope stability analysis and stabilization: new methods and insight, London ; New York : Routledge.

Cleary PW, editor. 2007. Proceedings of Fourth International Conference on Discrete Element Methods. Brisbane, Australia.

Crosta GB, Dal Negro P, Frattini P. 2003. Soil slips and debris flows on terraced slopes. Natural Hazards and Earth System Sciences 3: 31–42.

Crosta BG, Frattini P. 2008. Rainfall-induced landslides and debris flows, Hydrol. Process. 22: 473–477.

Cundall PA, Strack ODL. 1979. A discrete numerical model for granular assemblies. Geotechnique, 29(1):47–65.

Dietrich WE, Reiss R, Hsu ML, Montgomery DR. 1995. A process-based model for colluvial soil depth and shallow landsliding using digital elevation data. Hydrol Process 9:383–400.

Eigenbrod KD. 1993. Downslope movements at shallow depths related to cyclic pore-pressure changes. Canadian Geotechnical Journal 30(3): 464–475.

Ferentinou MD, Sakellariou M, Matziaris V, Charalambous S. 2006. An introduced methodology for estimating landslide hazard for seismic and rainfall induced landslides in a geographical information system environment. In: Nadim F, Pöttler R, Einstein H, Klapperich H, Kramer S (eds) Geohazards. Lillehammer, Norway, pp 1–8.

Frattini P, Crosta GB, Fusi N, Dal Negro P. 2004. Shallow landslides in pyroclastic soils: a distributed modelling approach for hazard assessment. Engineering Geology 73(3–4): 277–295.

Freer J, McDonnell JJ, Beven K, Burns D, Hooper R, Aulenbach B, Kendall C, Peters N. 2002. Understanding the spatial and temporal dynamic contributions of subsurface storm runoff at the hillslope scale. Water Resources Research 38(12): 5-1–5-16.

Gao HX, Yin KL. 2014. Study on spatial prediction and time forecast of landslide, Natural Hazards, 70(3):1735-1748.

Geib C, Taubenbock H. 2013. Remote sensing contributing to assess earthquake risk: from a literature review towards a roadmap, Natural Hazards, 68(1):7-48.

Godt JW, Baum RL, Lu N. 2009. Landsliding in partially saturated materials. Geophys Res Lett 36.

Haneberg WC. 2004. A rational probabilistic method for spatially distributed landslide hazard assessment. Environmental and Engineering Geoscience 10(1): 27–43.

Hatzor YH and Bakun-Mazor D. 2011. Modeling dynamic deformation in natural rock slopes and underground openings with DDA: review of recent results. Geomechanics and Geoengineering: An International Journal, 6(4):283-292.

Hjerdt KN, McDonnell JJ, Seibert J, Rodhe A. 2004. A new topographic index to quantify downslope controls on local drainage. Water Resources Research 40(5): W05602.

Holcombe E, Smith S, Wright E, Anderson MG. 2012. An integrated approach for evaluating the effectiveness of landslide risk reduction in unplanned communities in the Caribbean, Nat Hazards, 61:351–385

Hong Y, Adler RF, Huffman GJ. 2007. Use of satellite remote sensing data in the mapping of global landslide susceptibility. Nat Hazards 43(2):245–256.

ITSACA Consulting Group, Ltd., 2001. PFC codes manuals.

Iverson RM. 2000. Landslide triggering by rain infiltration. Water Resour Res 36(7):1897–1910.

Jenkins JT, Satake M, editors. 1983. Mechanics of granular materials: new models and constitutive relations. Amsterdam: Elsevier.

Jiang QH, Yeung MR. 2004. A model of point-to-face contact for three-dimensional discontinuous deformation analysis. Rock Mechanics and Rock Engineering, 37(2):95 – 116.

Jing L, Hudson JA. 2002. Numerical methods in rock mechanics, International Journal of Rock Mechanics & Mining Sciences, 2002; 39: 409–427.

Jing L. 2003. A review of techniques, advances and outstanding issues in numerical modelling for rock mechanics and rock engineering, International Journal of Rock Mechanics & Mining Sciences, 40: 283–353.

Joyce KE, Belliss SE, Samsonov SV. 2009. A review of the status of satellite remote sensing and image processing techniques for mapping natural hazards and disasters, Progress in Physical Geography, 33(2): 183-207.

Ke, T.-C., and Bray, J. D. 1995. Modeling of particulate media using discontinuous deformation analysis. J. Eng. Mech., 121(11), 1234–1243.

Ko CK, Chowdhury R, Flentje R. 2005. Hazard and risk assessment of rainfall-induced landsliding along a railway line. Quarterly Journal of Engineering Geology and Hydrogeology 38: 197–213.

Koo CY, Chern JC. 1998. Modification of the DDA method for rigid block problems. International Journal of Rock Mechanics and Mining Sciences, 35(6):684–693.

Koyama T, Nishiyama S, Yang M, Ohnishi Y. 2011. Modeling the interaction between fluid flow and particle movement with discontinuous deformation analysis (DDA) method, Int. J. Numer. Anal. Meth. Geomech., 35:1–20.

Lateh H, Anderson MG, Ahmad F. (2008) CHASM—the model to predict stability of gully walls along the east–west highway in Malaysia: a case study. Proceedings of the First World Landslide Forum. ISDR, Tokyo, Japan, pp. 340–343.

Liao Z, Hong Y, Kirschbaum D, Liu C. 2012. Assessment of shallow landslides from Hurricane Mitch in central America using a physically based model, Environ Earth Sci (2012) 66:1697–1705.

Liu L, Linde AT, Sacks IS, and He S. 1996. Aseismic fault slip and block deformation in north China, Pure Appl. Geophys., 146(3/4):717-740.
Liu J, Kong X, Lin G. 2004. Formulation of the three-dimensional discontinuous deformation analysis method. Acta Mechanica Sinica, 20(3):270-282.

Liu J, Nan Z, Yi P. 2012. Validation and application of three-dimensional discontinuous deformation analysis with tetrahedron finite element meshed block, Acta Mechanica Sinica, 28(6):1602–1616.

Lu N, Godt JW. 2008. Infinite-slope stability under steady unsaturated conditions. Water Resour Res 44:W11404.

MacLaughlin MM, Doolin DM. 2006. Review of validation of the discontinuous deformation analysis (DDA) method, Int J Numer Anal Meth Geomech, 30: 271-305.

McGuire KJ, McDonnell JJ, Weiler M, Kendall C, McGlynn BL, Welker JM, Seibert J. 2005. The role of topography on catchment-scale water residence time. Water Resources Research 41(5): W05002.

Munjiza A, editor. 2010. The Fifth International Conference on Discrete Element Methods. London, UK.

Mustoe GGW, Henriksen M, Huttelmaier HP, editors. 1989. Proceedings of the First Conference on DEM. CSM Press, Golden, CO, USA.

Nandia A, Shakoorb A. 2010. A GIS-based landslide susceptibility evaluation using bivariate and multivariate statistical analyses, Engineering Geology, 10(1): 11–20.

Ng CWW, Chiu ACF. 2001. Behavior of a loosely compacted unsaturated volcanic soil. Journal of Geotechnical and Geoenvironmental Engineering 127(12): 1027–1036.

Ohnishi Y, Nishiyama S. 2007. Recent insights of analyses using discontinuous methods in rock engineering in Japan, Proceedings of the 8th International Conference on Analysis of Discontinuous Deformation: Fundamentals and Applications to Mining and Civil Engineering, Beijing, China, August 14-19, pp. 15-26.

Pellenq J, Kalma J, Boulet G, Saulnier GM, Wooldridge S, Kerr Y, Chehbouni A. 2003. A disaggregation scheme for soil moisture based on topography and soil depth. Journal of Hydrology 276(1–4): 112–127.

Radjai and Dubois. 2011. Discrete-element Modeling of Granular Materials. John Wiley and Sons.

Rahardjo H, Lim TT, Chang MF, Fredlund DG. 1995. Shear-strength characteristics of a residual soil. Canadian Geotechnical Journal 32(1): 60–77.

Rein G, Andrés A. 2001. Computer simulation of granular material: vibrating feeders, Powder Handling & Processing, 13(2), 181-185.

Ren D, Wang J, Fu R, Karoly D, Yong Yang, Leslie LM, Fu C, Huang G. 2009. Mudslide caused ecosystem degradation following Wenchuan earthquake 2008. GRL 36.

Sakellariou M, Ferentinou M, Charalambous S. 2006. An integrated tool for seismic induced landslide hazards mapping. In: Agioutantis Z, Komnitsas K (eds) First European Conference on Earthquake Engineering and Seismology. Geneva, Switzerland, pp. 1365–1375.

Satake M, Jenkins JT, editors. 1988. Micromechanics of granular materials. Amsterdam: Elsevier.

Seibert J, Bishop K, Rodhe A, McDonnell J. 2003. Groundwater dynamics along a hillslope: a test of the steady-state hypothesis. Water Resources Research 39(1): 2-1–2-9.

Shi GH. 1988. Discontinuous deformation analysis: a new numerical model for the statics and dynamics of block systems, PhD thesis, Department of Civil Engineering, University of California, Berkeley.

Shi GH. 1993. Block System Modeling by Discontinuous Deformation Analysis. Computational Mechanics Publication: Southampton. UK.

Shi GH. 2001. Three dimensional discontinuous deformation analysis. In: Proceedings of the 38th US Rock Mechanics Symposium, D Elsworth et al, ed., p 1421-1428.

Shi GH. 2007. Applications of discontinuous deformation analysis (DDA) to rock stability analysis, Proceedings of the 8th International Conference on Analysis of Discontinuous Deformation: Fundamentals and Applications to Mining and Civil Engineering, Beijing, China, August 14-19, pp. 1-13.

Sidle RC, Noguchi S, Tsuboyama Y, Laursen K. 2001. A conceptual model of preferential flow systems in forested hillslopes: evidence of self-organization. Hydrological Processes 15(10): 1675–1692.

Thiebes B., Bell R., Glade T., Jäger S., Mayer J., Anderson M., Holcombe L. 2014. Integration of a limit-equilibrium model into a landslide early warning system, Landslides, DOI 10.1007/s10346-013-0416-2, in press.

Thiebes B, Bell R, Glade T, Jäger S, Anderson M, Holcombe L. 2013. A WebGIS decision-support system for slope stability based on limit-equilibrium modeling, Engineering Geology, 158:109–118.

Thomas, P. A. 1997. Discontinuous deformation analysis of particulate media. PhD thesis, University of California, Berkeley, Berkeley, CA.

Thomas, P. A., and Bray, J. D. 1999. Capturing nonspherical shape of granular media with disk clusters. J. Geotech. Geoenviron. Eng., 125(3), 169–178.

Tofani V, Ventisette CD, Moretti S, Casagli N. 2014. Integration of Remote Sensing Techniques for Intensity Zonation within a Landslide Area: A Case Study in the Northern Apennines, Italy, Remote Sens. 2014, 6(2), 907-924.

Uchida T, Kosugi K, Mizuyama T. 2001. Effects of pipeflow on hydrological process and its relation to landslide: a review of pipeflow studies in forested headwater catchments. Hydrological Processes 15(11): 2151–2174.

Van Asch TWJ. 2005. Modelling the hysteresis in the velocity pattern of slow-moving earth flows: the role of excess pore pressure. Earth Surface Processes and Landforms 30(4): 403–411.

Wang CX, Esaki T, Xie MW, Qiu C. 2006. Landslide and debris-flow hazard analysis and prediction using GIS in Minamata-Hougawachi area, Japan. Environmental Geology 51(1): 91–102.

Wen BP, Aydin A. 2005. Mechanism of a rainfall-induced slide-debris flow: constraints from microstructure of its slip zone. Engineering Geology 78(1–2): 69–88.

Western AW, Grayson RB, Bl¨oschl G, Willgoose GR, McMahon TA. 1999. Observed spatial organisation of soil moisture and its relation to terrain indices. Water Resources Research 35(3): 797–810.

Williams JR, Mustoe GGW, editors. 1993. Proceedings of the Second International Conference on DEM. IESL Publications, Boston, MIT, USA.

Wilkinson PL, Brooks SM, Anderson MG. 2000. Design and application of an automated non-circular slip surface search within a combined hydrology and stability model (CHASM). Hydrol Processes 14:2003–2017.

Wilkinson PL, Anderson MG, Lloyd DM, Renaud JP. 2002a. Landslide hazard and bioengineering: towards providing improved decision support through integrated numerical model development. Environ Model Softw 17:333–344.

Wilkinson PL, Anderson MG, Lloyd DM 2002b. An integrated hydrological model for rain-induced landslide prediction. Earth Surf Process Landforms 27:1285–1297.

Wu W, Sidle RC. 1995. A distributed slope stability model for steep forested basins. Water Resour Res, 31:2097–2110.

Wu JH, Ohnishi Y, Shi GH, Nishiyama S. 2005a. Theory of Three-Dimensional Discontinuous Deformation Analysis and Its Application to a Slope Toppling at Amatoribashi, Japan. International Journal of Geomechanics, 179-195.

Wu JH, Juang CH, Lin HM. 2005b. Vertex-to-face contact searching algorithm for three-dimensional frictionless contact problems. International Journal for Numerical Methods in Engineering, 63(6):876-897.

Wu JH. 2008. New edge-to-edge contact calculating algorithm in three-dimensional discrete numerical analysis. Advances in Engineering Software, 39(1):15-24.

Xu C, Dai F, Xu X, Lee YH. 2012. GIS-based support vector machine modeling of earthquake-triggered landslide susceptibility in the Jianjiang River watershed, China, Geomorphology, 145: 70–80.

Yagoda-Biran G, Hatzor YH. 2010. Constraining paleo PGA values by numerical analysis of overturned columns, Earthquake Engineering and Structural Dynamics, 39:463–472.

Yeung MR, Jiang QH, Sun N. 2003. Validation of block theory and three-dimensional discontinuous deformation analysis as wedge stability analysis method. Int J Rock Mech Min Sci, 40(2):265 –275.

Yeung MR, Sun N, Jiang QH, Blair SC. 2004. Analysis of large block test data using three-dimensional discontinuous deformation analysis. Int J Rock Mech Min Sci, 41(3):458–459.

Yeung MR, Jiang QH, Sun N. 2007. A model of edge-to-edge contact for three-dimensional discontinuous deformation analysis. Computers and Geotechnics, 34(3):175-186.

Chapter 2: A new contact model in disk-based DDA

(This chapter was published as Beyabanaki SAR and Bagtzoglou AC. (2013) Non-rigid disk-based DDA with a new contact model, Computers and Geotechnics 49: 25–35)

2.1. Introduction

The discontinuous deformation analysis (DDA) provides a useful tool to analyze the mechanical response of discrete blocks (Shi 1993). The DDA has attracted the attention of researchers and geotechnical engineers worldwide and has been widely used in geotechnical engineering due to its rigorous scheme of block kinematics and equilibrium conditions achieved by minimizing the total potential energy (Hatzor and Bakun-Mazor 2011). In the past two decades, a lot of studies have been done on the DDA to validate this approach and improve its performance. Applications of the DDA in rock mechanics and rock engineering are reviewed by Jing and Hudson (2002), Jing (2003) and Ohnishi and Nishiyama (2007). Moreover, more than 100 validation studies on the DDA are reviewed by MacLaughlin and Doolin (2006). Furthermore, Hatzor and Bakon-Mazor (2011) reviewed recent applications of the DDA to model rock slopes and underground openings. However, little work has been done on the development of the DDA in particulate media and it is still at an early stage. Among the few DDA applications for particulate media are the works of Ke and Bray (1995), Thomas (1997) and Thomas and Bray (1999) who demonstrated qualitatively the ability of the DDA to model the response of systems of disks, Soto-Yarritu and Martinez (2001) who used this algorithm to model granular transport in vibrating feeders, and most recently, Koyama et al. (2011) who

presented coupled solid circular particles movement and fluid flow processes in porous media using combined DDA-FEM approach.

The original disk-based DDA formulation (presented by Ke and Bray, 1995) considers disks as undeformable and rigid blocks; therefore, there is no deformation for disks at all. Moreover, it uses the penalty method to enforce disk contact constraints. Using the penalty method, the constraints are only satisfied in an approximate manner and the contact solution depends highly on the choice of the penalty number and the optimal number cannot be explicitly found beforehand (Mohammadi, 2003). If the penalty number is too low, the constraints are poorly satisfied, while if it is too large, the simultaneous equilibrium matrix equation becomes difficult to solve. The contact conditions can be satisfied exactly by using the classical Lagrange Multiplier Method (Mohammadi, 2003), but the method has several disadvantages. The number of governing equations is increased so that extra computational effort is needed to solve the system. Furthermore, the matrix contains a zero sub-matrix along its diagonal and in order to obtain a unique solution some special numerical procedures have to be invoked. Finally, the augmented Lagrangian method can be used to enforce the contact constraints. This method is used for polygon blocks in DDA by Lin et al. (1996).

The main features of the augmented Lagrangian method are (Mohammadi, 2003):

- This approach uses a penalty stiffness but iteratively updates the contact traction to impose the contact constraints with a specified precision.
- No additional equations are required.
- Large penalty values are not required; avoiding the ill conditioning of the stiffness matrices.

- The constraints are satisfied within a user defined required tolerance.
- The algorithm can be used effectively for applications where the contact pressures become very large.

In this paper, stiffness and force matrices in the DDA for non-rigid disks are derived. Moreover, a new contact model based on vector analysis is presented and the augmented Lagrangian method is used to eliminate the influence of the penalty number selection. In this model, unlike the contact model used in the original disk-based DDA, reference line can be obtained directly by using only coordinates of disk centers and their radii. The code developed for this model is verified by various examples. The results obtained showcase the capability of the new disk-based DDA formulation.

2.2. Displacement Approximation

It is assumed that circular blocks are deformable and the deformations at all directions are the same. This means that after deformation, the block is still a circle, not an ellipse or of any other configuration. It can be represented as:

$$\begin{cases} \varepsilon_x = \varepsilon_y = \varepsilon_0 \\ \gamma_{xy} = 0 \end{cases} \tag{2-1}$$

Consequently, for each block, by means of linear approximation, the displacement matrix at an arbitrary point (x, y) in the block is obtained from the corresponding location and the displacement vector $\{D\}$. The relation between them can be shown in the following equations:

$$\begin{pmatrix} u \\ v \end{pmatrix} = [T_i(x,y)].\{D_i\} \tag{2-2}$$

where

$$[T_i(x,y)] = \begin{pmatrix} 1 & 0 & -(y-y_0) & (x-x_0) \\ 0 & 1 & (x-x_0) & (y-y_0) \end{pmatrix} \tag{2-3}$$

$$\{D_i\}^T = \{u_0 \quad v_0 \quad r_0 \quad \varepsilon_0\} \tag{2-4}$$

and (x_0,y_0) are the co-ordinates of the block center, (u_0,v_0) indicate body translations; r_0 represents the rotation angle of block i with a rotation centre at (x_0,y_0). $[T_i(x,y)]$ is the first order displacement function, and $\{D_i\}$ is the displacement variable vector of block i in 2-D.

Assuming that (x_0, y_0) is the center of a circular block, a circular block can be represented by the following equation:

$$\begin{cases} x = r\cos(\alpha) + x_0 \\ y = r\sin(\alpha) + y_0 \end{cases} \qquad 0 \le \alpha \le 2\pi \tag{2-5}$$

where α is the angle between r (the radius of the circular block) and the positive direction of the x-axis.

The linear displacement function can also cause free expansion under body rotation. To reduce the error, extending the following body rotation, the exact solution for the displacements (Koo and Chern, 1998):

$$\begin{cases} u = u_0 + (x - x_0)(\cos r_0 - 1) - (y - y_0)\sin r_0 \\ v = v_0 + (x - x_0)\sin r_0 + (y - y_0)(\cos r_0 - 1) \end{cases} \tag{2-6}$$

is used to compute (u, v) due to rotation r_0. For this purpose, after solving the displacement vectors, Equation (6) is applied to update the coordinates of each circular block and to judge the contact patterns at the end of each time step.

2.3. Equilibrium Equations and Energy Minimization

DDA is an implicit method, involving formulation and solution of a system of simultaneous equilibrium equations. Individual blocks are connected and form a block system by contacts between blocks and by displacement constraints on single blocks. For a system of N disks, the system equations have the following form:

$$\begin{bmatrix} [K_{11}] & [K_{12}] & [K_{13}] & \dots & [K_{1N}] \\ [K_{21}] & [K_{22}] & [K_{23}] & \dots & [K_{2N}] \\ [K_{31}] & [K_{32}] & [K_{33}] & \dots & [K_{3N}] \\ \vdots & \vdots & \vdots & \ddots & \vdots \\ [K_{N1}] & [K_{N2}] & [K_{N3}] & \dots & [K_{NN}] \end{bmatrix} \begin{bmatrix} \{D_1\} \\ \{D_2\} \\ \{D_3\} \\ \vdots \\ \{D_N\} \end{bmatrix} = \begin{bmatrix} \{F_1\} \\ \{F_2\} \\ \{F_3\} \\ \vdots \\ \{F_N\} \end{bmatrix} \tag{2-7}$$

Because each block has four degrees of freedom $\{u_0 \;\; v_0 \;\; r_0 \;\; \varepsilon_0\}$ for each circular element, $[K_{ij}]$ in the coefficient matrix given by the above equation is a 4×4 Sub-matrix. $\{D_i\}$ and $\{F_i\}$ are 4×1 sub-matrices where $\{D_i\}$ is the deformation variables of block i:

$$\{D_i\}^T = \{u_0 \;\; v_0 \;\; r_0 \;\; \varepsilon_0\} = \{d_{1i} \;\; d_{2i} \;\; d_{3i} \;\; d_{4i}\} \tag{2-8}$$

and $\{F_i\}$ represents the loading on block i distributed to the four deformation variables.

The total potential energy Π is the summation over all potential energy forms (including the potential energies due to disk stiffness, π_e, initial stress, π_{is}, point loading, π_p, body force, π_b, inertia forces, π_i, constrained spring, π_C, normal contact, π_n, shear contact, π_s, and friction force, π_f). It is necessary to mention that the blocks are considered to be rigid bodies in the studies previously done on disk-based DDA. Therefore, the potential energy for elastic strain and initial stress in the previous studies are not considered. Moreover, sizes of matrices in the rigid disk-based DDA are different from those in non-rigid disk-based DDA.

The simultaneous equations are derived by minimizing the total potential energy Π of the block system.

$$\begin{aligned} [K_{ij}] &= \frac{\partial^2 \Pi}{\partial d_{ir}\, \partial d_{js}} \quad , \quad r,s = 1,\cdots,4 \\ \{F_i\} &= -\frac{\partial \Pi(0)}{\partial d_{ir}} \quad , \quad r = 1,\cdots,4 \end{aligned} \tag{2-9}$$

where 0 refers to the initial state of each time state.

2.4. Non-Contact Sub-Matrices of Equilibrium Equations

To solve Equation (7), it is necessary to calculate the contributed non-contact potential energy components. Since the derivations of the sub-matrices of point loading, body forces, inertia forces, and displacement constraint are similar to standard DDA derivations, only sub-matrices of disk stiffness and initial stress are derived in this section.

2.4.1. Sub-matrix of Disk Stiffness

At each time step, the elastic strain energy, π_e, stored by the stresses of disk i is:

$$\pi_e = \iint \frac{1}{2}\left(\varepsilon_x \sigma_x + \varepsilon_y \sigma_y + \gamma_{xy}\tau_{xy}\right) dxdy \tag{2-10}$$

Therefore, the relationship between stress $\{\sigma_i\}$ and strain $\{\varepsilon_i\}$ is expressed as:

$$\begin{pmatrix} \sigma_x \\ \sigma_y \\ \tau_{xy} \end{pmatrix} = \frac{E}{1-\upsilon^2} \begin{pmatrix} 1 & \upsilon & 0 \\ \upsilon & 1 & 0 \\ 0 & 0 & \frac{1-\upsilon}{2} \end{pmatrix} \begin{pmatrix} \varepsilon_x \\ \varepsilon_y \\ \gamma_{xy} \end{pmatrix} \tag{2-11}$$

that E is the Young's modulus and υ is the Poisson's ratio. Assuming equation (2-1), we have:

$$\pi_e = \frac{1}{2}\iint \left(\varepsilon_0 \sigma_x + \varepsilon_0 \sigma_y\right) dxdy = \frac{1}{2}\iint \begin{bmatrix} \varepsilon_0 & \varepsilon_0 \end{bmatrix} \begin{bmatrix} \sigma_x \\ \sigma_y \end{bmatrix} dxdy \tag{2-12}$$

and

$$\begin{pmatrix} \sigma_x \\ \sigma_y \end{pmatrix} = \frac{E}{1-\upsilon^2} \begin{pmatrix} 1 & \upsilon \\ \upsilon & 1 \end{pmatrix} \begin{pmatrix} \varepsilon_0 \\ \varepsilon_0 \end{pmatrix} = \frac{E}{1-\upsilon} \begin{pmatrix} \varepsilon_0 \\ \varepsilon_0 \end{pmatrix} \tag{2-13}$$

Therefore, the elastic strain energy can be written as:

$$\pi_e = \frac{1}{2}\iint \begin{bmatrix} \varepsilon_0 & \varepsilon_0 \end{bmatrix} \frac{E}{1-\upsilon} \begin{pmatrix} \varepsilon_0 \\ \varepsilon_0 \end{pmatrix} dxdy = \frac{1}{2} A \left(\varepsilon_0 \frac{2E}{1-\upsilon} \varepsilon_0 \right) \tag{2-14}$$

where

$$A = \iint dxdy = \pi R_i^{\,2} \tag{2-15}$$

where R_i is radius of disk i.

Equation (14) can be written in the following matrix form:

$$\pi_e = \{D_i\}_{1\times 4}^{\,T} [E]_{4\times 4} \{D_i\}_{4\times 1} \tag{2-16}$$

where

$$\{D_i\} = \begin{pmatrix} u_0 \\ v_0 \\ r_0 \\ \varepsilon_0 \end{pmatrix} \tag{2-17}$$

and

$$[E] = \frac{\pi E R_i^{\,2}}{1-\upsilon} \begin{pmatrix} 0 & 0 & 0 & 0 \\ 0 & 0 & 0 & 0 \\ 0 & 0 & 0 & 0 \\ 0 & 0 & 0 & 1 \end{pmatrix} \tag{2-18}$$

Minimizing the strain energy, π_e, gives a 4×4 matrix:

$$2[E] \rightarrow [K_{ii}] \tag{2-19}$$

which is added to the sub-matrix $[K_{ii}]$ in the global equation (2-7).

2.4.2. Sub-matrix of Initial Stress

Initial stress loadings, which are the computed stresses of the previous time step, will be transferred to the next step. The potential energy of the initial stresses, π_{is}, for the i–th disk is:

$$\pi_{is} = \iint \left(\varepsilon_x \sigma_x + \varepsilon_y \sigma_y + \gamma_{xy} \tau_{xy} \right) dxdy \tag{2-20}$$

where

$$\begin{pmatrix} \sigma_x \\ \sigma_y \\ \tau_{xy} \end{pmatrix} = \begin{pmatrix} \sigma_0 \\ \sigma_0 \\ 0 \end{pmatrix} = \frac{E}{1-\upsilon} \begin{pmatrix} \varepsilon_0 \\ \varepsilon_0 \\ 0 \end{pmatrix} \tag{2-21}$$

or

$$\sigma_0 = \frac{E}{1-\upsilon} \varepsilon_0 \tag{2-22}$$

Therefore,

$$\pi_{is} = \iint \begin{bmatrix} \varepsilon_0 & \varepsilon_0 & 0 \end{bmatrix} \begin{pmatrix} \sigma_0 \\ \sigma_0 \\ 0 \end{pmatrix} dxdy = \iint 2\varepsilon_0 \sigma_0 \, dxdy = 2A\varepsilon_0 \sigma_0 \tag{2-23}$$

Equation (2-23) can be written as:

$$\pi_{is} = 2\pi R_i^{\,2} \{D_i\}^T \begin{pmatrix} 0 \\ 0 \\ 0 \\ \sigma_0 \end{pmatrix} \tag{2-24}$$

By taking the derivatives, we have a 4×1 matrix:

$$-2\pi R_i^{\,2}\begin{pmatrix}0\\0\\0\\\sigma_0\end{pmatrix}\rightarrow\{F_i\} \tag{2-25}$$

that is added to $\{F_i\}$ in the global equation (7).

2.5. Contact Sub-Matrices of Equilibrium Equations

In this section, sub-matrices of disk-disk and disk-boundary contacts (including normal and shear contacts and frictional force) are derived by vector analysis.

2.5.1. Disk-disk contact

Sub-matrices of normal and shear contacts and frictional force are presented for the disk-disk contact type in the following sections.

- *Sub-matrices of normal contact*

As shown in Figure 2-1, the tangent line to the disk j, which is perpendicular to the line that connects the centers of the disks ($C_1(x_{ci},y_{ci})\,C_2(x_{cj},y_{cj})$), is reference line, and P_1 of disk i which is located on line C_1C_2 is reference point. Assume $P_1(x_1,y_1)$ is the reference point of disk i before a displacement increment and P_1^* is the point after the displacement increment (Figure 2-2).

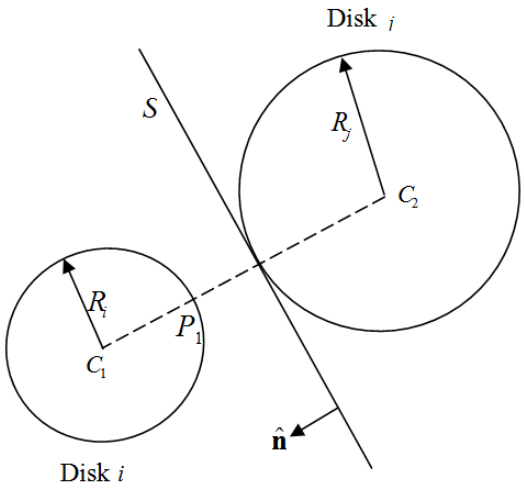

Figure 2-1. Disk-disk contact

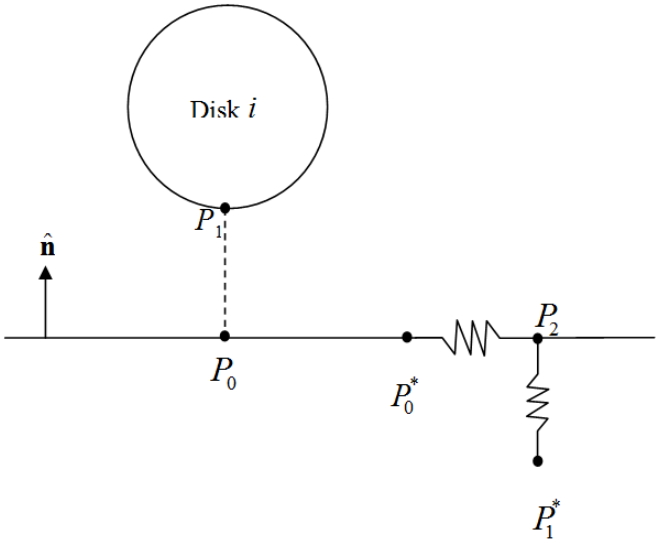

Figure 2-2. Springs for disk-disk and disk-boundary contacts

Moreover, $P_0(x_0, y_0)$ represents the projection of point P_1 on the reference line and P_0^* indicates this point after the displacement increment. Furthermore, assume (u_1, v_1) and (u_0, v_0) are the displacement increments of points P_1 and P_0, respectively, and the unit normal vector of the reference line is $\hat{\mathbf{n}}$. The normal distance d_n of point P_1^* from the reference line is:

$$d_n = \hat{\mathbf{n}}.\mathbf{P}_{\mathbf{01}}^* = \hat{\mathbf{n}}.\begin{bmatrix}(x_1+u_1)-(x_0+u_0)\\(y_1+v_1)-(y_0+v_0)\end{bmatrix} = \hat{\mathbf{n}}.\begin{bmatrix}x_1-x_0\\y_1-y_0\end{bmatrix} + \hat{\mathbf{n}}.\begin{bmatrix}u_1-u_0\\v_1-v_0\end{bmatrix} \tag{2-26}$$

where $\hat{\mathbf{n}}$ is unit normal vector of the reference line.

At the h-th iteration, the potential energy of the normal spring is given by:

$$\pi_n = \lambda_h d_n + \frac{1}{2} K_n d_n^2 \tag{2-27}$$

where λ_h is obtained as:

$$\lambda_h = \lambda_{h-1} + K_n d_n \tag{2-28}$$

and λ_h is the updated augmented Lagrangian multiplier, λ_{h-1} is the Lagrangian multiplier at $h-1$-th iteration, and K_n is the penalty number. This number can be variable and does not have to be a very large number as in the penalty method. The criterion for convergence is based on the L_2 norm of the residual forces:

$$\left(\frac{\| [K][D_k] - [K][D_{k-1}] \|}{\| [K][D_{k-1}] \|} \le Tol \right) \tag{2-29}$$

where Tol is a positive number close to zero that is specified by the user.

From Equation (2-27), we have:

$$\begin{aligned} \pi_n = \lambda_h \{G + [H_i]\{D_i\} - [Q_j]\{D_j\}\} + \frac{1}{2} K_n \{G + [H_i]\{D_i\} - [Q_j]\{D_j\}\} \\ .\{G + [H_i]\{D_i\} - [Q_j]\{D_j\}\} \end{aligned} \tag{2-30}$$

Expanding the right side of equation (30) and minimizing π_n by taking derivatives, four 4×4 stiffness sub-matrices and two 4×1 force sub-matrices are obtained:

$$\begin{aligned} & K_n [H_i]^T [H_i] \rightarrow [K_{ii}] \\ & -K_n [H_i]^T [Q_j] \rightarrow [K_{ij}] \\ & -K_n [Q_j]^T [H_i] \rightarrow [K_{ji}] \\ & K_n [Q_j]^T [Q_j] \rightarrow [K_{jj}] \\ & -(\lambda_k + K_n G)[H_i]^T \rightarrow [F_i] \\ & -(\lambda_h - K_n G)[Q_j]^T \rightarrow [F_j] \end{aligned} \tag{2-31}$$

which are added to Equation (2-7).

It is necessary to mention that as shown in Figure 2-3, the reference line in the original disk-based DDA presented by Ke and Bray (1995) is obtained using coordinates of two auxiliary points (points 2 and 3) which must be calculated in each iteration. By using the model presented in this paper, no more computations are needed to define the reference line and it can be obtained by only coordinates of disk centers and their radii, thus reducing the computational burden.

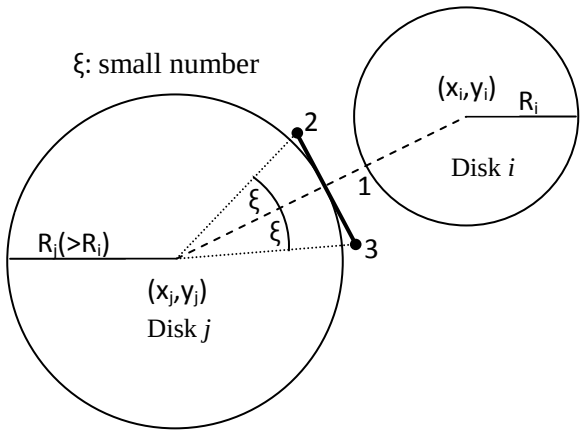

Figure 2-3. Reference line in the original disk-based DDA (Ke and Bray, 1995)

- *Sub-matrices of shear contact*

When the shear force is smaller than the shear resistance, a shear contact spring will be activated to reduce the relative displacement of the two disks.

The shear displacement along the $\mathbf{P}_0^*\mathbf{P}_2$ is obtained as:

$$d_s = \sqrt{\left|\mathbf{P_0^* P_1^*}\right|^2 - d_n^2} \tag{2-32}$$

The shear spring potential energy is:

$$\begin{aligned}\pi_s = \frac{1}{2}K_s d_s^2 = \frac{1}{2}K_s\left(\begin{bmatrix}x_1 - x_0 & y_1 - y_0\end{bmatrix} + [D_i]^T[T_i]^T - [D_j]^T[T_j]^T\right)^2 \\ -\frac{1}{2}K_s\left(G + [H_i]\{D_i\} - [Q_j]\{D_j\}\right)^2\end{aligned} \tag{2-33}$$

where K_s is stiffness of the shear spring. By expanding and minimizing the potential energy, we have:

$$\begin{aligned}&K_s[T_i]^T[T_i] - K_s[H_i]^T[H_i] \rightarrow [K_{ii}]_{4\times4} \\ &-K_s[T_i]^T[T_j] + K_s[H_i]^T[Q_j] \rightarrow [K_{ij}]_{4\times4} \\ &-K_s[T_j]^T[T_i] + K_s[Q_j]^T[H_i] \rightarrow [K_{ji}]_{4\times4} \\ &K_s[T_j]^T[T_j] - K_s[Q_j]^T[Q_j] \rightarrow [K_{jj}]_{4\times4}\end{aligned} \tag{2-34}$$

which are added to the sub-matrices $[K_{ii}], [K_{ij}], [K_{ji}],$ and $[K_{jj}]$ in the global stiffness matrix, and:

$$-K_s\left(G[H_i]^T + [T_i]^T\begin{bmatrix}x_1 - x_0 \\ y_1 - y_0\end{bmatrix}\right) \rightarrow \{F_i\} \tag{2-35}$$

$$K_s\left(G[Q_j]^T+[T_j]^T\begin{bmatrix}x_1-x_0\\y_1-y_0\end{bmatrix}\right)\rightarrow\{F_j\}$$

which are added to the global force vector.

- *Sub-matrices of frictional force*

The friction force potential energy is calculated as:

$$\pi_f=\lambda_h\tan(\varphi)\left(\begin{Bmatrix}u_1\\v_1\end{Bmatrix}^T-\begin{Bmatrix}u_0\\v_0\end{Bmatrix}^T\right)\begin{Bmatrix}p\\q\end{Bmatrix}=\lambda_h\tan(\varphi)\left(\{D_i\}^T.[T_i]^T-\{D_j\}^T.[T_j]^T\right)\begin{Bmatrix}p\\q\end{Bmatrix} \quad (2\text{-}36)$$

where λ_h is taken from the previous step and φ is the friction angle between disks, and

$$\begin{Bmatrix}p\\q\end{Bmatrix}=\frac{\mathbf{P_0^*P_2}}{\left|\mathbf{P_0^*P_2}\right|} \quad (2\text{-}37)$$

and $\mathbf{P_0^*P_2}$ represents the direction of the frictional force (Figure 2-2) and can be calculated as:

$$\mathbf{P_0^*P_2}=\mathbf{P_0^*P_1^*}-\left\langle\mathbf{P_0^*P_1^*},\hat{\mathbf{n}}\right\rangle.\hat{\mathbf{n}} \quad (2\text{-}38)$$

Let,

$$[M]=[T_i(x_1,y_1)]^T\begin{Bmatrix}p\\q\end{Bmatrix} \quad (2\text{-}39)$$

$$[N]=[T_j(x_0,y_0)]^T\begin{Bmatrix}p\\q\end{Bmatrix} \tag{2-40}$$

Equation (36) can be written as:

$$\pi_f=\lambda_h\tan(\varphi)\left(\{D_i\}^T.[M]-\{D_j\}^T.[N]\right) \tag{2-41}$$

After minimizing π_f, two 4×1 force sub-matrices are obtained:

$$\begin{aligned}&-\lambda_h\tan(\varphi)[M]\rightarrow\{F_i\}\\&\lambda_h\tan(\varphi)[N]\rightarrow\{F_j\}\end{aligned} \tag{2-42}$$

which are added to the global force vector.

2.5.2. Disk-boundary contact

Sub-matrices of normal and shear contacts and frictional force are presented for the disk-boundary contact type in the following sections.

- *Sub-matrices of normal contact*

At the h-th iteration, the potential energy of the normal spring is given by:

$$\pi_n=\lambda_h\{M+[H_i]\{D_i\}\}+\frac{1}{2}K_n\{M+[H_i]\{D_i\}\}.\{M+[H_i]\{D_i\}\} \tag{2-43}$$

By minimizing π_n by taking derivatives, a 4×4 stiffness sub-matrix and a 4×1 force sub-matrix are obtained:

$$K_n[H_i]^T[H_i] \rightarrow [K_{ii}]$$

$$-(\lambda_n + K_n M)[H_i]^T \rightarrow [F_i] \tag{2-44}$$

which are added to the sub-matrices $[K_{ii}]$ and $[F_i]$ in equation (7).

- *Sub-matrices of shear contact*

The shear spring potential energy is:

$$\pi_s = \frac{1}{2}K_s d_s^2 = \frac{1}{2}K_s\left(\begin{bmatrix} x_1 - x_0 & y_1 - y_0 \end{bmatrix} + [D_i]^T[T_i]^T\right)^2 - \frac{1}{2}K_s(M + [H_i]\{D_i\})^2 \tag{2-45}$$

By expanding and minimizing the potential energy, we have:

$$K_s[T_i]^T[T_i] - P_s[H_i]^T[H_i] \rightarrow [K_{ii}]_{4\times 4}$$

$$-K_s\left(M[H_i]^T + [T_i]^T\begin{bmatrix} x_1 - x_0 \\ y_1 - y_0 \end{bmatrix}\right) \rightarrow \{F_i\}_{4\times 1} \tag{2-46}$$

which are added to the sub-matrices of Equation (7).

- *Sub-matrix of frictional force*

The friction force potential energy is calculated as:

$$\pi_f = \lambda_n \tan(\varphi)\begin{Bmatrix} u_1 & v_1 \end{Bmatrix}\begin{Bmatrix} p \\ q \end{Bmatrix} = \lambda_n \tan(\varphi)\{D_i\}^T.[T_i]^T\begin{Bmatrix} p \\ q \end{Bmatrix} \tag{2-47}$$

After minimizing π_f, a 4×1 force sub-matrix is obtained:

$$-\lambda_h \tan(\varphi)[M] \rightarrow \{F_i\} \tag{2-48}$$

which is added to the global force vector.

2.6. Model Verification

In this section, five examples are presented to verify the model. The results are compared with analytical solutions and discussed in order to illustrate the capability of the proposed model.

2.6.1. Disk Deformation

In this example, the validity and capability of the derived formulation and developed code for the non-contact part of the model are studied. As shown in Figure 2-4, eight identical point forces are applied on a perimeter of a disk. The strain of the disk can be calculated as:

$$\varepsilon = \frac{(1-\upsilon)\sum_{i=1}^{n} F}{2\pi RE} \tag{2-49}$$

where F is magnitude of each applied force, n is number of applied point forces, and υ, E and R are Poisson's ratio, Young's Modulus and radius of the disk, respectively. In this example, it is assumed that $F = 10\,kN$, $\upsilon = 0.2$ and $R = 1\,m$. Moreover, the time step size is assumed to be 0.05s. The quasi-static analysis is used to model this problem. In this case, the disk velocity is set to zero at the start of each time step. Figure 2-5 shows the results of the proposed model for different values of Young's Modulus. As

can be seen, there is a very good agreement between the obtained results and the analytical solution.

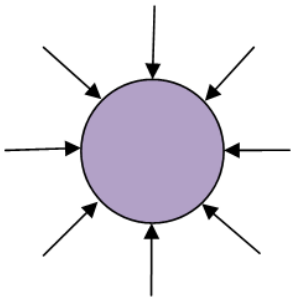

Figure 2-4. Deformation of a disk due to application of eight forces

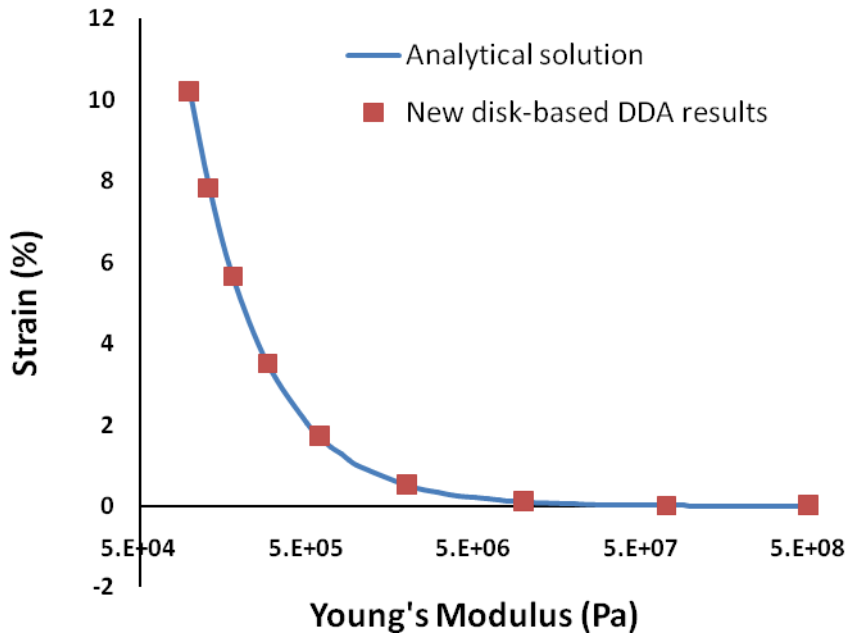

Figure 2-5. Comparison between the new disk-based DDA strain results and the analytical solution

2.6.2. Sliding Along an Incline

In this example, a single disk rests on an incline at angle 45^0 from horizontal and a surface friction angle of 15^0. Under the action of gravitational force, the displacement of the disk is determined analytically as:

$$s = \frac{1}{2} g \left(\sin(\alpha) - \tan(\varphi)\cos(\alpha)\right) t^2 \tag{2-50}$$

Where s is the displacement of the disk, α is the angle of incline, and t and φ are time and surface friction angle, respectively. Density, Young's modulus and Poisson's ratio for the disk are $2.6\times10^3\ kg/m^3$, $4\ GPa$, and 0.2, respectively. In addition, the stiffness of the normal contact spring and the time step size are $50\ MN/m$ and 0.05s, respectively. Figure 2-6 shows the simulation results of this example using the penalty method and the augmented Lagrangian method. As can be seen, when using the augmented Lagrangian method, a very good agreement with the analytical solutions is obtained. However, it is seen that the results obtained using the penalty method show a significant error compared with the analytical solutions. This example demonstrates the ability of the proposed disk-based DDA method to simulate sliding of disks on an incline.

2.6.3. Rockfall

Rockfall is one of the main hazards in rock slope cut for railways and highways. In order to model rockfall by the proposed disk-based DDA, one rock block with a horizontal initial velocity of $0.75\ m/s$ was allowed to drop from a height of $82m$. The radius and density of the falling rock are $1m$ and $2t/m^3$, respectively.

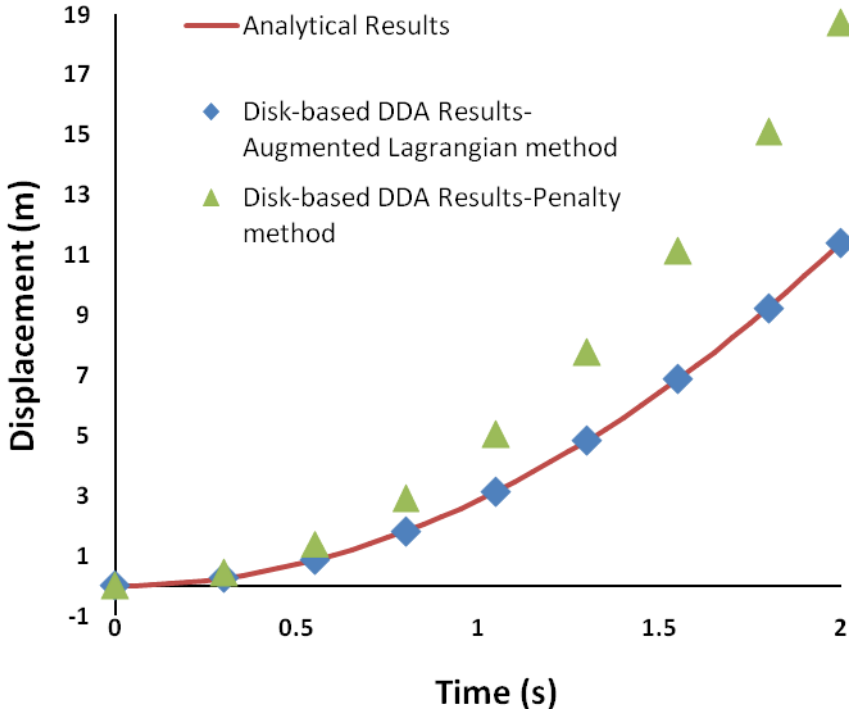

Figure 2-6. Comparison between the disk-based DDA results using the penalty method and the augmented Lagrangian method and the analytical solution

The friction angle is 10^{0}. Moreover, the penalty number and the simulation time step size are $5\times10^{6}\ N/m$ and $0.05s$, respectively. Figures 2-7a and 2-7b show the trajectory of the disk computed by the DDA using the augmented Lagrangian and the penalty method, respectively. As can be seen, the proposed disk-based DDA using the augmented Lagrangian method can simulate rockfall very well, whereas the penalty method is not able to model it.

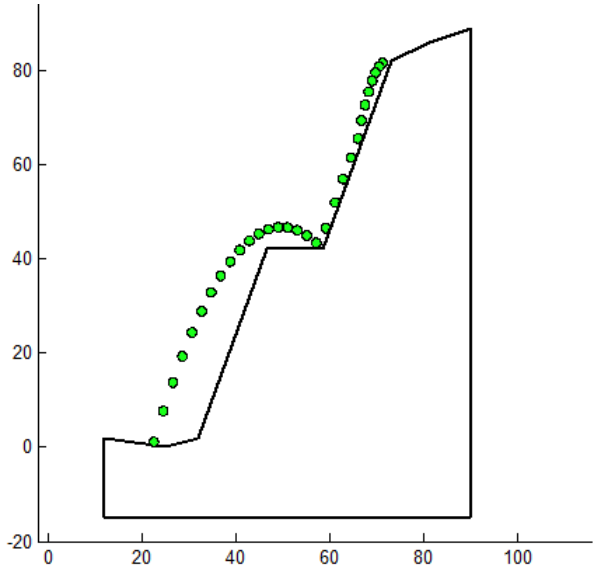

(a)

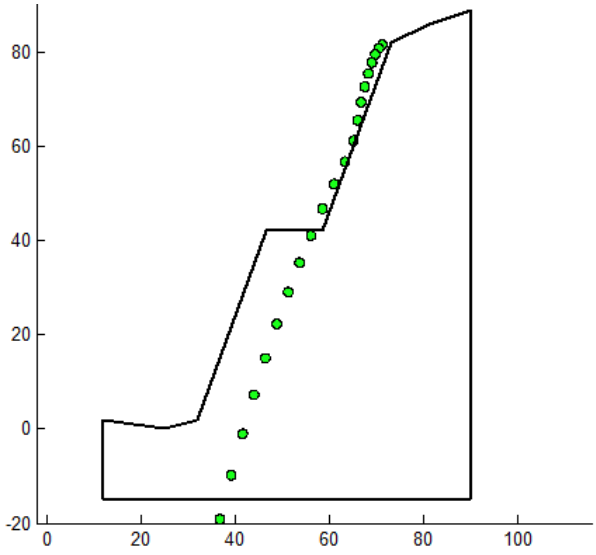

(b)

Figure 2-7. (a) The simulated trajectory using the augmented Lagrangian method (b) The simulated trajectory using the penalty method

2.6.4. Funnel flow

In this example the efficiency of the proposed model for collections of disks and two boundaries is investigated. As shown in Figure 2-8, there are three layers of disks with different sizes above a funnel which fall down due to gravity. Each disk has a density of $2500 kg/m^3$ and the stiffness of the normal contact spring, the time step size and the friction angle are $P = 5 \times 10^7 N/m$, $0.05s$ and 5°, respectively. Figures 2-9, 2-10 and 2-11 show the configuration of disks after 5.5s, 7.8s and 9.25s using the penalty method and the augmented Lagrangian method, respectively. As can be seen, unlike the penalty method, the disks flow through the funnel without any overlap between disks-disks or disks-boundaries when the augmented Lagrangian method is used. This example demonstrates that the model is able to represent geometrical movement of the granular assemblage reasonably well.

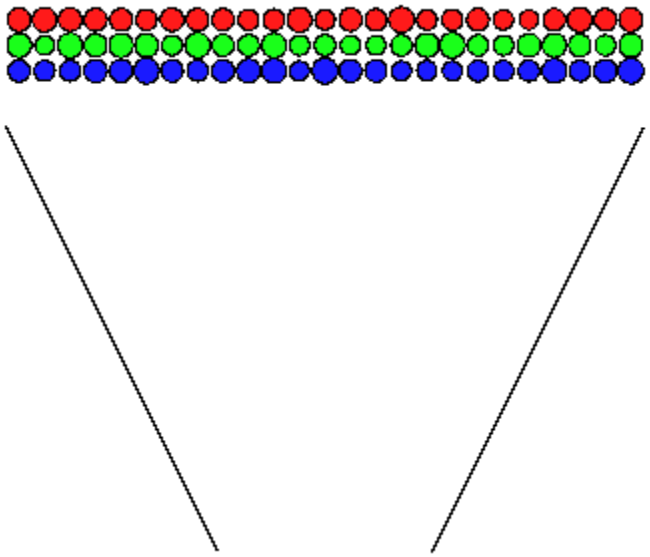

Figure 2-8. Initial configuration of funnel flow

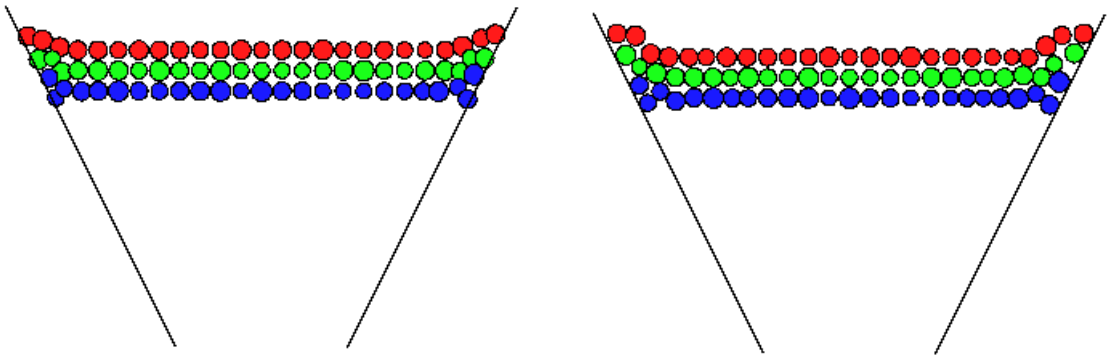

(a) (b)

Figure 2-9. Configuration of funnel flow after 5.5s (a) using the penalty method (b) using the augmented Lagrangian method

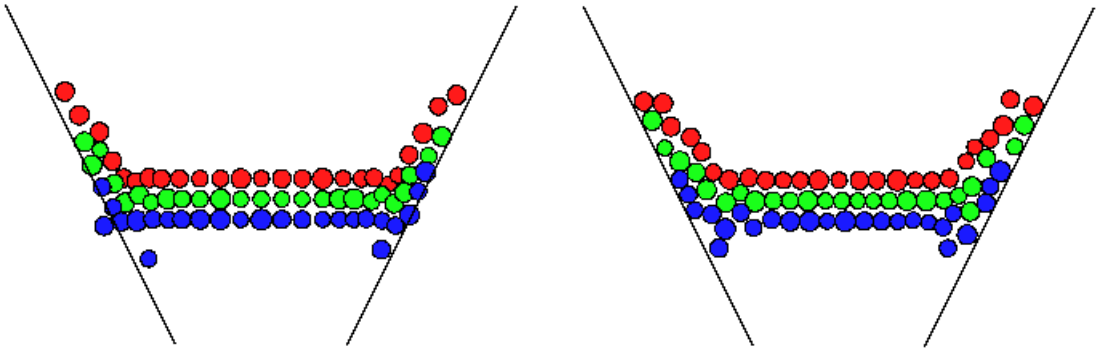

(a) (b)

Figure 2-10. Configuration of funnel flow after 7.8s (a) using the penalty method (b) using the augmented Lagrangian method

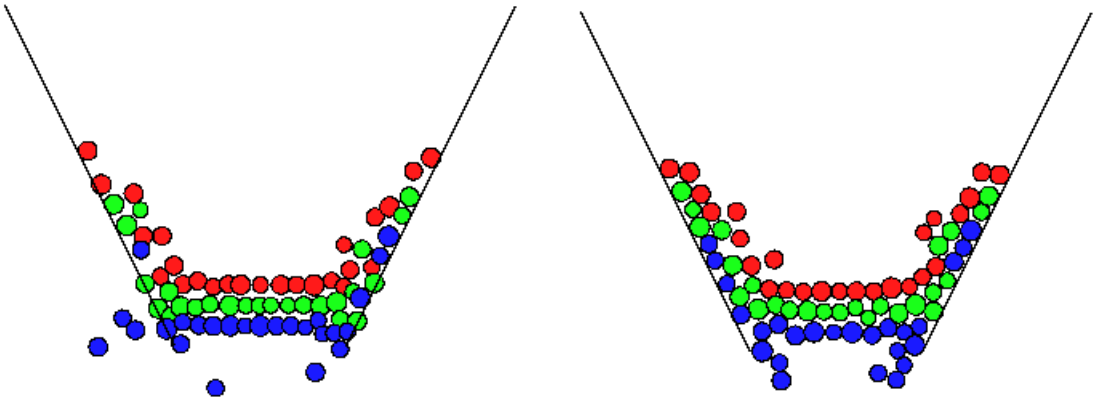

(a) (b)

Figure 2-11. Configuration of funnel flow after 9.25s (a) using the penalty method (b) using the augmented Lagrangian method

2.6.5. Multiple slopes

In this example, which is a landslide analogy, modeling of disks in contact with multi-boundaries is considered. The initial configuration of this example is shown in Figure 2-12. As can be seen a large number of disks rests on the highest incline of a slope including four inclines.

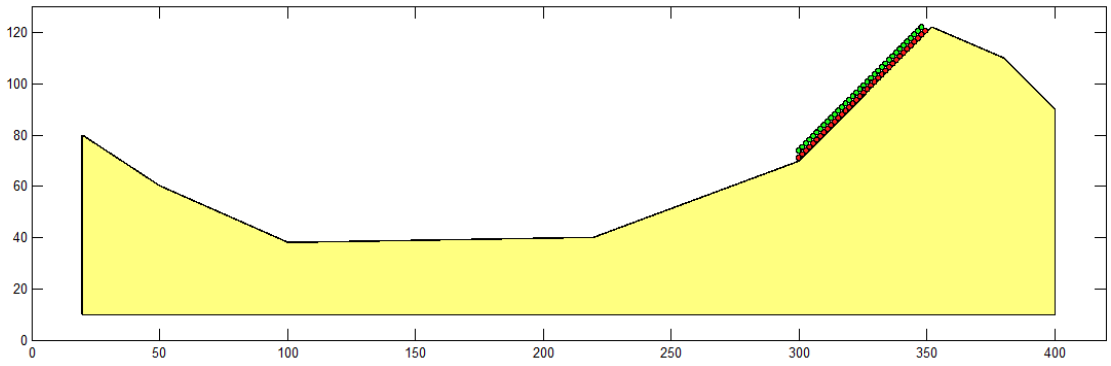

Figure 2-12. Initial configuration of multi-slopes modeling

The friction angle for disk-disk and disk-boundary is 20°. The disks move on the inclines under the action of gravitational force. The time step size, Young's modulus, Poisson's ratio and density of the disks are assumed to be $0.005s$, $5\,GPa$, 0.25 and $2700\,kg/m^3$. The penalty number is considered to be $1\times10^7\,N/m$. The results using the penalty method and the augmented Lagrangian method after 20s, 40s and 60s are shown in Figures 2-13, 2-14 and 2-15, respectively.

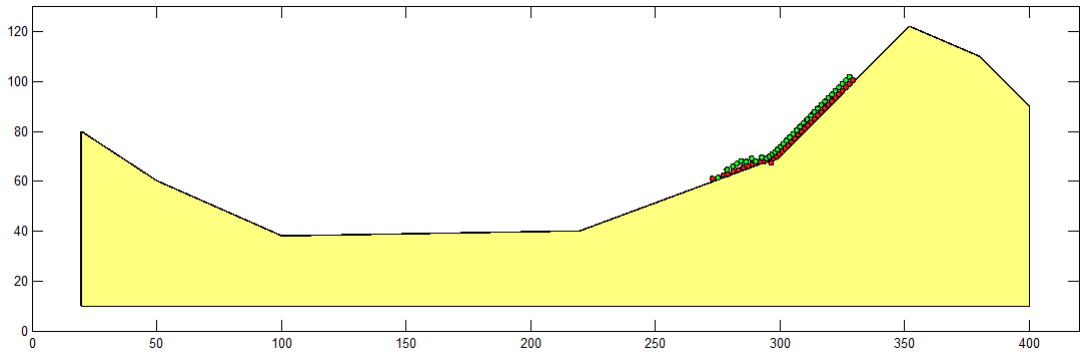

(a)

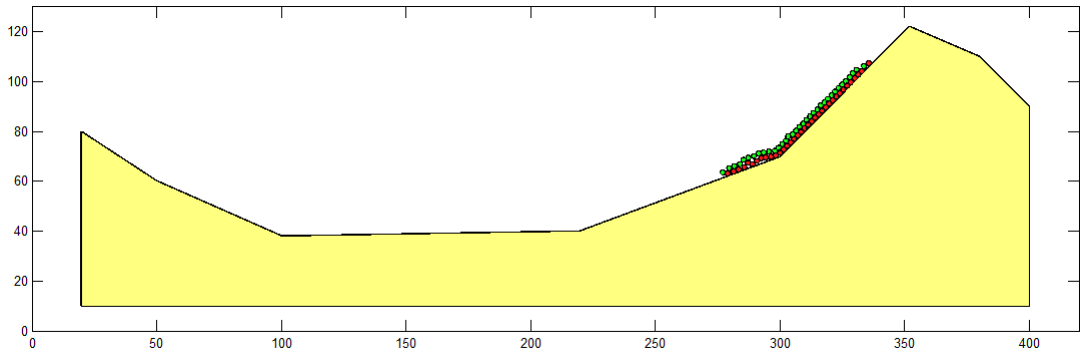

(b)

Figure 2-13. Configuration of multi-slopes modeling after 20s (a) using the penalty method (b) using the augmented Lagrangian method

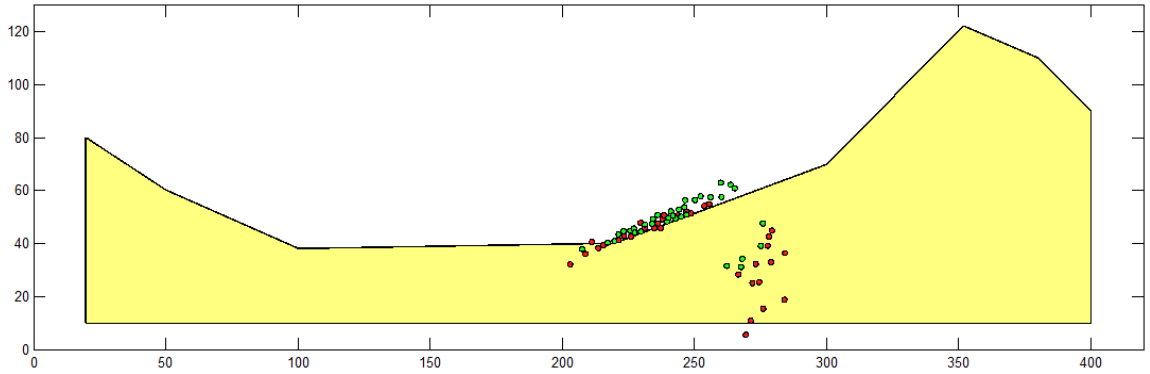

(a)

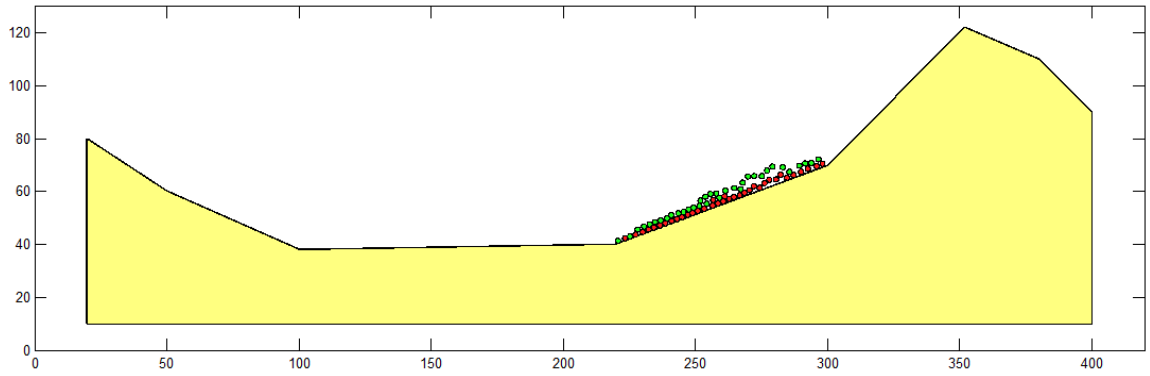

(b)

Figure 2-14. Configuration of multi-slopes modeling after 40s (a) using the penalty method (b) using the augmented Lagrangian method

As can be seen, the constraints of the problem are violated severely using the penalty method; however the proposed model using the augmented Lagrangian method can simulate this example very well without any violation of boundary constraints.

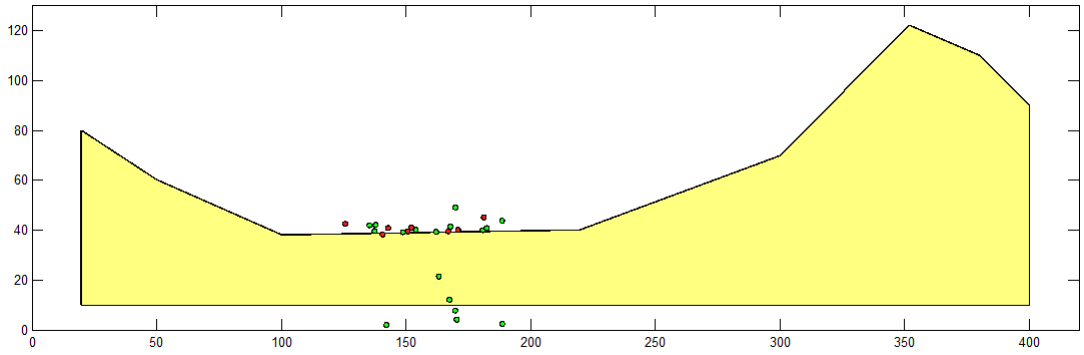

(a)

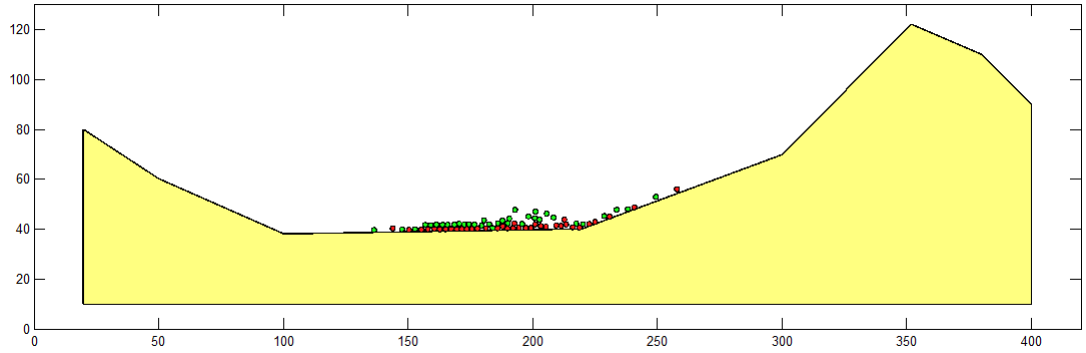

(b)

Figure 2-15. Configuration of multi-slopes modeling after 60s (a) using the penalty method (b) using the augmented Lagrangian method

2.6.6. Ground movement under high loading

In this example, which is similar to the last example presented by Ke and Bray (1995), ground movement under high loading is studied. As shown in Figure 2-16(a), a continuous footing moving downward at a rate of 1 m/s is located on the assemblage of 910 disks with a same size. It is assumed that there is no cohesion, and friction angle,

density, time step size and penalty number are 5°, $1500 kg/m^3$, $0.01\ s$, and $10^4\ kN/m$, respectively. The results obtained using the penalty method and the augmented Lagrangian method after 1.4s whence vertical displacement of the footing is 60% of the footing width, are shown in Figure 2-16(b) and 2-16(c), respectively. As can be seen, the proposed model using the augmented Lagrangian method is able to represent geometrical deformation of the granular assemblage reasonably well (Das, 2011), but using the penalty method causes several penetrations and the results are not acceptable.

2.7. Conclusions

In this chapter, a formulation of the DDA method for non-rigid disks with a new contact model has been derived and presented. In this model, disk-disk and disk-boundary contacts can be converted to point-to-line contacts. Contact formulae, including those for the normal and shear springs and the frictional force sub-matrices are derived in detail using vector analysis and the augmented Lagrangian method. The success and accuracy of the formulation are demonstrated through several examples. The following conclusions are derived from this study:

- The number of governing equations is not increased because of the contacts. The proposed model is simple and efficient and can be easily coded into a computer program.
- Unlike the original disk-based DDA, disks are not completely rigid and more accurate results can be obtained by using the derived formulations. However, disks are not

considered rigid, and there are no more computations needed for contact detection since disks remain circles all the time.

- In the presented model, unlike the original disk-based DDA, there is no need to calculate coordinates of two auxiliary points in each iteration to find the reference line. The new contact model simply uses only coordinates of disk centers and their radii to obtain the reference line.
- The accuracy of the contact solution depends highly on the choice of the penalty number in the existing disk-based DDA and the optimal number cannot be explicitly found a priori. These limitations can lead to significant inaccuracy and violation of physical constraints of the problem so the simulation results may easily be affected and the results can be unreliable. As shown by the examples presented, these disadvantages are overcome by using the augmented Lagrangian method. However, if the initial penalty number is too small, many iterations are required.

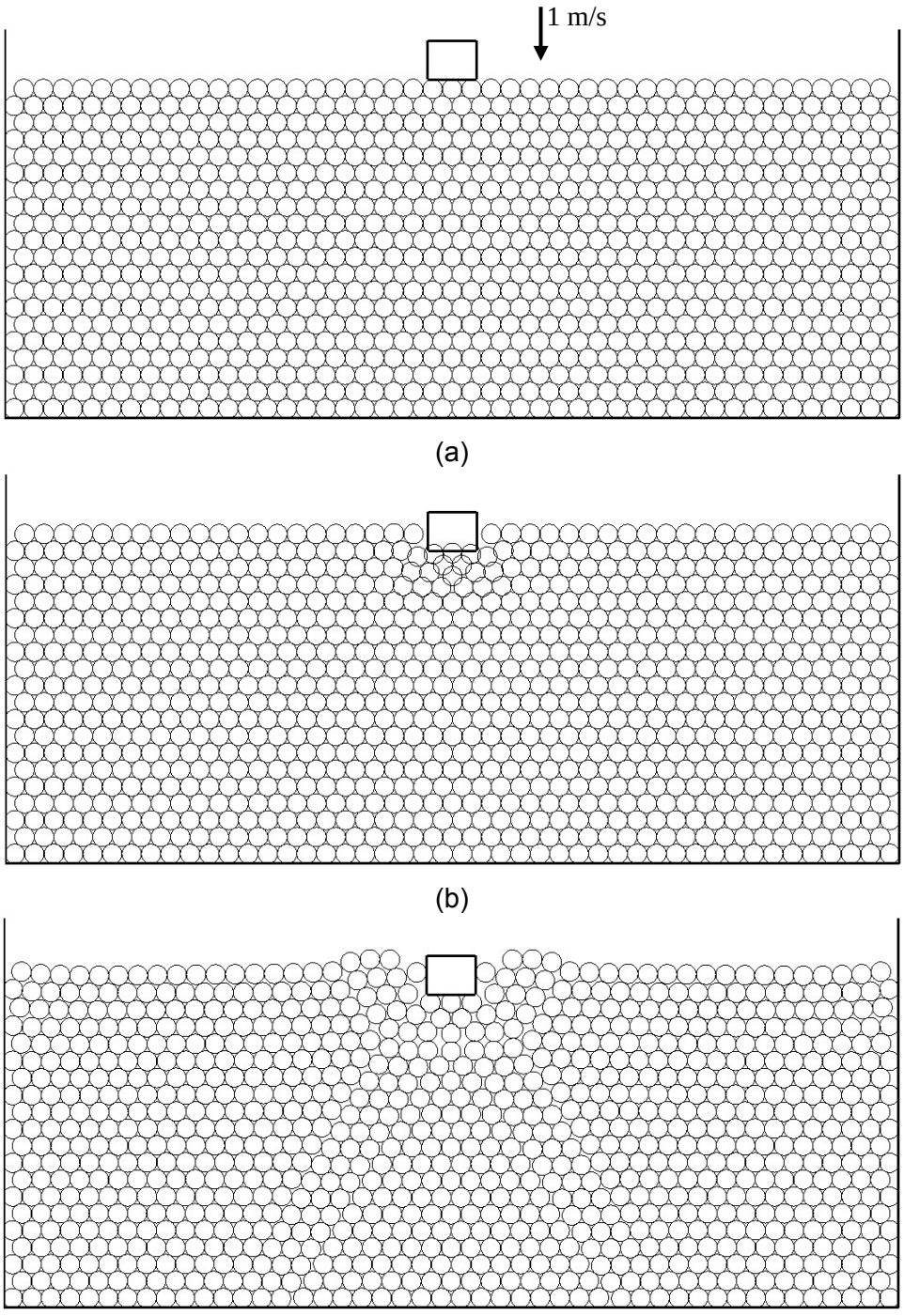

Figure 2-16. Ground movement under high loading (a) initial configuration(t=0) (b) results obtained by penalty method (t=1.4s) (c) results obtained using the augmented Lagrangian method (t=1.4s)

2.8. References

Das B. 2011. Principles of Foundation Engineering. Stanford, CT :Cengage Learning.

Hatzor YH and Bakun-Mazor D. 2011. Modeling dynamic deformation in natural rock slopes and underground openings with DDA: review of recent results. Geomechanics and Geoengineering: An International Journal; 6(4):283-292.

Jing L. 2003. A review of techniques, advances and outstanding issues in numerical modelling for rock mechanics and rock engineering. International Journal of Rock Mechanics and Mining Sciences, 40(3): 283–353.

Jing L and Hudson JA. 2002. Numerical methods in rock mechanics, International Journal of Rock Mechanics & Mining Sciences, 39: 409–427.

Ke TC and Bray JD. 1995. Modeling of particulate media using discontinuous deformation analysis. J. Eng. Mech. 121(11): 1234–1243.

Koo CY and Chern JC. 1998. Modification of the DDA method for rigid block problems. International Journal of Rock Mechanics and Mining Sciences, 35(6):684–693.

Koyama T, Nishiyama S, Yang M, Ohnishi Y. 2011. Modeling the interaction between fluid flow and particle movement with discontinuous deformation analysis (DDA) method, Int. J. Numer. Anal. Meth. Geomech. 35:1–20.

Lin CT, Amadei B, Jung J and Dwyer J. 1996. Extensions of discontinuous deformation analysis for jointed rock masses. International Journal of Rock Mechanics and Mining Science, 33(7):671-694.

MacLaughlin MM, Doolin DM. 2006. Review of validation of the discontinuous deformation analysis (DDA) method, Int J Numer Anal Meth Geomech, 30: 271-305.

Mohammadi S. 2003. Discontinuum Mechanics: Using Finite and Discrete Elements. WIT Press.

Ohnishi Y and Nishiyama S. 2007. Recent insights of analyses using discontinuous methods in rock engineering in Japan. In: Ju Y, Fang X, Bian H, editors Proceedings of the eighth international conference on the analysis of discontinuous deformation, Beijing, China, p.15–26.

Shi GH. 1993. Block System Modeling by Discontinuous Deformation Analysis. Computational Mechanics Publication: Southampton, U.K.

Soto-Yarritu GR and Martinez A. 2001. Computer simulation of granular material: Vibrating feeders. Powder Handling Process, 13(2):181–184.

Thomas PA. 1997. Discontinuous deformation analysis of particulate media. PhD thesis, Univ. of California, Berkeley, Berkeley, Calif.

Thomas PA and Bray JD. 1999. Capturing nonspherical shape of granular media with disk clusters. J. Geotech. Geoenviron. Eng. 125(3), 169–178.

Chapter 3: 3-D DDA Method for Particulate Media Applications

(This chapter was published as Beyabanaki SAR and Bagtzoglou AC. 2012. Three-dimensional discontinuous deformation analysis (3-D DDA) method for particulate media applications, Geomechanics and Geoengineering: An International Journal 7(4): 239-253)

3.1. Introduction

Materials formed by multiple solid particles, such as soil, flour, sugar, cement and pills, are defined as particulate materials. Industries like geotechnics, mining, construction, metallurgy, chemical, food processing and many others use particulate materials in their applications and processes.

The Micro-mechanical behaviour of discrete materials can be studied by numerical modelling of particular assemblies. 2-D circular blocks and 3-D spherical blocks are the best particle shapes for representing particulate materials in terms of computational convenience (Poschel and Schwager 2005). Using these particle shapes, computer memory requirements and computer processing time are minimized and analysis with large numbers of particles is possible.

A discrete numerical simulation of granular soils with the Discrete Element Method (DEM) is presented by Cundall and Strack (1979). The development and applications of the DEM for micro-mechanics of granular materials are presented in a series of conference and symposia proceedings (Jenkins and Satake 1983, Satake and Jenkins 1988, Mustoe et al. 1989, Williams and Mustoe 1993, Cook and Jensen 2002, Cleary

2007, Munjiza 2010). A comprehensive review of DEM work can be found in Radjai and Dubois (2011). The PFC (Particle Flow Code) codes for both 2-D and 3-D problems (Itasca 2001) are the most renowned codes in this field.

The Discontinuous Deformation Analysis (DDA) technique was introduced by Shi (1988, 1993) to analyze the mechanical response of discrete blocks. An implicit approach is used by the DDA to solve for displacement unknowns at discrete time intervals. A penalty method is used to model the block interactions by springs. The DDA method has four main advantages over the DEM (Jing and Hudson 2002, Jing 2003, MacLaughlin and Doolin 2006, Bobet et al. 2009, Koyama et al. 2011): (1) The DDA is unconditionally stable due to its implicit time integration and can use significantly larger time steps. (2) The DDA method does not require an artificial damping term to dissipate energy by using an energy approach. (3) In the DEM, dashpot is used to prevent the oscillation during the analysis, whereas in the DDA, only penalty springs are used for contact mechanics. (4) In the DDA method, closed-form integrations for the stiffness matrices of blocks can be derived without the need for Gaussian quadrature techniques.

Even though a lot of work has been done on DDA to date (a review of more than 100 published and unpublished validation studies on the DDA is presented by MacLaughlin and Doolin (2006)) the development of the DDA in particulate media is still at an early stage. Ke and Bray (1995), Thomas and Bray (1999) and Thomas (1997) have demonstrated qualitatively the ability of the DDA to model the response of systems of disks. Soto- Yarritu and Martinez (2001) have used this algorithm to model granular transport in vibrating feeders. O'Sullivan and Bray (2003) modified the spring formulation for the DDA. Recently, Koyama et al. (2011) presented coupled solid circular particles

movement and fluid flow processes in porous media using combined DDA-FEM approach.

Unlike the plane strain/stress situation in continuum mechanics, there is no 2-D granular assemblage in reality. In some cases, approximations in 2-D may be good enough, but almost always 3-D simulations could present more realistic results. To resolve the limitations of 2-D approaches, a few discrete numerical computer codes in 3-D have been presented by some researchers (Cundall 1988, Hart et al. 1988, Ghaboussi and Barbosa 1990, Walton 1993, Lin and Ng 1994, Wang and Tonon 2010).

However, relatively little work on DDA development in 3-D has been published. Shi (2001) and Wu et al. (2005c) provided basic formulations for matrices for different potential terms. Liu et al. (2004) and Yeung et al. (2003, 2004) highlighted the application of 3-D DDA. Jiang and Yeung (2004) developed a point-to-face model for 3-D DDA. Wu et al. (2005a) developed a new contact searching algorithm for frictionless vertex-to-face contact problems and presented the 3-D DDA formulation for normal contact force. Yeung et al. (2007) and Wu (2008) presented algorithms for edge-to-edge contacts. Beyabanaki et al. (2008a) presented a new algorithm to search and calculate geometrical contacts in the 3-D DDA. Grayeli and Hatami (2008) used four-noded tetrahedral elements to improve the accuracy of the 3-D DDA. Beyabanaki et al. (2009a, 2009b) implemented Trilinear and Serendipity hexahedron meshes into 3-D DDA to improve its deformability. Beyabanaki et al. (2008b, 2009c, 2010a) presented 3-D DDA with high-order displacement functions. Beyabanaki et al. (2009d) presented 3-D DDA with nth-order displacement functions. Beyabanaki et al. (2009e) presented a new point-to-face contact algorithm for contacts between two polyhedral with planar boundaries in 3-D DDA. Beyabanaki et al. (2009f) examined the validity of 3-D DDA by comparing its

solution for dynamic block displacement with analytical solution. Moreover, they improved edge-to-edge contact constraints by using the augmented Lagrangian method. Contact theory of nth-order 3-D DDA is presented by Beyabanaki et al. (2010b). Bakun-Mazor et al. (2013) proposed an analytical solution for dynamic, single and double face sliding and use it to validate 3-D DDA. Recently, Beyabanaki and Yeung (2011) modified contact constraints in high-order 3-D DDA and presented the corresponding formulations.

In this study, 3-D DDA is used to model particulate media. Stiffness and force matrices in 3-D DDA for sphere blocks bounded by rigid boundaries are presented and the developed code is verified by various examples. Results of simulations demonstrate that the model is able to represent geometrical deformation of the granular assemblages reasonably well and can be used to efficiently carry out analyses.

3.2. Approximation of Displacements in 3-D DDA

Static and dynamic analyses are performed by DDA. The large relative movements between blocks and the large deformation in a block are accumulated over many time steps. In 3-D DDA, for each block, the displacement matrix at an arbitrary point (x, y, z) in the block is obtained by means of linear approximation from the corresponding location and the displacement vector $\{D\}$. Assuming that the spheres (spherical blocks) are rigid, the relation between them can be shown as below:

$$\begin{Bmatrix} u \\ v \\ w \end{Bmatrix} = [T_i(x, y, z)].\{D_i\} \tag{3-1}$$

where

$$[T_i(x,y,z)] = \begin{pmatrix} 1 & 0 & 0 & 0 & (z-z_0) & -(y-y_0) \\ 0 & 1 & 0 & -(z-z_0) & 0 & (x-x_0) \\ 0 & 0 & 1 & (y-y_0) & -(x-x_0) & 0 \end{pmatrix} \tag{3-2}$$

$$\{D_i\}^T = \{u_0 \quad v_0 \quad w_0 \quad r_x \quad r_y \quad r_z\} \tag{3-3}$$

(x_0, y_0, z_0) are the coordinates of the sphere center, and (u_0, v_0, w_0) represents rigid body translations; (r_x, r_y, r_z) indicates the rotation angles in radians of sphere i with a rotation centre at (x_0, y_0, z_0). $[T_i(x,y,z)]$ is the first order displacement function, and $\{D_i\}$ is the vector of displacements of sphere i in three dimensions.

The linear displacement function can cause free expansion under rigid body rotation. To eliminate the possibility for this error, the exact solution for the displacements can be used to compute the components of (u,v,w) due to (r_x, r_y, r_z) by extending the following rigid body rotation (Wu et al. 2005b):

$$\begin{cases} u = u_0 + (x-x_0)(\cos r_z - 1) - (y-y_0)\sin r_z + (z-z_0)\sin r_y + (x-x_0)(\cos r_y - 1) \\ v = v_0 + (x-x_0)\sin r_z + (y-y_0)(\cos r_z - 1) + (y-y_0)(\cos r_x - 1) - (z-z_0)\sin r_x \\ w = w_0 + (z-z_0)(\cos r_y - 1) - (x-x_0)\sin r_y + (y-y_0)\sin r_x + (z-z_0)(\cos r_x - 1) \end{cases} \tag{3-4}$$

3.3. Simultaneous Equations

3-D DDA, is an implicit technique, and involves formulation and solution of a system of simultaneous equilibrium equations. In this method, blocks are connected and form a block system by displacement constraints on single blocks and contacts between blocks.

As the minimum total potential energy principle is applied in 3-D DDA, the total potential energy is the summation of all potential energy sources for each block which involves the potential energy contributed by the point loads on a block, inertia forces, volume forces, fixed points, and potential energy when the blocks contact each other.

The total potential energy for an N blocks (spheres) system can be expressed in matrix form as follows:

$$\begin{bmatrix} [K_{11}] & [K_{12}] & [K_{13}] & \dots & [K_{1N}] \\ [K_{21}] & [K_{22}] & [K_{23}] & \dots & [K_{2N}] \\ [K_{31}] & [K_{32}] & [K_{33}] & \dots & [K_{3N}] \\ \vdots & \vdots & \vdots & \ddots & \vdots \\ [K_{N1}] & [K_{N2}] & [K_{N3}] & \dots & [K_{NN}] \end{bmatrix} \begin{Bmatrix} \{D_1\} \\ \{D_2\} \\ \{D_3\} \\ \vdots \\ \{D_N\} \end{Bmatrix} = \begin{Bmatrix} \{F_1\} \\ \{F_2\} \\ \{F_3\} \\ \vdots \\ \{F_N\} \end{Bmatrix} \tag{3-5}$$

where $\{D_i\}$ and $\{F_i\}$ indicate displacement variables and loading and moments caused by the stresses and external forces acting on sphere i , respectively. The stiffness sub-matrices $[K_{ij}]\big|_{i=j}$ depend on the material properties of sphere i, and $[K_{ij}]\big|_{i\neq j}$ are defined by the contacts between spheres i and j.

The equilibrium equations for each time step are derived by minimizing the total potential energy in each variable for only one sphere. For sphere i, the following equations indicate the equilibrium of all contact forces and loads acting on sphere i along X, Y and Z directions, respectively:

$$\frac{\partial \pi}{\partial u} = 0 \quad , \qquad \frac{\partial \pi}{\partial v} = 0 \quad , \qquad \frac{\partial \pi}{\partial w} = 0 \tag{3-6}$$

where π is the total potential energy (including the potential energy due to body force, π_b, point loading, π_P, inertia forces, π_I, constrained spring, π_C, normal contact, π_n, shear contact, π_s, and friction force, π_f).

The moment equilibrium of all contact forces and loads acting on sphere i is represented by the following equations:

$$\frac{\partial \pi}{\partial r_x} = 0 \quad , \qquad \frac{\partial \pi}{\partial r_y} = 0 \quad , \qquad \frac{\partial \pi}{\partial r_z} = 0 \tag{3-7}$$

A 6×6 sub-matrix, which is the sub-matrix $[K_{ij}]$ in the global Equation (3-5), is formed by the following differentiations:

$$\frac{\partial^2 \pi}{\partial d_{ri} \partial d_{sj}} \quad , \qquad r, s = 1, 2, ..., 6 \tag{3-8}$$

where

$$\{D_i\}^T = \{d_{1i} \quad d_{2i} \quad d_{3i} \quad d_{4i} \quad d_{5i} \quad d_{6i}\}$$

$$\{D_j\}^T = \{d_{1j} \quad d_{2j} \quad d_{3j} \quad d_{4i} \quad d_{5j} \quad d_{6j}\} \tag{3-9}$$

The following differentiations:

$$-\frac{\partial \pi(0)}{\partial d_{ri}} \quad , \qquad r = 1, 2, ..., 6 \tag{3-10}$$

lead to a 6×1 sub-matrix, which is the sub-matrix $\{F_i\}$ in Equation (3-5).

After solving the displacement vectors, Equation (3-4) is applied to update the coordinates of each sphere and to judge the contact patterns at the end of each time step.

3.4. Derivations of Non-Contact Sub-Matrices of Equilibrium Equation

In this section, the sub-matrices of the global equilibrium equation (3-5) are derived as follows.

3.4.1. Sub-matrix of Body Forces

Assuming that a given load $(f_{x_i}, f_{y_i}, f_{z_i})$ is the constant body force acting on the entire volume of the i-th sphere, the potential energy due to body forces, π_b, is:

$$\pi_b = -\iiint_V \begin{Bmatrix} u & v & w \end{Bmatrix} \begin{Bmatrix} f_{x_i} \\ f_{y_i} \\ f_{z_i} \end{Bmatrix} dxdydz = -\{D_i\}^T \left(\iiint_V [T_i(x_0, y_0, z_0)]^T \, dxdydz \right) \begin{pmatrix} f_{x_i} \\ f_{y_i} \\ f_{z_i} \end{pmatrix} \quad (3\text{-}11)$$

Minimizing the potential energy, π_b, gives:

$$\iiint_V [T_i(x_0, y_0, z_0)]^T \, dxdydz \begin{pmatrix} f_{x_i} \\ f_{y_i} \\ f_{z_i} \end{pmatrix} \rightarrow \{F_i\} \quad (3\text{-}12)$$

Therefore,

$$\begin{pmatrix} \left(\frac{4}{3}\pi R_i^3\right) f_x & 0 & 0 & 0 & 0 & 0 \\ 0 & \left(\frac{4}{3}\pi R_i^3\right) f_y & 0 & 0 & 0 & 0 \\ 0 & 0 & \left(\frac{4}{3}\pi R_i^3\right) f_z & 0 & 0 & 0 \end{pmatrix}^T \rightarrow \{F_i\} \tag{3-13}$$

which is added to the global equation (3-5). In (3-13), R_i is radius of the i-th sphere.

3.4.2. Sub-matrix of Point Loading

Consider (F_x, F_y, F_z) is applied to a point (x, y, z) within i-th sphere. The potential energy of the point loading (F_x, F_y, F_z) is:

$$\pi_P = -\{u_0 \quad v_0 \quad w_0\} \begin{Bmatrix} F_x \\ F_y \\ F_z \end{Bmatrix} = -\{D_i\}^T [T_i(x, y, z)]^T \begin{Bmatrix} F_x \\ F_y \\ F_z \end{Bmatrix} \tag{3-14}$$

where $\{u_0 \quad v_0 \quad w_0\}$ is displacement at point (x, y, z). Minimizing π_P, we have:

$$[T_i(x, y, z)]^T \begin{Bmatrix} F_x \\ F_y \\ F_z \end{Bmatrix} \rightarrow \{F_i\} \tag{3-15}$$

which is added to $\{F_i\}$ in the global equation (3-5).

3.4.3. Sub-matrix of Inertia Forces

DDA uses both statics and dynamics computations. The velocity is zero in the beginning of each time step in the statics computation while in the dynamics computation, the velocity is inherited from the previous time step.

The inertia force potential energy of the i-th sphere, π_I, is:

$$\pi_I = \iiint_V M\{u\ v\ w\} \frac{\partial^2}{\partial t^2} \begin{Bmatrix} u(t) \\ v(t) \\ w(t) \end{Bmatrix} dxdydz \tag{3-16}$$

where M is density, $u(t)$, $v(t)$ and $w(t)$ are the time-dependent displacements of any point of the i-th sphere.

Assuming constant acceleration at each time step, $\{D_i(0)\} = \{0\}$ as the displacements at the beginning of the time step, and using the Taylor approximation, we have:

$$\frac{\partial^2 \{D_i(0)\}}{\partial t^2} = \frac{2}{\Delta^2}\{D_i\} - \frac{2}{\Delta}\frac{\partial \{D_i(0)\}}{\partial t} = \frac{2}{\Delta^2}\{D_i\} - \frac{2}{\Delta}\{a_i(0)\} \tag{3-17}$$

where Δ is time interval of this time step, $\{D_i(\Delta)\} = \{D_i\}$ is the displacements at the end of the time step, and $\{a_i(0)\}$ is the velocity at the beginning of the time step.

Therefore:

$$\begin{aligned} \pi_I &= M\{D_i\}^T \left[\iiint_V \left[T_i(x,y,z)\right]^T \left[T_i(x,y,z)\right] dxdydz \right] \frac{\partial^2 \{D_i(0)\}}{\partial t^2} \\ &= \{D_i\}^T \left[\iiint_V \left[T_i(x,y,z)\right]^T \left[T_i(x,y,z)\right] dxdydz \right] \left(\frac{2M}{\Delta^2}\{D_i\} - \frac{2M}{\Delta}\{a_i(0)\} \right) \end{aligned} \tag{3-18}$$

Minimizing π_I, we have:

$$\frac{2M}{\Delta^2}\left[\iiint_V \left[T_i(x,y,z)\right]^T\left[T_i(x,y,z)\right]dxdydz\right] \rightarrow [K_{ii}] \tag{3-19}$$

$$\frac{2M}{\Delta}\left[\iiint_V \left[T_i(x,y,z)\right]^T\left[T_i(x,y,z)\right]dxdydz\right]\{a_i(0)\} \rightarrow \{F_i\} \tag{3-20}$$

which are then added to the global simultaneous equations (3-5).

The integral in equations (3-19) and (3-20) is obtained as below:

$$\iiint_V \left[T_i(x,y,z)\right]^T\left[T_i(x,y,z)\right]dxdydz = \begin{pmatrix} \frac{4}{3}\pi R_i^3 & 0 & 0 & 0 & 0 & 0 \\ 0 & \frac{4}{3}\pi R_i^3 & 0 & 0 & 0 & 0 \\ 0 & 0 & \frac{4}{3}\pi R_i^3 & 0 & 0 & 0 \\ 0 & 0 & 0 & \frac{8}{15}\pi R_i^5 & 0 & 0 \\ 0 & 0 & 0 & 0 & \frac{8}{15}\pi R_i^5 & 0 \\ 0 & 0 & 0 & 0 & 0 & \frac{8}{15}\pi R_i^5 \end{pmatrix} \tag{3-21}$$

3.4.4. Sub-matrix of displacement constraint

Spheres can be constrained at specific points as a boundary condition. In this situation, three pairs of very stiff springs with stiffness P are used along x, y and z directions to impose to the constraint.

The potential energy of the constrained spring, π_C, is:

$$\pi_C = \frac{p}{2}\left\{(u^c - u) \quad (v^c - v) \quad (w^c - w)\right\}\begin{Bmatrix} u^c - u \\ v^c - v \\ w^c - w \end{Bmatrix}$$

$$= \frac{p}{2}\{D_i\}^T\left[T_i(x,y,z)\right]^T\left[T_i(x,y,z)\right]\{D_i\} - p\ \{D_i\}^T\left[T_i(x,y,z)\right]^T\begin{Bmatrix} u^c \\ v^c \\ w^c \end{Bmatrix} + \frac{p}{2}\left\{u^c \quad v^c \quad w^c\right\}\begin{Bmatrix} u^c \\ v^c \\ w^c \end{Bmatrix} \tag{3-22}$$

where $\left\{u^c \quad v^c \quad w^c\right\}^T$ is the constrained displacement vector for the point (x, y, z) of sphere i, $\left\{u^c - u \quad v^c - v \quad w^c - w\right\}^T$ is the displacement vector of the spring. When the spheres are fixed at the original configuration, $(u^c, v^c, w^c) = (0,0,0)$.

Minimizing π_C, we have:

$$p\ [T_i(x,y,z)]^T\ [T_i(x,y,z)]\ \rightarrow\ [K_{ii}]$$

$$p\ [T_i(x,y,z)]^T\begin{Bmatrix} u^c \\ v^c \\ w^c \end{Bmatrix} \rightarrow \{F_i\} \tag{3-23}$$

which are added to the simultaneous equation (3-5).

3.4.5. Sub-matrix of directional constraint

Spheres may be constrained at a specific point along a specified direction as a boundary condition. Using the same technique as boundary condition of displacement constraint, a very stiff spring with stiffness P can be used to apply to the point (x, y, z) of sphere i.

Assuming the point (x, y, z) with the displacement of δ is constrained along the direction with unit vector of $\{l_x \ l_y \ l_z\}^T$, the spring displacement, d, is:

$$d = \delta - \{u \ v \ w\}.\{l_x \ l_y \ l_z\}^T \tag{3-24}$$

The directional constrained spring potential energy, π_{DC}, is:

$$\pi_{DC} = \frac{p}{2}\left(\delta - \{u \ v \ w\}\begin{pmatrix} l_x \\ l_y \\ l_z \end{pmatrix}\right)^2 = \frac{P}{2}\left(\delta - \{D_i\}^T \ [T_i(x, y, z)]^T \begin{pmatrix} l_x \\ l_y \\ l_z \end{pmatrix}\right)^2 \tag{3-25}$$

Minimizing π_{DC} with respect to $\{D_i\}^T$, gives:

$$p[T_i(x, y, z)]^T \begin{pmatrix} l_x \\ l_y \\ l_z \end{pmatrix}\begin{pmatrix} l_x \\ l_y \\ l_z \end{pmatrix}^T [T_i(x, y, z)] \ \rightarrow \ [K_{ii}] \tag{3-26}$$

$$p\,\delta[T_i(x, y, z)]^T \begin{pmatrix} l_x \\ l_y \\ l_z \end{pmatrix} \ \rightarrow \ \{F_i\} \tag{3-27}$$

which are added to the global coefficient matrix and the global force matrix, respectively in the equilibrium equations (3-5).

3.5. Contact Detection

A robust contact model describing the interaction of many 3-D discontinuous blocks is a vital part of 3-D DDA. ‘Contact detection’ and ‘contact mechanics’ are the two main

components of the contact model. Contact detection is referred to as neighbor search that provides a list of all possible particles in contact to find the contact points. A review of neighbor search methods is presented by Munjiza (2004) and Bergen (2003). In the contact mechanics step, the contact forces are calculated. There are three possible contact states:

1. No lock or stiff spring is needed: In this case, the contact force component along the direction of the line that connects two sphere centers is tensile; In this case, the contact is open.
2. A very stiff spring is needed in the normal direction: In this case, the normal contact force component is compressive and the shear component of the contact force along the surface is large enough to cause sliding. In this state, the sliding between two spheres can happen.
3. Both normal and shear springs lock the contact point: In this case, the shear component of the contact force along the surface is less than that predicted by Coulomb's law and the normal component of the contact force is compressive. In this state, sliding is not allowed.

The procedure of adding and removing stiff springs depending on the changes in contact states is known as ''open-close'' iteration (Jiang and Yeung 2004).

In the following sections, a simple method of contact detection (the contact between sphere and sphere, and the contact between sphere and plane) and contact mechanics are presented.

3.5.1. Sphere-sphere contact detection

We can define the minimum distance between two spheres as a criterion to detect a contact between them. This minimum distance can be calculated as:

$$dis_1 = \sqrt{(x_2 - x_1)^2 + (y_2 - y_1)^2 + (z_2 - z_1)^2} - (R_i + R_j) \tag{3-28}$$

where point $C_1(x_1, y_1, z_1)$ is the center of sphere i and point $C_2(x_2, y_2, z_2)$ is the center of sphere j. R_i, and R_j are the radii of sphere i and sphere j, respectively (Figure 3-1).

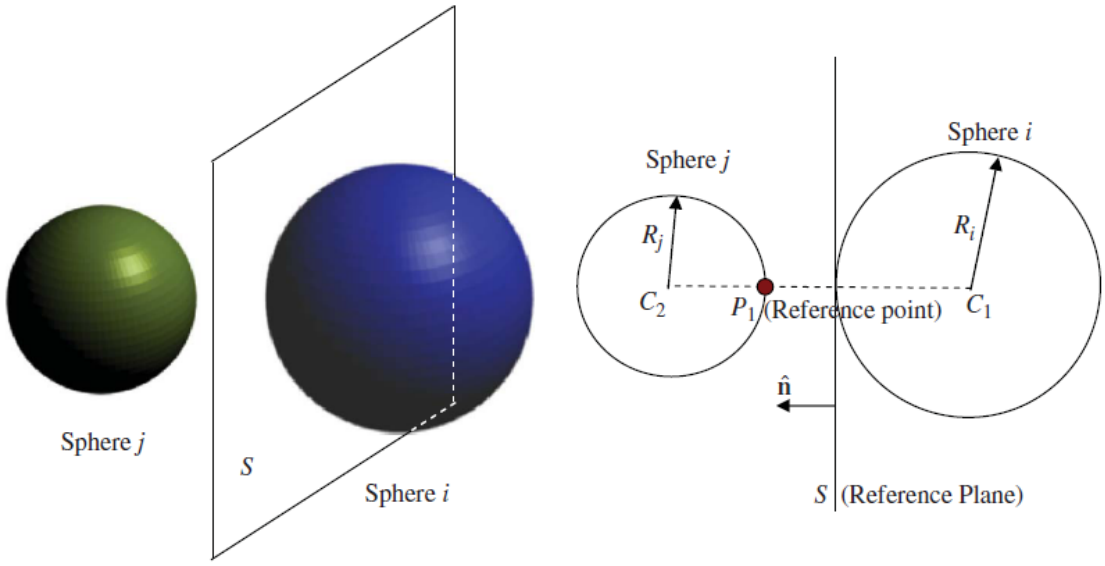

Figure 3-1. Sphere-sphere contact detection

It is possible for sphere i and sphere j to contact each other during the next step, if dis_1 is less than two times the maximum displacement of points of the spheres. In this case, the tangent plane to the sphere i, which is perpendicular to the line that connects

centers of the spheres (C_1C_2), is the reference plane (as shown in Figure 3-1), and P_1 of sphere j, which is located on the line C_1C_2, is the reference point. The unit normal vector of the reference plane, $\hat{\mathbf{n}}(a,b,c)$, can be obtained by the following equations:

$$a = \frac{x_2 - x_1}{\sqrt{(x_2 - x_1)^2 + (y_2 - y_1)^2 + (z_2 - z_1)^2}} \tag{3-29}$$

$$b = \frac{y_2 - y_1}{\sqrt{(x_2 - x_1)^2 + (y_2 - y_1)^2 + (z_2 - z_1)^2}} \tag{3-30}$$

$$c = \frac{z_2 - z_1}{\sqrt{(x_2 - x_1)^2 + (y_2 - y_1)^2 + (z_2 - z_1)^2}} \tag{3-31}$$

The reference point and plane are used for contact mechanics computations and will be discussed later in the section “contact mechanics”.

3.5.2. Sphere-plane contact detection

Assuming sphere i is located near a fixed rigid boundary plane S, the distance between them is (Figure 3-2):

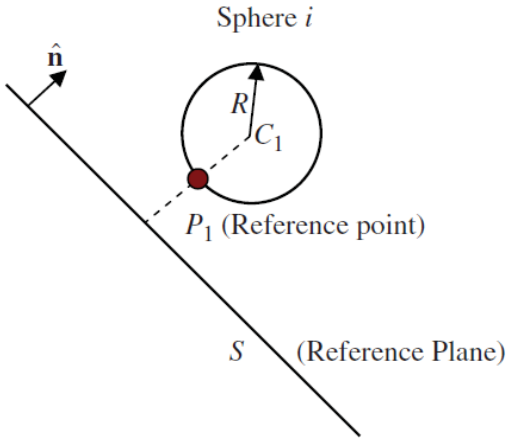

Figure 3-2. Sphere-plane contact detection

$$dis_2 = \hat{\mathbf{n}}.\hat{\mathbf{m}} - R_i \tag{3-32}$$

where $\hat{\mathbf{n}}(a,b,c)$ is the unit normal vector of plane S, $\hat{\mathbf{m}}$ is $(x_0 - x_2, y_0 - y_2, z_0 - z_2)$, $C_1(x_0, y_0, z_0)$ is the center of sphere i, and (x_2, y_2, z_2) is coordinates of a point on plane S and R_i is radius of the sphere. If the distance is less than two times the maximum displacement of points of all spheres, sphere i may meet plane S. In this case, as shown in Figure 5-2, point P_1 on the perimeter of the sphere is the reference point and plane S is the reference plane.

3.6. Contact Mechanics

In the previous section, the reference plane and point are determined for each type of contact. In this section, contact mechanics for each type of contact is presented.

3.6.1. Sphere-sphere contact

Contact between two spheres can be modeled using a pair of springs as shown in Figure 3-3. Sub-matrices of normal and shear contacts and frictional force are derived as follows:

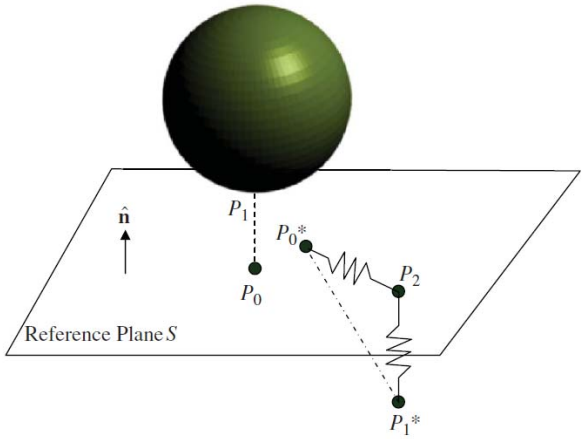

Figure 3-3. Springs for sphere-sphere and sphere-plane contacts

- *Sub-matrix of normal contact*

Assume $P_1(x_1, y_1, z_1)$ indicates the location of the reference point of sphere i before a displacement increment and P_1^* represents the location after the displacement increment. $P_0(x_0, y_0, z_0)$ represents the projection of point P_1 on the reference plane S and P_0^* indicates this point after the displacement increment. Moreover, assume (u_1, v_1, w_1) and (u_0, v_0, w_0) are the displacement increments of points P_1 and P_0, respectively, and the unit normal vector of the reference plane S is $\hat{\mathbf{n}}$. The normal distance d_n of point P_1^* from the reference plane S is:

$$d_n = \hat{\mathbf{n}}.\mathbf{P}_{\mathbf{01}}^{*} = \hat{\mathbf{n}}.\begin{bmatrix}(x_1+u_1)-(x_0+u_0)\\(y_1+v_1)-(y_0+v_0)\\(z_1+w_1)-(z_0+w_0)\end{bmatrix} = \hat{\mathbf{n}}.\begin{bmatrix}x_1-x_0\\y_1-y_0\\z_1-z_0\end{bmatrix} + \hat{\mathbf{n}}.\begin{bmatrix}u_1-u_0\\v_1-v_0\\w_1-w_0\end{bmatrix} = M + \hat{\mathbf{n}}\begin{bmatrix}u_1-u_0\\v_1-v_0\\w_1-w_0\end{bmatrix} \quad (3\text{-}33)$$

where $M = \hat{\mathbf{n}}.\begin{bmatrix}x_1-x_0\\y_1-y_0\\z_1-z_0\end{bmatrix}$.

We can write the displacements of points P_1 and P_0 as:

$$\begin{Bmatrix}u_1\\v_1\\w_1\end{Bmatrix} = [T_i(x_1, y_1, z_1)].\{D_i\} \quad (3\text{-}34)$$

$$\begin{Bmatrix}u_0\\v_0\\w_0\end{Bmatrix} = [T_j(x_0, y_0, z_0)].\{D_j\} \quad (3\text{-}35)$$

Therefore,

$$d_n = M + [H_i]\{D_i\} - [Q_j]\{D_j\} \tag{3-46}$$

where

$$[H_i] = \hat{\mathbf{n}}.T_i(x_1, y_1, z_1) \tag{3-37}$$

$$[Q_j] = \hat{\mathbf{n}}.T_j(x_0, y_0, z_0) \tag{3-38}$$

The normal contact potential energy can be calculated as:

$$\pi_n = \frac{1}{2} P_n d_n^2 \tag{3-39}$$

where P_n is the normal spring stiffness in the direction normal to reference plane S.

Therefore, we have:

$$\pi_n = \frac{1}{2} P_n (M + [H_i]\{D_i\} - [Q_j]\{D_j\})^2 \tag{3-40}$$

minimizing π_n with respect to $\{D_i\}^T$ and $\{D_j\}^T$ gives:

$$[K_{ii}] = P_n[H_i]^T[H_i] \tag{3-41}$$

$$[K_{ij}] = -P_n[H_i]^T[Q_j] \tag{3-42}$$

$$[K_{ji}] = -P_n[Q_j]^T[H_i] \tag{3-43}$$

$$[K_{jj}] = P_n[Q_j]^T[Q_j] \tag{3-44}$$

These sub-matrices are added to $[K_{ii}],[K_{ij}],[K_{ji}]$, and $[K_{jj}]$ in the global stiffness matrix, and:

$$[F_i] = -P_n M [H_i]^T \tag{3-45}$$

$$[F_j] = P_n M [Q_j]^T \tag{3-46}$$

are added to the global force vector.

- *Sub-matrix of shear contact*

In Figure 3-3, point P_2 is the projection of point P_1 on the contact face after the displacement increment. When the shear force is smaller than the shear resistance [i.e., $F_s < F_n \tan(\phi)$], where F_s is the shear contact force; F_n is the normal contact force; and φ is friction angle), a shear contact spring will be activated to reduce the relative displacement of the two spheres. Normal and shear forces can be obtained by the following equations:

$$F_n = P_n d_n \tag{3-47}$$

$$F_s = P_s d_s \tag{3-48}$$

where P_s is stiffness of the shear spring.

The shear displacement along the $\mathbf{P_0^* P_2}$ is obtained as:

$$d_s = \sqrt{\left|\mathbf{P_0^* P_1^*}\right|^2 - d_n^2} \tag{3-49}$$

The shear spring potential energy is:

$$\pi_s = \frac{1}{2}P_s d_s^2 = \frac{1}{2}P_s \left(\begin{bmatrix} x_1 - x_0 \\ y_1 - y_0 \\ z_1 - z_0 \end{bmatrix}^T + [D_i]^T [T_i]^T - [D_j]^T [T_j]^T \right) \cdot \left(\begin{bmatrix} x_1 - x_0 \\ y_1 - y_0 \\ z_1 - z_0 \end{bmatrix} + [T_i][D_i] - [T_j][D_j] \right) - \frac{1}{2}P_s \left(M + [H_i]\{D_i\} - [Q_j]\{D_j\} \right)^2 \quad (3\text{-}50)$$

By expanding and minimizing the potential energy, we have:

$$[K_{ii}] = P_s[T_i]^T[T_i] - P_s[H_i]^T[H_i] \quad (3\text{-}51)$$

$$[K_{ij}] = -P_s[T_i]^T[T_j] + P_s[H_i]^T[Q_j] \quad (3\text{-}52)$$

$$[K_{ji}] = -P_s[T_j]^T[T_i] + P_s[Q_j]^T[H_i] \quad (3\text{-}53)$$

$$[K_{jj}] = P_s[T_j]^T[T_j] - P_s[Q_j]^T[Q_j] \quad (3\text{-}54)$$

These are added to the sub-matrices $[K_{ii}]$,$[K_{ij}]$,$[K_{ji}]$, and $[K_{jj}]$ in the global stiffness matrix, and:

$$\{F_i\} = -P_s[T_i]^T \begin{bmatrix} x_1 - x_0 \\ y_1 - y_0 \\ z_1 - z_0 \end{bmatrix} - P_s M [H_i]^T \quad (3\text{-}55)$$

$$\{F_j\} = P_s[T_j]^T \begin{bmatrix} x_1 - x_0 \\ y_1 - y_0 \\ z_1 - z_0 \end{bmatrix} + P_s M [Q_j]^T \quad (3\text{-}56)$$

are added to the global force vector.

- *Sub-matrix of frictional force*

One of the sources of energy consumption in DDA is the friction force. A pair of equal and opposite frictional forces along the sliding direction is applied at P_1 and P_0 in the state of the contact sliding. The friction force can be calculated by the normal contact compressive force, and the direction of the friction force which are obtained from the previous step.

The friction force potential energy is calculated as below:

$$\begin{aligned}\pi_f &= \left(P_n\, d_1\, tg\,\varphi\right)\left(\{u_1 \;\; v_1 \;\; w_1\} - \{u_0 \;\; v_0 \;\; w_0\}\right)\begin{Bmatrix} l \\ m \\ n \end{Bmatrix} \\ &= \left(P_n\, d_1\; tg\,\varphi\right)\left(\{D_i\}^T.[T_i(x_1, y_1, z_1)]^T - \{D_j\}^T.[T_j(x_0, y_0, z_0)]^T\right)\begin{Bmatrix} l \\ m \\ n \end{Bmatrix}\end{aligned} \tag{3-57}$$

where d_1 is the normal penetration and is taken from the previous step, and

$$\begin{Bmatrix} l \\ m \\ n \end{Bmatrix} = \frac{\mathbf{P_0^* P_2}}{\left|\mathbf{P_0^* P_2}\right|} \tag{3-58}$$

where $\mathbf{P_0^* P_2}$ represents the direction of the frictional force (Figure 3-3) and can be calculated as:

$$\mathbf{P_0^* P_2} = \mathbf{P_0^* P_1^*} - \left\langle \mathbf{P_0^* P_1^*}, \hat{\mathbf{n}} \right\rangle . \hat{\mathbf{n}} \tag{3-59}$$

After minimizing π_f, we have:

$$-\left(P_n\, d_1\, tg\,\varphi\right)[T_i(x_1, y_1, z_1)]^T \begin{Bmatrix} l \\ m \\ n \end{Bmatrix} \rightarrow \{F_i\} \tag{3-60}$$

$$\left(P_n\, d_1\, tg\,\varphi\right)[T_j(x_0, y_0, z_0)]^T \begin{Bmatrix} l \\ m \\ n \end{Bmatrix} \rightarrow \{F_j\} \tag{3-61}$$

which are added to the global force vector.

3.6.2. Sphere-boundary contact

Sphere-boundary contact is similar to sphere-sphere contact but in this case we must let $(u_0, v_0, w_0) = (0,0,0)$. In the following sections, sub-matrices of normal and shear contacts are presented for the sphere-boundary contact type.

- *Sub-matrix of normal contact*

The normal distance of point P_1^* from plane S is:

$$d_n = M + [H_i]\{D_i\} \tag{3-62}$$

and the potential energy of the normal spring can be calculated as:

$$\pi_n = \frac{1}{2} P_n (M + [H_i]\{D_i\})^2 \tag{3-63}$$

Minimizing the potential energy gives:

$$[K_{ii}] = P_n [H_i]^T [H_i] \tag{3-64}$$

$$\{F_i\} = -P_n M [H_i]^T \tag{3-65}$$

which are added to the global stiffness matrix and the global force vector (equation (3-5)), respectively.

- *Sub-matrix of shear contact*

In this case, formulation of sphere-sphere shear contact can be used with $(u_0, v_0, w_0) = (0,0,0)$. Therefore:

$$\pi_s = \frac{1}{2} P_s \left(\begin{Bmatrix} x_1 - x_0 \\ y_1 - y_0 \\ z_1 - z_0 \end{Bmatrix}^T + \{D_i\}^T [T_i]^T \right) . \left(\begin{Bmatrix} x_1 - x_0 \\ y_1 - y_0 \\ z_1 - z_0 \end{Bmatrix} + [T_i]\{D_i\} \right) \tag{3-66}$$

By expanding and minimizing the potential energy π_s, we have:

$$[K_{ii}] = P_s [T_i]^T [T_i] - P_s [H_i]^T [H_i] \tag{3-67}$$

$$\{F_i\} = -P_s [T_i]^T \begin{Bmatrix} x_1 - x_0 \\ y_1 - y_0 \\ z_1 - z_0 \end{Bmatrix} + P_s M [H_i]^T \tag{3-68}$$

which are added to the global stiffness matrix and the global force vector, respectively.

- *Sub-matrix of frictional force*

The potential energy of friction force $f = P_n d_1 \tan(\phi)$ at contact point P_1 on sphere i is given by:

$$\pi_f = \left(P_n\, d_1\, tg\,\varphi\right)\left(u_1 \;\; v_1 \;\; w_1\right)\begin{Bmatrix} l \\ m \\ n \end{Bmatrix} = \left(P_n\, d_1\, tg\,\varphi\right)\{D_i\}^T\,[T_i(x_1, y_1, z_1)]^T\begin{Bmatrix} l \\ m \\ n \end{Bmatrix} \tag{3-69}$$

To minimize π_f, we get:

$$-\left(P_n\, d_1\, tg\,\varphi\right)\,[T_i(x_1, y_1, z_1)]^T\begin{Bmatrix} l \\ m \\ n \end{Bmatrix} \rightarrow \{F_i\} \tag{3-70}$$

which is added to the global force vector.

3.7. Model Verification

In this section, three examples are used to verify the model. The results are compared with analytical solutions and discussed in order to illustrate the application of the 3-DDA to particulate media.

3.7.1. Central collision of spheres

Figure 3-4(a) shows an initial condition for the impact of two spheres. The initial velocities of frictionless spheres S_1 and S_2 are $1.5 m/s$ and $0.0 m/s$, respectively. The initial coordinates of the spheres are: $S_1(0,0,0)$ and $S_2(0,2.5,0)$. The density of each sphere is $2500 kg/m^3$. Furthermore, the stiffness of the normal contact spring and the simulation time interval are $4\ GN/m$ and $0.005 s$, respectively.

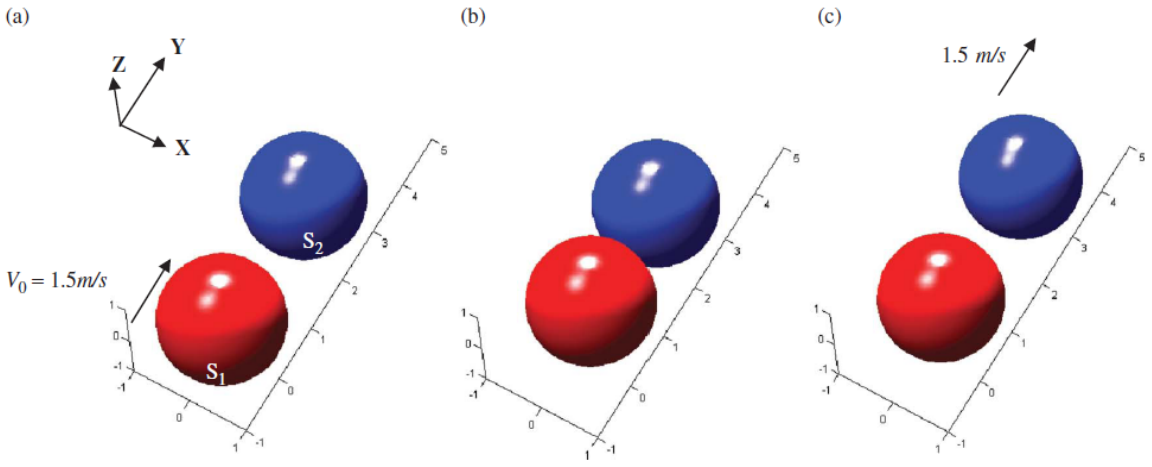

Figure 3-4. Sphere-sphere central collision (a) initial condition (b) after the first impact (c) after the second impact

The configurations of the spheres immediately after the impact and after 0.7s are shown in Figure 3-4(b). and 3-4(c), respectively. Figure 3-5 shows velocities of the two spheres versus time.

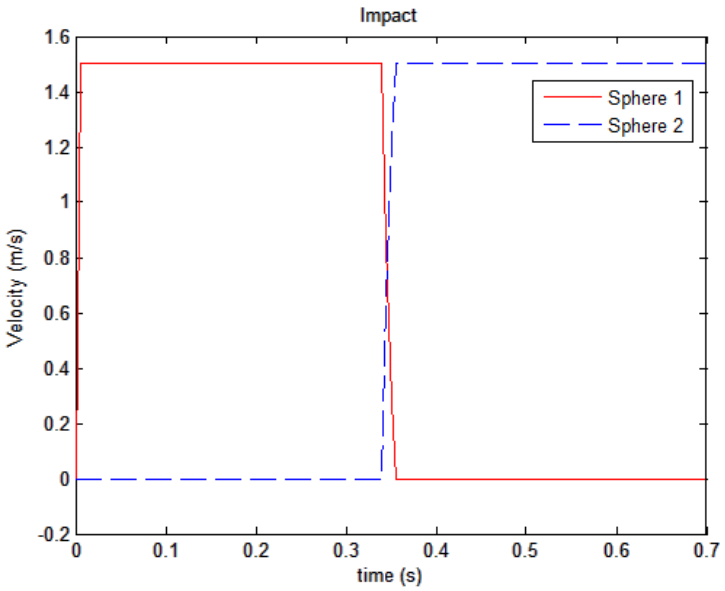

Figure 3-5. Velocities of the spheres versus time

As can be seen, immediately after impact sphere S_1 stops (its velocity = $0.0 m/s$), and the velocity of sphere S_2 = $1.5 m/s$. The velocities right after impact can be determined using the momentum equation and kinetic energy equation, which are equal to the obtained velocities. This example shows the capability of the proposed model to simulate impacts of rigid spheres.

3.7.2. Sliding Along an Inclined Plane

This example demonstrates the ability of 3-D DDA to simulate sliding of spheres on an inclined plane. In this study, sliding of a sphere along an inclined plane with friction angle φ at an angle α to the horizontal direction is modeled (Figure 3-6).

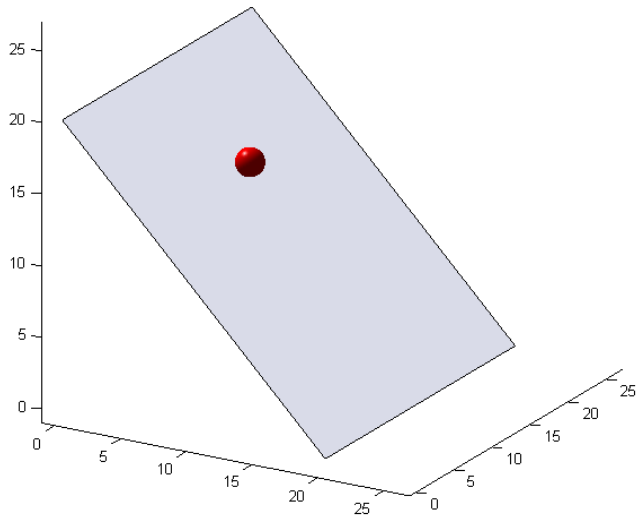

Figure 3-6. Sphere sliding on an inclined plane

In this case, the displacement of the sphere under the action of gravitational force can be calculated analytically as:

$$s = \frac{1}{2} g \left(\sin(\alpha) - \tan(\varphi)\cos(\alpha)\right) t^2 \tag{3-71}$$

where s is the displacement of the sphere, g is the gravitational acceleration, and t is time. In this study, the values chosen for the plane slope and radius of the sphere are 45^0 and $1m$, respectively. When:

$$\varphi \le \tan^{-1}\left(\frac{\tan(\alpha)}{3}\right) \tag{3-75}$$

(for this example: $\varphi \le 18.43^0$) the sphere will slide on the plane (Ke and Bray 1995). Moreover, the sphere density is taken to be $2600 kg/m^3$ and the penalty spring stiffness is $P = 5\times10^6 kN/m$. Three different friction angles (0^0, 10^0, and 15^0) are used in this study. A comparison of predicted displacements from 3-D DDA and analytical solutions for different values of friction angle are presented in Figure 3-7. As can be seen, there is a good agreement between the obtained results by the 3-D DDA and the analytical solution. Absolute and relative errors for the calculated displacements by 3-D DDA are shown in Figures 3-8 and 3-9, respectively. These figures show that the absolute value of the error increases at every time step, but the relative error with respect to sphere displacement decreases and the 3-D DDA results get closer to the analytical solution. Similar behavior for sliding a rectangular block in 2-D and a cube in 3-D on an inclined plane is reported by Doolin and Sitar (2002) and Beyabanki et al. (2008a).

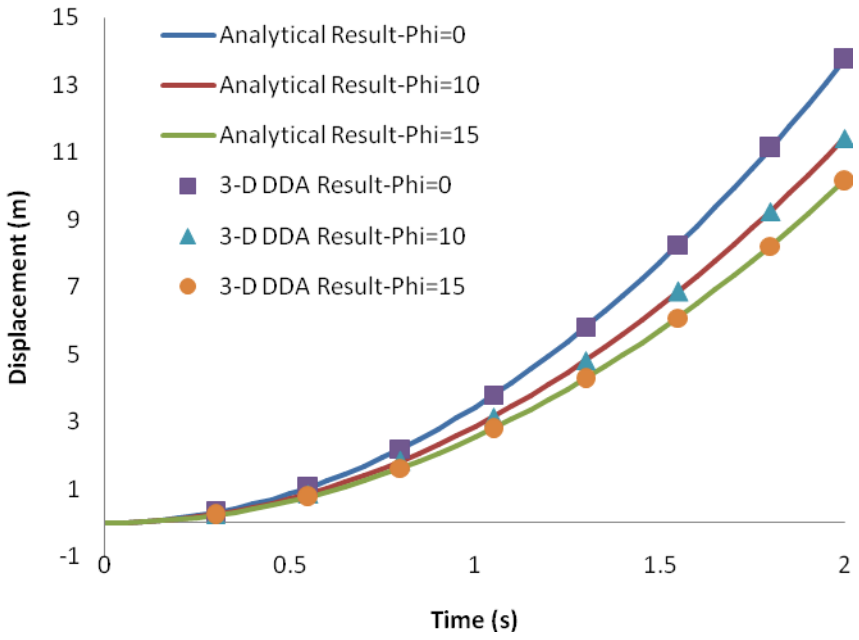

Figure 3-7. Results of displacement obtained by 3-D DDA and analytical solution

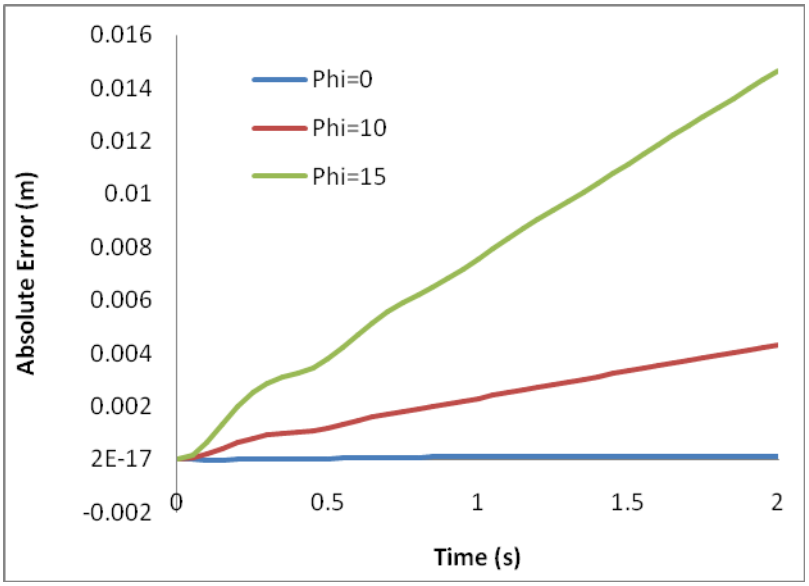

Figure 3-8 Absolute errors in the obtained displacements using the 3-D DDA with respect to the analytical solution

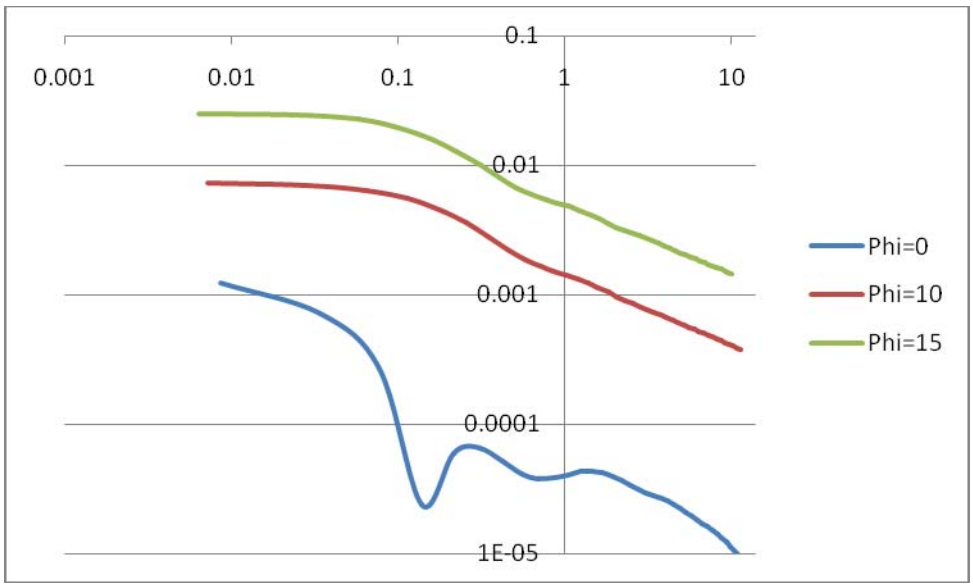

Figure 3-9 Relative errors in the obtained sphere displacement by the 3-D DDA

3.7.3. Rotation on an Inclined Plane

In this example the ability of the model to simulate rotation on an inclined plane is studied. When:

$$\varphi \succ \tan^{-1}\left(\frac{\tan(\alpha)}{3}\right) \tag{3-72}$$

the sphere will rotate on the plane (Ke and Bray 1995). In equation (3-72), φ and α are friction angle and angle of the plane to the horizontal direction. In this case, the accumulated sphere rotation, θ, after t seconds is given by (O'Sullivan and Bray 2001):

$$\theta = \left(\frac{g\sin(\alpha)}{3R}\right)t^2 \tag{3-73}$$

where g is the gravitational acceleration and R is radius of the sphere. In this study, it is assumed that $\alpha = 45^{\circ}$, $\varphi = 30^{0}$ and $R = 1m$. The time interval and the penalty spring stiffness are $0.001s$ and $1\times10^{6}\,kN/m$, respectively. According to equation (3-77), since $\varphi \succ 18.43^{\circ}$, the sphere will rotate on the inclined plane. Figure 3-10 shows the results obtained using the 3-D DDA. The calculated results using the 3-D DDA agree well with the theoretical solution.

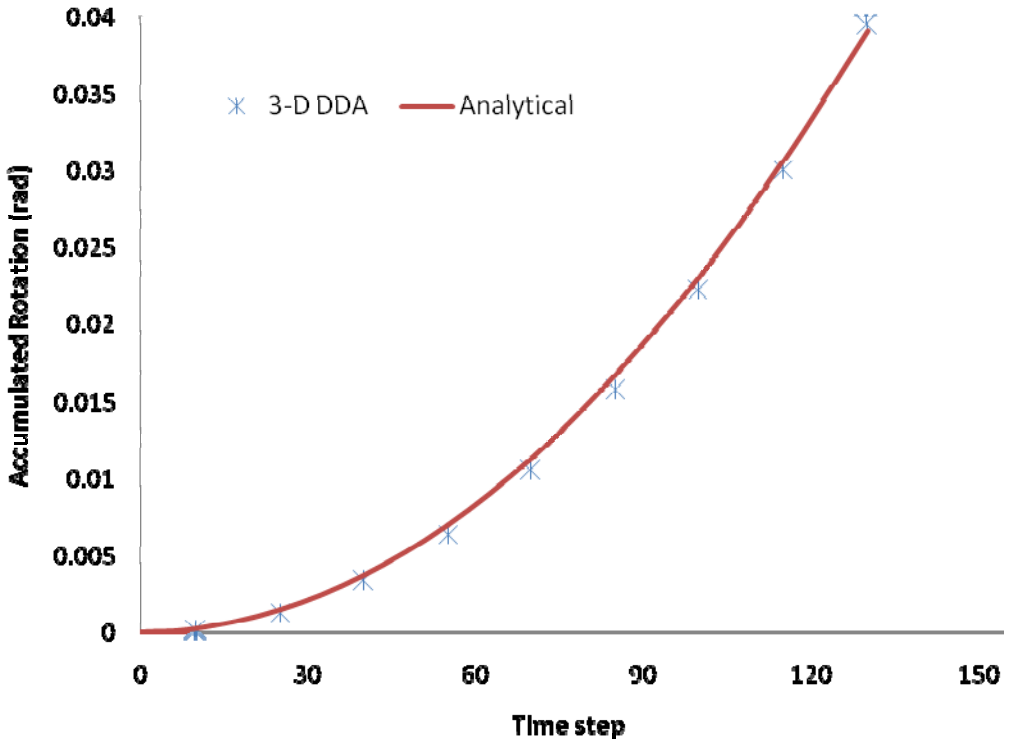

Figure 3-10 Results of accumulated sphere rotation obtained by 3-D DDA and analytical solution

3.7.4. Billiard

Example simulation of billiard involves 15 balls that are hit by a ball. Figure 3-11(a) shows the initial configuration for this example. The friction angle, normal spring

stiffness, time interval and initial velocity of the ball are 0^0, $5\times10^6 kPa$, $0.05s$, and $2m/s$, respectively. Configuration of the balls at times $3s$ and $10s$ are shown in Figures 3-11(b) and 3-11(c), respectively. As can be seen, movement of balls is simulated well. As it is expected, the movement is symmetric. This example demonstrates the capability of the proposed model to simulate impact of several spheres.

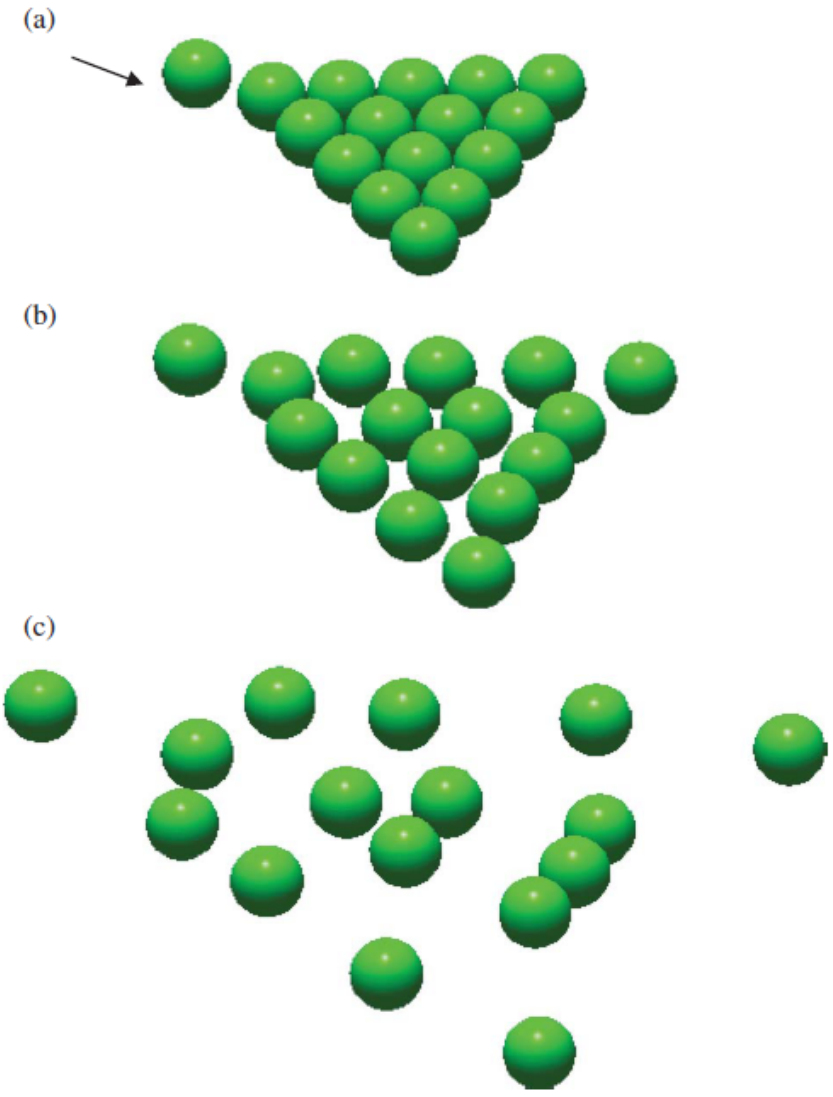

Figure 3-11 Simulation of a Billiard (a) Initial configuration (b) after 3s (c) after 10s

3.7.5. Funnel flow

In order to verify the contact model for a large number of spheres and some planes, particle flow from a funnel using 3-D DDA is studied in this example. There are 1156 spheres with different sizes in four layers above a funnel which fall down due to gravity. The initial configuration for particles and funnel is shown in Figure 3-12. Each sphere has a density of $2500 kg/m^3$ and the stiffness of the normal contact spring, the time interval and the friction angle are $P = 1 \times 10^7 kN/m$, $0.05s$ and 10°, respectively. Figures 3-13 and 3-14 show the configuration of spheres after 6.2s and 8.5s, respectively. As can be seen, the spheres flow through the funnel without any overlap between spheres-spheres or spheres-boundaries. This example demonstrates that the proposed model can simulate contact between large number of spheres and their contact with rigid boundaries.

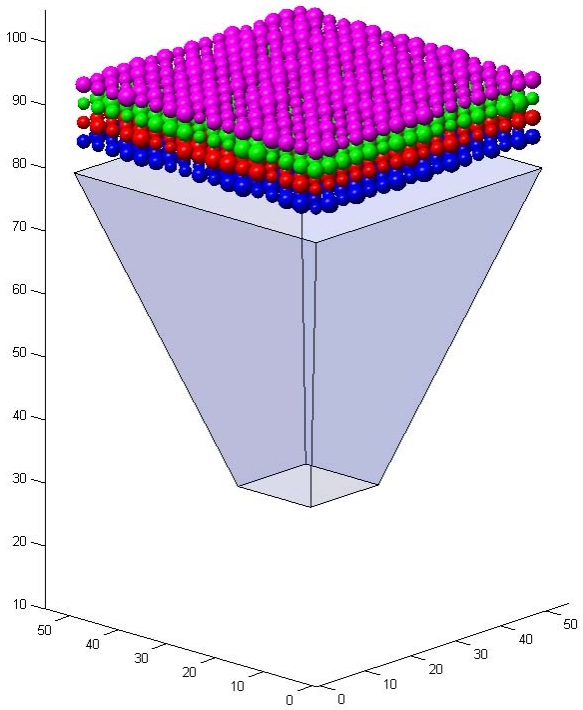

Figure 3-12 Initial configuration of funnel flow

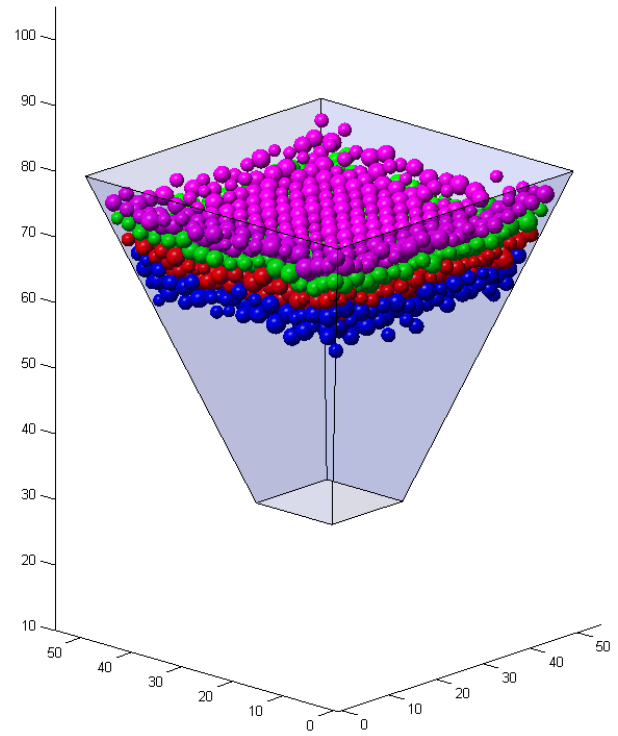

Figure 3-13 configuration of funnel flow after 6.6 s

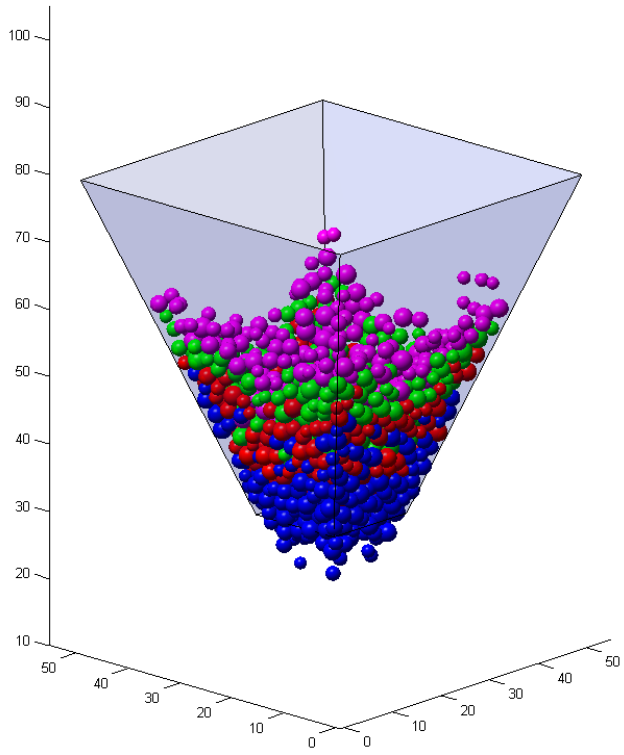

Figure 3-14 configuration of funnel flow after 10.2 s

3.7.6. Multiple slopes

In this section, a simulation of spheres in contact with multi-boundaries is studied. This case is a landslide analogy. In this study, as shown in Figure 3-15(a), a slope including five inclined planes is considered. 180 spheres rest on the highest inclined plane. The friction angles for sphere-sphere and sphere-plane are 5° and 15°, respectively. Under the action of gravitational force, the spheres move on the planes. Density of the spheres is $3500\,kg/m^3$ and the stiffness of the normal contact spring and the time interval are assumed to be $P = 5\times10^7\,kN/m$ and $0.05s$, respectively. Figures 3-15(b), 3-15(c) and 3-15(d) show the configuration of the spheres after 20s, 47s and 63s, respectively. As can be seen, the spheres move along the inclined planes without any violation of boundary constraints.

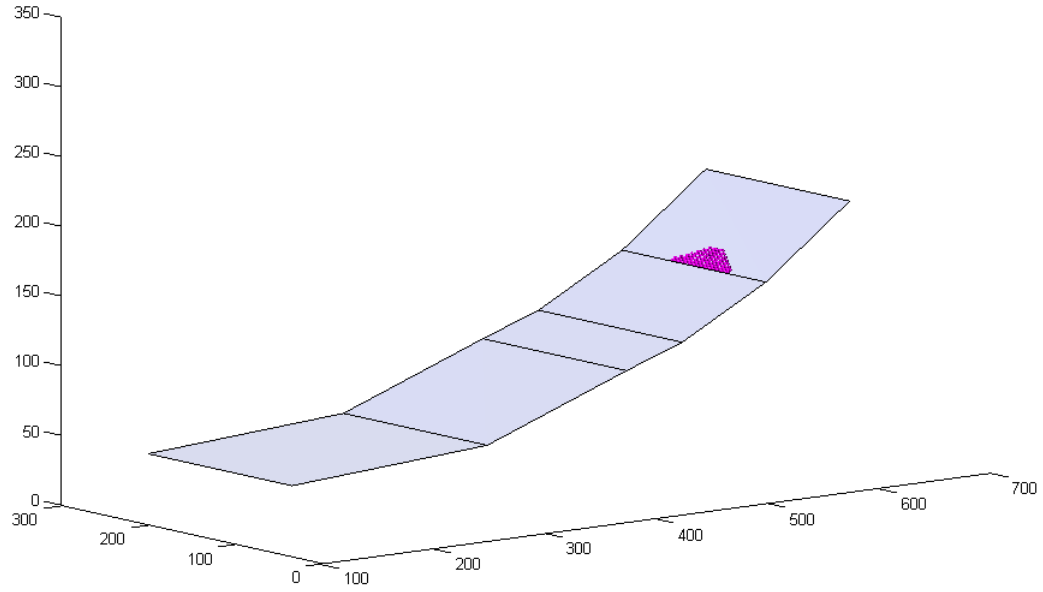

(a)

Figure 3-15 multi-slopes simulation (a) Initial configuration (b) after 20s (c) after 47s (d) after 63s

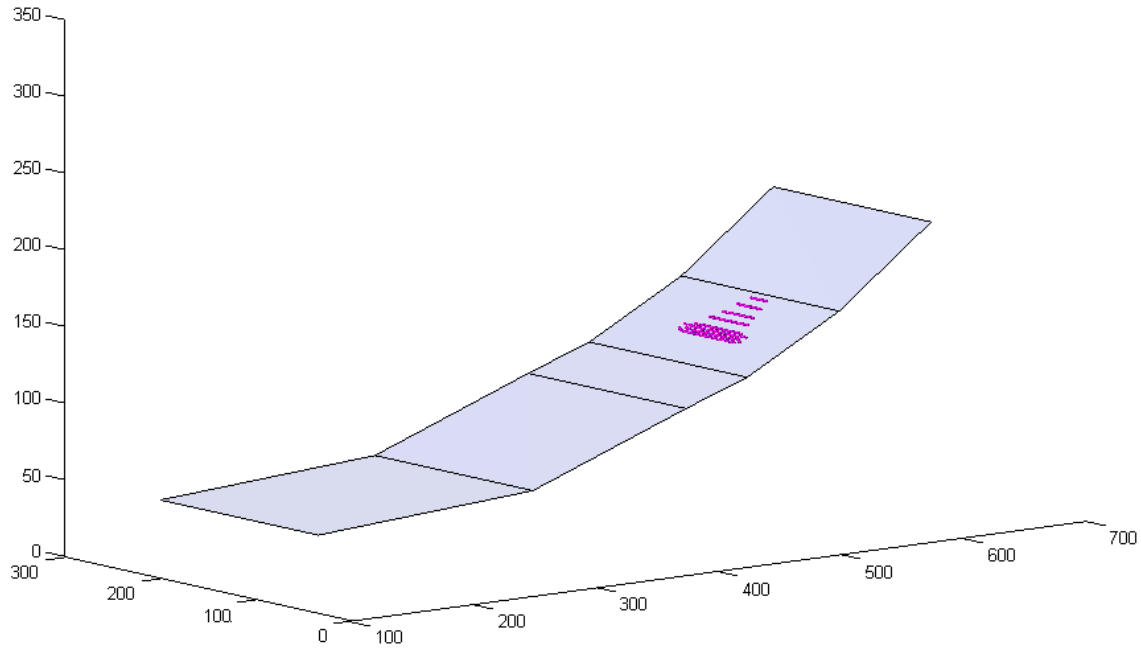

(b)

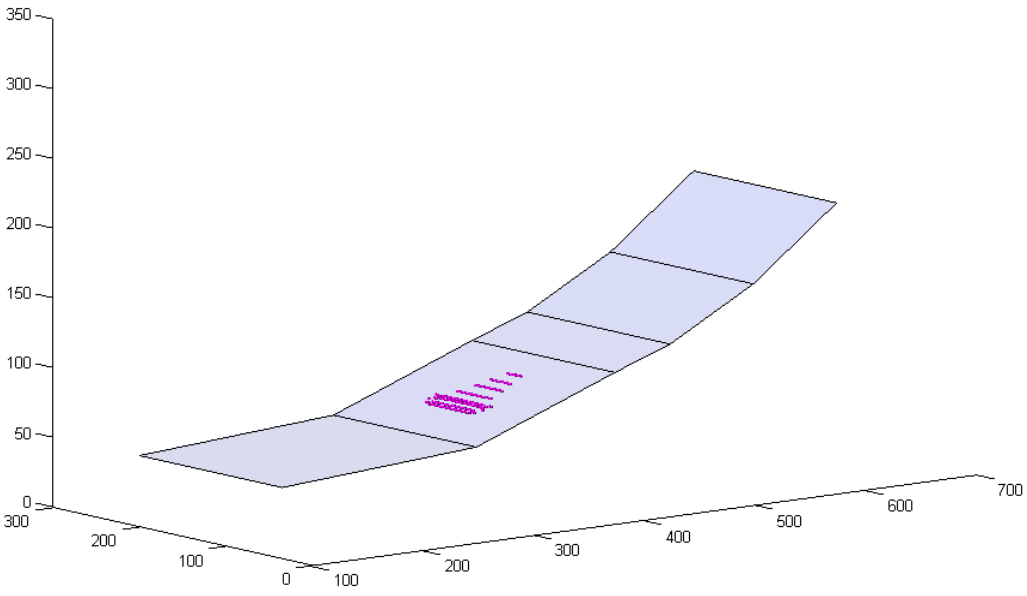

(c)

Figure 3-15 multi-slopes simulation (a) Initial configuration (b) after 20s (c) after 47s (d) after 63s (Cont.)

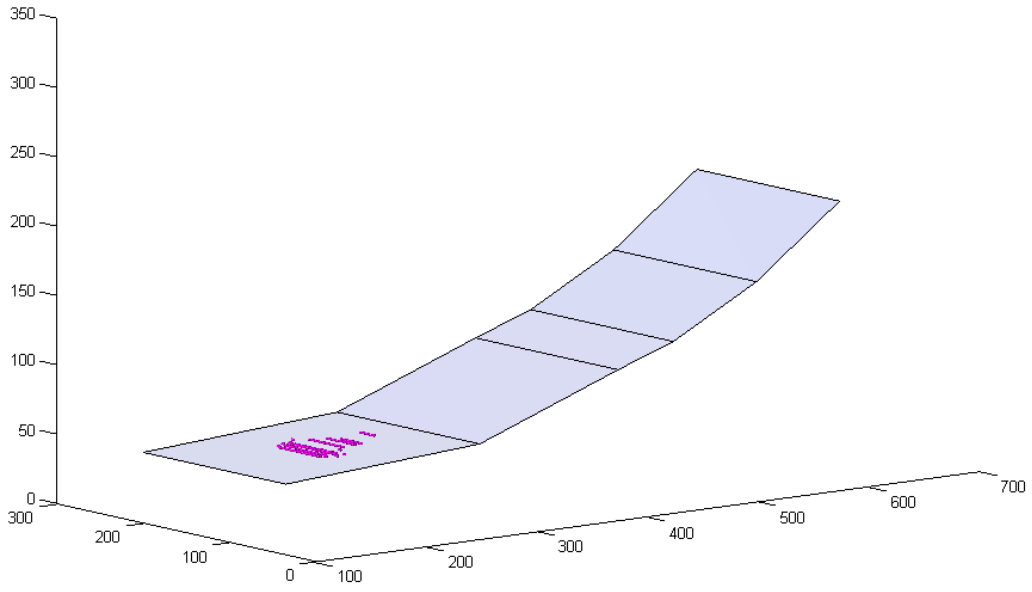

(d)

Figure 3-15 multi-slopes simulation (a) Initial configuration (b) after 20s (c) after 47s (d) after 63s (Cont.)

3.8. Conclusions

Two-dimensional analysis of most practical engineering problems can only be approximate. For these problems, 3-D instead of 2-D analysis would be more appropriate. In this paper, a new numerical model to simulate particulate media is presented. This model is based on the 3-D DDA for spheres and rigid boundaries. The complete formulation for stiffness and force matrices due to body forces, point loading, inertia forces, and displacement and directional constraints is presented. Moreover, a model for sphere-sphere and sphere-boundary contacts is presented. In this model, all contacts can be converted to one or more point-to-plane contacts. Using vector analysis contact formulae, including those for the normal and shear springs and the frictional

force sub-matrices are derived in detail. The numerical model developed can be readily implemented into a computer code. To verify the model, three illustrative examples are presented (central collision of spheres, sliding along an inclined plane and rotation on an inclined plane). The model results agree very well with analytical solutions. Three other more demanding test cases (billiard, funnel flow and multiple slopes) show that the proposed contact model can work well for several spheres and boundaries. Results of simulations demonstrate that the model is able to represent geometrical deformation of the granular assemblages reasonably well and can be used to efficiently carry out complex analyses.

3.9. References

Bakun-Mazor, D., Hatzor, Y.H. and Glaser, S.D., 2012. Dynamic sliding of tetrahedral wedge: The role of interface friction. International Journal for Numerical and Analytical Methods in Geomechanics. 36 (3), 327–343.

Bergen, G.V.D., 2003. Collision Detection in Interactive 3-D Environments. New York: Morgan Kaufmann.

Beyabanaki, S.A.R., Grayeli, R. and Hatami, K., 2008a. Three-dimensional discontinuous deformation analysis (3-D DDA) using a new contact resolution algorithm. Computers and Geotechnics, 35, 346–356.

Beyabanaki, S.A.R., Jafari, A. and Yeung, M.R., 2008b. Development of Three-Dimensional Discontinuous Deformation Analysis (3-D DDA) with 3rd Order Displacement Function. In: Proceedings of 42nd U.S. Rock Mechanics Symposium and 2nd U.S.-Canada Rock Mechanics Symposium, June 29-July 2 2008 San Francisco, CA, USA, paper number ARMA 08–349.

Beyabanaki, S.A.R., Jafari, A., Biabanaki, S.O. and Yeung, M.R., 2009a. A Coupling Model of 3-D Discontinous Deformation Analysis (3-D DDA) and Finite Element Method. Arabian Journal for Science and Engineering, 34 (2B), 107–119.

Beyabanaki, S.A.R., Jafari, A., Biabanaki, S.O. and Yeung, M.R., 2009b. Nodal-based Three-Dimensional Discontinuous Deformation Analysis (3-D DDA). Computers and Geotechnics, 36, 359–372.

Beyabanaki, S.A.R., Jafari, A. and Yeung, M.R., 2009c. Second-Order Displacement Functions for Three-Dimensional Discontinuous Deformation Analysis (3-D DDA). International Journal of Science and Technology, 16 (3), 216–225.

Beyabanaki, S.A.R., Yeung, M.R. and Vosogh, A.H., 2009d. Three-Dimensional Discontinuous Deformation Analysis (3-D DDA) with nth-order polynomial displacement functions. In: Proceedings of 43rd U.S. Rock Mechanics Symposium and 4th U.S.-Canada Rock Mechanics Symposium, June 28–July 1 2009, Asheville, North Carolina, USA, paper number ARMA 09-5.

Beyabanaki, S.A.R., Mikola, G.R., Biabanaki, S.O. and Mohammadi, S., 2009e. New Point-to-Face Contact Algorithm for 3-D Contact Problems using the Augmented Lagrangian Method. Geomechanics and Geoengineering: An International Journal, 4 (3), 221–236.

Beyabanaki, S.A.R., Ferdosi, B. and Mohammadi, S., 2009f. Validation of dynamic block displacement analysis and modification of edge-to-edge contact constraints in 3-D DDA. International Journal of Rock Mechanics and Mining Sciences, 46, 1223–1234.

Beyabanaki, S.A.R., Jafari, A. and Yeung, M.R., 2010a. High - order three - dimensional discontinuous deformation analysis (3-D DDA). International Journal for Numerical Methods in Biomedical Engineering, 26 (12), 1522–1547.

Beyabanaki, S.A.R., Yeung, M.R., Mohammadi, S. and Gao, Y., 2010b. Contact Theory for Deformable Blocks in Three-Dimensional Discontinuous Deformation Analysis (3-D DDA). In: Proceedings of 44th U.S. Rock Mechanics Symposium and 5th U.S.-Canada Rock Mechanics Symposium, June 27–30 2010, Salt Lake City, UT, paper number ARMA 10-316.

Beyabanaki, S.A.R. and Yeung, M.R., 2011. Modification of Contact Constraints in High-Order Three-Dimensional Discontinuous Deformation Analysis (3-D DDA). In: Proceedings of 45th U.S. Rock Mechanics / Geomechanics Symposium, June 26–29 2011, San Francisco, CA, paper number ARMA 11-203.

Bobet, A., Fakhimi, A., Johnson, S., Morris, J., Tonon, F. and Yeung, M.R., 2009. Numerical Models in Discontinuous Media: Review of Advances for Rock Mechanics Applications Journal of Geotechnical and Geoenvironmental Engineering, 135 (11), 1547–1561.

Cleary, P.W., editor, 2007. Proceedings of Fourth International Conference on Discrete Element Methods. Brisbane, Australia. Cook, B.K. and Jensen, R.P., editors, 2002. Proceedings of the Third International Conference on Discrete Element Methods. Santa Fe, NM: ASCE.

Cundall, P.A. and Strack, O.D.L., 1979. A discrete numerical model for granular assemblies. Geotechnique, 29 (1), 47–65.

Cundall, P.A., 1988. Formulation of a Three-Dimensional Distinct Element Model — Part I. A Scheme to Detect and Represent Contacts in a System Composed of Many Polyhedral Blocks. International Journal of Rock Mechanics and Mining Sciences & Geomechanics Abstracts, 25 (3), 107–116.

Doolin, D.M. and Sitar, N., 2002. Displacement accuracy of discontinuous deformation analysis method applied to sliding block. Journal of Engineering Mechanics, 128, 1158–1168.

Ghaboussi, J. and Barbosa, R., 1990. Three-Dimensional Discrete Element Method for Granular Materials. Inter. Jour. for Num. and Anal. Meth. In Geomech., 14, 451–472.

Grayeli, R. and Hatami, K., 2008. Implementation of the finite element method in the three-dimensional discontinuous

deformation analysis (3D-DDA). International Journal for Numerical and Analytical Methods in Geomechanics, 32 (15), 1883–1902.

Hart, R., Cundall, P.A. and Lemos, J., 1988. Formulation of a Three-Dimensional Distinct Element Model — Part II. Mechanical Calculations for Motion and Interaction of a System Composed of Many Polyhedral Blocks. International Journal of Rock Mechanics and Mining Sciences & Geomechanics Abstracts, 25 (3), 117–125.

Itasca Consulting Group, 2001. PFC codes manuals. Itasca Consulting Group, Minneapolis.

Jenkins, J.T. and Satake, M., editors, 1983. Mechanics of granular materials: new models and constitutive relations. Amsterdam: Elsevier.

Jiang, Q.H. and Yeung, M.R., 2004. A model of point-to-face contact for three-dimensional discontinuous deformation analysis. Rock Mechanics and Rock Engineering, 37 (2), 95–116.

Jing, L., 2003. A review of techniques, advances and outstanding issues in numerical modelling for rock mechanics and rock engineering. International Journal of Rock Mechanics & Mining Sciences, 40, 283–353.

Jing, L. and Hudson, J.A., 2002. Numerical methods in rock mechanics. International Journal of Rock Mechanics & Mining Sciences, 39, 409–427.

Ke, T.-C. and Bray, J.D., 1995. Modeling of particulate media using discontinuous deformation analysis. Journal of Engineering Mechanics, 121 (11), 1234–1243.

Koyama, T., Nishiyama, S., Yang, M. and Ohnishi, Y., 2011. Modeling the interaction between fluid flow and particle movement with discontinuous deformation analysis (DDA) method. International Journal for Numerical and Analytical Methods in Geomechanics, 35, 1–20.

Lin, X. and Ng, T.-T., 1994. Numerical Modeling of Granular Soil Using Random Arrays of Three-Dimensional Elastic Ellipsoids, Computer Methods and Advances in Geomechanics, In: H. Siriwardane and M. Zaman, eds., Proceedings of 8th International Conference on Computer Methods and Advances in Geomechanics Rotterdam: Balkema, pp. 605–610.

Liu, J., Kong, X. and Lin, G., 2004. Formulation of the three dimensional discontinuous deformation analysis method. Acta Mechanica Sinica, 20 (3), 270–282.

MacLaughlin, M.M. and Doolin, D.M., 2006. Review of validation of the discontinuous deformation analysis (DDA) method. International Journal for Numerical and Analytical Methods in Geomechanics, 30, 271–305.

Munjiza, A., 2004. The Combined Finite-Discrete Element Method. London: Wiley.

Munjiza, A., editor, 2010. The Fifth International Conference on Discrete Element Methods. University of London, London.

Mustoe, G.G.W., Henriksen, M. and Huttelmaier, H.P., editors, 1989. Proceedings of the First Conference on DEM. Golden, CO: CSM Press.

O'Sullivan, C. and Bray, J.D.A., 2001. Comparative evaluation of two approaches to discrete element modeling of particulate media. In: N. Bicanic, ed., Proceedings of the Fourth International Conference on Discontinuous Deformation, Scotland, UK, 97–110.

O'Sullivan, C. and Bray, J.D., 2003. Modified Shear Spring Formulation for Discontinuous Deformation Analysis of

Particulate Media. Journal of Engineering Mechanics, 129 (7), 830–834.

Poschel, T. and Schwager, T., 2005. Computational Granular Dynamics, Models and Algorithms. New York: Springer.

F. Radjaï and F. Dubois, 2011. Discrete-element Modeling of Granular Materials. London: John Wiley & Sons.

Satake, M. and Jenkins, J.T., editors, 1988. Micromechanics of granular materials. Amsterdam: Elsevier.

Shi, G.H., 1988. Discontinuous deformation analysis: a new numerical model for the statics and dynamics of block systems. Thesis (PhD). Department of Civil Engineering, University of California, Berkeley.

Shi, G.H., 1993. Block System Modeling by Discontinuous Deformation Analysis. Southampton, UK: Computational Mechanics Publication.

Shi, G.H., 2001. Three dimensional discontinuous deformation analysis. In: D. Elsworth, ed. Proceedings of the 38th US Rock Mechanics Symposium, Taylor & Francis, Washington, DC, pp. 1421–1428.

Soto-Yarritu, G.R. and Martinez, A.de A., 2001. Computer simulation of granular material: Vibrating feeders. Powder Handling Process, 13 (2), 181–184.

Thomas, P.A., 1997. Discontinuous deformation analysis of particulate media. Thesis (PhD). University of California, Berkeley, CA.

Thomas, P.A. and Bray, J.D., 1999. Capturing nonspherical shape of granular media with disk clusters. Journal of Geotechnical and Geoenvironmental Engineering, 125 (3), 169–178.

Walton, O.R., 1993. Numerical Simulation of Inclined Chute Flows of Monodispersed, Inelastic, Frictional Spheres. Mechanics of Materials, 16, 239–247.

Wang, Y. and Tonon, F., 2010. Calibration of a discrete element model for intact rock up to its peak strength. International Journal for Numerical and Analytical Methods in Geomechanics, 34 (5), 447–469.

Williams, J.R. and Mustoe, G.G.W., editors, 1993. Proceedings of the Second International Conference on DEM. Boston, MI: IESL Publications.

Wu, J.H., 2008. New edge-to-edge contact calculating algorithm in three-dimensional discrete numerical analysis. Advances in Engineering Software, 39 (1), 15–24.

Wu, J.H., Juang, C.H. and Lin, H.M., 2005a. Vertex-to-face contact searching algorithm for three-dimensional frictionless contact problems. International Journal for Numerical Methods in Engineering, 63 (6), 876–897.

Wu, J.H., Ohnishi, Y. and Nishiyama, S., 2005b. A development of the discontinuous deformation analysis for rock fall analysis. International Journal for Numerical and Analytical Methods in Geomechanics, 29, 971–988.

Wu, J.H., Ohnishi, Y., Shi, G.H. and Nishiyama, S., 2005c. Theory of Three-Dimensional Discontinuous Deformation Analysis and Its Application to a Slope Toppling at Amatoribashi, Japan. International Journal of Geomechanics, 5 (3), 179–195.

Yeung, M.R., Jiang, Q.H. and Sun, N., 2003. Validation of block theory and three-dimensional discontinuous deformation analysis as wedge stability analysis method. International Journal of Rock Mechanics and Mining Sciences, 40 (2), 265–275.

Yeung, M.R., Sun, N., Jiang, Q.H. and Blair, S.C., 2004. Analysis of large block test data using three-dimensional discontinuous deformation analysis. International Journal of Rock Mechanics and Mining Sciences, 41 (3), 458–459.

Yeung, M.R., Jiang, Q.H. and Sun, N., 2007. A model of edge-to edge contact for three-dimensional discontinuous deformation analysis. Computers and Geotechnics, 34 (3), 175–186.

Chapter 4: Sphere-boundary edge and sphere-boundary corner contacts model in DDA for simulating particulate media in 3-D

(This chapter will be published as Beyabanaki SAR and Bagtzoglou AC. (2014) Sphere-boundary edge and sphere-boundary corner contacts model in DDA for simulating particulate media in 3-D, Geomechanics and Geoengineering: An International Journal, in press, doi: 10.1080/17486025.2014.933892)

4.1. Introduction

Discontinuous Deformation analysis (DDA) is a displacement-based method that was developed by Shi (1988, 1993) to provide a useful tool to analyze the mechanical response of discrete blocks. There have been a lot of studies conducted to validate and develop this method. Jing and Hudson (2002), Jing (2003), Ohnishi and Nishiyama (2007) reviewed applications of the DDA in rock mechanics and rock engineering. Furthermore, MacLaughlin and Doolin (2006) reviewed more than 100 validation studies on the DDA. Also, Shi (2007) presented applications of the DDA to rock stability analysis. Recently, Hatzor and Bakon-Mazor (2011) reviewed applications of the DDA to model rock slopes and underground openings.

Details of basic formulations of matrices for different potential terms are presented by Shi (2001) and Wu et al. (2005a). Liu et al. (2004) and Yeung et al. (2003, 2004) demonstrated the application of 3-D DDA. Jiang and Yeung (2004) presented a point-to-face model for contacts between polyhedral blocks in 3-D DDA. Wu et al. (2005a) developed a new contact searching algorithm for vertex-to-face contact problems. They assumed contacts to be frictionless and derived the 3-D DDA formulation for the normal contact force. Different algorithms for edge-to-edge contacts were presented by Yeung et al. (2007) and Wu (2008). Beyabanaki et al. (2008) presented a new algorithm to

search and calculate geometrical contacts in 3-D and validate their algorithm by some illustrative examples. Beyabanaki et al. (2009a, 2009b) implemented Trilinear (8-node) and Serendipity (20-node) hexahedral isoparametric finite elements into 3-D DDA to improve deformability of blocks. As an alternative method to improve block deformability in 3-D DDA, high-order displacement functions were used by Beyabanaki et al. (2009c, 2010). A new point-to-face contact algorithm for contacts between two polyhedral blocks with planar faces in 3-D DDA was presented by Beyabanaki et al. (2009d). Beyabanaki et al. (2009e) compared 3-D DDA solution for dynamic block displacement with analytical solution to study the validity of the method. Ahn and Song (2011) presented a new contact definition algorithm for 3-D DDA. Bakun-Mazor et al. (2012) validated 3-D DDA by comparing the numerical results obtained for modeling dynamic, single and double face sliding of a block with their proposed analytical solution. Liu et al. (2012) presented validation and application of 3-D DDA with tetrahedron finite element meshed block.

Although a lot of work has been done on DDA to date, the development of the DDA for particulate media applications is still at an early stage. Ke and Bray (1995), presented disk-based DDA in 2-D to model particulate media. Rein and Andrés (2001) used the method to model granular transport in vibrating feeders. Thomas and Bray (1999), Thomas (1999), and Koyama et al. (2011) demonstrated the ability of the DDA to model the response of systems of disks. The authors presented a formulation of the sphere-based 3-D DDA (Beyabanaki and Bagtzoglou 2012) and disk-based 2-D DDA with a new contact model (Beyabanaki and Bagtzoglou 2013). Moreover, recently, they studied accuracy of dynamic disk-based DDA (Beyabanaki and Bagtzoglou 2014).

In the paper presented by the authors on modeling particulate media using 3-D DDA (Beyabanaki and Bagtzoglou 2012), contact model for sphere-boundary edge and sphere-boundary corner contacts in sphere-based 3-D DDA are not studied. This paper, as a complementary study to (Beyabanaki and Bagtzoglou 2012), presents a new contact model for those two types of contacts. Details of the proposed algorithm to search contacts, detect the contact types, and calculate contact points are presented. Moreover, sub-matrices of contacts are derived. This proposed contact model has been implemented into a sphere-based 3-D DDA computer program and the results obtained for three illustrative examples are presented to show the capability of the model.

4.2. Formulation of Sphere-Based 3-D DDA

Discontinuous Deformation Analysis (DDA) is an implicit method, which solves the equilibrium equations by minimization of potential energies of single blocks and contacts between two blocks. Using the displacement of each block centroid, deformation functions calculate the deformation of all the blocks. Coulomb's law is applied to the contact interfaces when the blocks are in contact and the simultaneous equilibrium equations are generated and solved at each time step. The accumulation of incremental displacements and deformations at each time step form the large displacements. Since the incremental displacements of all points within each time step are small, they can be approximated by a first-order displacement function.

Recently, Beyabanaki and Bagtzoglou (2012) derived the formulation of 3-D DDA for rigid spheres using the Penalty method. In this section, formulation of sphere-based 3-D DDA with non-rigid blocks within the scope of this study is presented briefly. This formulation (including approximation of displacements, and sub-matrices of block

stiffness and initial stress) as well as the formulation presented by Beyabanaki and Bagtzoglou (2012) are required to model particulate media with non-rigid spheres by the DDA method in 3-D.

4.2.1. Approximation of Displacements

Considering the deformations of all spheres at all directions are the same, we have:

$$\begin{cases} \varepsilon_x = \varepsilon_y = \varepsilon_z = \varepsilon_0 \\ \gamma_{xy} = \gamma_{xz} = \gamma_{yz} = 0 \end{cases} \tag{4-1}$$

where $(\varepsilon_x, \varepsilon_y, \varepsilon_z)$ and $(\gamma_{xy}, \gamma_{xz}, \gamma_{yz})$ represent the normal and shear strains of a sphere, respectively.

Therefore:

$$\begin{pmatrix} u \\ v \\ w \end{pmatrix} = [T_i(x, y, z)].\begin{Bmatrix} u_0 & v_0 & w_0 & r_x & r_y & r_z & \varepsilon_0 \end{Bmatrix}^T \tag{4-2}$$

where (u, v, w) are the displacements at any point (x, y, z) of a sphere.

$$[T_i(x, y, z)] = \begin{pmatrix} 1 & 0 & 0 & 0 & (z - z_0) & -(y - y_0) & (x - x_0) \\ 0 & 1 & 0 & -(z - z_0) & 0 & (x - x_0) & (y - y_0) \\ 0 & 0 & 1 & (y - y_0) & -(x - x_0) & 0 & (z - z_0) \end{pmatrix} \tag{4-3}$$

where (u_0, v_0, w_0) and (x_0, y_0, z_0) represent body translations and the co-ordinates of the sphere center, respectively; (r_x, r_y, r_z) indicates the rotation angle of sphere i with a rotation centre at (x_0, y_0, z_0). $[T_i(x, y, z)]$ is the first order function of displacement.

4.2.2. Simultaneous Equations

By minimizing the total potential energy Π of the block system (including the potential energies due to sphere stiffness, initial stress, point loading, body force, inertia forces, constrained spring, normal contact, shear contact, and friction force), the simultaneous equations are derived:

$$\begin{aligned} [K_{ij}] &= \frac{\partial^2 \Pi}{\partial d_{ir}\, d_{js}} \quad , \quad r,s = 1,\cdots,7 \\ \{F_i\} &= -\frac{\partial \Pi(0)}{\partial d_{ir}} \quad , \quad r = 1,\cdots,7 \end{aligned} \tag{4-4}$$

In equation (4-4), 0 refers to the initial state of each time step, and

$$\{D_i\}^T = \{d_{1i} \quad d_{2i} \quad d_{3i} \quad d_{4i} \quad d_{5i} \quad d_{6i} \quad d_{7i}\} \tag{4-5}$$

and

$$\{D_j\}^T = \{d_{1j} \quad d_{2j} \quad d_{3j} \quad d_{4i} \quad d_{5j} \quad d_{6j} \quad d_{7j}\} \tag{4-6}$$

The equations for a system of N spheres can be expressed in matrix form as follows:

$$\begin{bmatrix} [K_{11}] & [K_{12}] & [K_{13}] & \dots & [K_{1N}] \\ [K_{21}] & [K_{22}] & [K_{23}] & \dots & [K_{2N}] \\ [K_{31}] & [K_{32}] & [K_{33}] & \dots & [K_{3N}] \\ \vdots & \vdots & \vdots & \ddots & \vdots \\ [K_{N1}] & [K_{N2}] & [K_{N3}] & \dots & [K_{NN}] \end{bmatrix} \begin{bmatrix} \{D_1\} \\ \{D_2\} \\ \{D_3\} \\ \vdots \\ \{D_N\} \end{bmatrix} = \begin{bmatrix} \{F_1\} \\ \{F_2\} \\ \{F_3\} \\ \vdots \\ \{F_N\} \end{bmatrix} \tag{4-7}$$

where $\{D_i\}$ and $\{F_i\}$ indicate displacement variables and loading and moments caused by the stresses and external forces acting on sphere i, respectively. The stiffness sub-

matrices $[K_{ij}]\big|_{i=j}$ depend on the material properties of sphere i, and $[K_{ij}]\big|_{i\neq j}$ are defined by the contacts between spheres i and j.

4.2.3. Sub-matrix of Block Stiffness

The strain energy, π_e, of the elastic stresses of sphere i is:

$$\pi_e = \iiint \frac{1}{2}\left(\varepsilon_x \;\varepsilon_y \;\varepsilon_z \;\gamma_{xy} \;\gamma_{yz} \;\gamma_{zx}\right)\left(\sigma_x \;\sigma_y \;\sigma_z \;\tau_{xy} \;\tau_{yz} \;\tau_{zx}\right)^T \tag{4-8}$$

Considering equation (4-1), the relation between stress and strain can be presented as below:

$$\begin{pmatrix}\sigma_x\\ \sigma_y\\ \sigma_z\end{pmatrix} = \frac{E}{1-2\upsilon}\begin{pmatrix}\varepsilon_0\\ \varepsilon_0\\ \varepsilon_0\end{pmatrix} \tag{4-9}$$

Where E and υ are the Young's modulus and the Poisson's ratio, respectively.

Therefore,

$$\pi_e = \frac{1}{2}\{D_i\}^T [E_i]\{D_i\} \tag{4-10}$$

where,

$$\{D_i\} = \begin{pmatrix} u_0 \\ v_0 \\ w_0 \\ r_x \\ r_y \\ r_z \\ \varepsilon_0 \end{pmatrix} \tag{4-11}$$

and

$$[E_i] = \frac{4\pi E R_i^3}{1-2\upsilon} \begin{pmatrix} 0 & 0 & 0 & 0 & 0 & 0 & 0 \\ 0 & 0 & 0 & 0 & 0 & 0 & 0 \\ 0 & 0 & 0 & 0 & 0 & 0 & 0 \\ 0 & 0 & 0 & 0 & 0 & 0 & 0 \\ 0 & 0 & 0 & 0 & 0 & 0 & 0 \\ 0 & 0 & 0 & 0 & 0 & 0 & 0 \\ 0 & 0 & 0 & 0 & 0 & 0 & 1 \end{pmatrix} \tag{4-12}$$

Minimizing the strain energy, π_e, forms a 7×7 matrix:

$$[E_i] \rightarrow [K_{ii}] \tag{4-13}$$

that is added to the sub-matrix $[K_{ii}]$ in the global equation (4-7).

4.2.4. Sub-matrix of Initial Stress

In the DDA, the computed stresses (σ_0) of the previous time step will be transferred to the next step as initial stress loading. The potential energy of the initial stress, π_{σ_0}, is given by:

$$\pi_e = \iiint (\varepsilon_0 \ \varepsilon_0 \ \varepsilon_0 \ 0 \ 0 \ 0)(\sigma_0 \ \sigma_0 \ \sigma_0 \ 0 \ 0 \ 0)^T = 4\pi R_i^3 \{D_i\}^T \begin{pmatrix} 0 \\ 0 \\ 0 \\ 0 \\ 0 \\ 0 \\ \sigma_0 \end{pmatrix} \tag{4-14}$$

Minimizing the potential energy of the initial stress, π_{σ_0} , gives a 7×1 matrix:

$$-4\pi R_i^3 \begin{pmatrix} 0 \\ 0 \\ 0 \\ 0 \\ 0 \\ 0 \\ \sigma_0 \end{pmatrix} \rightarrow \{F_i\} \tag{4-15}$$

that is added to the sub-matrix $\{F_i\}$ in the global equation (4-7).

4.3. Contact Model

The contact model is the main part of the DDA. It includes algorithms for detecting contact types, finding contact locations and reference planes and contact mechanics. Before detecting contact types, it is necessary to identify the spheres that are in contact or likely to be in contact with each other or with boundaries. This process is called ‘contact detection’. The algorithm used for contact detection is important since as the number of spheres increases, the simulation time will increase significantly. Munjiza (2004), Poschel and Schwager (2005) and O’Sullivan (2011) presented and compared

different algorithms for contact detection. In this section, detecting contact type, finding contact locations and reference plane, and contact mechanics are presented.

4.3.1. Detecting Contact Types

There are four types of contacts in modeling particulate media including sphere to sphere, sphere to boundary face, sphere to boundary edge, and sphere to boundary corner contacts (Figure 4-1). As can be seen in this figure, when we are dealing with concave polyhedrons, the type of contacts would be sphere-boundary face contact which was recently studied by the authors (Beyabanaki and Bagtzoglou 2012).

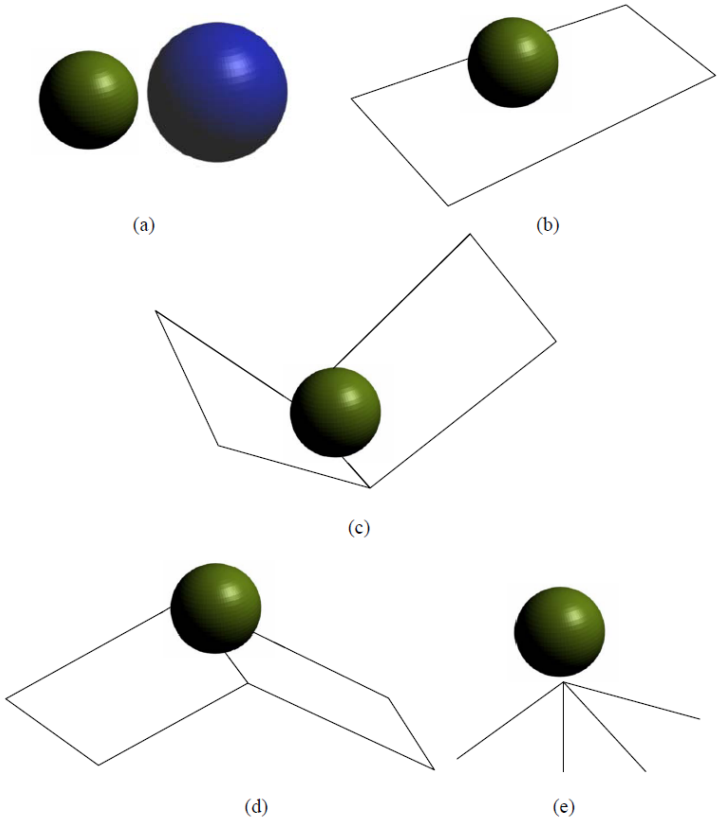

Figure 4-1 Different types of contact in particulate media (a) sphere-sphere contact (b) sphere-boundary face contact (c) sphere-boundary contact in concave polyhedrons (d) sphere-boundary edge (e) sphere-boundary corner contact

In this section, a new algorithm to find contact types between spheres and boundaries is presented. To detect contact type, the first step is finding the vertex/vertices of boundaries that has/have the minimum distance to the center of sphere i detected in contact detection process. Next, for each pair of sphere i and boundary face j sharing the detected vertex/vertices the following steps should be carried out:

1. Find the projection of the center of sphere i on the plane of boundary face j (point A)
2. Check if point A is inside boundary face j or on one of its edges or vertices. If so, call the point 'B' (Figure 4-2a).
3. If point A is not inside face j, find the vertex of face j with least distance to point A (vertex V). Then find the point on the edges sharing vertex V with the least distance to point A. Call it 'B' (Figure 4-2b).

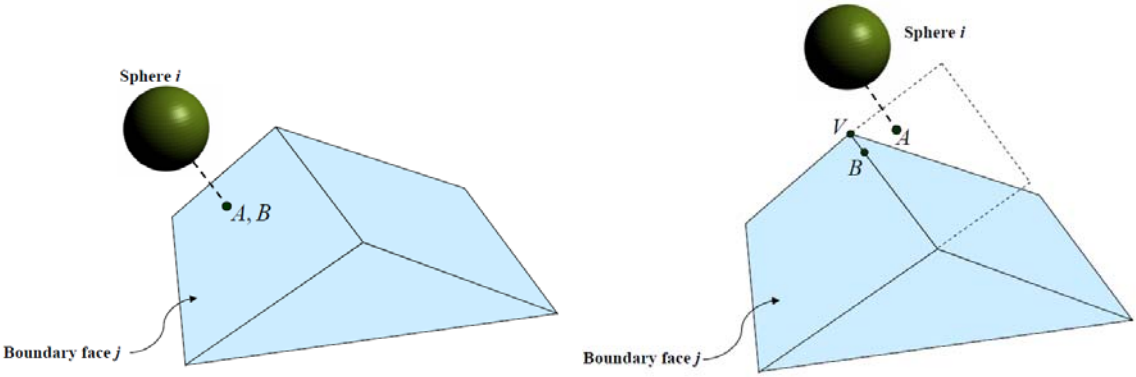

Figure 4-2 Projection of center of sphere i on the plane of boundary face j (a) inside the boundary face (b) outside the boundary face

There would be a contact between sphere i and boundary face j if:

$$d \le R_i + Tol \tag{4-16}$$

where

d = distance between center of sphere i and point B,

R_i = radius of sphere i, and

Tol = tolerance level.

Based on the situation of point B, the contact types can be identified as below:

1. If point B is located inside boundary face j, the contact type would be 'sphere to boundary face'.
2. If point B is located on one of the edges of boundary face j, the contact type would be 'sphere to boundary edge'.
3. If point B is located on one of the vertices of boundary face j, the contact type would be 'sphere to boundary corner'.

Since the change in positions of spheres between two time steps is very small in the sphere-based DDA, it is assumed that the contact type during one step does not change.

4.3.2. Finding Reference Plane

Details of sphere to sphere and sphere to boundary face contacts are presented by Beyabanaki and Bagtzoglou (2012). Therefore, the emphasis in this paper is on sphere to boundary edge and sphere to boundary corner contacts.

To find the reference plane, there would be two cases based on the value of d :

Case I ($d > 0$): in this case we have:

1. If the contact type is sphere to boundary face, then the reference plane would be boundary face j .
2. If the contact type is sphere to boundary edge or sphere to boundary corner, then the reference plane would be the plane with the unit normal vector of a line from point B to the center of sphere i .

Case II ($d \leq 0$): in this case we have:

1. If the contact type is sphere to boundary face, then like case I, the reference plane would be boundary face j .
2. If the contact type is sphere to boundary edge, then the reference plane would be the plane with average of the unit normal vector of the faces sharing the edge.
3. If the contact type is sphere to boundary corner, then the unit normal vector of the reference plane would be average of the unit normal vector of the faces sharing the vertex.

As shown in Figure 4-3, Ke and Bray (1995) presented a method to define the reference line in 2-D. In this method, it is necessary to calculate coordinates of two auxiliary points (points 2 and 3) in each iteration. As shown in the figure, points 2 and 3 must be obtained in each time step, and then it is possible to define the reference line 2-3 using them. In order to find points 2 and 3, it is necessary to consider a small angle (ξ) between the lines connecting the center of the disk to points 2, 3, and the boundary corner. This procedure must be repeated in each iteration to find the reference line.

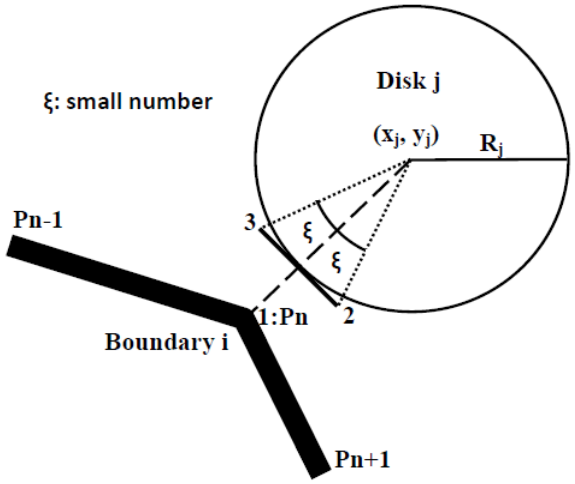

Figure 4-3 Reference line in 2-D (Ke and Bray 1995)

Although it was possible to generalize this method in 3-D, the authors preferred to present a new method in order to reduce the computational burden. By using the above-mentioned method presented, no more computations are needed to define the reference plane.

4.3.3. Contact Mechanics

At the beginning of each time step, the reference planes are computed and if spheres tend to penetrate into the boundaries, a reaction force is activated to keep the spheres and boundaries separated.

The reference point (P_1) is intersection of the sphere with a line from point B obtained from section 3.1 and center of the sphere (Figure 4-4).

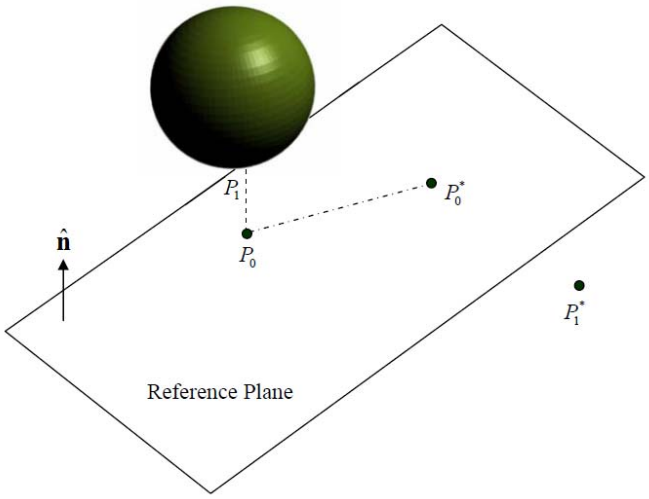

Figure 4-4 The reference plane

As shown in Figure 4-4, assume $P_1(x_1, y_1, z_1)$ and $P_1^*(x_1^*, y_1^*, z_1^*)$ denote the locations of the reference point of sphere i before and after a displacement increment, respectively; $P_0(x_0, y_0, z_0)$ indicates the projection of the reference point $P_1(x_1, y_1, z_1)$ on the reference plane and $P_0^*(x_0^*, y_0^*, z_0^*)$ represents this point after the displacement increment. (u_1, v_1, w_1) and (u_0, v_0, w_0) are the displacement increments of the reference point (P_1) and its projection on the reference plane (P_0), respectively and $\hat{\mathbf{n}}$ represents the unit

normal vector of the reference plane. The normal distance of point $P_1^*(x_1^*, y_1^*, z_1^*)$ from the reference plane can be presented as below:

$$d_n = \hat{\mathbf{n}}.\mathbf{P_0^*P_1^*} = \hat{\mathbf{n}}.\begin{bmatrix} x_1 - x_0 \\ y_1 - y_0 \\ z_1 - z_0 \end{bmatrix} + \hat{\mathbf{n}}.\begin{bmatrix} u_1 - u_0 \\ v_1 - v_0 \\ w_1 - w_0 \end{bmatrix} = M + [H_i][D_i] - [Q_j][D_j] \quad (4\text{-}17)$$

where

$$M = \hat{\mathbf{n}}.\begin{bmatrix} x_1 - x_0 \\ y_1 - y_0 \\ z_1 - z_0 \end{bmatrix} \quad (4\text{-}18)$$

$$[H_i] = \hat{\mathbf{n}}.T_i(x_1, y_1, z_1) \quad (4\text{-}19)$$

and

$$[Q_j] = \hat{\mathbf{n}}.T_j(x_0, y_0, z_0) \quad (4\text{-}20)$$

In the original sphere-based 3-D DDA, the Penalty method is used. However, the augmented Lagrangian method has some advantages over the Penalty method. The most important ones are (Mohammadi 2003):

- Since the contact solution depends highly on the choice of the penalty number and the optimal number cannot be explicitly found beforehand, in the Penalty method, the constraints are only satisfied in an approximate manner. In contrast, using the augmented Lagrangian method, the constraints are satisfied accurately within a user defined required tolerance.

- In the penalty method, if the penalty number is too low, the constraints are poorly satisfied, while if it is too large, the simultaneous equilibrium matrix becomes difficult to solve. On the contrary, in the augmented Lagrangian method, large penalty values are not required. It would avoid the ill conditioning of the stiffness matrices.

Because of these advantages, the authors used the augmented Lagrangian method in this section to enforce contact constrains.

The contact force at the contact point can be accurately approximated by iteratively calculating the Lagrange multiplier λ^* when the augmented Lagrangian method is used. λ^* can be updated as below:

$$\lambda \approx \lambda^*_{l+1} = \lambda^*_l + P_n.d_n \tag{4-21}$$

where P_n is the penalty number; λ^*_{l+1} and λ^*_l are the updated Lagrange multiplier and its value at the l-th iteration, respectively. The reader is referred to Mohammadi (2003) for details of the augmented Lagrangian method.

At the l-th iteration, the potential energy of the contact force, π_c, can be expressed as follows:

$$\pi_c = \lambda^*_l d_n + \frac{1}{2} P_n d_n{}^2 \tag{4-22}$$

Minimizing the calculated potential energy, π_c, gives the following 7×7 matrices that would be added to sub-matrices $[K_{ii}],[K_{ij}],[K_{ji}]$, and $[K_{jj}]$ in the global equation (4-7):

$$[K_{ii}] = P_n[H_i]^T[H] \tag{4-23}$$

$$[K_{ij}] = P_n[H_i]^T[Q_j] \tag{4-24}$$

$$[K_{ji}] = P_n[Q_j]^T[H_i] \tag{4-25}$$

$$[K_{jj}] = P_n[Q_j]^T[Q_j] \tag{4-26}$$

and the following 7×1 vectors are calculated and then added to the global force vector:

$$\{F_i\} = -(\lambda_l^* + P_n \frac{M}{l}).[H_i]^T \tag{4-27}$$

$$\{F_j\} = -(\lambda_l^* + P_n \frac{M}{l}).[Q_j]^T \tag{4-28}$$

4.4. Examples

In this section, three examples are presented to investigate the newly proposed contact model.

4.4.1. Sphere-Boundary Corner Contact

The geometry of the first example is shown in Figure 4-5a. In this case, the calculation of a contact between a sphere and vertex of a pyramid using the proposed model is simulated. The pyramid is fixed and the sphere falls down due to gravity with an initial velocity of 0.0 m/s. The sphere's density, Young's modulus and Poisson's ratio are $2.5\times10^3\ kg/m^3$, 4 GPa and 0.25, respectively. Moreover, the penalty number is 400 MN/m.

Figures 4-5b-4-5d shows the geometry after 0.67, 0.81 and 1.1s when the proposed algorithm is used. As can be seen, after the contact between the sphere and the pyramid happens, the sphere would rebound. This case was simulated again without considering the sphere-boundary corner model. The result is shown in Figure 4-5e and indicates that the sphere penetrates the pyramid due to the absence of the model. This example shows that the proposed contact model can handle a sphere-boundary corner contact well.

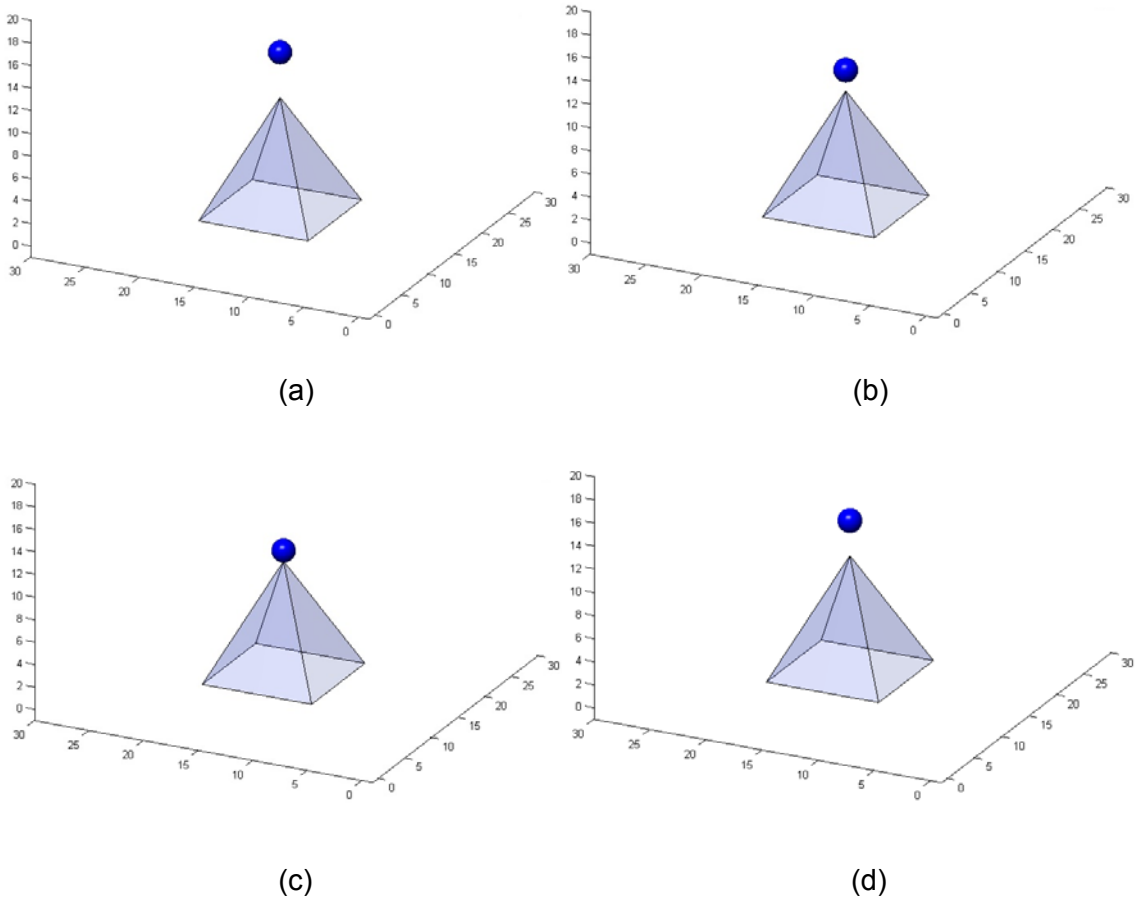

(a) (b)

(c) (d)

Figure 4-5 Sphere to boundary corner contact using the proposed model (a) Initial configuration (b) after 0.67s (c) after 0.81s (d) after 1.1s using the proposed model (e) after 1.1s without using the proposed model

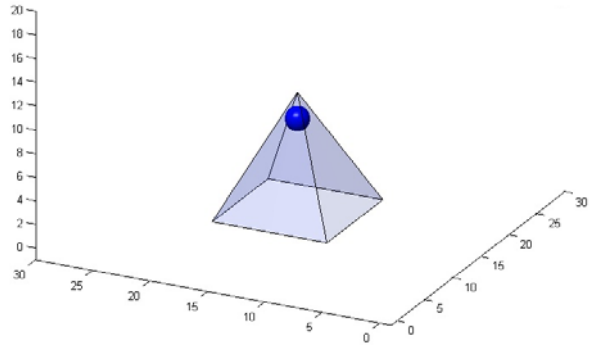

(e)

Figure 4-5 Sphere to boundary corner contact using the proposed model (a) Initial configuration (b) after 0.67s (c) after 0.81s (d) after 1.1s using the proposed model (e) after 1.1s without using the proposed model (Cont.)

4.4.2. Sphere-Boundary Edge Contact

In this example, sphere to boundary edge contact is investigated. A sphere located above a fixed wedge falls down due to the gravity force. The sphere's properties are similar to example 4.4.1. The sphere's initial velocity is 0.0 m/s and the penalty number is 400 MN/m. Initial configuration is shown in Figure 4-6a. Results of simulation using the proposed contact model are shown in Figures 4-6b and 4-6c after 63 and 88s, respectively. As can be seen, the model is able to simulate the sphere-boundary edge contact. Moreover, Figure 6d shows the results obtained for the simulation without considering the proposed contact model. As can be seen in the figure, there is a penetration between the sphere and the wedge when sphere-boundary edge contact model is not used.

4.4.3. Funnel Flow

This example covers all possible contact types in particulate media including sphere to sphere, sphere to boundary face, sphere to boundary edge, and sphere to boundary corner contacts. As shown in Figure 4-7, there are three layers of spheres above a funnel and there is a pyramid below the funnel. The spheres fall down due to gravity. Each sphere has a density of $2500\,kg/m^3$ and the stiffness of the normal contact spring, the time interval and the friction angle are $P = 10^7\,kN/m$, $0.05s$ and 10°, respectively. Young's modulus and Poisson's ratio for the disks are 4 GPa, and 0.2, respectively. The configuration of spheres after 6s, 9.2s, and 10.9s are shown in Figures 4-8a, 4-8b, and 4-8c, respectively.

As can be seen, the spheres flow through the funnel (including sphere to sphere and sphere to boundary face contacts) and on the pyramid (including sphere to sphere, sphere to boundary face, sphere to boundary edge, and sphere to boundary corner contacts) with no overlap between spheres and boundaries. This example demonstrates that the proposed model can simulate all possible contact types between a large number of spheres and boundaries.

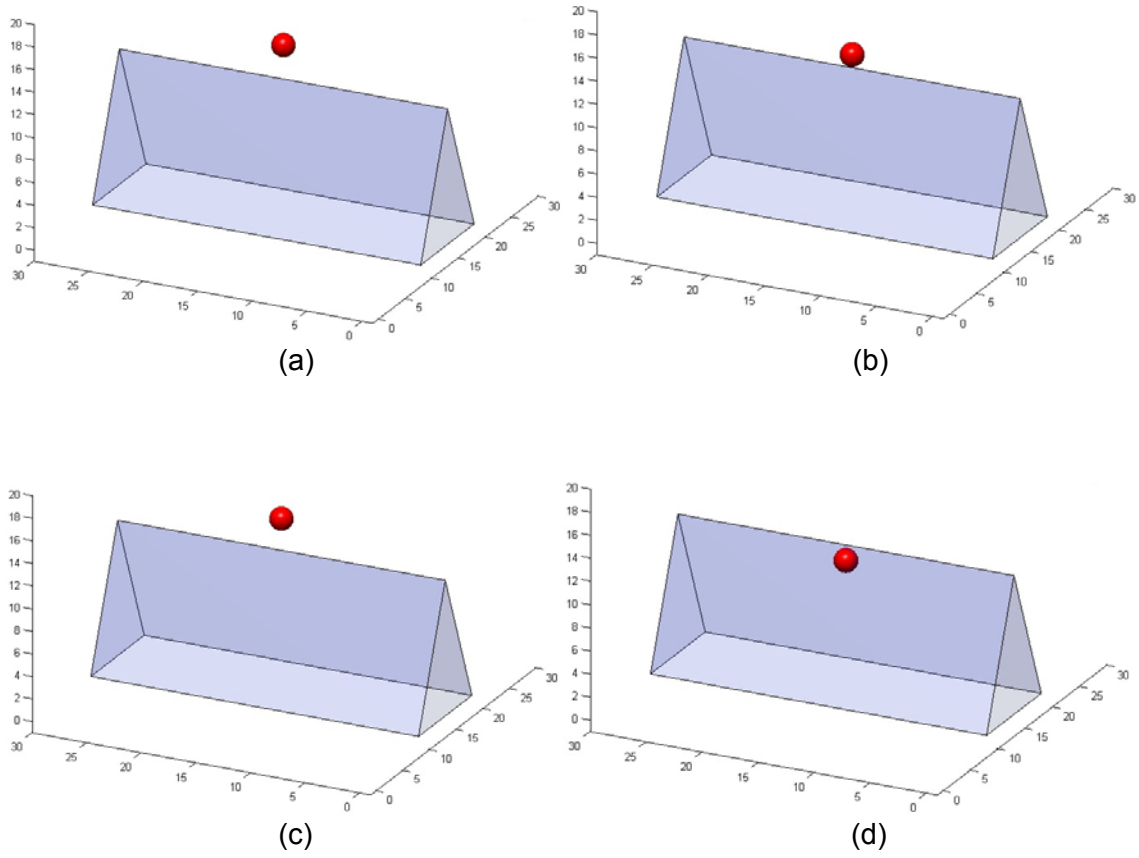

Figure 4-6 Sphere to boundary edge contact using the proposed model (a) Initial configuration (b) after 0.63s (c) after 0.88s using the proposed model (d) after 0.88s without using the proposed model

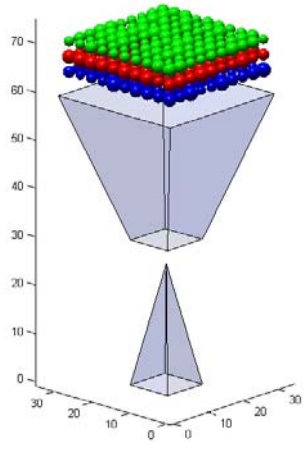

Figure 4-7 Initial configuration

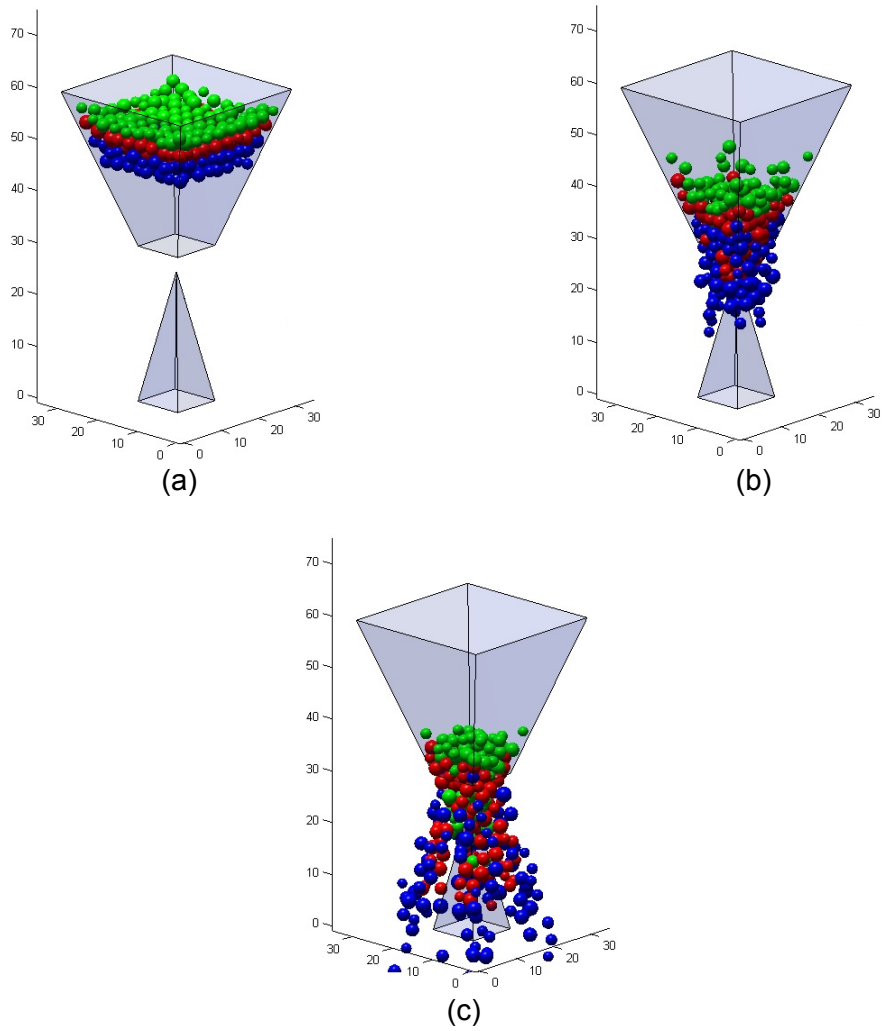

Figure 4-8 Configuration of the spheres (a) after 6s (b) after 9.2s (c) after 10.9s

4.5. Conclusions

To model particulate media, four types of contacts must be considered in order to obtain accurate results. Two of them, including sphere to sphere and sphere to boundary face contacts, were presented in the authors' previous paper (Beyabanaki and Bagtzoglou 2012). As a complementary study to (Beyabanaki and Bagtzoglou 2012), this paper describes a new contact model for sphere-boundary edge and sphere-boundary corner

contacts in 3-D DDA for modeling of particulate media. Details of the model are given including a new algorithm to search contacts, detect the contact types and calculate contact points. Moreover, formulas for contact sub-matrices are derived. In order to reduce the computational burden, unlike the contact model presented in disk-based 2-D DDA, there is no need to calculate coordinates of auxiliary points in each iteration to find the reference plane in the proposed model. The new contact model has been implemented into a sphere-based 3-D DDA program and three examples are presented to verify its capability. The results show that the model, involving the contact searching algorithm in 3-D and formulations, successfully and correctly simulates the behavior of spheres in contact with boundaries with different situations in 3-D domain. They also show that without considering the presented contact model, the results of modeling of particulate media can be unreasonable.

4.6. References

Ahn TY, Song JJ. 2011. New Contact-Definition Algorithm using Inscribed Spheres for 3D Discontinuous Deformation, International Journal of Computational Methods, 8(2): 171–191.

Bakun-Mazor D, Hatzor YH, Glaser SD. 2012. Dynamic sliding of tetrahedral wedge: The role of interface friction. International Journal for Numerical and Analytical Methods in Geomechanics, 36(3): 327–343.

Bakun-Mazor D, Hatzor YH, Glaser SD, Santamarina JC. 2013. Thermally vs. seismically induced block displacements in Masada rock slopes, International Journal of Rock Mechanics & Mining Sciences, 61:196–211.

Bao H, Hatzor YH, Huang X. 2012. A New Viscous Boundary Condition in the Two-Dimensional Discontinuous Deformation Analysis Method for Wave Propagation Problems, Rock Mech Rock Eng, 45:919–928.

Beyabanaki SAR, Grayeli R, Hatami K. 2008. Three-dimensional discontinuous deformation analysis (3-D DDA) using a new contact resolution algorithm. Computers and Geotechnics, 35:346-356.

Beyabanaki SAR, Jafari A, Biabanaki SO, Yeung MR. 2009a. A Coupling Model of 3-D Discontinous Deformation Analysis (3-D DDA) and Finite Element Method, AJSE, 34:2B:107-119.

Beyabanaki SAR, 2009b. Jafari A, Biabanaki SO, and Yeung MR. Nodal-based Three-Dimensional Discontinuous Deformation Analysis (3-D DDA), Computers and Geotechnics, 36:359-372.

Beyabanaki SAR, Jafari A, Yeung MR. 2009c. Second-Order Displacement Functions for Three-Dimensional Discontinuous Deformation Analysis (3-D DDA), International Journal of Science and Technology, 16(3):216-225.

Beyabanaki SAR, Mikola GR, Biabanaki SO, Mohammadi S. 2009d. New Point-to-Face Contact Algorithm for 3-D Contact Problems using the Augmented Lagrangian Method, Geomechanics and Geoengineering: An International Journal, Taylor & Francis, 4 (3):221-236.

Beyabanaki SAR, Ferdosi B, Mohammadi S. 2009e. Validation of dynamic block displacement analysis and modification of edge-to-edge contact constraints in 3-D DDA, International Journal of Rock Mechanics and Mining Sciences, Elsevier, 46:1223-1234.

Beyabanaki SAR, Jafari A, and Yeung MR. 2010. High - order three - dimensional discontinuous deformation analysis (3-D DDA), International Journal for Numerical Methods in Biomedical Engineering, 26 (12):1522–1547.

Beyabanaki SAR and Bagtzoglou AC. 2012. Three-dimensional discontinuous deformation analysis (3-D DDA) method for particulate media applications, Geomechanics and Geoengineering: An International Journal 7(4):239-253.

Beyabanaki SAR and Bagtzoglou AC, 2013. Non-rigid disk-based DDA with a new contact model, Computers and Geotechnics 49:25–35.

Beyabanaki SAR and Bagtzoglou AC, 2014b. Accuracy of Dynamic Disk-Based DDA with Respect to a Single Sliding Disk Cluster, Geomechanics and Geoengineering: An International Journal, DOI: 10.1080/17486025.2013.838645.

Hatzor YH and Bakun-Mazor D. 2011. Modeling dynamic deformation in natural rock slopes and underground openings with DDA: review of recent results. Geomechanics and Geoengineering: An International Journal, 6(4):283-292.

Jiang QH, Yeung MR. 2004. A model of point-to-face contact for three-dimensional discontinuous deformation analysis. Rock Mechanics and Rock Engineering, 37(2):95 – 116.

Jing L, Hudson JA. 2002. Numerical methods in rock mechanics, International Journal of Rock Mechanics & Mining Sciences, 2002; 39: 409–427.

Jing L. 2003. A review of techniques, advances and outstanding issues in numerical modelling for rock mechanics and rock engineering, International Journal of Rock Mechanics & Mining Sciences, 40: 283–353.

Ke, T.-C., and Bray, J. D. 1995. Modeling of particulate media using discontinuous deformation analysis. J. Eng. Mech., 121(11), 1234–1243.

Koo CY, Chern JC. 1998. Modification of the DDA method for rigid block problems. International Journal of Rock Mechanics and Mining Sciences, 35(6):684–693.

Koyama T, Nishiyama S, Yang M, Ohnishi Y. 2011. Modeling the interaction between fluid flow and particle movement with discontinuous deformation analysis (DDA) method, Int. J. Numer. Anal. Meth. Geomech., 35:1–20.

Li X, He S, Luo Y, Wu Y. 2012. Simulation of the sliding process of Donghekou landslide triggered by the Wenchuan earthquake using a distinct element method, Environ Earth Sci, 65:1049–1054.

Liu L, Linde AT, Sacks IS, and He S. 1996. Aseismic fault slip and block deformation in north China, Pure Appl. Geophys., 146(3/4):717-740.

Liu J, Kong X, Lin G. 2004. Formulation of the three-dimensional discontinuous deformation analysis method. Acta Mechanica Sinica, 20(3):270-282.

Liu J, Nan Z, Yi P. 2012. Validation and application of three-dimensional discontinuous deformation analysis with tetrahedron finite element meshed block, Acta Mechanica Sinica, 28(6):1602–1616.

MacLaughlin MM, Doolin DM. 2006. Review of validation of the discontinuous deformation analysis (DDA) method, Int J Numer Anal Meth Geomech, 30: 271-305.

Mohammadi S. 2003. Discontinuum Mechanics: Using Finite and Discrete Elements. WIT Press.

Munjiza A. 2004. The combined finite-discrete element methods. John Wiley.

Ohnishi Y, Nishiyama S. 2007. Recent insights of analyses using discontinuous methods in rock engineering in Japan, Proceedings of the 8th International Conference on Analysis of Discontinuous Deformation: Fundamentals and Applications to Mining and Civil Engineering, Beijing, China, August 14-19, pp. 15-26.

O'Sullivan C. 2011. Particulate Discrete Element Modelling: A Geomechanics Perspective, Taylor & Francis.

Poschel T, Schwager. 2005. Computational Granular Dynamics: Models and Algorithms, Springer-Verlag.

Rein G, Andrés A. 2001. Computer simulation of granular material: vibrating feeders, Powder Handling & Processing, 13(2), 181-185.

Shi GH. 1988. Discontinuous deformation analysis: a new numerical model for the statics and dynamics of block systems, PhD thesis, Department of Civil Engineering, University of California, Berkeley.

Shi GH. 1993. Block System Modeling by Discontinuous Deformation Analysis. Computational Mechanics Publication: Southampton. UK.

Shi GH. 2001. Three dimensional discontinuous deformation analysis. In: Proceedings of the 38th US Rock Mechanics Symposium, D Elsworth et al, ed., p 1421-1428.

Shi GH. 2007. Applications of discontinuous deformation analysis (DDA) to rock stability analysis, Proceedings of the 8th International Conference on Analysis of Discontinuous Deformation: Fundamentals and Applications to Mining and Civil Engineering, Beijing, China, August 14-19, pp. 1-13.

Thomas, P. A. 1997. Discontinuous deformation analysis of particulate media. PhD thesis, University of California, Berkeley, Berkeley, CA.

Thomas, P. A., and Bray, J. D. 1999. Capturing nonspherical shape of granular media with disk clusters. J. Geotech. Geoenviron. Eng., 125(3), 169–178.

Wu JH, Ohnishi Y, Shi GH, Nishiyama S. 2005a. Theory of Three-Dimensional Discontinuous Deformation Analysis and Its Application to a Slope Toppling at Amatoribashi, Japan. International Journal of Geomechanics, 179-195.

Wu JH, Juang CH, Lin HM. 2005b. Vertex-to-face contact searching algorithm for three-dimensional frictionless contact problems. International Journal for Numerical Methods in Engineering, 63(6):876-897.

Wu JH. 2008. New edge-to-edge contact calculating algorithm in three-dimensional discrete numerical analysis. Advances in Engineering Software, 39(1):15-24.

Yagoda-Biran G, Hatzor YH. 2010. Constraining paleo PGA values by numerical analysis of overturned columns, Earthquake Engineering and Structural Dynamics, 39:463–472.

Yeung MR, Jiang QH, Sun N. 2003. Validation of block theory and three-dimensional discontinuous deformation analysis as wedge stability analysis method. Int J Rock Mech Min Sci, 40(2):265 –275.

Yeung MR, Sun N, Jiang QH, Blair SC. 2004. Analysis of large block test data using three-dimensional discontinuous deformation analysis. Int J Rock Mech Min Sci, 41(3):458–459.

Yeung MR, Jiang QH, Sun N. 2007. A model of edge-to-edge contact for three-dimensional discontinuous deformation analysis. Computers and Geotechnics, 34(3):175-186.

Chapter 5: Accuracy of dynamic disk-based DDA

(This chapter was published as Beyabanaki SAR and Bagtzoglou AC. (2014) Accuracy of Dynamic Disk-Based DDA with Respect to a Single Sliding Disk Cluster, Geomechanics and Geoengineering: An International Journal, 9(3): 231-240)

5.1. Introduction

Discontinuous deformation analysis (DDA) is a displacement based method that was developed by Shi (Shi and Goodman 1985, Shi 1988, 1992, 1993) during the 1980s for modeling large deformation in fractured rock masses. Numerous studies have been conducted on DDA to validate this approach and improve its performance. MacLaughlin and Doolin (2006) presented a comprehensive review including more than 100 validation studies on DDA. This method is conventionally used to analyze the behavior of a jointed rock mass in rock mechanics and rock engineering. Jing and Hudson (2002), Jing (2003) and Ohnishi and Nishiyama (2007) reviewed the applications of DDA in rock engineering. DDA has been applied successfully to analysis of stability problems. Dynamic DDA for rock problems is investigated by Hatzor and Feintuch (2001), Tsesarsky et al. (2002, 2005), Kamai and Hatzor (2008), Beyabanaki et al. (2009a) and Bakun-Mazor et al. (2012). Hatzor and Bakon-Mazor (2011) presented a review on recent applications of the DDA to model rock slopes and underground openings.

Unlike the development of the DDA applications in rock mechanics and rock engineering, little work has been done on the development of DDA to simulate the behavior of soils, and it is still at an early stage. Ke and Bray (1995) presented disk based DDA to model particulate media with the application to granular soils. Thomas (1997) and Thomas and Bray (1999) demonstrated qualitatively the ability of the DDA to model the response of systems of disks, and Koyama et al. (2011) presented coupled

solid circular particles movement and fluid flow processes in porous media using combined DDA-FEM approach. Lately, the authors presented the spherical-based DDA to model particulate media in 3-D (Beyabanaki and Bagtzoglou 2012).

To model particulate media, researchers often use circular elements to minimize computation times. However, due to excessive rolling of the perfectly circular particles, the results are not accurate (Rothenburg and Bathurst 1992, Ng and Dobry 1994). A circle is an unrealistic simplification of the particle shapes of particulate media. The use of circular particles also limits the range of possible void ratios and fabrics (Mitchell 1993). To overcome these problems, Thomas and Bray (1999) presented a new particle type called ‘disk clusters’. A disk cluster is an assembly of circular disks that are permanently attached to form an irregularly shaped particle. Unlike circular disks, disk clusters more closely represent the actual shape of granular materials and have less tendency to rotate. Thomas (1997) and Thomas and Bray (1999) used successfully disk based DDA to simulate the geotechnical problems of biaxial shear, anchor pullout and bearing capacity using a large number of disk clusters.

Earthquake induced motion is one of the major triggers for slope and landslide failures, which is an engineering hazard, with life threatening consequences. Numerical methods provide useful tools to analyze stability of slopes. Before applying dynamic disk-based DDA to a full-scale problem in geotechnical engineering, e.g. an earthquake-triggered landslide, it is necessary to investigate the validity of the method under dynamic conditions. The first step to validate dynamic disk-based DDA is to check whether results obtained by this method are in agreement with analytical solutions. Then, a comparison with physical models would be performed. However, the analytical validation of the numerical method can only be carried out for a single block (Hatzor and Feintuch 2001).

Hence, as the first necessary step to validate disk-based DDA under dynamic conditions, the accuracy of disk-based DDA is studied by a number of investigators that concentrated on exploring the dynamic response of a disk cluster on an inclined plane. It provides guidelines for future, more detailed analyses. Unlike the previous works on dynamic DDA, the behavior of velocity obtained by DDA compared with the analytical solution under dynamic load is studied in this research. Moreover, a comparison between the results obtained in the case of sliding due to gravitational force only and the case of sliding due to dynamic force is performed for different contact friction angles.

Thomas and Bray (1999) presented an example of sliding a disk cluster on a rigid incline under gravitational force only, but they did not perform sensitivity analysis and did not present the errors associated with their analysis. In this paper, displacement of a disk cluster subjected to only gravitational force and resting on an incline with different friction angles is investigated. Moreover, the behavior of velocity and displacement obtained by disk-based DDA compared with the analytical solution under dynamic load is studied. Our interest is in how varying model parameters affect the behavior of disk-based DDA under dynamic conditions. Lin et al. (1996) and Beyabanki et al. (2009a, 2009b) showed that by using the augmented Lagrangian method (ALM), the accuracy of the contact solution would not depend on the choice of the penalty number. Recently, the authors used a modified version of disk-based DDA (Beyabanaki and Bagtzoglou 2013) that employs the ALM and investigated the effect of time step size and friction angle on the results of simulations as well as the errors for rigid disks. In this study, three different accelerations following sinusoidal input functions of increasing complexity are used to perform a sensitivity study on disk-based DDA under dynamic conditions.

5.2. Theory of Disk-Based DDA

Disk-based DDA models particulate media as a collection of discrete disks. For each disk, the displacement matrix at an arbitrary point (x, y) in the disk is obtained from the corresponding location and the displacement vector $\{D\}$. The relation between them can be shown in the following equations:

$$\begin{pmatrix} u \\ v \end{pmatrix} = [T_i(x, y)].\{D_i\} \tag{5-1}$$

where

$$[T_i(x, y)] = \begin{pmatrix} 1 & 0 & -(y - y_0) \\ 0 & 1 & (x - x_0) \end{pmatrix} \tag{5-2}$$

$$\{D_i\}^T = \{u_0 \quad v_0 \quad r_0\} \tag{5-3}$$

and (x_0, y_0) are the coordinates of the disk center, (u_0, v_0) indicate body translations; r_0 represents the rotation angle of disk i with a rotation centre at (x_0, y_0). The behavior of an individual disk includes the rigid body translations and rigid body rotations.

Since disk-based DDA conforms to the principle of minimum total potential energy, the total potential energy is the summation of all potential energy sources for each disk including the potential energies due to point loading, body force, inertia forces, constrained spring, normal contact, shear contact, and friction force. Details can be found in (Ke and Bray,1995).

Individual disks are connected and form a disk system by contacts between disks and by displacement constraints on single disks. For a system of N disks, the system of equations has the following form:

$$\begin{bmatrix} [K_{11}] & [K_{12}] & [K_{13}] & \dots & [K_{1N}] \\ [K_{21}] & [K_{22}] & [K_{23}] & \dots & [K_{2N}] \\ [K_{31}] & [K_{32}] & [K_{33}] & \dots & [K_{3N}] \\ \vdots & \vdots & \vdots & \ddots & \vdots \\ [K_{N1}] & [K_{N2}] & [K_{N3}] & \dots & [K_{NN}] \end{bmatrix} \begin{bmatrix} \{D_1\} \\ \{D_2\} \\ \{D_3\} \\ \vdots \\ \{D_N\} \end{bmatrix} = \begin{bmatrix} \{F_1\} \\ \{F_2\} \\ \{F_3\} \\ \vdots \\ \{F_N\} \end{bmatrix} \tag{5-4}$$

Because each disk has three degrees of freedom, $[K_{ij}]$ in the coefficient matrix given by the above equation is a 3×3 Sub-matrix. $\{D_i\}$ and $\{F_i\}$ are 3×1 sub-matrices. $\{F_i\}$ represents the loading on disk i distributed to the three deformation variables. The algorithm of disk-based DDA for modeling of particulate media is listed in Algorithm 5-1.

Algorithm 5-1. Disk-based DDA for modeling of particulate media

(Beyabanaki and Bagtzoglou 2012)

1: Input geometry, boundary condition, constraints, forces, …

2: **For** i = 1, ..., n time steps **Do**

3: Detect contact between disks, and disks and boundaries

4: Find reference point and line

5: **Repeat** {open-close iteration}

6: Compute the contact forces between the disks including frictional, normal and shear forces

7: Assemble the generalized stiffness, K, and force, F, matrices; integrate over time and solve

8: $\mathbf{D = K^{-1}F}$ using open-close iteration,

9: **Until** no-tension, no-penetration (within tolerances)

10: Update disks center positions

11: **End For**

Disk clusters have been developed to represent the non-spherical shape of granular materials more accurately and to minimize excessive rolling (Thomas and Bray 1999). A disk cluster is defined as a collection of individual disks which are connected rigidly and permanently. In this case, the displacements of the cluster centroid are the unknowns (see Thomas and Bray (1999) for more details). Five types of disk cluster particles and some different ones that can be made by changing the relative sizes of individual disks within a cluster are shown in Figure 5-1(a) and 5-1(b).

5.3. Sliding Under the Action of Gravitational Force Only

Verification using simple geometries, which allow analytical solutions, is an important aspect of numerical modeling in geomechanics (Doolin and Sitar 2002). Moreover, it is important to validate a numerical code that has implemented a proposed new method.

(a) (b)

Figure 5-1. (a) Different types of disk clusters (b) Examples of possible disk clusters (Thomas and Bray 1999)

In this section, the sliding behavior of a single disk cluster comprising three disks on a rigid incline due to gravity only is investigated with the centroid of the cluster being tracked. The density of the disks is taken to be $2500\,kg/m^3$ and the penalty spring stiffness, time step, and disk radii are $P = 10^7\,N/m$, $0.05\,s$, and $1\,m$, respectively.

This example is presented to investigate the behavior of a single disk cluster on an incline with different friction angles. Sliding of a disk on an inclined plane with friction angle φ at an angle α to the horizontal direction is simulated (Figure 5-2). In this case, the analytical solution for displacement of the disk due to gravity can be obtained as:

$$s = \frac{1}{2} g \left(\sin(\alpha) - \tan(\varphi)\cos(\alpha)\right) t^2 \qquad (5\text{-}5)$$

where s is the displacement of the disk, g is the gravitational acceleration, and t is time. According to Ke and Bray (1995), when:

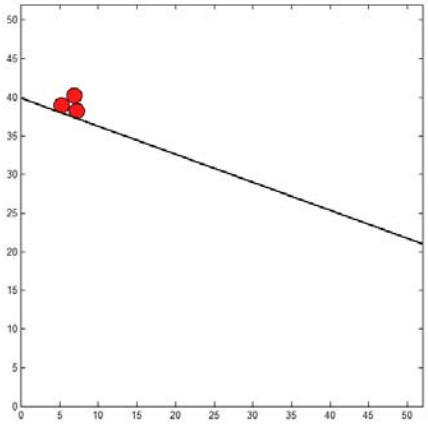

Figure 5-2. Sliding of a disk cluster including three disks on an incline

$$\varphi \le \tan^{-1}\left(\frac{\tan(\alpha)}{3}\right) \tag{5-6}$$

the disk will slide on the plane. In this example, $\alpha = 40^0$; therefore, $\varphi \le 15.63^0$. Four different interface friction angles (0^0, 5^0, 10^0, and 15^0) are used in this study. A comparison of predicted displacements from disk-based DDA and the analytical solution for different values of friction angle are presented in Figure 5-3.

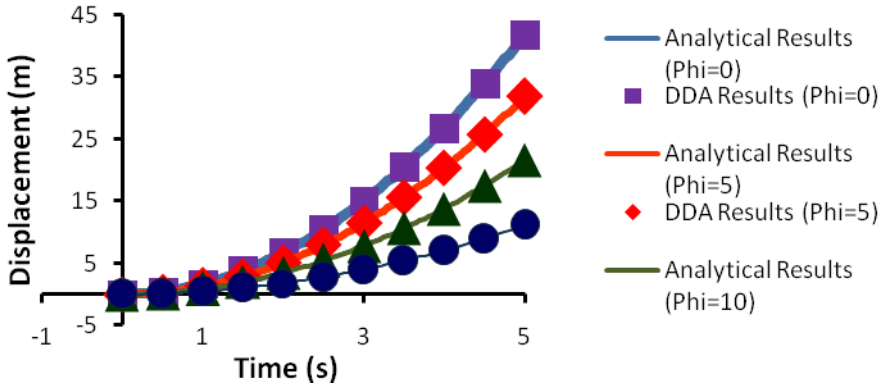

Figure 5-3. Displacement versus time for a single disk cluster comprising three disks sliding on an inclined plane Sliding of a disk cluster including three disks on an incline

As can be seen, there is a good agreement between the results obtained by the disk-based DDA and the analytical solution. Furthermore, Figures 5-4(a) and 5-4(b) show absolute and relative errors for the displacements by disk-based DDA, respectively. As shown, the absolute value of the error increases at every time step, but the relative error with respect to disk displacement decreases and the disk-based DDA results get closer to the analytical solution.

The absolute and relative errors for lower friction angles are less than those for a higher friction angle. Moreover, the relative errors are linear in logarithm-logarithm space except minor perturbations at early times. Details of the perturbation of the system in DDA during the first few time steps are explained by Doolin and Sitar (2002) and will be discussed later in this paper.

This study shows that the disk-based DDA computation gets more accurate as the system progresses through time, independent of friction angle value and the initial perturbation. Doolin and Sitar (2002) and Beyabanki et al. (2009a) reported a similar behavior for sliding a rectangular block in 2-D and a cube in 3-D on an inclined plane, respectively.

As shown in this part of the paper, the disk-based DDA predicts well the analytical displacements of disk clusters. The prediction is sufficiently accurate over a common range of time and friction angles in geomechanical modeling.

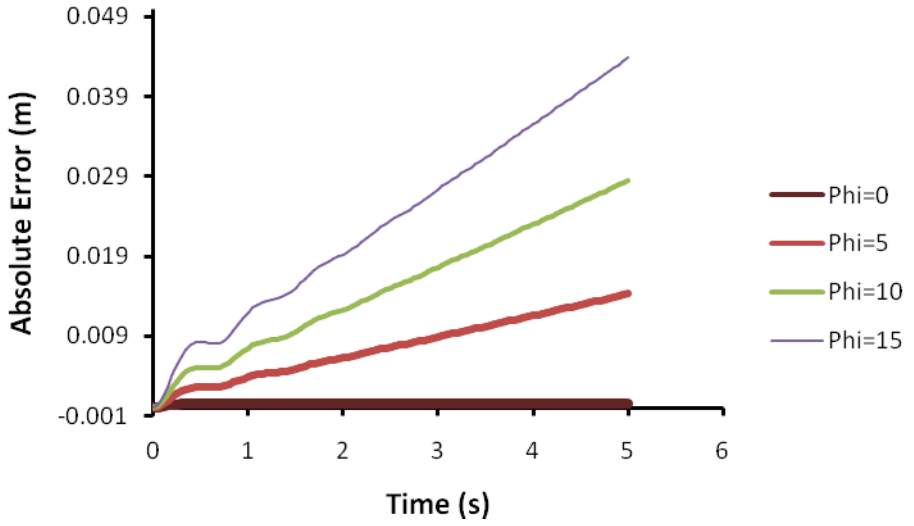

(a)

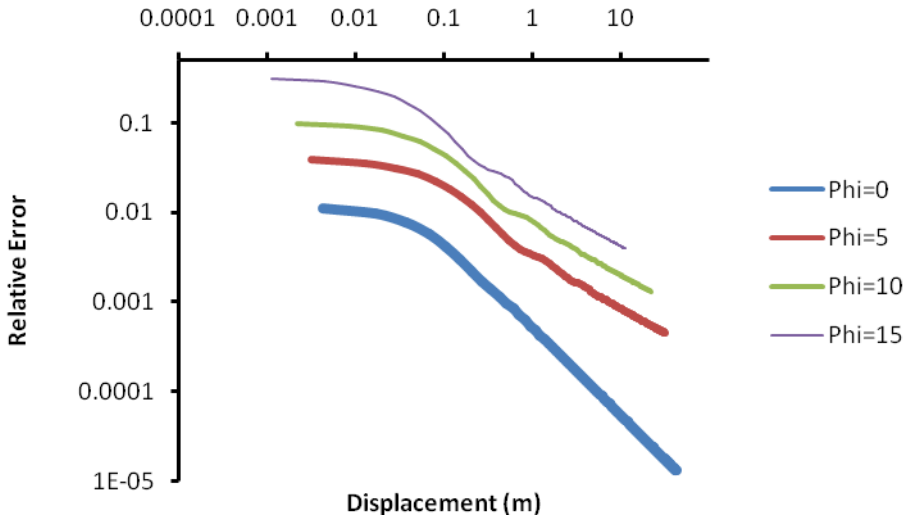

(b)

Figure 5-3. Calculated error for a single disk cluster comprising three disks sliding on an inclined plane (a) Absolute error (b) Relative error

5.4. Sliding Under the Action of Dynamic Loading

Newmark (1965) and Goodman and Seed (1995) presented a displacement-based sliding block model called “Newmark method” that obtains displacement of a mass along a planar sliding surface under earthquake loading. In this method, which is only valid for a single, rigid, block undergoing sliding deformation, in order to determine the displacement due to an earthquake, horizontal acceleration is required to initiate slope motion, known as “yield acceleration”. For a block resting on an inclined plane, horizontal, yield acceleration for frictional sliding only with no cohesion for down-slope sliding is given by Goodman and Seed (1995):

$$a_y = \tan(\varphi - \alpha).g \tag{5-7}$$

where φ is friction angle, α and g are the slope inclination and the gravitational acceleration, respectively.

When yield acceleration is exceeded, the displacement can be obtained by double integration of the acceleration time history, with the yield acceleration used as reference datum (Tsesarsky et al. 2005). Beyabanaki et al. (2009a) derived the analytical solution for down-slope sliding based on a method proposed originally by Hatzor and Feintuch (2001) and Kami and Hatzor (2008).

In this section, behavior of a disk cluster including three disks resting on a plane inclined at an angle of 20^0, and subjected to gravitational acceleration and a horizontal, time-dependent, sinusoidal acceleration input as driving forces is compared with the analytical solution for down-slope sliding. In this study, three different sinusoidal functions of increasing complexity are used for the dynamic load input function and the

results for three different friction angles along the interface and four different time steps are investigated. The type of the analysis performed is fully dynamic (i.e., the velocity of the disk cluster in each time step is fully transferred to the next time step). In this study, $P = 10^7\, N/m$, $\Delta t = 0.05\, s$, and radii and density of disks are assumed to be $1\, m$ and $2500\, kg/m^3$, respectively.

5.4.1. A typical harmonic function

In this case, acceleration has the following form:

$$\ddot{u}(t) = a_1.g.\sin(\omega_1 t) \tag{5-8}$$

where a_1 is a constant coefficient, t is time and g is gravitation acceleration. Parameter ω_1 is the angular velocity of the function used to model ground motion frequencies.

The time interval until yield acceleration is attained for down-slope sliding is given by:

$$t_0 = \frac{1}{\omega_1}\sin^{-1}\left(\frac{a_1}{\tan(\varphi - \alpha)}\right) \tag{5-9}$$

The corresponding analytical solutions for the velocity $v(t)$ and displacement $d(t)$ taking into account the frictional resistance offered by the inclined slope are given by Beyabanaki et al. (2009a):

$$v(t) = M\,(t - t_0) + a_1.N.P_1 \tag{5-10}$$

and

$$d(t)=\left[\frac{1}{2}M\,(t-t_0)+a_1.N.R_1\right](t-t_0)+a_1.N.Q_1 \tag{5-11}$$

where

$$M=g\left(\sin\alpha-\cos\alpha.tg\phi\right) \tag{5-12}$$

$$N=g\left(\cos\alpha+\sin\alpha.tg\phi\right) \tag{5-13}$$

$$P_1=\left(\frac{\cos(\omega_1 t_0)-\cos(\omega_1 t)}{\omega_1}\right) \tag{5-14}$$

$$Q_1=\left(\frac{\sin(\omega_1 t_0)-\sin(\omega_1 t)}{{\omega_1}^2}\right) \tag{5-15}$$

$$R_1=\left(\frac{\cos(\omega_1 t_0)}{\omega_1}\right) \tag{5-16}$$

To investigate whether friction angle affects the error, a set of numerical experiments was performed with different values of friction angles. Considering a plane inclined at 20°, $a_1=1.25$, $\omega_1=2$, and three different interface friction angles (φ = 22°, 26°, and 30°), the parameters used are shown in Table 5-1.

Figure 5-5 shows a comparison between the analytical solution for velocity and displacement and disk-based DDA results up to 5s. As can be seen from these figures, there is very good agreement between the computed results and analytical solutions for all friction angles.

Table 5-1 Parameters used for different functions

Friction Angle (φ)	Yield acceleration ($a_y, m/s^2$)	Time interval (t_0, s)		
		$\ddot{u}(t) = a_1.g.\sin(\omega_1 t)$	$\ddot{u}(t) = a_1.g.\sin\omega_1 t + a_2.g.\sin\omega_2 t$	$\ddot{u}(t) = a_1.g.\sin\omega_1 t + a_2.g.\sin\omega_2 t + a_3.g.\sin\omega_3 t$
22°	0.034921 g	0.01397	0.01269	0.00698
26°	0.105104 g	0.042091	0.03825	0.02103
30°	0.176327 g	0.070767	0.06426	0.03531

Relative errors between disk-based DDA computed velocity and displacement and analytical solution are shown in Figure 5-6. It shows some minimum and maximum points in both graphs. This behavior will be discussed in detail later.

To investigate the effect of time step on the relative error, the sliding disk cluster analyses are performed with different time steps $\Delta t = 0.01,\ 0.04,\ 0.07,$ and $0.1\,s$. The friction angle chosen is 26^0. The results are reported in Figure 5-7. As can be seen, in general, the most accurate results are obtained when smaller time steps are used.

5.4.2. A sum of two sines

In this case, we have:

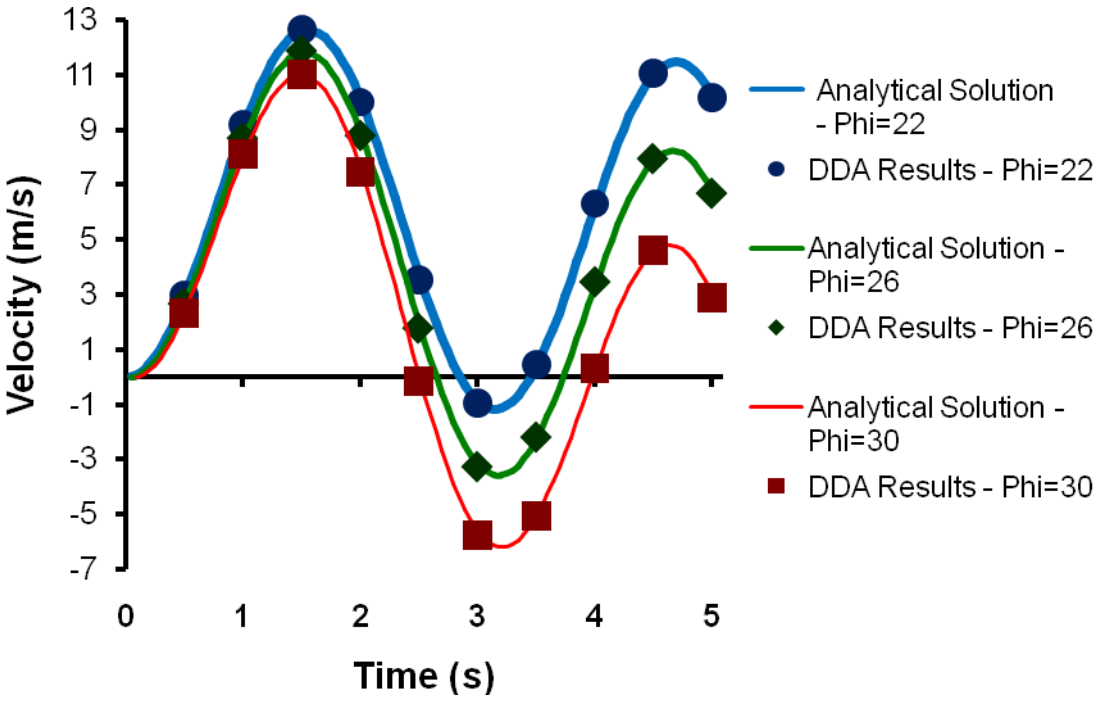

(a)

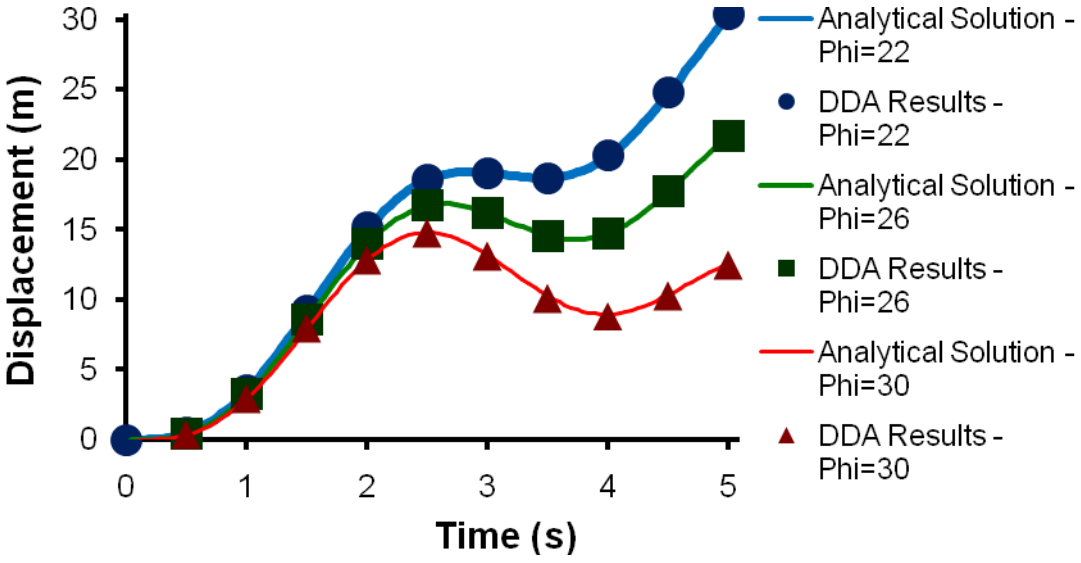

(b)

Figure 5-5. Comparison between analytical solution and disk-based DDA results for $\ddot{u}(t) = a_1.g.\sin(\omega_1 t)$ (a) Velocity (b) Displacement

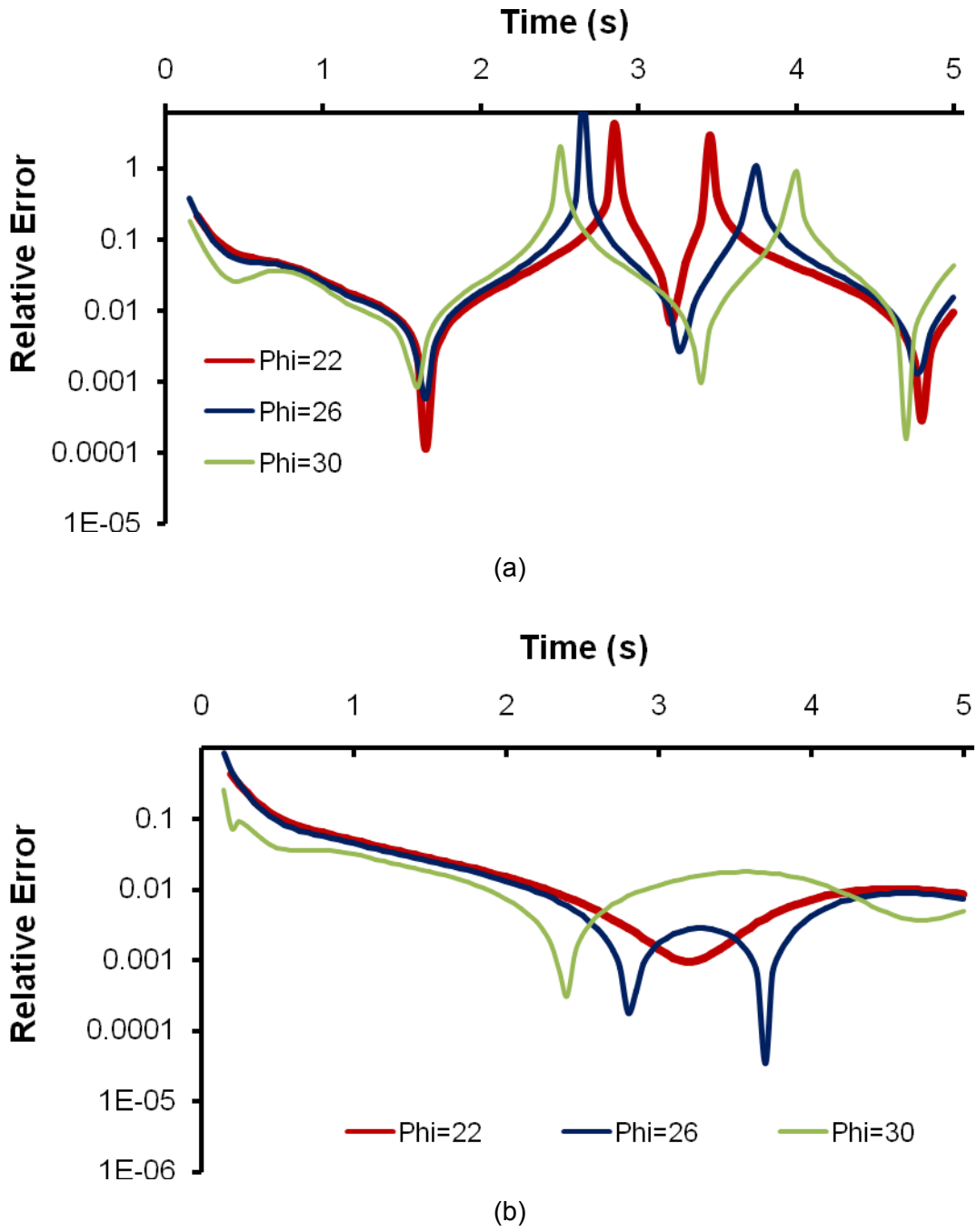

Figure 5-6. Relative error of disk-based DDA results and analytical solution for different friction angles for $\ddot{u}(t) = a_1.g.\sin(\omega_1 t)$ (a) Velocity (b) Displacement

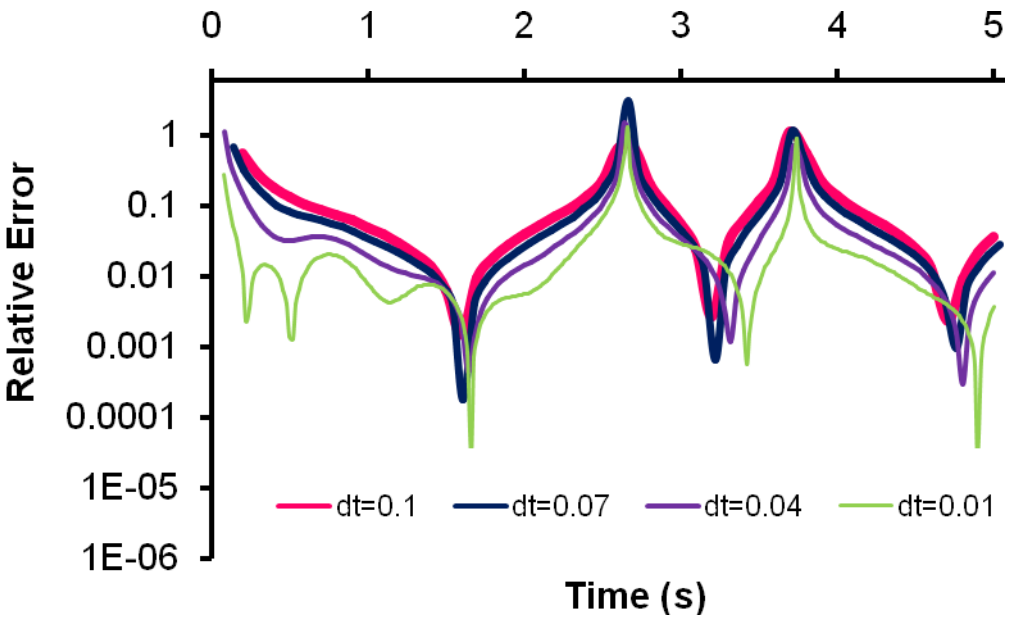

(a)

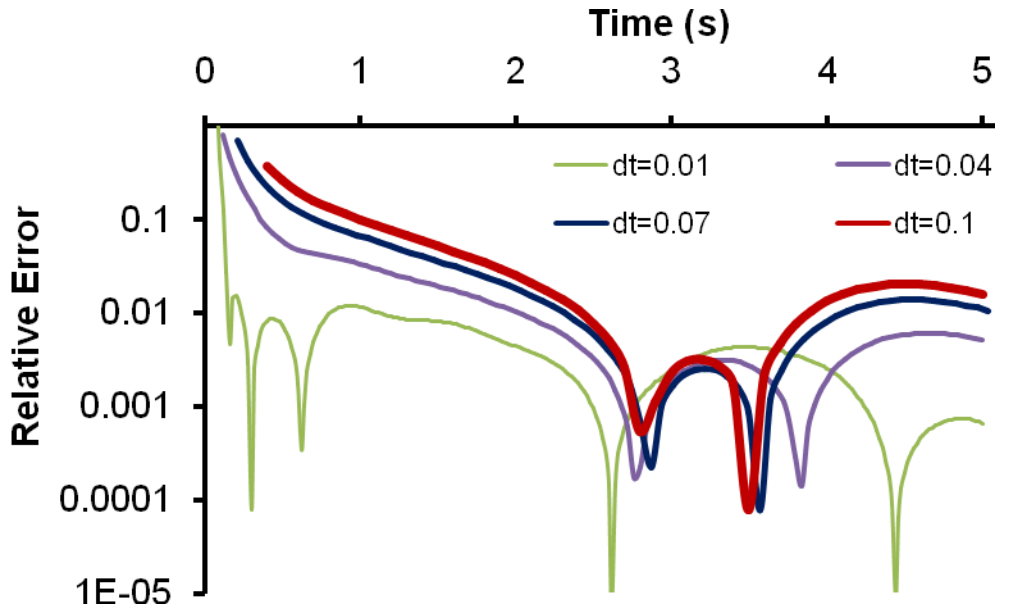

(b)

Figure 5-7. Relative error of disk-based DDA results for different time steps for $\ddot{u}(t) = a_1.g.\sin(\omega_1 t)$ (a) Velocity (b) Displacement

$$\ddot{u}(t) = a_1.g.\sin\omega_1 t + a_2.g.\sin\omega_2 t \tag{5-17}$$

The analytical solutions for velocity and displacement corresponding to this function are given by:

$$v(t) = M\,(t - t_0) + N(a_1.P_1 + a_2.P_2) \tag{5-18}$$

and

$$d(t) = \frac{1}{2}M\,(t - t_0)^2 + N(a_1.R_1 + a_2.R_2)(t - t_0) + N(a_1.Q_1 + a_2.Q_2) \tag{5-19}$$

where

$$P_2 = \left(\frac{\cos(\omega_2 t_0) - \cos(\omega_2 t)}{\omega_2}\right) \tag{5-20}$$

$$Q_2 = \left(\frac{\sin(\omega_2 t_0) - \sin(\omega_2 t)}{{\omega_2}^2}\right) \tag{5-21}$$

$$R_2 = \left(\frac{\cos(\omega_2 t_0)}{\omega_2}\right) \tag{5-22}$$

Considering $a_1 = 0.75$, $a_2 = 1$, $\omega_1 = 1$ and $\omega_2 = 2$, Table 5-1 shows the parameters used for this case.

A comparison between analytical solutions for velocity and displacement and disk-based DDA results up to 5 seconds is shown in Figure 5-8. In addition, relative errors between disk-based DDA computed velocity and displacement and analytical solution are shown in Figure 5-9.

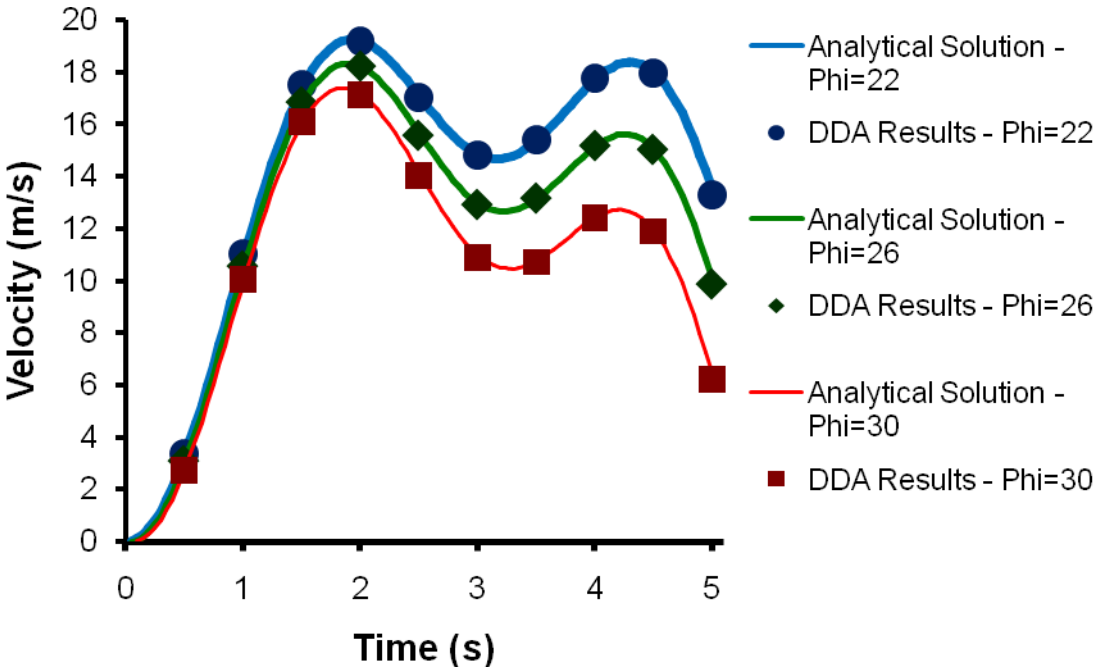

(a)

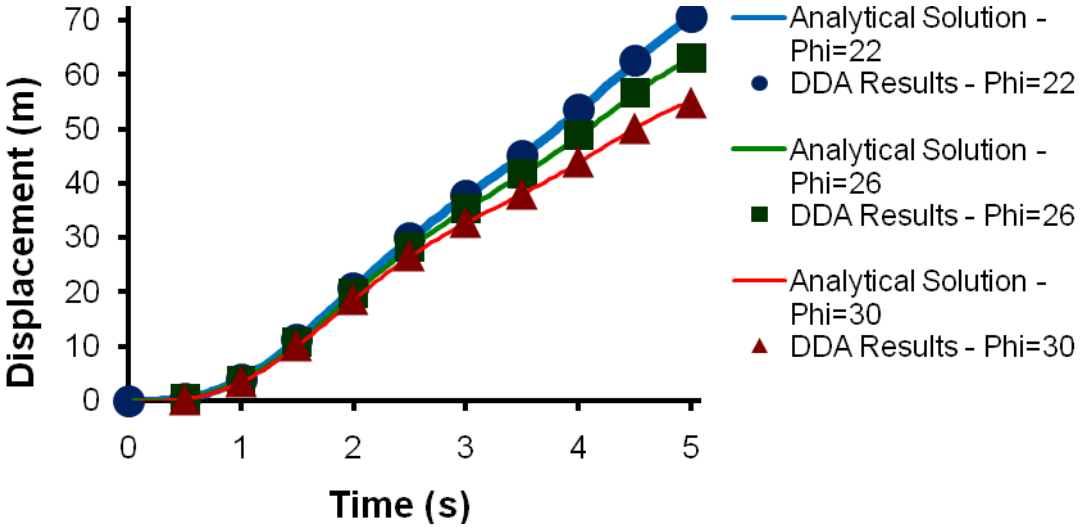

(b)

Figure 5-8. Comparison between analytical solution and disk-based DDA results for $\ddot{u}(t) = a_1.g.\sin\omega_1 t + a_2.g.\sin\omega_2 t$ (a) Velocity (b) Displacement

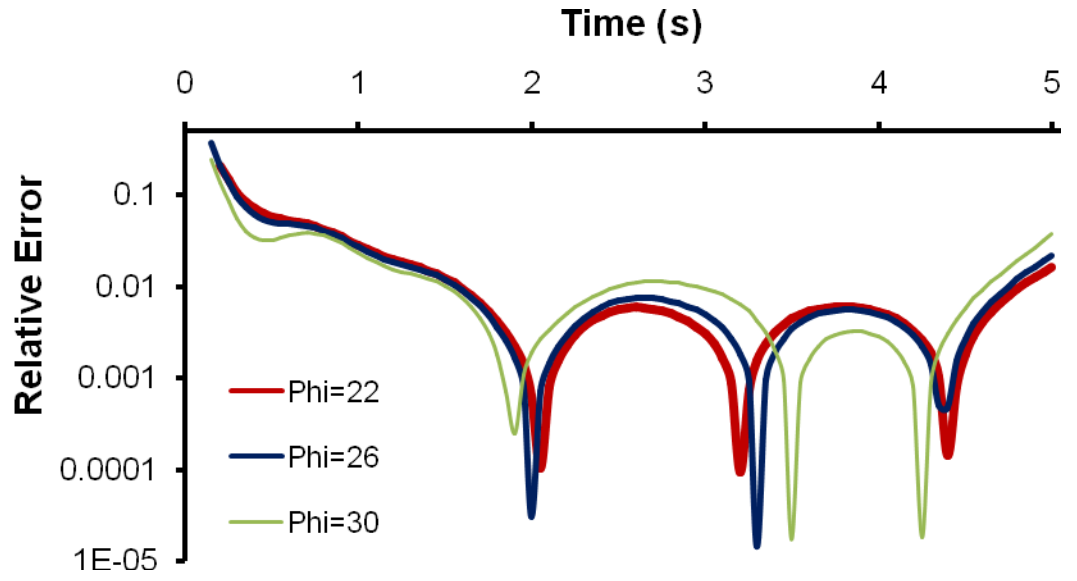

(a)

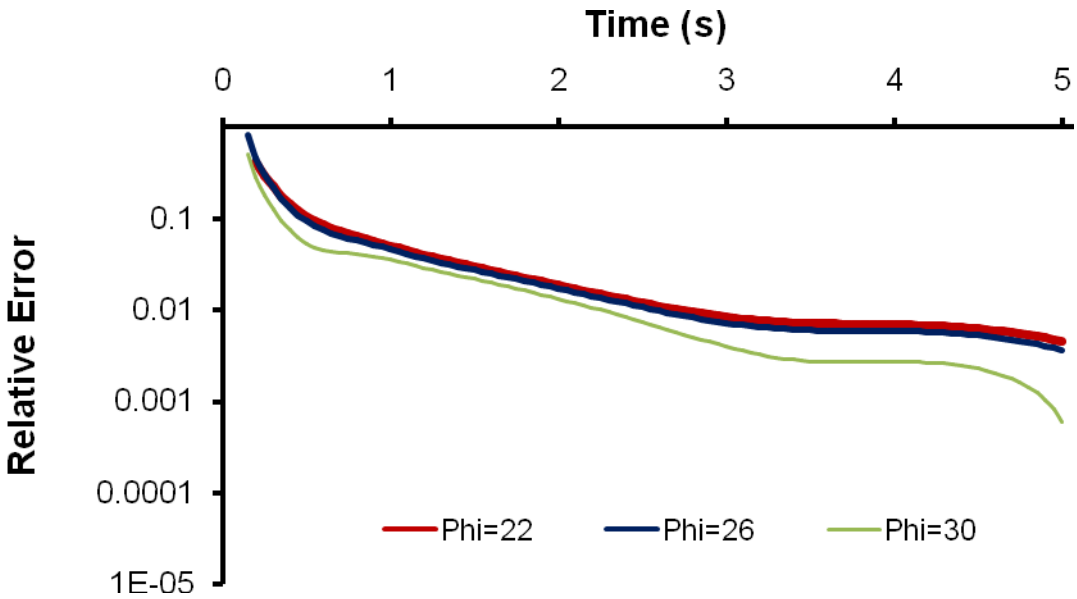

(b)

Figure 5-9. Relative error of disk-based DDA results for different friction angles for $\ddot{u}(t) = a_1.g.\sin\omega_1 t + a_2.g.\sin\omega_2 t$ (a) Velocity (b) Displacement

As can be seen in these figures, there is a remarkably good agreement between the analytical solution and disk-based DDA for all three different interface friction angles. In the first decisecond of time, a significant amount of error occurs in the displacement solution, but the system evolves towards a smaller error independent of the initial perturbation. As mentioned before, details of the initial perturbation are given by Doolin and Sitar (2002) and will be discussed in the discussion section of this paper. They obtained similar behavior for sliding a rectangular block under gravitational force only. The relative error of displacement after 5s decreases to 0.45%, 0.36% and 0.06% for $\varphi = 22^0,\ 26^0$, and 30^0 respectively.

Figure 5-10 shows relative error of computed velocity and displacement for different time step sizes. The friction angle of the interface is assumed to be 26^0. As can be seen, lower accuracy is obtained with larger time steps. For $\Delta t = 0.01s$, the numeric error of velocity does not exceed 2% (except for first 0.18s), and the error of displacement does not go beyond 1.3% (except for first 0.3s). The relative error of displacement decreases to below 0.09% after 5 seconds when $\Delta t = 0.01s$. Comparing the relative error graph in Figure 9 with the velocity graph presented in Figure 5-8 one observes that the minimum errors occur at around the time of minimum or maximum velocities (when acceleration is zero) for each friction angle. Moreover, the relative error graph in Figure 5-9 shows that before the first minimum, increasing friction angle decreases the error, but this behavior is reverse between the first and second minimums. A comparison between the error graph (Figure 5-9) with the velocity graph (Figure 5-8) shows larger change in velocity results in more errors.

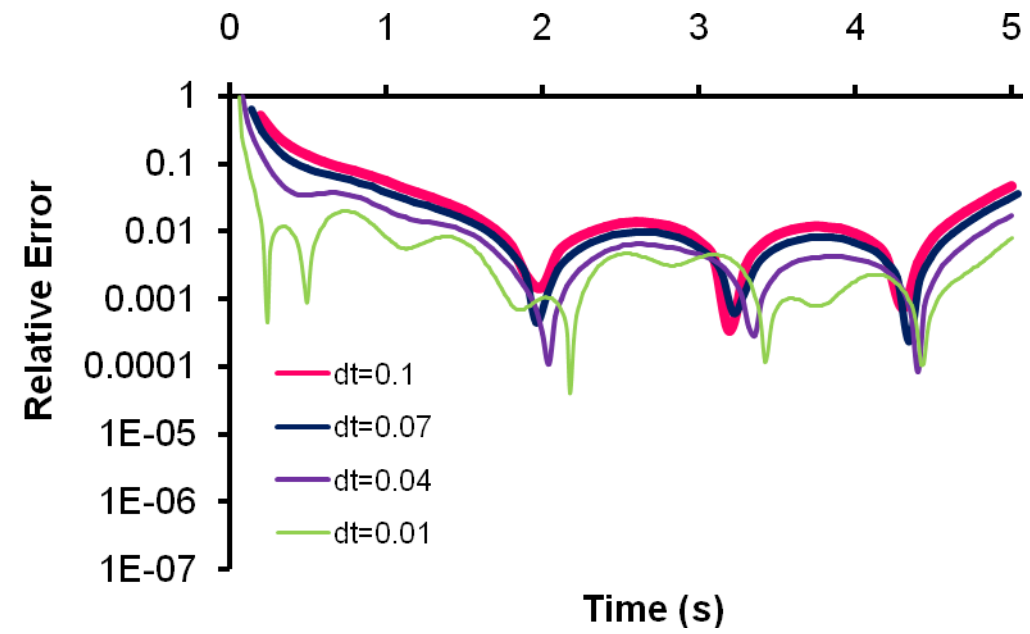

(a)

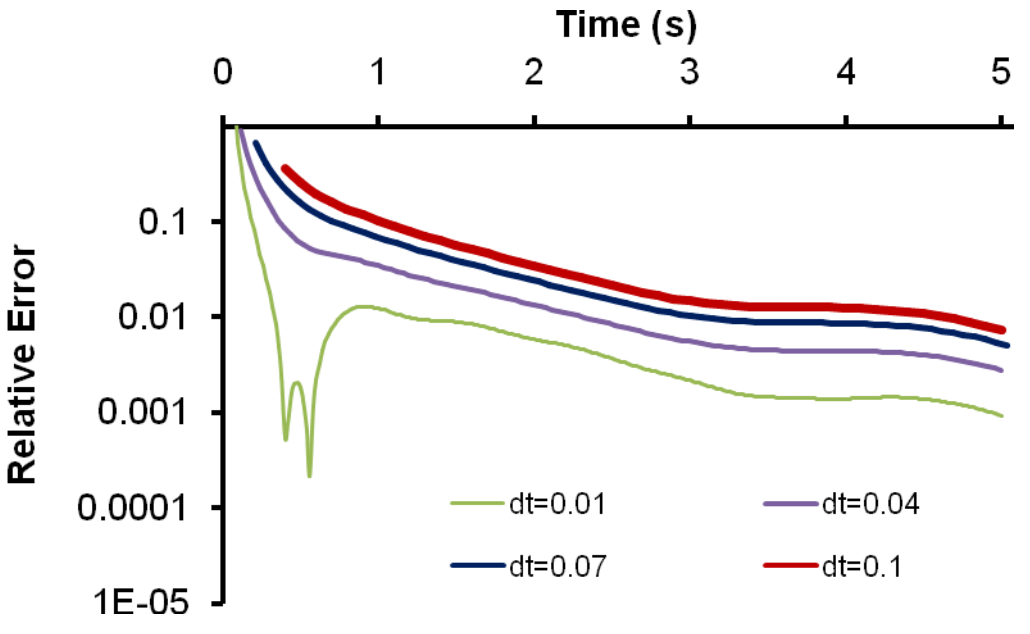

(b)

Figure 5-10. Relative error of disk-based DDA results for different time steps for $\ddot{u}(t) = a_1.g.\sin\omega_1 t + a_2.g.\sin\omega_2 t$ (a) Velocity (b) Displacement

For example, the change in velocity from the first maximum to the first minimum for $\varphi = 30^0$ (Figure 5-8) is more than that for $\varphi = 22^0$; therefore, the error in the case of $\varphi = 30^0$ is more than that in the case of $\varphi = 22^0$ during the time between the first and second minimums in Figure 5-9. It can be generalized to understand the behavior of the errors of both velocity and displacement for all sinusoidal acceleration functions. As can be seen from the results presented in the next section, including higher terms in the series of sine functions makes this behavior more obvious.

5.4.3. A sum of three sines

In this case, acceleration would have the form:

$$\ddot{u}(t) = a_1.g.\sin \omega_1 t + a_2.g.\sin \omega_2 t + a_3.g.\sin \omega_3 t \qquad (5\text{-}23)$$

The analytical solutions for the velocity and displacement in this case are given by Beyabanaki et al. (2009a):

$$v(t) = M\,(t - t_0) + N(a_1.P_1 + a_2.P_2 + a_3.P_3) \qquad (5\text{-}24)$$

and

$$d(t) = \frac{1}{2}M\,(t - t_0)^2 + N(a_1.R_1 + a_2.R_2 + a_3.R_3)(t - t_0) + N(a_1.Q_1 + a_2.Q_2 + a_3.Q_3) \qquad (5\text{-}25)$$

where

$$P_3 = \left(\frac{\cos(\omega_3 t_0) - \cos(\omega_3 t)}{\omega_3} \right) \tag{5-26}$$

$$Q_3 = \left(\frac{\sin(\omega_3 t_0) - \sin(\omega_3 t)}{\omega_3{}^2} \right) \tag{5-27}$$

$$R_3 = \left(\frac{\cos(\omega_3 t_0)}{\omega_3} \right) \tag{5-28}$$

Table 5-1 shows the parameters used for different values of friction angles considering $a_1 = 0.5,\ a_2 = 0.75,\ a_3 = 1,\ \omega_1 = 1,\ \omega_2 = 2$ and $\omega_3 = 3$.

Comparing the performance of the disk-based DDA with analytical solutions for both velocity and displacement presented in Figure 5-11 shows a strong agreement between them. Figure 5-12 shows that except for the first second, and for all three friction angles, the relative error of velocity oscillates around 0.1% which indicates a very accurate solution. Moreover, the displacement relative error reduces to less than 0.5% after 5 seconds. The results for different time step sizes are shown in Figure 5-13. As indicated in the figure, the numerical error decreases below 1% for velocity after some initial perturbations for all time steps. Although, higher time step values result in larger errors for both velocity and displacement, the disk-based DDA solution tracks the analytical solution remarkably well.

5.5. Discussion

As mentioned by Doolin and Sitar (2002), the errors in the case of a frictional sliding block are controlled by the perturbation in the initial time steps of the simulation.

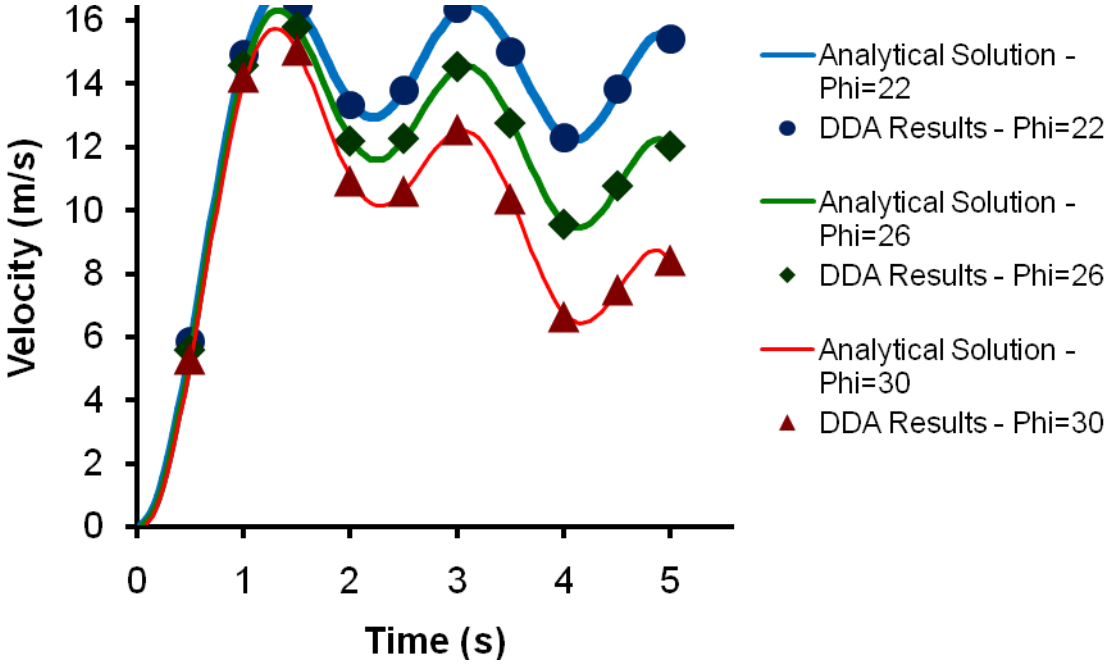

(a)

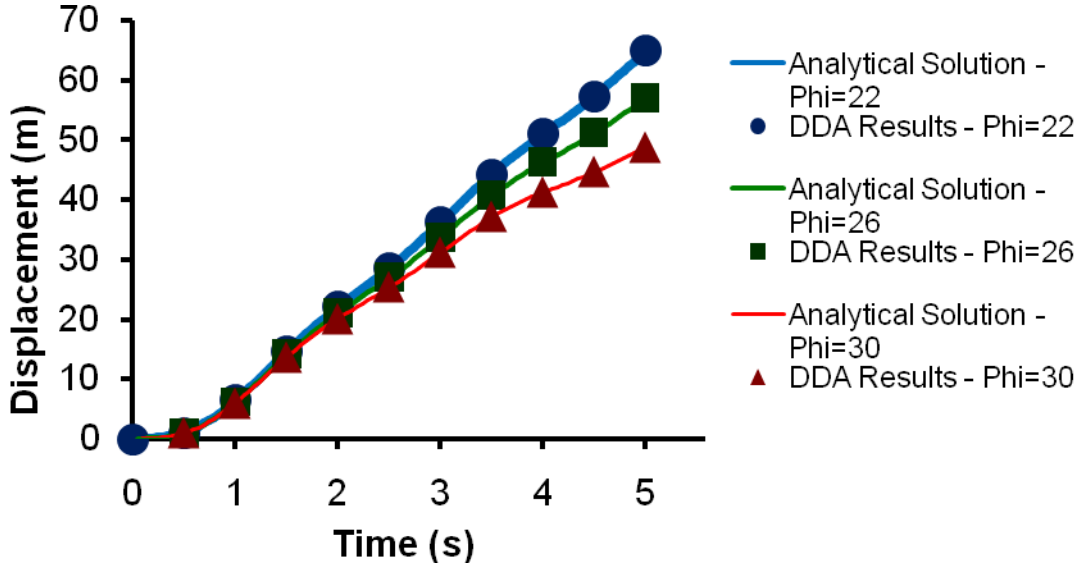

(b)

Figure 5-11. Comparison between analytical solution and disk-based DDA results for $\ddot{u}(t) = a_1.g.\sin\omega_1 t + a_2.g.\sin\omega_2 t + a_3.g.\sin\omega_3 t$ (a) Velocity (b) Displacement

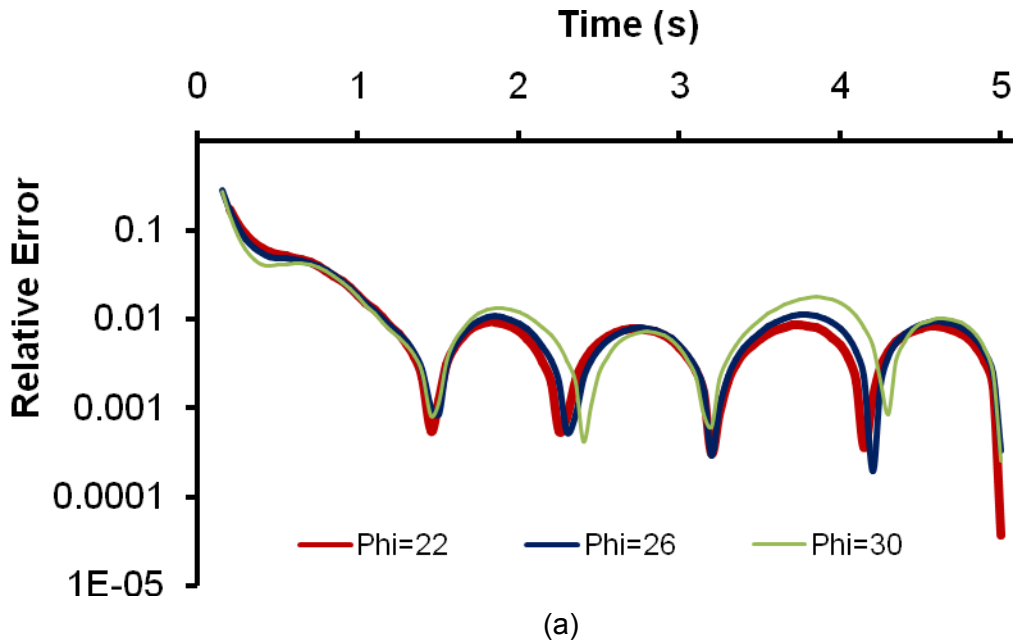

(a)

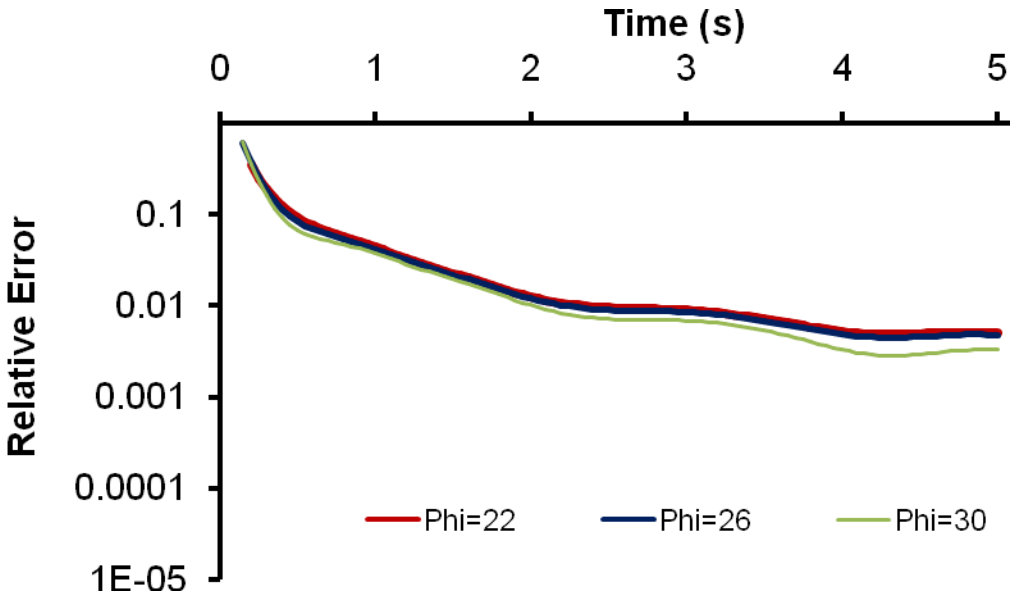

(b)

Figure 5-12. Relative error of disk-based DDA results for different friction angles for $\ddot{u}(t) = a_1.g.\sin\omega_1 t + a_2.g.\sin\omega_2 t + a_3.g.\sin\omega_3 t$ (a) Velocity (b) Displacement

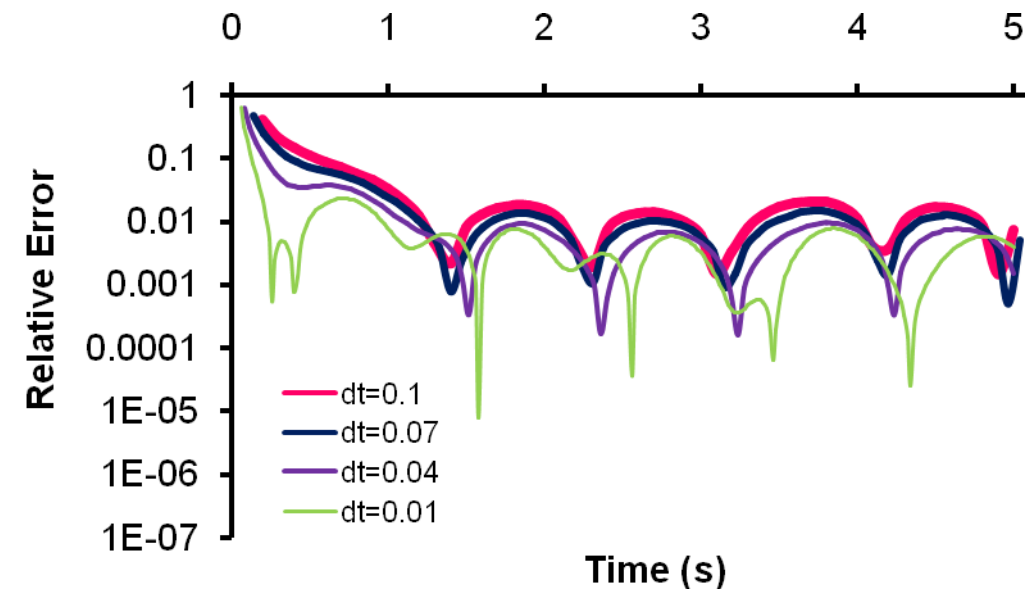

(a)

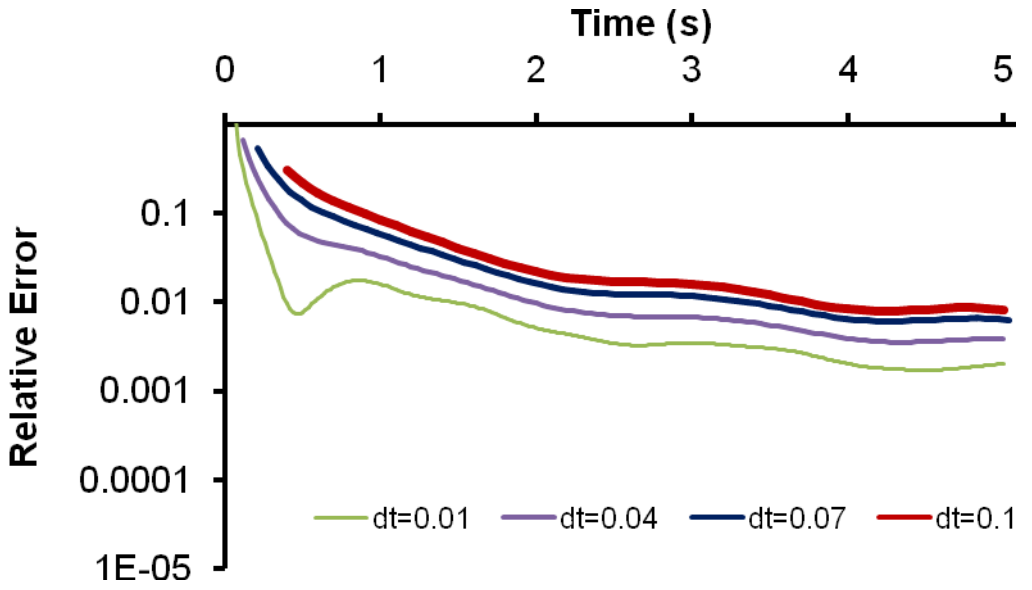

(b)

Figure 5-13. Relative error of disk-based DDA results for different time steps for $\ddot{u}(t) = a_1.g.\sin\omega_1 t + a_2.g.\sin\omega_2 t + a_3.g.\sin\omega_3 t$ (a) Velocity (b) Displacement

The graphs of errors presented in Figure 5-4 show that increasing the friction angle increases the error in the case of sliding due to gravitational force only. However, as can be seen in Figures 5-6, 5-9 and 5-12, decreasing the friction angle increases the error of the predicted displacement in the case of sliding under dynamic loads in most cases. The reason is that in the first case, at $t = 0$, the block begins to slide on the incline, but in the sliding case under dynamic loads, the block starts to slide at $t = t_0$ (e.g., in the case of typical harmonic function, $t_0 = 0.01397\,\mathrm{s}$, $0.042091\mathrm{s}$, and $0.070767\,\mathrm{s}$ for $\varphi = 22^0$, 26^0, and 30^0, respectively). Therefore, in this case, unlike the case of sliding due to gravity only, disk-based DDA has more time to run before the block starts moving. During this time, the perturbation of the system would be improved. As a result, a higher friction angle which has larger t_0 gives a solution with less error. Because of this different behavior, the effects of friction angle on the results obtained in these two cases are different.

All analyses show that, although the relative error is almost always highest in the initial few time steps, the accuracy of both velocity and displacement for a long runout simulation is very reasonable for geomechanics problems.

5.6. Conclusions

In this paper, the first and necessary step of analytical validation of disk-based DDA via the case of a single cluster on an inclined plane with different friction angles is studied. For this purpose, a comprehensive sensitivity analysis of sliding behavior of a single cluster under the action of gravitational force and dynamic loading is performed to investigate the applicability of disk-based DDA to dynamic problems (like earthquake-

triggered landslides). It was shown that the agreement between disk-based DDA and analytical solution is very reasonable. Several conclusions emerge from this study:

- In the case of sliding under gravitational force only, the absolute error increases at a linear rate at every time step, but the relative error decreases and more accurate results are obtained over time.
- Reducing the initial perturbation of the system during the first few time steps improves the accuracy of the computations.
- Increasing the frictional resistance increases the relative error but disk-based DDA follows the analytical results with a very good agreement and with decreasing relative error over time.
- It was found that solutions of disk-based DDA under dynamic conditions are sensitive to time step size. Increasing time step size for a constant friction angle increases error. However, this study shows that time step size could be as high as 0.1 s to get accurate results for both velocity and displacement.
- In the first few deciseconds, a significant amount of error occurs in the solution for both velocity and displacement, but the system progresses towards an accurate solution independently of the initial error.
- Under dynamic conditions, unlike the case of sliding due to gravity only, decreasing the frictional angle increases the initial perturbation and relative errors.

5.7. References

Bakun-Mazor, D., Hatzor, Y.H. and Glaser, S.D., 2012. Dynamic sliding of tetrahedral wedge: The role of interface friction. International Journal for Numerical and Analytical Methods in Geomechanics, 36, 327–343.

Beyabanaki, S.A.R. and Bagtzoglou, A.C., 2012. Three-dimensional discontinuous deformation analysis (3-D DDA) method for particulate media applications. Geomechanics and Geoengineering: An International Journal, 2012, 7 (4), 239–253.

Beyabanaki, S.A.R. and Bagtzoglou, A.C., 2013. Non-rigid disk-based DDA with a new contact model. Computers and Geotechnics, 49, 25–35.

Beyabanaki, S.A.R., Ferdosi, B. and Mohammadi, S., 2009a. Validation of dynamic block displacement analysis and modification of edge-to-edge contact constraints in 3-D DDA. International Journal of Rock Mechanics and Mining Sciences, 46, 1223–1234.

Beyabanaki, S.A.R., Mikola, G.R., Biabanaki, S.O. and Mohammadi, S., 2009b. New point-to-face contact algorithm for 3-D contact problems using the augmented Lagrangian method. Geomechanics and Geoengineering: An International Journal, 4 (3), 221–236.

Doolin, D.M. and Sitar, N., 2002. Displacement accuracy of discontinuous deformation analysis method applied to sliding block. J. Eng. Mech. (ASCE)., 128, 1158–1168.

Goodman, R.E. and Seed, H.B., 1995. Earthquake induced displacements in sands and embankments. J. Soil Mech. Foundation Div., ASCE, 92 (SM2), 125–146.

Hatzor, Y.H. and Bakun-Mazor, D., 2011. Modeling dynamic deformation in natural rock slopes and underground openings with DDA: review of recent results. Geomechanics and Geoengineering: An International Journal, 6 (4),283–292.

Hatzor, Y.H. and Feintuch, A., 2001. The validity of dynamic block displacement prediction using DDA. International Journal of Rock Mechanics and Mining Science, 38, 599–606.

Jing, L., 2003. A review of techniques, advances and outstanding issues in numerical modelling for rock mechanics and rock engineering. International Journal of Rock Mechanics and Mining Sciences, 40 (3), 283–353.

Jing, L. and Hudson, J.A., 2002. Numerical methods in rock mechanics. International Journal of Rock Mechanics & Mining Sciences, 39, 409–427.

Kamai, R. and Hatzor, Y.H., 2008. Numerical analysis of block stone displacements in ancient masonry structures: a new method to estimate historic ground motions. International Journal for Numerical and Analytical Methods in Geomechanics, 32 (11), 1321–1340.

Ke, T.C. and Bray, J.D., 1995. Modeling of particulate media using discontinuous deformation analysis. Journal of Engineering Mechanics, 121 (11), 1234–1243.

Koyama, T., Nishiyama, S., Yang, M. and Ohnishi, Y., 2011. Modeling the interaction between fluid flow and particle movement with discontinuous deformation analysis (DDA) method. International Journal for Numerical and Analytical Methods in Geomechanics, 35, 1–20.

Lin, C.T., Amadei, B., Jung, J. and Dwyer, J., 1996. Extensions of discontinuous deformation analysis for jointed rock masses. International Journal of Rock Mechanics and Mining Science, 33 (7), 671–694.

MacLaughlin, M.M. and Doolin, D.M., 2006. Review of validation of the discontinuous deformation analysis (DDA) method. International Journal for Numerical and Analytical Methods in Geomechanics, 30, 271–305.

Mitchell, J.K., 1993. Fundamentals of soil behaviour. New York: Wiley.

Newmark, N.M., 1965. Effects of earthquake on dams and embankments. Geotechnique, 15 (2), 139–160.

Ng, T.T. and Dobry, R.A., 1994. Nonlinear numerical model for soil mechanics. Journal of Geotechnical Engineering, 120 (2), 388–403.

Ohnishi, Y. and Nishiyama, S., 2007. Recent insights of analyses using discontinuous methods in rock engineering in Japan. In: Y. Ju, X. Fang and H. Bian, eds. Proceedings of the eighth international conference on the analysis of discontinuous deformation, Beijing, China, August 14–19, 2007, 15–26.

Rothenburg, L. and Bathurst, R.L., 1992. Micromechanical features of granular assemblies with planar elliptical particles. Geotechnique, 42 (1), 79–95.

Shi, G.H., 1988. Discontinuous deformation analysis-a new model for the statics and dynamics of block systems. Thesis (PhD), University of California, Berkeley.

Shi, G.H., 1992. Discontinuous deformation analysis: a new numerical model for the statics and dynamics of deformable block structures. Engineering Computations, 9 (2), 157–162.

Shi, G.H., 1993. Block system modeling by discontinuous deformation analysis. Southampton, UK: Computational Mechanics Publications.

Shi, G.H. and Goodman, R.E., 1985. Two-dimensional discontinuous deformation analysis. International Journal for Numerical and Analytical Methods in Geomechanics, 9, 541–556.

Thomas, P.A., 1997. Discontinuous deformation analysis of particulate media. Thesis (PhD), University of California, Berkeley, CA.

Thomas, P.A. and Bray, J.D., 1999. Capturing non-spherical shape of granular media with disk clusters. Journal of Geotechnical and Geoenvironmental Engineering, 125 (3), 169–178.

Tsesarsky, M., Hatzor, Y.H. and Sitar, N., 2002. Dynamic block displacement prediction-validation of DDA using analytical solutions and shaking table experiments. In: Y Hatzor, ed. Proceedings of ICADD-5, 5th International Conference of Analysis of Discontinuous Deformation, Beer-Sheva, Israel, October 6–10, 2002, Lisse (NL): Balkema Publishers, 195–203.

Tsesarsky, M., Hatzor, Y.H. and Sitar, N., 2005. Dynamic displacement of a block on an inclined plane: analytical, experimental and DDA results. Rock Mechanics and Rock Engineering, 38 (2), 153–167.

Chapter 6. Applying disk-based DDA to simulate the Donghekou landslide

6.1. Introduction

Discontinuous Deformation Analysis (DDA) is a displacement-based method that was introduced by Shi (1988, 1999). This method provides a useful tool to analyze the mechanical response of discrete blocks. A lot of studies have been conducted to validate and develop this numerical approach. Applications of the DDA in rock mechanics and rock engineering are reviewed by Jing and Hudson (2002), Jing (2003), Ohnishi and Nishiyama (2007). Furthermore, MacLaughlin and Doolin (2006) reviewed more than 100 validation studies on the DDA. Moreover, Shi (2007) presented applications of the DDA to rock stability analysis. Applications of the DDA to model slopes and underground openings are reviewed by Hatzor and Bakon-Mazor (2011).

However, relatively little work on DDA development in 3-D has been published. Basic formulations of matrices for different potential terms in details are presented by Shi (2001) and Wu et al. (2005a). Applications of 3-D DDA were demonstrated by Liu et al. (2004) and Yeung et al. (2003, 2004). A point-to-face model for contacts between polyhedral blocks in 3-D DDA was presented by Jiang and Yeung (2004). Wu et al. (2005b) developed a new contact searching algorithm for frictionless vertex-to-face contact problems. Yeung et al. (2007) and Wu (2008) presented different algorithms for edge-to-edge contacts. A new algorithm to search and calculate geometrical contacts in 3-D was presented by Beyabanaki et al. (2008). Beyabanaki et al. (2009a, 2009b) implemented 8-node and 20-node hexahedral isoparametric finite elements into 3-D

DDA to improve deformability of blocks. As an alternative method to improve block deformability in 3-D DDA, high-order displacement functions were used by Beyabanaki et al. (2009c, 2010). Beyabanaki et al. (2009d) presented a new point-to-face contact algorithm for contacts between two polyhedral blocks with planar faces in 3-D DDA. Beyabanaki et al. (2009e) compared 3-D DDA solution for dynamic block displacement with analytical solutions to study the validity of the method. Ahn and Song (2011) presented a new contact definition algorithm for 3-D DDA. Bakun-Mazor et al. (2012) validated 3-D DDA by comparing the numerical results obtained for modeling dynamic, single and double face sliding of a block with their proposed analytical solution. Validation and application of 3-D DDA with tetrahedron finite element meshed block was presented by Liu et al. (2012).

Although a lot of work has been done on DDA to date, the development of the DDA for particulate media applications is still at an early stage. Disk-based DDA in 2-D to model particulate media was presented by Ke and Bray (1995). Rein and Andrés (2001) used the method to model granular transport in vibrating feeders. The ability of the DDA to model the response of systems of disks was presented by Thomas and Bray (1999), Thomas (1999), and Koyama et al. (2011). Beyabanaki and Bagtzoglou (2012) presented a formulation of the sphere-based 3-D DDA. Also, they presented disk-based 2-D DDA with a new contact model (Beyabanaki and Bagtzoglou, 2013, 2014a), and recently investigated the accuracy of dynamic disk-based DDA (Beyabanaki and Bagtzoglou, 2014b).

Although several works have been published on dynamic DDA (e.g., Liu et al. 1996, Hatzor and Feintuch 2001, Moosavi et al. 2005, Yagoda-Biran and Hatzor 2010, Bao et al. 2012, Bakun-Mazor et al. 2012, 2013), there is only one work published on dynamic

disk-based DDA presented by Beyabanaki and Bagtzoglou (2014b). They studied the accuracy of disk-based DDA under dynamic conditions by a comprehensive sensitivity analysis. It was shown that the agreement between disk-based DDA and analytical solution is very reasonable. In order to show the ability of disk-based DDA to model landslides triggered by earthquakes, the Donghekou landslide is modeled using disk-based DDA. Moreover, the results obtained by using disk-based DDA are compared with actual data.

6.2. Theory of Disk-Based DDA

Disk-based DDA models particulate media as a collection of discrete disks. In this section, the theory of disk-based DDA is presented briefly.

6.2.1. Displacement Approximation

For each disk, the displacement matrix at an arbitrary point (x, y) in the disk is obtained from the corresponding location and the displacement vector $\{D\}$. The relation between them can be shown in the following equations:

$$\begin{pmatrix} u \\ v \end{pmatrix} = [T_i(x, y)].\{D_i\} \tag{6-1}$$

where

$$[T_i(x, y)] = \begin{pmatrix} 1 & 0 & -(y - y_0) \\ 0 & 1 & (x - x_0) \end{pmatrix} \tag{6-2}$$

$$\{D_i\}^T = \{u_0 \quad v_0 \quad r_0\} \tag{6-3}$$

and (x_0, y_0) are the coordinates of the disk center, (u_0, v_0) indicate body translations; r_0 represents the rotation angle of disk i with a rotation centre at (x_0, y_0). $[T_i(x, y)]$ is the first order displacement function, and $\{D_i\}$ is the displacement variable vector of block i in 2-D.

Assuming that (x_0, y_0) is the center of a circular block, a circular block can be represented by the following equation:

$$\begin{cases} x = r\cos(\alpha) + x_0 \\ y = r\sin(\alpha) + y_0 \end{cases} \qquad 0 \le \alpha \le 2\pi \tag{6-4}$$

where α is the angle between r (the radius of the circular block) and the positive direction of the x-axis.

The linear displacement function can also cause free expansion under body rotation. To reduce the error, extending the following body rotation, the exact solution for the displacements (Koo and Chern, 1998):

$$\begin{cases} u = u_0 + (x - x_0)(\cos r_0 - 1) - (y - y_0)\sin r_0 \\ v = v_0 + (x - x_0)\sin r_0 + (y - y_0)(\cos r_0 - 1) \end{cases} \tag{6-5}$$

is used to compute (u, v) due to rotation r_0. For this purpose, after solving the displacement vectors, Equation (6-5) is applied to update the coordinates of each circular block and to judge the contact patterns at the end of each time step.

6.2.2. Equilibrium Equations

Disk-based DDA is an implicit method, involving formulation and solution of a system of simultaneous equilibrium equations. Individual disks are connected and form a disk system by contacts between disks and by displacement constraints on single disks. For a system of N disks, the system equations have the following form:

$$\begin{bmatrix} [K_{11}] & [K_{12}] & [K_{13}] & \dots & [K_{1N}] \\ [K_{21}] & [K_{22}] & [K_{23}] & \dots & [K_{2N}] \\ [K_{31}] & [K_{32}] & [K_{33}] & \dots & [K_{3N}] \\ \vdots & \vdots & \vdots & \ddots & \vdots \\ [K_{N1}] & [K_{N2}] & [K_{N3}] & \dots & [K_{NN}] \end{bmatrix} \begin{bmatrix} \{D_1\} \\ \{D_2\} \\ \{D_3\} \\ \vdots \\ \{D_N\} \end{bmatrix} = \begin{bmatrix} \{F_1\} \\ \{F_2\} \\ \{F_3\} \\ \vdots \\ \{F_N\} \end{bmatrix} \tag{6-6}$$

Because each disk has three degrees of freedom $\{u_0 \;\; v_0 \;\; r_0\}$ for each circular element, $[K_{ij}]$ in the coefficient matrix given by the above equation is a 3×3 Sub-matrix. $\{D_i\}$ and $\{F_i\}$ are 3×1 sub-matrices where $\{D_i\}$ is the deformation variables of disk i (Equation (6-3)) and $\{F_i\}$ represents the loading on disk i distributed to the four deformation variables.

The total potential energy Π is the summation over all potential energy forms calculated as below:

$$\Pi = \pi_e + \pi_{is} + \pi_p + \pi_b + \pi_i + \pi_C + \pi_n + \pi_s + \pi_f \tag{6-7}$$

where,

π_e = the potential energies due to disk stiffness;

π_{is} = initial stress;

π_p = point loading;

π_b = body force;

π_i = inertia forces;

π_C = constrained spring;

π_n = normal contact;

π_s = shear contact; and

π_f = friction force.

The simultaneous equations are derived by minimizing the total potential energy Π of the disk system.

$$[K_{ij}] = \frac{\partial^2 \Pi}{\partial d_{ir}\, \partial d_{js}} \quad , \quad r, s = 1, \cdots, 4$$
$$\{F_i\} = -\frac{\partial \Pi(0)}{\partial d_{ir}} \quad , \quad r = 1, \cdots, 4 \tag{6-8}$$

where 0 refers to the initial state of each time state.

6.2.3. Methodology of disk-based DDA

The methodology of disk-based DDA for modeling of particulate media is listed in Algorithm 6.1.

Algorithm 6.1. Disk-based DDA for modeling of particulate media

1: Input geometry, boundary condition, constraints, forces, …

2: **For** i = 1, ..., n time steps **Do**

3: Detect contact between disks, and disks and boundaries

4: Find reference point and line

5: **Repeat** {open-close iteration}

6: Compute the contact forces between the disks including frictional, normal and shear forces

7: Assemble the generalized stiffness, K, and force, F, matrices; integrate over time and solve

8: $\mathbf{D = K^{-1}F}$ using open-close iteration,

9: **Until** no-tension, no-penetration (within tolerances)

10: Update disks center positions

11: **End For**

6.3. Packing Algorithm

The first step in a DEM or DDA simulation is to generate the packing of disks for the system of interest. Random packing of discs is a research topic that has attracted considerable attention in different areas with different objectives. Up to now, several packing approaches have been developed. A review of existing packing algorithms in both 2D and 3D is presented in Feng et al. (2003), Bagi (2005), Benabbou et al. (2009), and Liu et al. (2012). It is possible to classify the currently available algorithms into two categories: the dynamic method and the constructive method. If the positions and sizes of generated particles remain unchanged during the subsequent calculation, the algorithm belongs to the constructive method. Otherwise, the approach would fall under the dynamic method class (Lohner and Onate, 2004).

In this study, the algorithm presented by Feng et al. (2003) is used to fill the initial geometry of the landslide with random disks with different radii. This algorithm is briefly discussed in this section.

6.3.1. Initial front generation

As the first step, three disks denoted as D1, D2 and D3 are generated in the densest packing manner possible so that they are in contact with each other. It is assumed that these directions are positive: D1→D2, D2→D3 and D3→D1. The oriented triangle generated by these directed segments is called “initial front” and can be represented as D1→D2 →D3 →D1.

6.3.2. New disk generation

To generate new disk D4, it should be in contact with both disks 1 and 2 and lie on the right-hand side of segment D1→D2. In this case, segment D1→D2 is removed from the initial front and two new segments D1→D4 and D4→D2 will be inserted into the front. Therefore, D1→D4→D2 →D3 →D1 will become the new front. All new generated disks should be placed on the right-hand side of the segments (Figure 6-1).

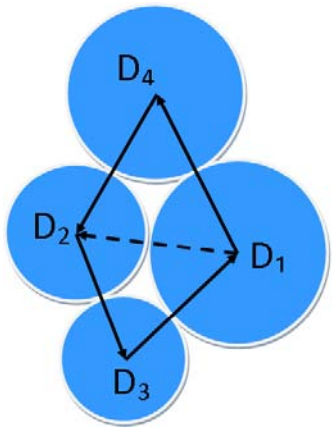

Figure 6-1. Generation of a new disk (Feng et al. 2003)

This procedure can be performed until the whole domain is filled. Details of this procedure can be found in Feng et al. (2003).

In this procedure, it is possible that existing disks may overlap with new disks on the front. In this case, certain actions should be taken in order to generate disks without overlapping the existing disks.

6.3.3. Segment deactivation

A segment becomes deactivated if both centers of the two disks on the same segment are outside the domain to be filled. In this case, the segment will no longer be selected to generate new disks in subsequent steps. The domain is considered fully filled and the procedure is terminated when all the segments on the front become deactivated. All disks generated should be checked to exclude those that have parts lying outside the domain.

6.4. Donghekou landslide

The Wenchuan earthquake struck the Longmenshan area, Sichuan Province, China on 12 May 2008. The seismograms of this earthquake are shown in Figure 6-2.

The earthquake triggered thousands of mass movements in the Longmenshan area, where some huge landslides caused an extreme loss of life and property (Dai et al., 2010). The Donghekou landslide was exceptional among these landslides.

The Donghekou slide (32.432°N 105.109°E) is located at the Donghekou village, Hongguang Town, Qingchuan County (Figure 6-3), where the Hongshihe River joins the Qingzhujiang River (Li et al. 2012). The Donghekou landslide-debris flow is a typical rapid, long run-out, compound landslide with the height difference between the toe and main scarp of 540 m, a sliding distance of 2,270 m, and a volume of 15 million m^3. This landslide buried seven villages and killed 780 people, and it dammed two confluent rivers forming a massive lake. It is composed of sandstone, shale, and schist of Cambrian age and is located about 4 km from the active fault-rupture trace.

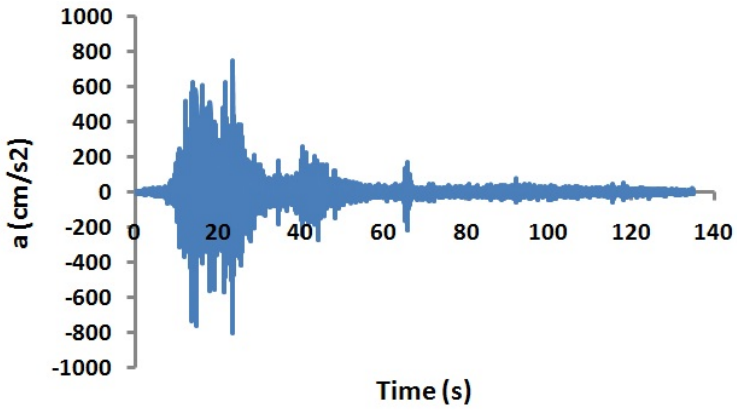

(a)

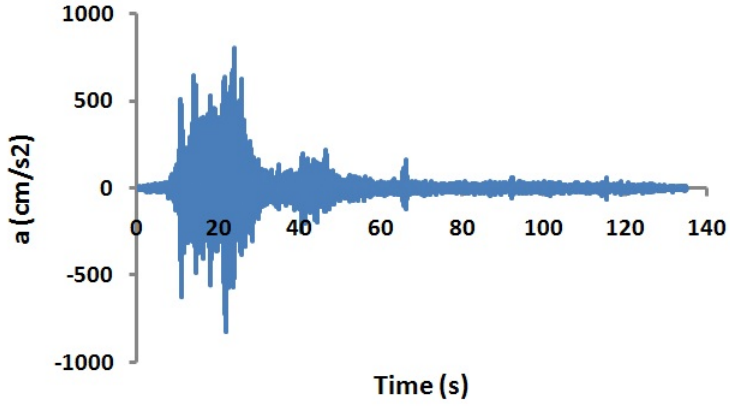

(b)

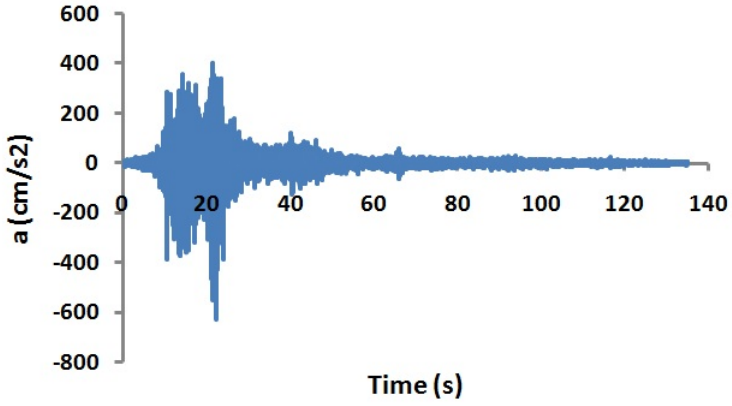

(c)

Figure 6-2. Acceleration records of the Wenchuan earthquake (a) north-south direction (b) east-west direction and (c) up-down direction at Qingping station

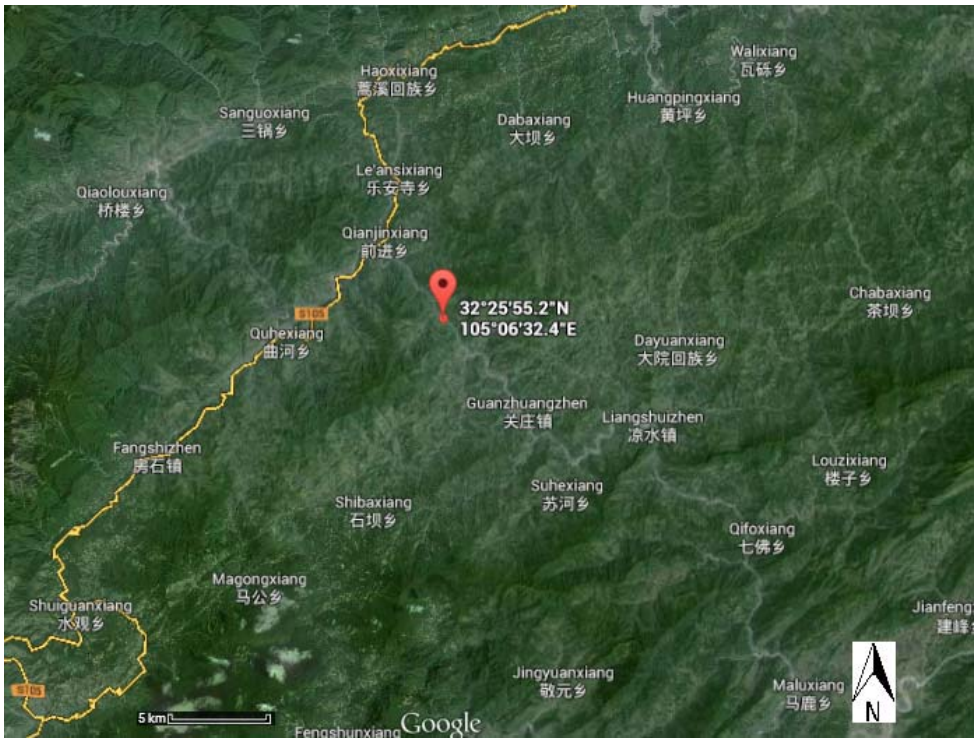

Figure 6-3. Map showing location of the landslide

6.5. Modeling Using Disk-Based DDA

The disk-based DDA is used to simulate the movement of the Donghekou landslide. The model dimensions of the landslide are 2400 m in length and 774 m in height, as shown in Figure 6-4. In the numerical model, “boundary elements” are used to represent the rocks under the sliding surface and the debris is simulated with circular disks. Also, the ground motions shown in Figure 6-2 are incorporated into two seismic accelerations in horizontal and vertical directions in DDA (considering strike of the cross section of the slope) and are applied to the disks.

Based on in situ observations in the landslide area, the particle radii range from 0.6 to 2.4 m and follow a uniform distribution (Li et al. 2012). In our work, we employ disks with sizes varying between 1 m and 3.7 m that are randomly generated inside the whole deforming region.

A sketch of the disk-based DDA model of the slope is shown in Figure 6-4. A total of 1,012 circular disks are employed in this study and we are currently enhancing our simulations to generate 1,826 disks, similar to the DEM model performed by Li et al. (2012).

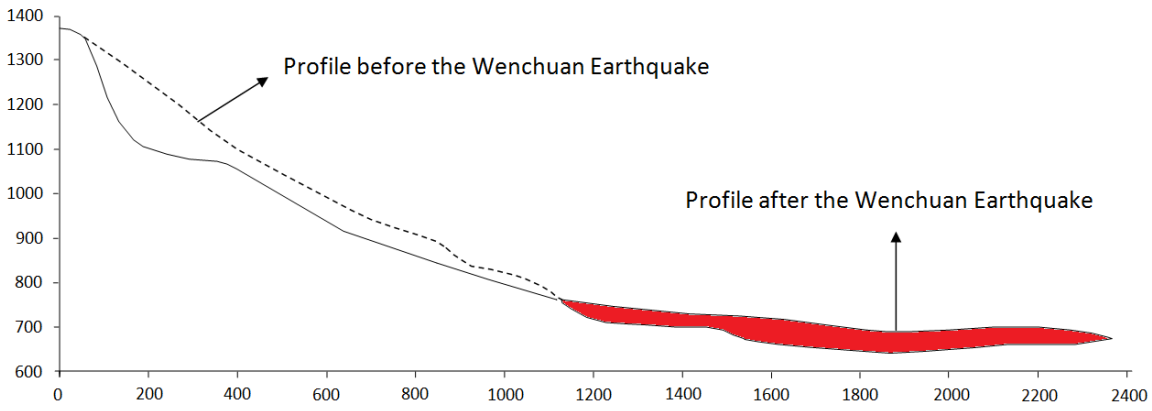

Figure 6-4. Schematic cross section of the Donghekou landslide (adapted from Li et al. 2012)

In this simulation, the disk density is assumed to be 2,500 kg/m^3 and the inter-disk and base friction coefficient is set to 0.3. Also, the time step size is 0.005 s and the contact spring stiffness is assumed to be 5 x 10^9 N/m.

The simulation results obtained using the disk-based DDA are shown in Figure 6-5. In order to compare the results obtained by modeling with actual data, the center of mass

and the spreading standard deviation around the center of mass for the final position of debris for both observations and DDA simulation are calculated. The center of mass for the observation is (1722.3, 689.1) and the center of mass of the final position obtained by disk-based DDA is (1603.9, 710). The distance from the center of mass to the origin for observation and DDA results are 1855.0 m and 1754.01 m, respectively (error = 5.4%). The spreading standard deviation is 359.7 m and 375.3 m for the observation and DDA results, respectively (error = 4.3%).

Therefore, an acceptable result is obtained. However, a larger number of disks is being considered in the model in order to improve our results.

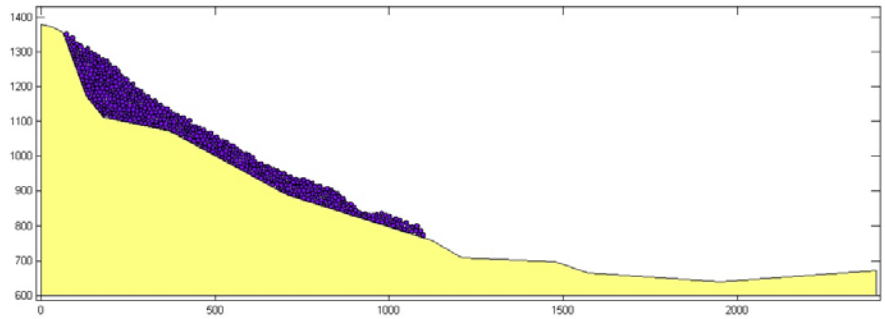

(a)

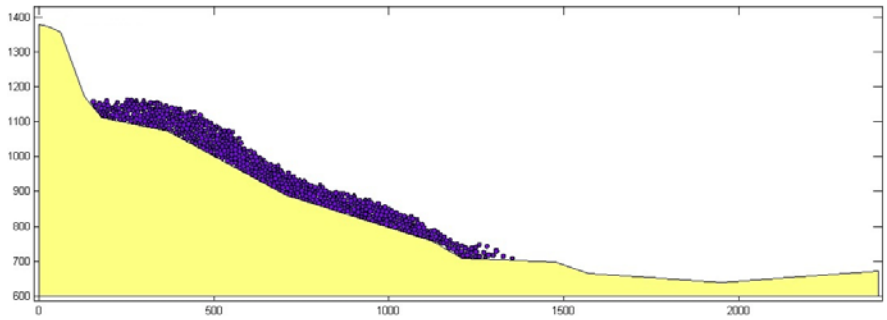

(b)

Figure 6-5. Results obtained using disk-based DDA for the Donghekou landslide simulation after (a) 0s (b) 60s (c) 90s (d) 120s (e) 250s

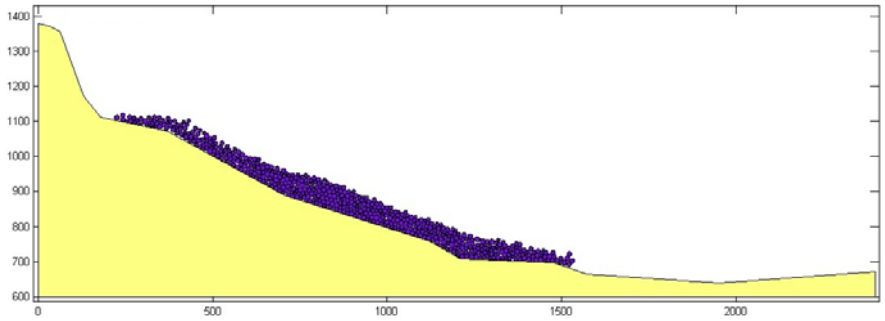

(c)

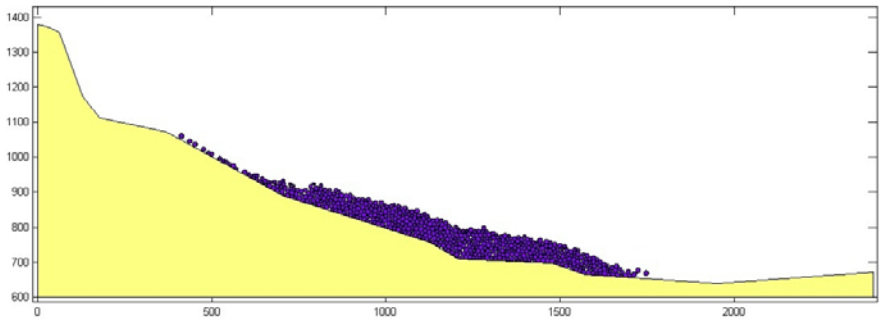

(d)

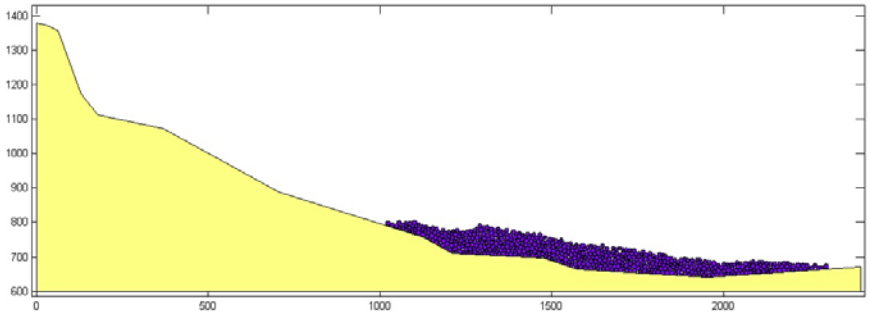

(e)

Figure 6-5. Results obtained using disk-based DDA for the Donghekou landslide simulation after (a) 0s (b) 60s (c) 90s (d) 120s (e) 250s (Cont.)

6.6. Conclusions

In this study, we show the capability of disk-based DDA to model landslides triggered by an earthquake by simulating the post-failure behavior of the Donghekou landslide during the Wenchuan earthquake. The results obtained using disk-based DDA are compared

with actual data. The run-out distance of the landslide and topography of final deposition obtained by the disk-based DDA simulation agree with the actual post-failure landform. However, more number of disks is required in our model to get better results.

6.7. References

Ahn TY, Song JJ. 2011. New Contact-Definition Algorithm using Inscribed Spheres for 3D Discontinuous Deformation, International Journal of Computational Methods, 8(2): 171–191.

Bagi K. 2005. An algorithm to generate random dense arrangements for discrete element simulations of granular assemblies, Granular Matter, 7:31–43.

Bakun-Mazor D, Hatzor YH, Glaser SD. 2012. Dynamic sliding of tetrahedral wedge: The role of interface friction. International Journal for Numerical and Analytical Methods in Geomechanics, 36(3): 327–343.

Bakun-Mazor D, Hatzor YH, Glaser SD, Santamarina JC. 2013. Thermally vs. seismically induced block displacements in Masada rock slopes, International Journal of Rock Mechanics & Mining Sciences, 61:196–211.

Bao H, Hatzor YH, Huang X. 2012. A New Viscous Boundary Condition in the Two-Dimensional Discontinuous Deformation Analysis Method for Wave Propagation Problems, Rock Mech Rock Eng, 45:919–928.

Benabbou A, Borouchaki H, Laug P, et al. 2009. Geometrical modeling of granular structures in two and three dimensions.Application to nanostructures. International Journal for Numerical Methods in Engineering, 80:425–454.

Beyabanaki SAR, Grayeli R, Hatami K. 2008. Three-dimensional discontinuous deformation analysis (3-D DDA) using a new contact resolution algorithm. Computers and Geotechnics, 35:346-356.

Beyabanaki SAR, Jafari A, Biabanaki SO, Yeung MR. 2009a. A Coupling Model of 3-D Discontinous Deformation Analysis (3-D DDA) and Finite Element Method, AJSE, 34:2B:107-119.

Beyabanaki SAR, Jafari A, Biabanaki SO, and Yeung MR. 2009b. Nodal-based Three-Dimensional Discontinuous Deformation Analysis (3-D DDA), Computers and Geotechnics, 36:359-372.

Beyabanaki SAR, Jafari A, Yeung MR. 2009c. Second-Order Displacement Functions for Three-Dimensional Discontinuous Deformation Analysis (3-D DDA), International Journal of Science and Technology, 16(3):216-225.

Beyabanaki SAR, Mikola GR, Biabanaki SO, Mohammadi S. 2009d. New Point-to-Face Contact Algorithm for 3-D Contact Problems using the Augmented Lagrangian Method, Geomechanics and Geoengineering: An International Journal, Taylor & Francis, 4 (3):221-236.

Beyabanaki SAR, Ferdosi B, Mohammadi S. 2009e. Validation of dynamic block displacement analysis and modification of edge-to-edge contact constraints in 3-D DDA, International Journal of Rock Mechanics and Mining Sciences, Elsevier, 46:1223-1234.

Beyabanaki SAR, Jafari A, and Yeung MR. 2010. High - order three - dimensional discontinuous deformation analysis (3-D DDA), International Journal for Numerical Methods in Biomedical Engineering, 26 (12):1522–1547.

Beyabanaki SAR and Bagtzoglou AC. 2012. Three-dimensional discontinuous deformation analysis (3-D DDA) method for particulate media applications, Geomechanics and Geoengineering: An International Journal 7(4):239-253.

Beyabanaki SAR and Bagtzoglou AC, 2013. Non-rigid disk-based DDA with a new contact model, Computers and Geotechnics 49:25–35.

Beyabanaki SAR and Bagtzoglou AC, 2014a. Sphere-boundary edge and sphere-boundary corner contacts model in DDA for simulating particulate media in 3-D, Geomechanics and Geoengineering: An International Journal, in press, doi: 10.1080/17486025.2014.933892.

Beyabanaki SAR and Bagtzoglou AC, 2014b. Accuracy of Dynamic Disk-Based DDA with Respect to a Single Sliding Disk Cluster, Geomechanics and Geoengineering: An International Journal, 9(3); 231-240.

Dai, F. C., Xu, C., Yao, X., Xu, L., Tu, X. B., and Gong, Q. M. 2010. Spatial distribution of landslides triggered by the 2008 Ms 8.0 Wenchuan earthquake, China, J. Asian. Earth Sci., 40, 883–895.

Feng YT, Han K, Owen DRJ. 2003. Filling domains with disks: an advancing front approach. International Journal for Numerical Methods in Engineering, 56(5):699–713.

Hatzor YH and Bakun-Mazor D. 2011. Modeling dynamic deformation in natural rock slopes and underground openings with DDA: review of recent results. Geomechanics and Geoengineering: An International Journal, 6(4):283-292.

Jiang QH, Yeung MR. 2004. A model of point-to-face contact for three-dimensional discontinuous deformation analysis. Rock Mechanics and Rock Engineering, 37(2):95 – 116.

Jing L, Hudson JA. 2002. Numerical methods in rock mechanics, International Journal of Rock Mechanics & Mining Sciences, 2002; 39: 409‑427.

Jing L. 2003. A review of techniques, advances and outstanding issues in numerical modelling for rock mechanics and rock engineering, International Journal of Rock Mechanics & Mining Sciences, 40: 283‑353.

Ke, T.-C., and Bray, J. D. 1995. Modeling of particulate media using discontinuous deformation analysis. J. Eng. Mech., 121(11), 1234–1243.

Koo CY, Chern JC. 1998. Modification of the DDA method for rigid block problems. International Journal of Rock Mechanics and Mining Sciences, 35(6):684–693.

Koyama T, Nishiyama S, Yang M, Ohnishi Y. 2011. Modeling the interaction between fluid flow and particle movement with discontinuous deformation analysis (DDA) method, Int. J. Numer. Anal. Meth. Geomech., 35:1–20.

Li X, He S, Luo Y, Wu Y. 2012. Simulation of the sliding process of Donghekou landslide triggered by the Wenchuan earthquake using a distinct element method, Environ Earth Sci, 65:1049–1054.

Liu L, Linde AT, Sacks IS, and He S. 1996. Aseismic fault slip and block deformation in north China, Pure Appl. Geophys., 146(3/4):717-740.

Liu J, Kong X, Lin G. 2004. Formulation of the three-dimensional discontinuous deformation analysis method. Acta Mechanica Sinica, 20(3):270-282.

Liu J, Nan Z, Yi P. 2012. Validation and application of three-dimensional discontinuous deformation analysis with tetrahedron finite element meshed block, Acta Mechanica Sinica, 28(6):1602–1616.

Liu J, Yun B., Zhao C. 2012. An improved specimen generation method for DEM based on local Delaunay tessellation and distance function. International Journal for Numerical and Analytical Methods In Geomechanics, 36:653–674.

Lohner R, Onate E. 2004. A general advancing-front technique for filling space with arbitrary objects. International Journal for Numerical Methods in Engineering, 61:1977–1991.

MacLaughlin MM, Doolin DM. 2006. Review of validation of the discontinuous deformation analysis (DDA) method, Int J Numer Anal Meth Geomech, 30: 271-305.

Moosavi M, Jafari A, Beyabanaki SA. 2005. Dynamic Three-Dimensional Discontinuous Deformation Analysis (3-D DDA) Validation Using Analytical Solution, Proceedings of the Seventh International Conference on Analysis of Discontinuous Deformation (ICADD-7), Hawaii, USA, Dec. 10-12, pp. 37-48.

Ohnishi Y, Nishiyama S. 2007. Recent insights of analyses using discontinuous methods in rock engineering in Japan, Proceedings of the 8th International Conference on Analysis of Discontinuous Deformation: Fundamentals and Applications to Mining and Civil Engineering, Beijing, China, August 14-19, pp. 15-26.

Rein G, Andrés A. 2001. Computer simulation of granular material: vibrating feeders, Powder Handling & Processing, 13(2), 181-185.

Shi GH. 1988. Discontinuous deformation analysis: a new numerical model for the statics and dynamics of block systems, PhD thesis, Department of Civil Engineering, University of California, Berkeley.

Shi GH. 1993. Block System Modeling by Discontinuous Deformation Analysis. Computational Mechanics Publication: Southampton. UK.

Shi GH. 2001. Three dimensional discontinuous deformation analysis. In: Proceedings of the 38th US Rock Mechanics Symposium, D Elsworth et al, ed., p 1421-1428.

Shi GH. 2007. Applications of discontinuous deformation analysis (DDA) to rock stability analysis, Proceedings of the 8th International Conference on Analysis of Discontinuous Deformation: Fundamentals and Applications to Mining and Civil Engineering, Beijing, China, August 14-19, pp. 1-13.

Thomas, P. A. 1997. Discontinuous deformation analysis of particulate media. PhD thesis, University of California, Berkeley, Berkeley, CA.

Thomas, P. A., and Bray, J. D. 1999. Capturing nonspherical shape of granular media with disk clusters. J. Geotech. Geoenviron. Eng., 125(3), 169–178.

Wu JH, Ohnishi Y, Shi GH, Nishiyama S. 2005a. Theory of Three-Dimensional Discontinuous Deformation Analysis and Its Application to a Slope Toppling at Amatoribashi, Japan. International Journal of Geomechanics, 179-195.

Wu JH, Juang CH, Lin HM. 2005b. Vertex-to-face contact searching algorithm for three-dimensional frictionless contact problems. International Journal for Numerical Methods in Engineering, 63(6):876-897.

Wu JH. 2008. New edge-to-edge contact calculating algorithm in three-dimensional discrete numerical analysis. Advances in Engineering Software, 39(1):15-24.

Yagoda-Biran G, Hatzor YH. 2010. Constraining paleo PGA values by numerical analysis of overturned columns, Earthquake Engineering and Structural Dynamics, 39:463–472.

Yeung MR, Jiang QH, Sun N. 2003. Validation of block theory and three-dimensional discontinuous deformation analysis as wedge stability analysis method. Int J Rock Mech Min Sci, 40(2):265 –275.

Yeung MR, Sun N, Jiang QH, Blair SC. 2004. Analysis of large block test data using three-dimensional discontinuous deformation analysis. Int J Rock Mech Min Sci, 41(3):458–459.

Yeung MR, Jiang QH, Sun N. 2007. A model of edge-to-edge contact for three-dimensional discontinuous deformation analysis. Computers and Geotechnics, 34(3):175-186.

Chapter 7. Effects of groundwater table position, soil strength properties and rainfall on instability of earthquake-triggered landslides

(This chapter will be submitted to a journal for publication, by Beyabanaki SAR, Bagtzoglou AC, and Anagnostou EN)

7.1. Introduction

One of the most important natural hazards that often result in serious structural damage and loss of life are landslides induced by rainfall and/or earthquakes. There are several publications on the effects of hydrological parameters on instability of landslides triggered by rainfall. For example, Cho and Lee (2002) investigated the influence of infiltration on surficial stability of slopes by the limit equilibrium method. Cai and Ugai (2004) studied effects of hydraulic characteristics, rainfall intensity and rainfall duration on water pressure in slopes and thus on the stability of slopes under rainfall. Rahardjo et al. (2007) investigated the impact of rainfall intensity and initial water table location on instability of slopes due to rainfall. The effects of soil hydraulic properties on rainfall-triggered slope failure were investigated through a series of parametric studies by Rahimi et al. (2010). Also, parametric studies were carried out to study the effect of groundwater table position and rainfall intensity on stability of slopes during rainfall by Rahardjo et al. (2010a). Rahardjo et al. (2010b) investigated the effect of rainfall intensity on instability of soil slopes under rainfall. Impacts of unsaturated zone soil moisture and groundwater table on slope instability were studied by Ray et al. (2010). Rahimi et al. (2011) studied the effect of antecedent rainfall patterns on rainfall-induced slope failure.

Although landslides triggered by earthquakes are widely studied by several researchers (Zhang et al. 2010 and Wasowski et al. 2011), less attention has been focused on hydrological parameters and their effects on instability of earthquake-induced landslides. Lin et al. (2006) investigated impacts of the Chi-Chi earthquake on rainfall-induced landslides in central Taiwan. Lin et al. (2008) studied the influence of typhoons and earthquakes on rainfall-induced landslides. They investigated four events in the Chenyoulan River catchment of central Taiwan during 1996 to 2004 in order to identify their controlling factors. Chen and Hawkins (2009) studied the relationship between earthquake disturbance, tropical rainstorms and debris movement in Taiwan. A conceptual model was developed by Shou et al. (2011) to investigate the time effect of the earthquake impact on the landslide–rainfall correlation. A comparative analysis of the impact of the 2008 Wenchuan earthquake and heavy rainfall events on landslide evolution was performed by Tang et al. (2011).Tang et al. (2011, 2012) studied landslides triggered by rainfall at the epicenter of the Wenchuan earthquake and concluded that the whole area shaken by the Wenchuan earthquake is much more susceptible to debris flow, initiated by localized heavy rainfall, than what had been assumed earlier. Ma et al. (2013) compared debris-flow volume and activity under different formation conditions and found that there is a strong empirical relationship between debris-flow volume and loose materials volume in the earthquake region. The relationship between the occurrence of post-seismic debris flow and characteristic rainfall patterns was studied by Zhou et al. (2014) who obtained characteristics of rainfall events that triggered debris flows after earthquakes by analyzing the rainfall data. Chung et al. (2014) estimated the threshold water table depths to initiate seismically induced landslides in the uplands of alluvial floodplains under an earthquake with a peak ground

acceleration of 0.20 to 0.40 g. Recently, Zhou and Tang (2014) studied rainfall thresholds for debris flow initiation in the Wenchuan earthquake-stricken area.

Although the effects of controlling parameters on instability of landslides triggered by rainfall have been studied by several researchers, no published studies exist on the instability of landslides triggered by earthquakes during rainfall. This aspect is investigated in this paper focusing on the combined effects of groundwater table position, soil strength properties, rainfall intensity and soil saturation on the instability of earthquake-triggered landslides under rainfall. For this purpose, a new combined hydrology and slope stability model is developed and a series of parametric studies are performed to highlight the importance of each controlling parameter in assessing the instability of a homogeneous soil slope under different rainfall and earthquake conditions.

In the next section we describe the developed combined hydrology and slope stability model. In section 7.3, we explain parametric study performed in this research. We present the effects of groundwater table location, soil strength properties, rainfall intensity and soil saturation on instability of landslides in sections 7.4, 7.5, and 7.6, respectively. We close this study with conclusions and future research directions.

7.2. Developed Combined Model

A new combined hydrology and slope stability model is developed in order to investigate the impact of rainfall on instability of landslides triggered by earthquakes. In this model, pore-water pressures are calculated by simulating saturated and unsaturated

hydrological processes. Then, pore-water pressures are incorporated into the computation of slope stability by limit equilibrium analysis.

A similar combined model named CHASM (Combined Hydrology and Stability Model) was presented by Wilkinson et al. (2000).This model has been used for various environmental conditions in different countries, for example, in Hong Kong (Wilkinson et al. 2002a), Malaysia (Wilkinson et al. 2000; Wilkinson et al. 2002b; Lateh et al. 2008), Greece (Ferentinou et al. 2006; Sakellariou et al. 2006), the Caribbean (Anderson et al. 2008; Holcombe et al., 2012), and Germany (Thiebes et al. 2014).

The basic modeling methodology employed in our model is presented in this section. We describe the hydrology, slope stability and soil shear strength models employed in our developed combined model and compare it with the CHASM model in sub-sections 7.2.1, 7.2.2, and 7.2.3, respectively. Also, in sub-section 7.2.4, we verify our model.

7.2.1. Hydrology Model

In our model, it is possible to simulate changes in pore water pressures in response to individual rainfall events and to consider their role in modeling slope stability. For this purpose, the slope is divided into a series of one-dimensional columns and each column is discretized into computational cells. Flow continues from top to bottom of each column until the water table is reached. To model one-dimensional, vertical infiltration, Richards' equation is used:

$$\frac{\partial \theta}{\partial t} = \frac{\partial}{\partial z}\left[K(\theta)\left(\frac{\partial \psi}{\partial z} + 1 \right) \right] \tag{7-1}$$

where:

K = hydraulic conductivity;

ψ = pressure (suction) head;

z = elevation;

θ = water content; and

t = time.

The water content of a soil is related to the matric suction by the soil-moisture characteristic curve. Several empirical and semi-empirical functions have been proposed by researchers to represent the soil-moisture characteristic curves. In our combined model, one of the most widely used soil–moisture characteristic curve functions is employed (van Genuchten 1980):

$$S_e = \left(\frac{\theta - \theta_r}{\theta_s - \theta_r} \right) = \left(\frac{1}{1 + \left[a(u_a - u_w) \right]^n} \right)^m \tag{7-2}$$

where:

S_e = relative degree of saturation;

θ_s = saturated water content;

θ_r = residual water content;

u_a = pore air pressure;

u_w = pore water pressure;

u_a-u_w = ψ= matric suction; and

a, n, and *m* = constants.

Our model also allows for the implementation of other constitutive formulations, such as the one proposed by Haverkamp et al. (1977). The non-linear hydraulic conductivity terms are evaluated explicitly and the numerical solution is fully backward in time.

Contrary to CHASM, which links flow between soil columns using one-dimensional saturated Darcy fluxes (Wilkinson et al. 2000), our model employs a two-dimensional saturated flow model that allows for spatially heterogeneous soil parameters and variable water table depths. Again, the numerical solution is implicit in time.

7.2.2. Slope Stability Model

The analysis of the stability of slopes using Limit Equilibrium Methods (LEM) necessitates determination of the critical slip surface that yields the minimum factor of safety. In our model, Spencer's method is used to perform the slope stability analysis. Spencer's method is one of the most accurate limit equilibrium methods used for slope stability analysis (Das 2010) and satisfies complete force and moment equilibrium (Abramson et al. 2002). In CHASM, Bishop's and Janbu's methods are employed as the slope stability method of choice. However, Bishop's method fails to satisfy horizontal force equilibrium and Janbu's method does not satisfy moment equilibrium.

Earthquake acceleration is also considered in the model in order to analyze the effect of seismic activity on slope stability and is implemented via an Earthquake Acceleration Coefficient (EAC). Moreover, our model is able to automatically determine geometry of the potential landslide. For this purpose, after specifying the slope geometry, the model requires the soil parameters and grid of circle centers with variable radii for which the

corresponding factor of safety will be calculated. Then, contours of the factor of safety are produced. The geometry associated with the minimum factor of safety is obtained and this, in turn, specifies the geometry of the potential landslide.

7.2.3 Soil Shear Strength Model

In CHASM, the equation proposed by Fredlund et al. (1978) is used to calculate shear strength of unsaturated soils:

$$\tau = c' + (\sigma_n - u_a)\tan(\phi') + (u_a - u_w)\tan(\phi^b) \tag{7-3}$$

where:

σ_n = the total normal stress on the failure plane at failure;

c' = the effective soil cohesion;

ϕ' = the effective angle of internal friction; and

ϕ^b = the angle defining the rate of increase in shear strength with respect to soil suction.

In this formulation, ϕ^b is considered constant and does not change during rainfall. Its most common values ranges from 15 to 20 degrees (Krahn 2004).

In our model a modified equation for calculating shear strength of unsaturated soils is used (Fredlund 2006):

$$\frac{\tan(\phi^b)}{\tan(\phi')} = S_e \tag{7-4}$$

$$\tau = c' + \left[(\sigma_n - u_a) + S_e(u_a - u_w)\right]\tan(\phi')$$

(7-5)

As can be seen, ϕ^b is a function of soil water content and can change during rainfall events as infiltration continues.

7.2.4. Model Verification

To verify our model, two case studies are considered and the results obtained by the developed model are compared with data.

- *Laboratory Shaking Table Test*

Since the LEM used in our model is able to model slopes in both rocks and soils (Li et al. 2009), the results obtained by the laboratory shaking table test presented by Irie et al. (2012) were used to verify the dynamic part of our model.

Irie et al. (2012) performed a series of laboratory shaking table tests to investigate the seismic response of a multilayer block model representing a rock slope consisting of many discontinuous rock masses (Figure 7-1).

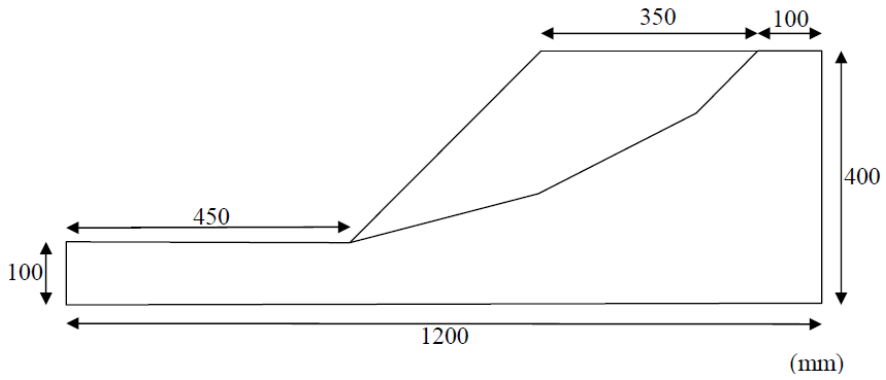

Figure 7-1. Schematic of a model representing slope of the shaking table tests adapted from Irie et al. (2012)

The slope consists of the foundation and block element parts and the width, height and thickness of the block element part are 650 mm, 300 mm and 50 mm, respectively. Only horizontal acceleration is applied to the slope and the seismic input signal was based on the acceleration observed in Hachinohe City during the Tokachioki Earthquake in 1968, which was characterized by a maximum acceleration of about 800 gal (0.816 g). Material properties used in the test are: unit weight = 26.4 kN/m^3; friction angle = 20°, and cohesion = 0 kPa. Test results are presented in schematic form in Figure 7-2.

The slope was simulated using our developed combined model. The results of modeling including contours of factor of safety and the failure surface are shown in Figure 7-3.The failure surface can be determined by finding the area where factor of safety is 1.0 (shown in Figure 7-3 as rigid thick line). As can be seen, the slope is not stable and the areas of the real and obtained failure surfaces are 80848 mm^2 and 78708 mm^2, respectively. Therefore, the failure surface obtained by the model is in good agreement with the failure surface observed during the test (error = 2.65%). This verification test lends credence that the LEM implemented in our model is able to model a slope under earthquake excitation very well.

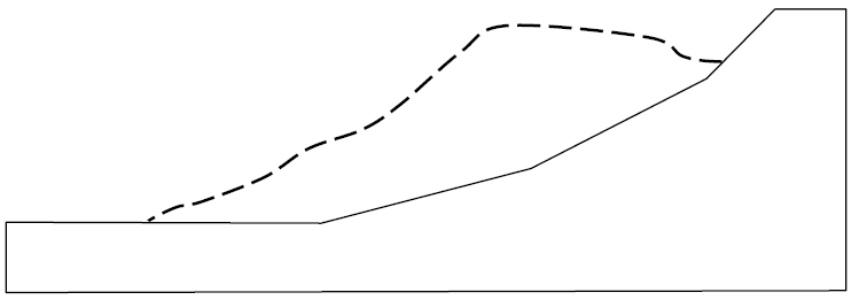

Figure 7-2. Schematic of results observed after the shaking table tests adapted from Irie et al. (2012)

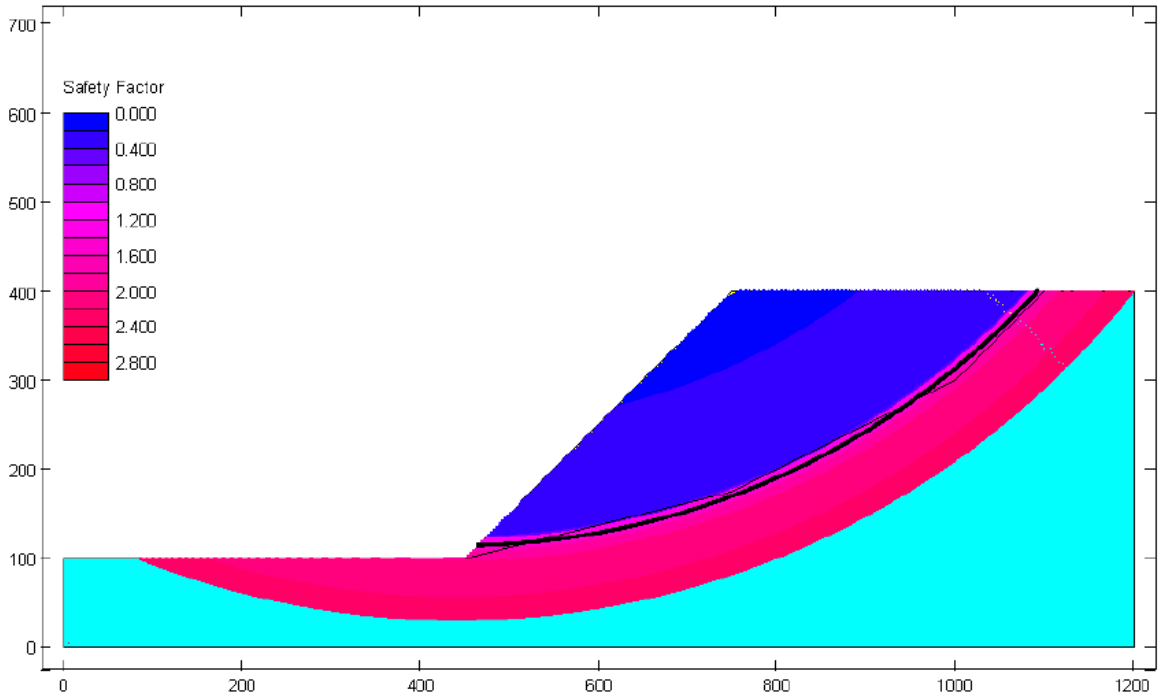

Figure 7-3. Results obtained by the developed combined model (rigid thick line shows the failure surface determined by our model)

- *The Swabian Alb Case Study*

Thiebes et al. (2014) used CHASM to study rainfall-triggered landslides in Lichtenstein-Unterhausen in the Swabian Alb, south of the city of Reutlingen in Germany. They worked on one specific slope profile, for which hydrological monitoring data were available, and for which slope movements had been confirmed by previous investigations. In order to verify the hydrology part of our model, the same slope was simulated by using the combined model and the results are compared with results obtained by CHASM. The slope profile is located on the main western landslide body with a total length of 300 m and a slope height of 165 m. Four material types (Upper Jurassic limestone, Middle Jurassic marl, limestone scree, and slope debris) were

identified and accounted for in modeling slope stability with CHASM and our model. The properties for the material layers used in the simulations are presented in Table 7-1.

Table 7- 1 Parameters used for different layers in CHASM simulations for the Swabian Alb test case (Thiebes et al. 2014)

Parameter	Upper Jurassic	Middle Jurassic	Slope debris	Limestone scree
Effective Cohesion (kPa)	300	1,500	19	0
Internal Friction (◦)	35	15	20	33
Hydraulic Conductivity (m/s)	10^{-6}	10^{-9}	6.78^{-7}	10^{-1}
Moisture Content (m3/m3)	40.7	44.7	52.6	48.3
Saturated Density (kN/m3)	25	23	16	16
Unsaturated Density (kN/m3)	23	21	15	15

The slope profile and the surfaces selected by Thiebes et al. (2014) are shown in Figure 7-4. The factor of safety obtained by CHASM and our model for the surfaces shown in Figure 7-4 are presented in Table 7-2.

There are four stability classes identified based on the factor of safety values (Acharya et al. 2006): highly susceptible (FS<=1), moderately susceptible (1<FS<1.25), slightly susceptible (1.25<FS<1.5) and not susceptible (FS>=1.5). Based on Table 7-2, the projected stability class of all surfaces except surface S2 is the same for both CHASM and our model. The reason of having two different stability classes for surface S2 is the difference of 0.17 in safety factor obtained by CHASM and our model.

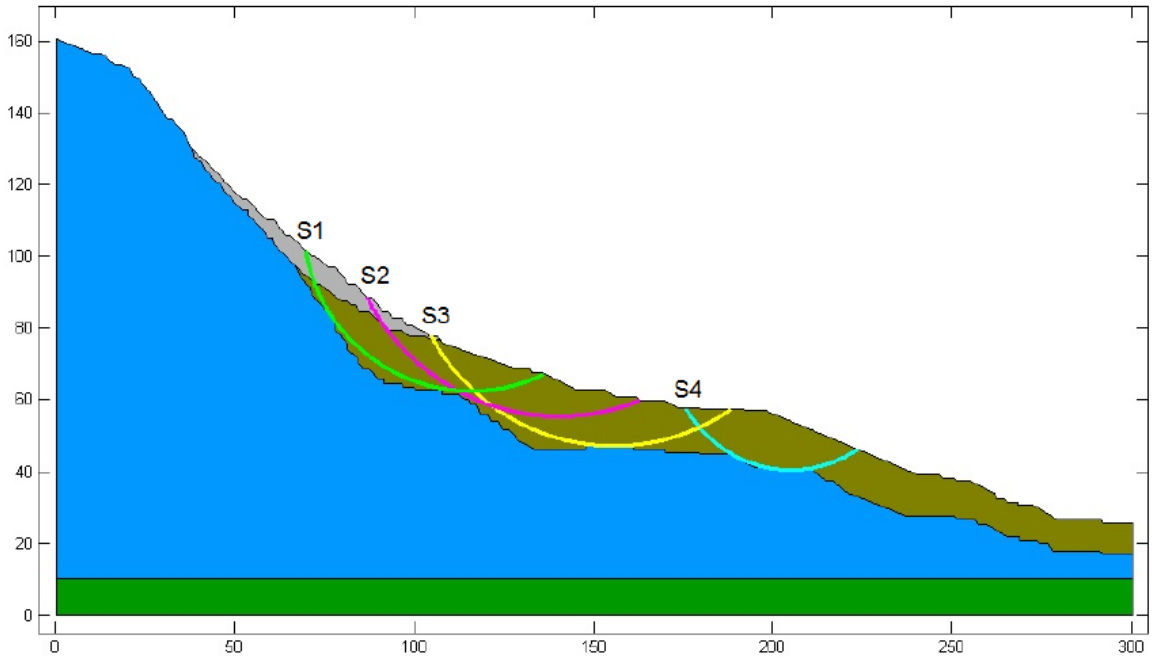

Figure 7-4. Slope profile of the Swabian Alb test case modeled using CHASM and our model and the slip surfaces selected by Thiebes et al. (2014)

The reasons of this difference is modeling groundwater flow in 2-D and using different slope stability and soil shear strength methods in our developed model. Therefore, there is reasonable agreement between our model results and the results obtained by CHASM.

7.3. Parametric Study

In this study, effects of location of groundwater table, soil properties and rainfall intensity on instability of landslides triggered by earthquakes during rainfall events are investigated. For this purpose, a series of parametric studies are performed on a typical geometry of a homogeneous soil slope shown in Figure 7-5.

Table 7- 2 Factor of safety (FS) obtained by CHASM and our model for the surfaces shown in Figure 7-4

Surface No.	FS obtained by CHASM	FS obtained by our model	Stability Class obtained by CHASM	Stability Class obtained by our model
S1	0.75	0.88	highly susceptible	highly susceptible
S2	1.4	1.23	slightly susceptible	moderately susceptible
S3	1.05	1.14	moderately susceptible	moderately susceptible
S4	1.61	1.84	not susceptible	not susceptible

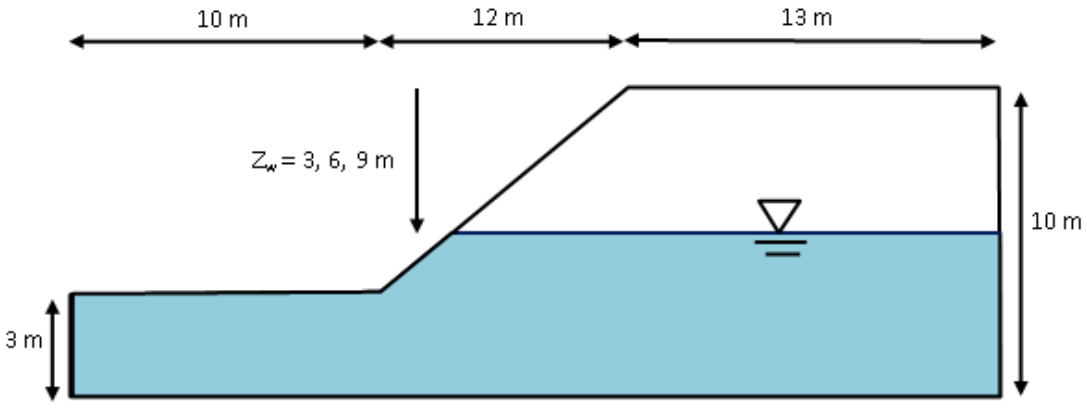

Figure 7-5. Schematic of slope geometry used in the parametric studies

As can be seen in the figure, similar to Mahmood et al. (2013), it is assumed that the water table is horizontal to simplify the problem. A constant total head boundary condition is applied along the sides of the slope below the water table (Rahardjo et al. 2010a; Rahimi et al. 2010, 2011).

In this parametric study, different depths to groundwater table (3, 6, and 9 m), soil cohesions (5, 20, and 35 kPa), friction angles (5, 25 and 45 degrees), rainfall intensities (1, 8, and 15 cm/h), and earthquake acceleration coefficients (0.05, 0.35, 0.65, 0.95, and 1.25) are used in different parametric series. Soil saturated hydraulic conductivity, residual and saturated water contents, and unit weight are assumed to be 5×10^{-5} (m/s), 0.05, 0.45, and 20 (kN/m^3), respectively.

The pseudo-static approach implemented in our model is used in the vast majority of geotechnical earthquake designs. It is applicable to situations for which liquefaction is not an issue (Shukha and Baker 2008), and the present study is limited to such situation. Also, in this study, it is assumed that the rainfall intensity is lower than the soil saturated hydraulic conductivity.

7.4. Effect of Groundwater Table Location

In this section, the effect of groundwater table location on stability of a homogeneous soil slope is studied. For this purpose, depth of water table is varied with different values of 3, 6, and 9 m for a soil slope with constant friction angle of 45° and cohesion of 35 kPa. In this study, rainfall intensities, I_r, are assumed to be 1, 8 and 15 cm/h with a duration of 30 h for different values of earthquake acceleration coefficients (0.05, 0.35, 0.65, 0.95 and 1.25). Even though we recognize 15 cm/h is extremely high and possibly unrealistic, similar to other studies, we use it as an upper limit for our sensitivity analysis (e.g.,

Rahardjo et al. (2007, 2010a) used 36 cm/h in their studies). For each combination of parameters, the minimum factor of safety is obtained using our model. The results for different values of parameters are presented in Figure 7-6.

As can be seen, increasing earthquake acceleration coefficient (EAC) decreases the factor of safety significantly. For example, when depth to groundwater table is 3m and EAC increases from 0.05 to 0.95, under rainfall with I_r = 1 cm/h, the factor of safety decreases from 2.98 to 0.93 and under I_r = 15 cm/h, decreases from 1.1 to 0.58.

Figure 7-6 shows that the factor of safety decreases when depth to groundwater table decreases regardless of amount of EAC or rainfall intensity. For example, under rainfall with intensity of 8 cm/h and EAC = 0.65, when depth to groundwater table decreases from 9 m to 3 m, the factor of safety decreases from 1.44 to 0.95 and a landslide would be considered possible. Also, it can be seen that increasing rainfall intensity decreases the stability of the slope in all cases.

7.5. Effect of Soil Strength Properties

The effect of soil strength properties on the instability of homogeneous soil slopes is studied in this section. It is assumed that the groundwater table depth is 6 m and the rainfall duration is 30 h.

7.5.1. Friction Angle

In order to investigate the effect of soil friction angle on instability of slopes, different rainfall intensities, Ir, (1, 8 and 15 cm/h) with earthquake acceleration coefficients of 0.05, 0.35, 0.65, 0.95 and 1.25 are considered. Also, friction angles are varied at 5, 25 and 45 degrees.

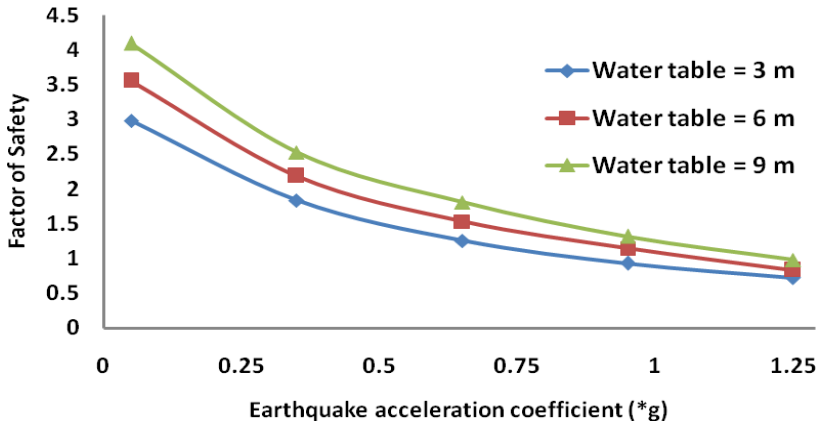

(a)

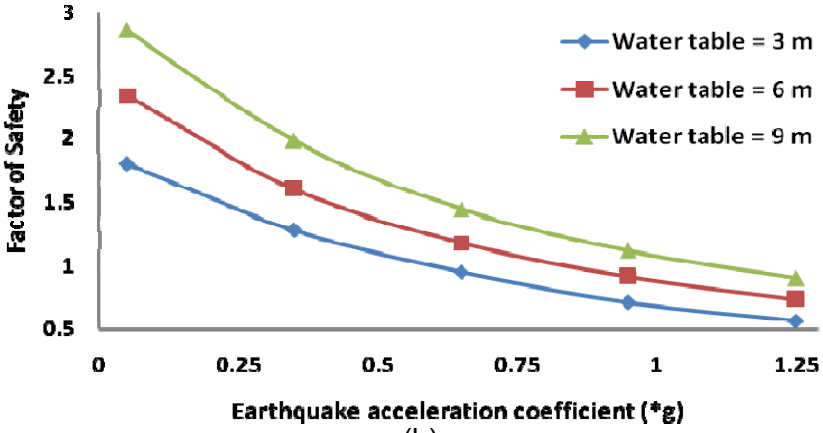

(b)

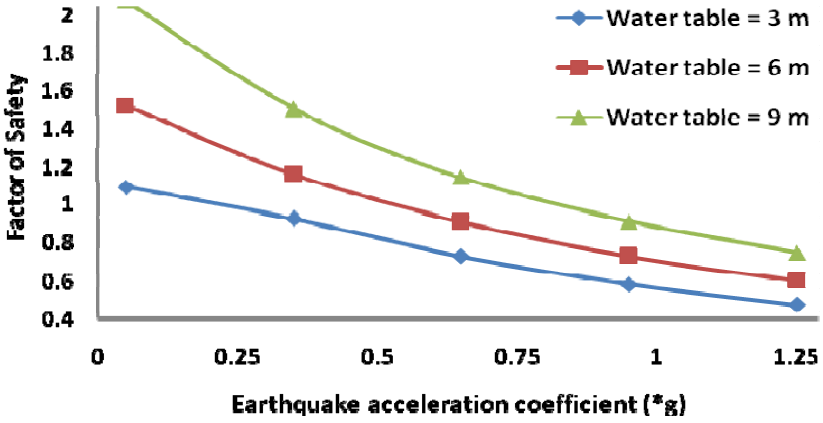

(c)

Figure 7-6. Results obtained for different groundwater table depths and rainfall intensity of (a) 1 cm/h (b) 8 cm/h and (c) 15 cm/h

By using the developed combined model, the minimum factor of safety for each parameter combination is obtained and the results for this sensitivity analysis are presented in Figure 7-7. In this study, it is assumed that soil cohesion = 30 kPa.

As can be seen, friction angle has a significant effect on the factor of safety and larger values lead to a larger factor of safety. For example, under rainfall with intensity of 8 cm/h and EAC = 0.35, when soil friction angle decreases from 45 degrees to 5 degrees, the factor of safety decreases from 1.99 to 0.83. Also, increasing rainfall intensity decreases the factor of safety in all cases.

7.5.2. Cohesion

In this section, the effect of cohesion on stability of the soil slope is studied. For this purpose, soil cohesion is varied at 5, 20, and 35 kPa for soils with constant friction angle of 45° and depth to groundwater table of 6 m. It is assumed that I_r = 1, 8 and 15 cm/h and EAC = 0.05, 0.35, 0.65, 0.95 and 1.25. The results of the minimum factors of safety obtained for all parameter combinations by the developed combined model are presented in Figure 7-8.

As can be seen in the figure, soil cohesion has a significant effect on the stability of the slope. For example, with I_r = 8 cm/h, EAC = 0.35, the factor of safety increases from 0.81 (unstable mode) to 1.56 (stable mode) when soil cohesion increases from 5 kPa to 35 kPa. Furthermore, decreasing the rainfall intensity increases the stability of the slope. For example, with EAC = 0.35 and cohesion = 20 kPa, when the rainfall intensity decreases from 15 cm/h to 1 cm/h the factor of safety increases from 0.86 (unstable mode) to 1.68 (stable mode).

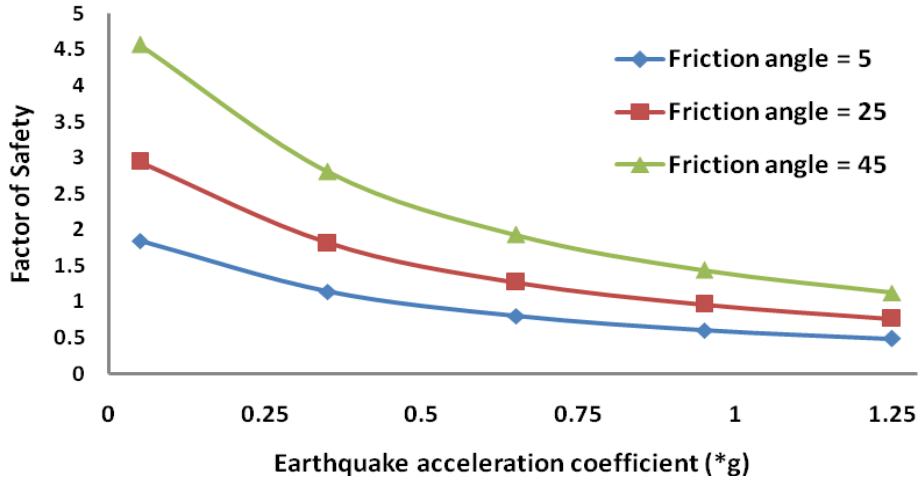

(a)

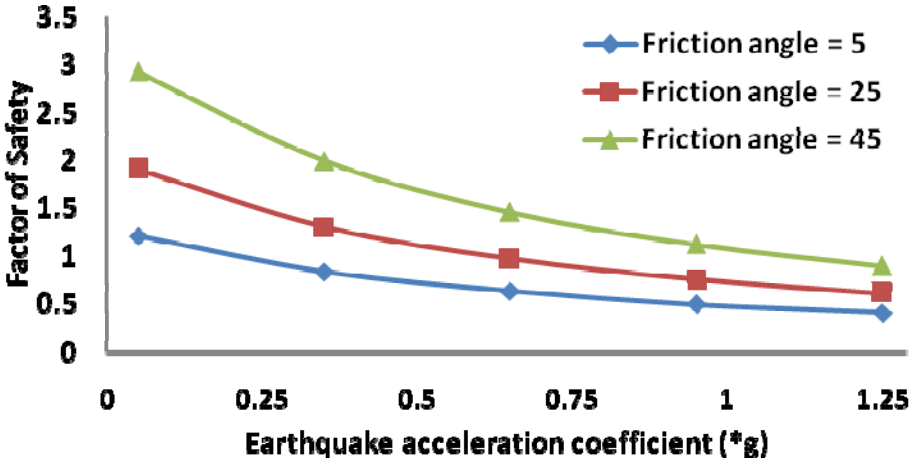

(b)

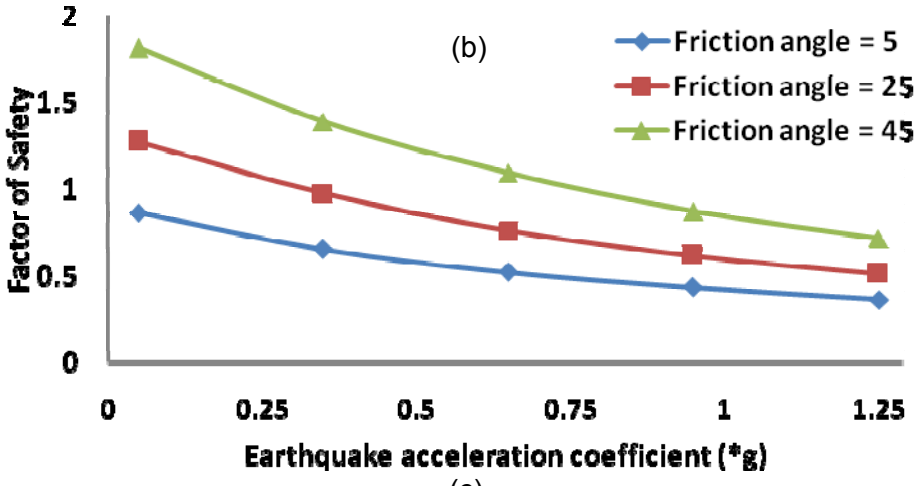

(c)

Figure 7-7. Results obtained for different soil friction angles and rainfall intensity of (a) 1 cm/h (b) 8 cm/h and (c) 15 cm/h

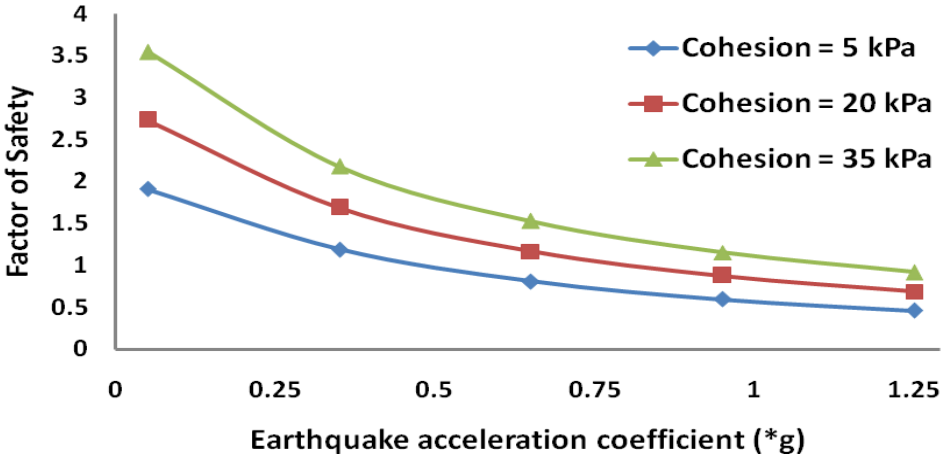

(a)

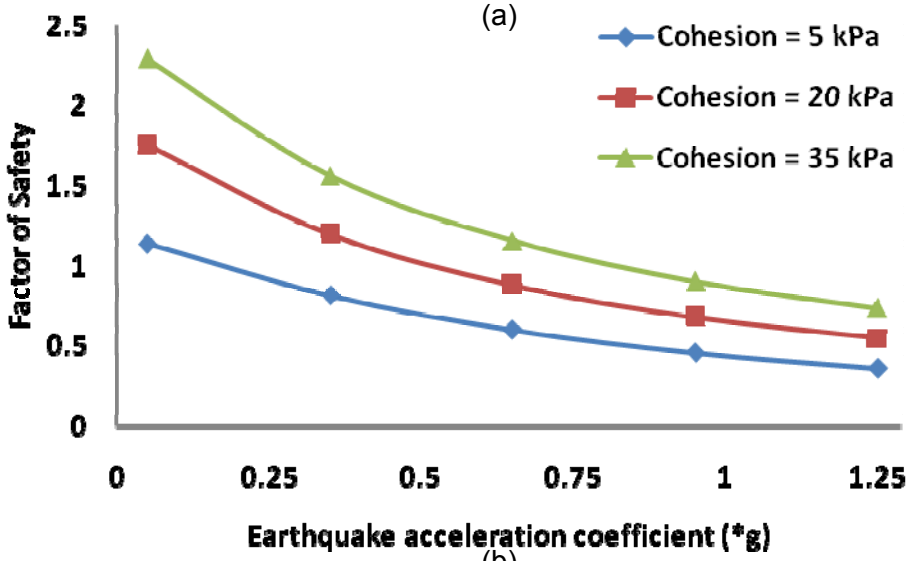

(b)

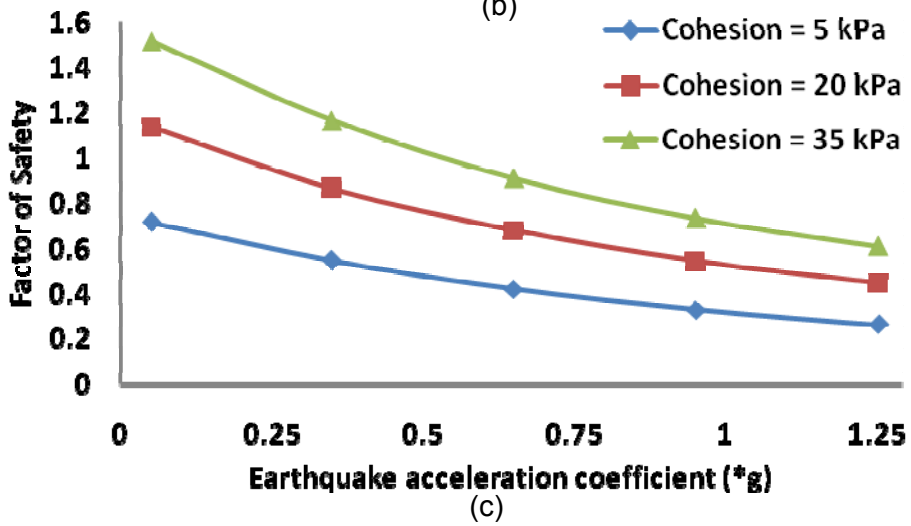

(c)

Figure 7-8. Results obtained for different soil cohesions and rainfall intensity of (a) 1 cm/h (b) 8 cm/h and (c) 15 cm/h

7.6. Effect of Rainfall Intensity, Duration and Soil Saturation

In this section, the effects of rainfall intensify on slope stability considering the soil strength and depth to groundwater table effects are investigated. For this purpose, different rainfall intensities with a duration of 30 h with EAC = 0.05, 0.35, 0.65, 0.95 and 1.25 are considered and the factor of safety for different groundwater table depths, soil friction angles and cohesions is obtained. Moreover, the effects of rainfall duration and soil saturation are considered as surrogate to precipitation event accumulation.

7.6.1. Effect of Rainfall Intensity

In order to compare the effects of depth of groundwater table and rainfall intensity on the stability of slopes, the factor of safety obtained for different depths to groundwater table and rainfall intensities are presented in Figure 7-9. From the results, it can be concluded that compared with the rainfall intensity effect, depth of groundwater table has more significant effect on the factor of safety under earthquake conditions. For example, when depth to groundwater table is 6 m and EAC = 0.05, increasing rainfall intensity from 1 cm/h to 15 cm/h decreases the factor of safety from 3.55 to 1.52 (-57% change) and it decreases from 0.83 to 0.60 (-28% change) when EAC = 1.25. Therefore, increasing EAC decreases the effect of rainfall intensity on slope stability. However, increasing EAC does not decrease the effect of depth of groundwater table on the stability of slopes. For example, when rainfall intensify is 8 cm/h and EAC = 0.05, increasing depth to groundwater table from 3 m to 9 m increases the factor of safety from 1.8 to 2.87 (59% change) and it increases from 0.56 to 0.89 (59% change) when EAC = 1.25. Therefore, the effect of the depth of groundwater table is more dominant than the effect of the rainfall intensity on the stability of a soil slope under earthquake conditions.

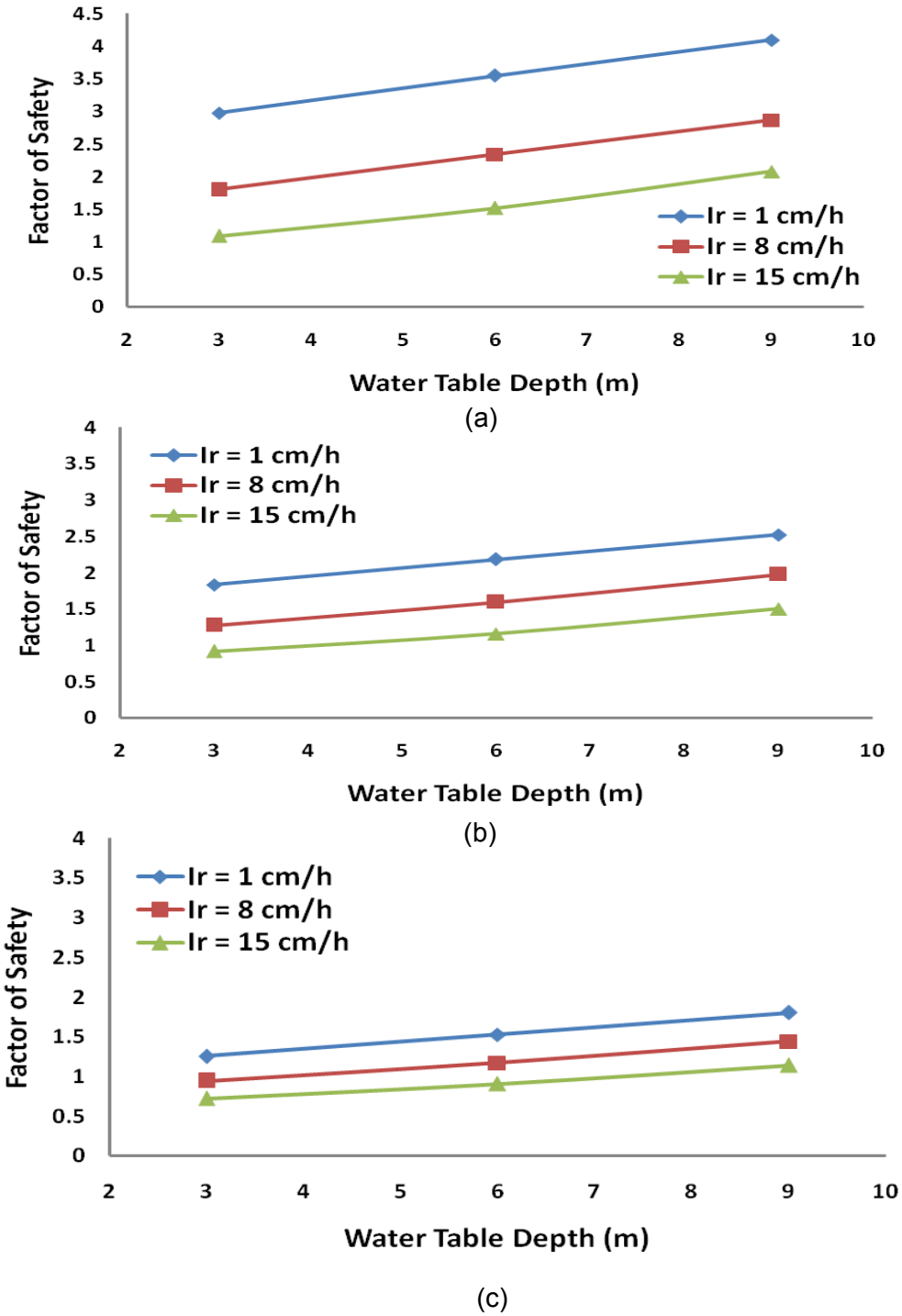

Figure 7-9. Results obtained for different groundwater table depths and EAC of (a) 0.05 (b) 0.35 (c) 0.65 (d) 0.95 and (e) 1.25

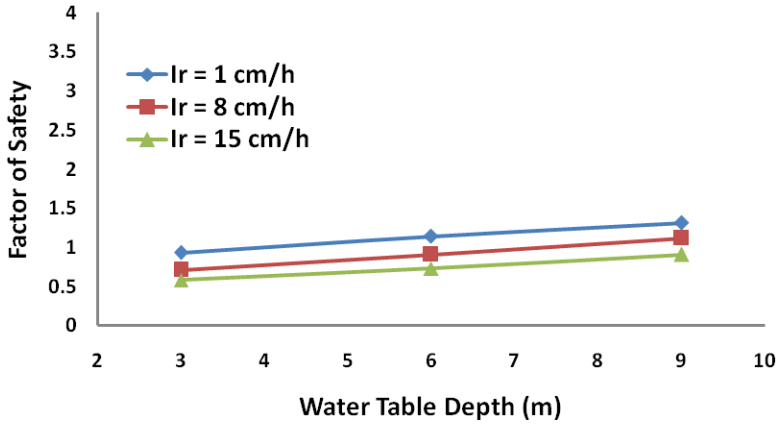

(d)

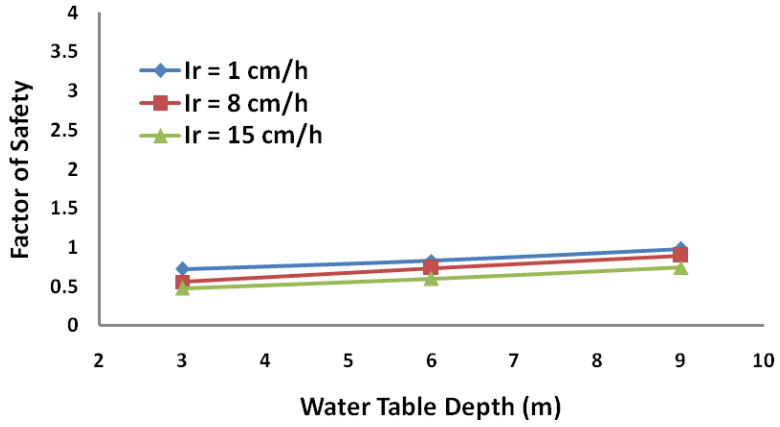

(e)

Figure 7-9. Results obtained for different groundwater table depths and EAC of (a) 0.05 (b) 0.35 (c) 0.65 (d) 0.95 and (e) 1.25 (Cont.)

Figure 7-10 shows the results obtained for different soil friction angles. As can be seen, for example, when friction angle is 25 degrees and EAC = 0.05, increasing rainfall intensity from 1 cm/h to 15 cm/h decreases the factor of safety from 2.94 to 1.27 (-57% change), while the factor of safety decreases from 0.76 to 0.51 (-32% change) when EAC = 1.25. Therefore, increasing EAC significantly decreases the effect of rainfall intensity on slope stability. However, this behavior is not observed for soil friction angles. For example, under rainfall with I_r = 8 cm/h, decreasing the soil friction angle from 45

degrees to 5 degrees, decreases the safety factor from 2.92 to 1.20 (-59% change) and 0.90 to 0.40 (-55 % change) for EAC = 0.05 and 1.25, respectively. Therefore, the effect of the soil friction angle is more dominant than the effect of the rainfall intensity.

In order to compare the effects of soil cohesion and rainfall intensity on the stability of slopes, the results obtained for different rainfall intensities and soil cohesions are presented in Figure 7-11. As can be seen, when soil cohesion is 20 kPa and EAC = 0.05, increasing the rainfall intensity from 1 cm/h to 15 cm/h decreases the factor of safety from 2.73 to 1.14 (-58% change). Also, under the same conditions, the factor of safety decreases from 0.68 to 0.45 (-34% change) when EAC = 1.25. However, increasing EAC does not decrease the effect of soil cohesion on the stability of slopes. For example, when rainfall intensify is 8 cm/h and EAC = 0.05, decreasing soil cohesion from 35 kPa to 5 kPa decreases the factor of safety from 2.29 to 1.13 (-51% change) and decreases from 0.73 to 0.36 (-51% change) when EAC = 1.25. Therefore, the rainfall intensity is less dominant than soil cohesion in controlling slope stability under earthquake conditions.

7.6.2. Effect of Rainfall Duration

In this section we assess the effect of varying rainfall duration on the stability of soil slopes. For this purpose, different earthquake excitations are applied to the model after different durations of rainfall. In this study, it is assumed that rainfall intensity I_r= 8 cm/h, soil friction angle = 25 degrees, soil cohesion = 20 kPa, depth to groundwater table = 6 m. The results for different rainfall durations and EACs are presented in Figure 7-12.

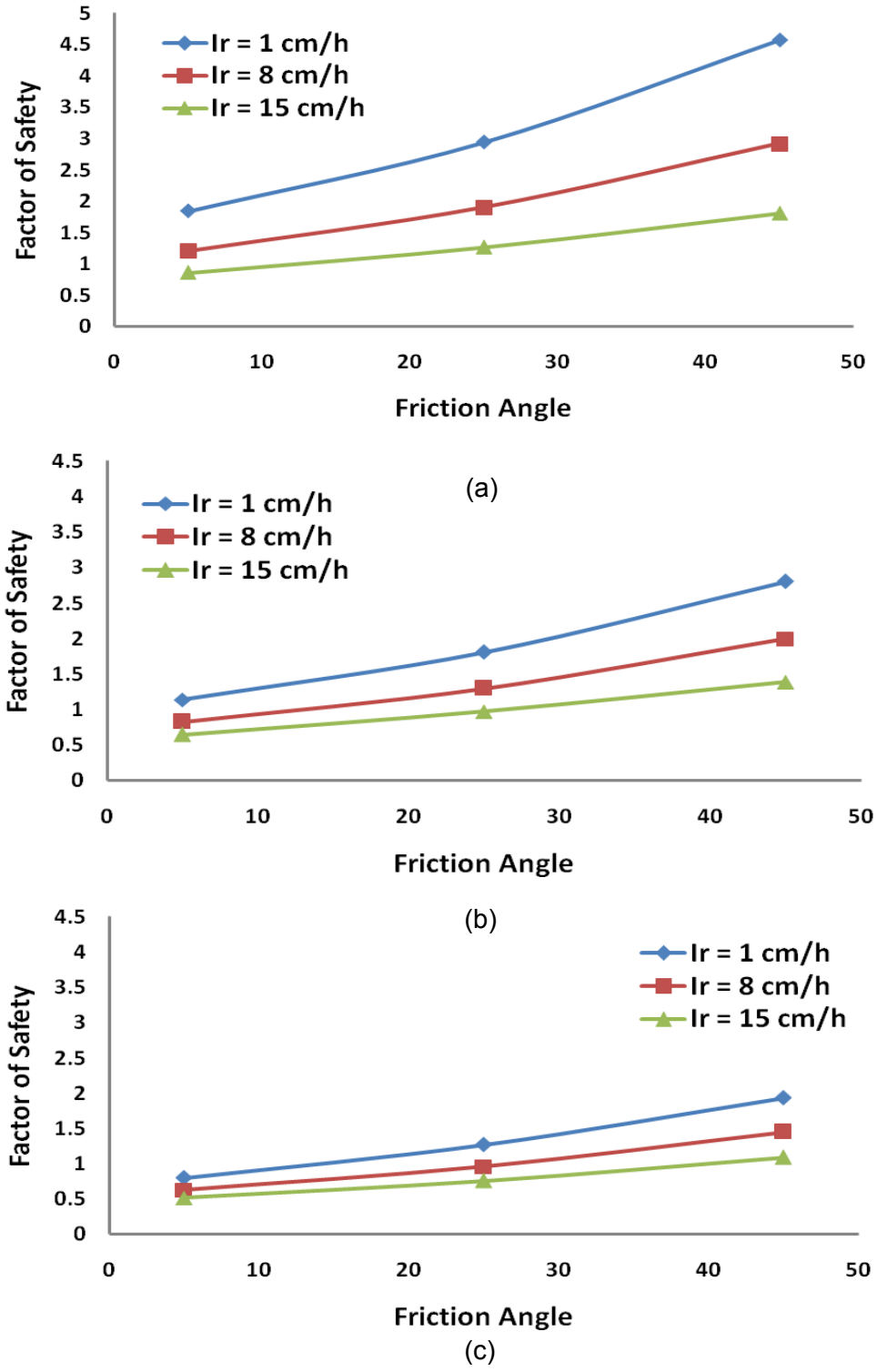

Figure 7-10. Results obtained for different soil friction angles and EAC of (a) 0.05 (b) 0.35 (c) 0.65 (d) 0.95 and (e) 1.25

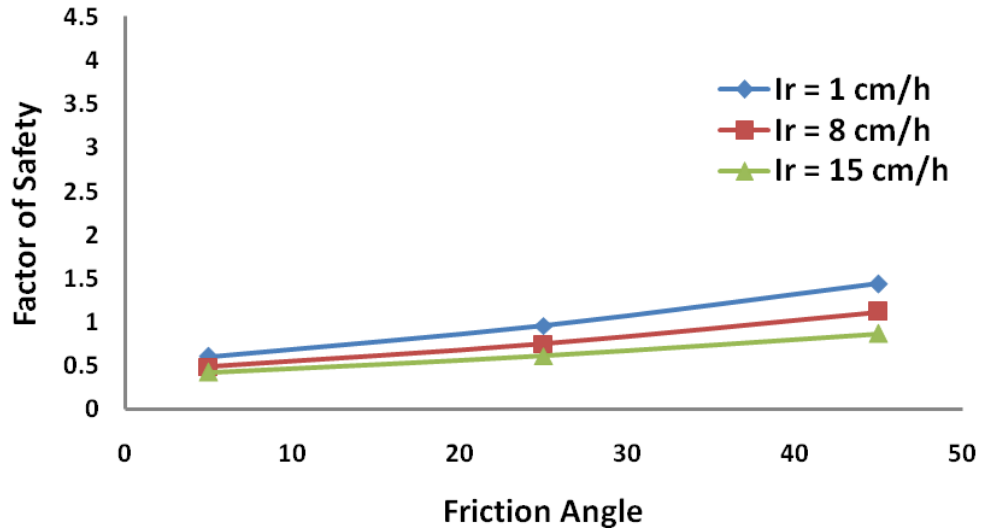

(d)

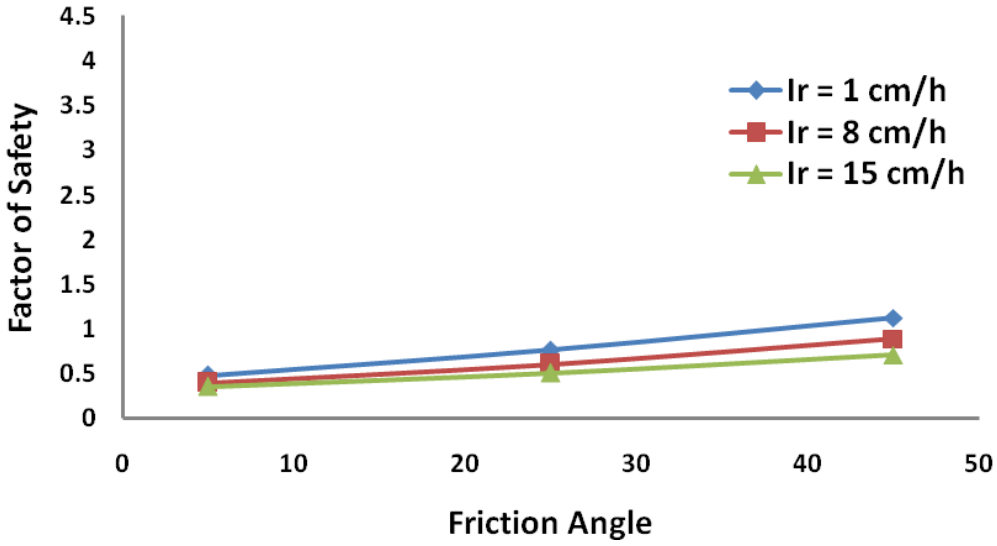

(e)

Figure 7-10. Results obtained for different soil friction angles and EAC of (a) 0.05 (b) 0.35 (c) 0.65 (d) 0.95 and (e) 1.25 (Cont.)

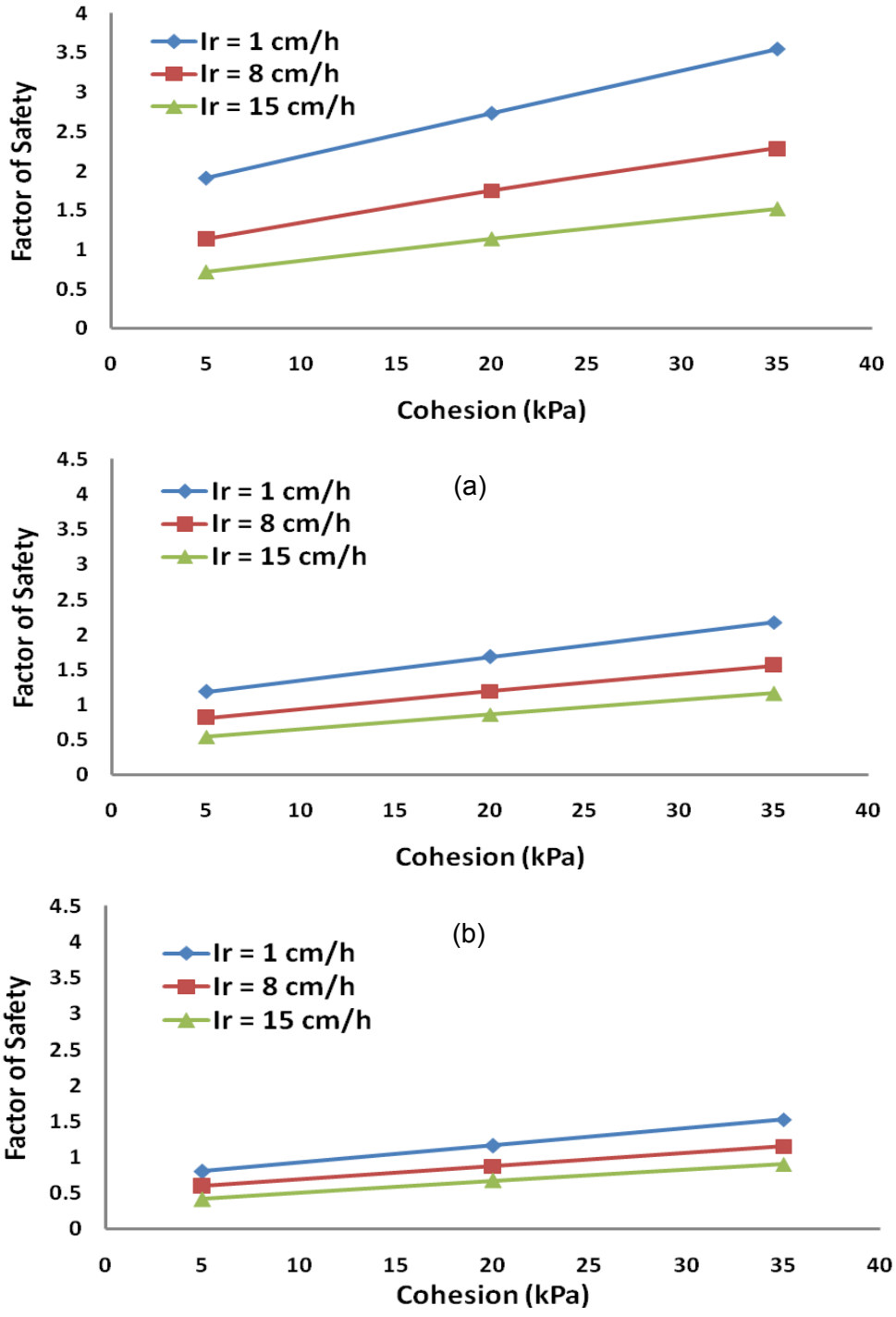

Figure 7-11. Results obtained for different soil cohesions and EAC of (a) 0.05 (b) 0.35 (c) 0.65 (d) 0.95 and (e) 1.25

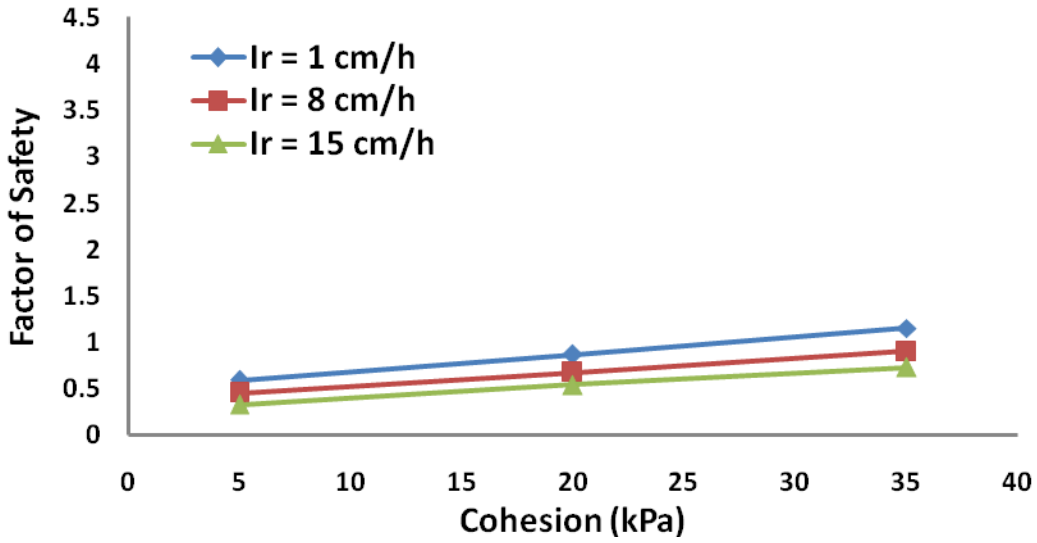

(d)

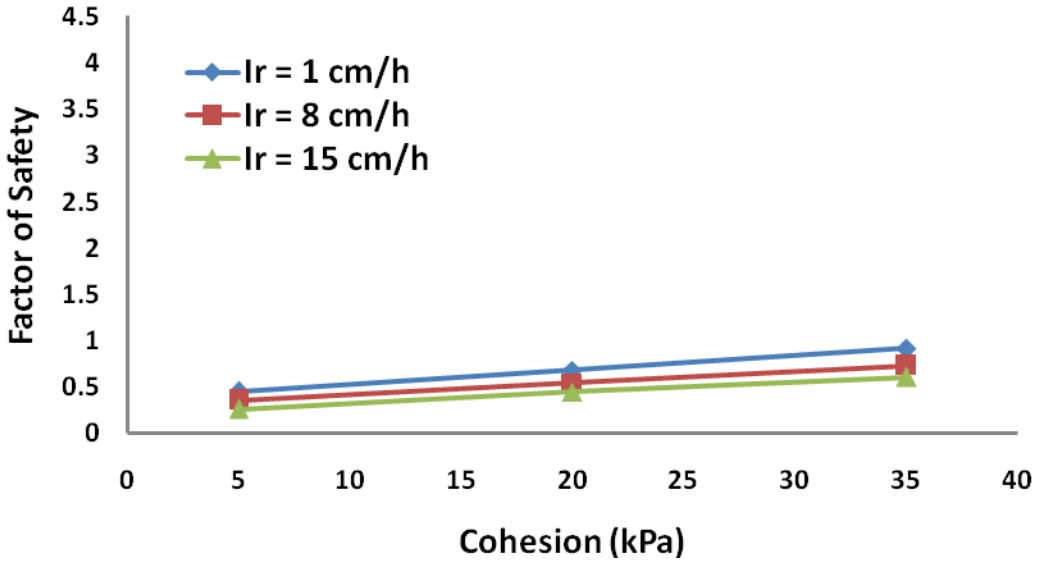

(e)

Figure 7-11. Results obtained for different soil cohesions and EAC of (a) 0.05 (b) 0.35 (c) 0.65 (d) 0.95 and (e) 1.25 (Cont.)

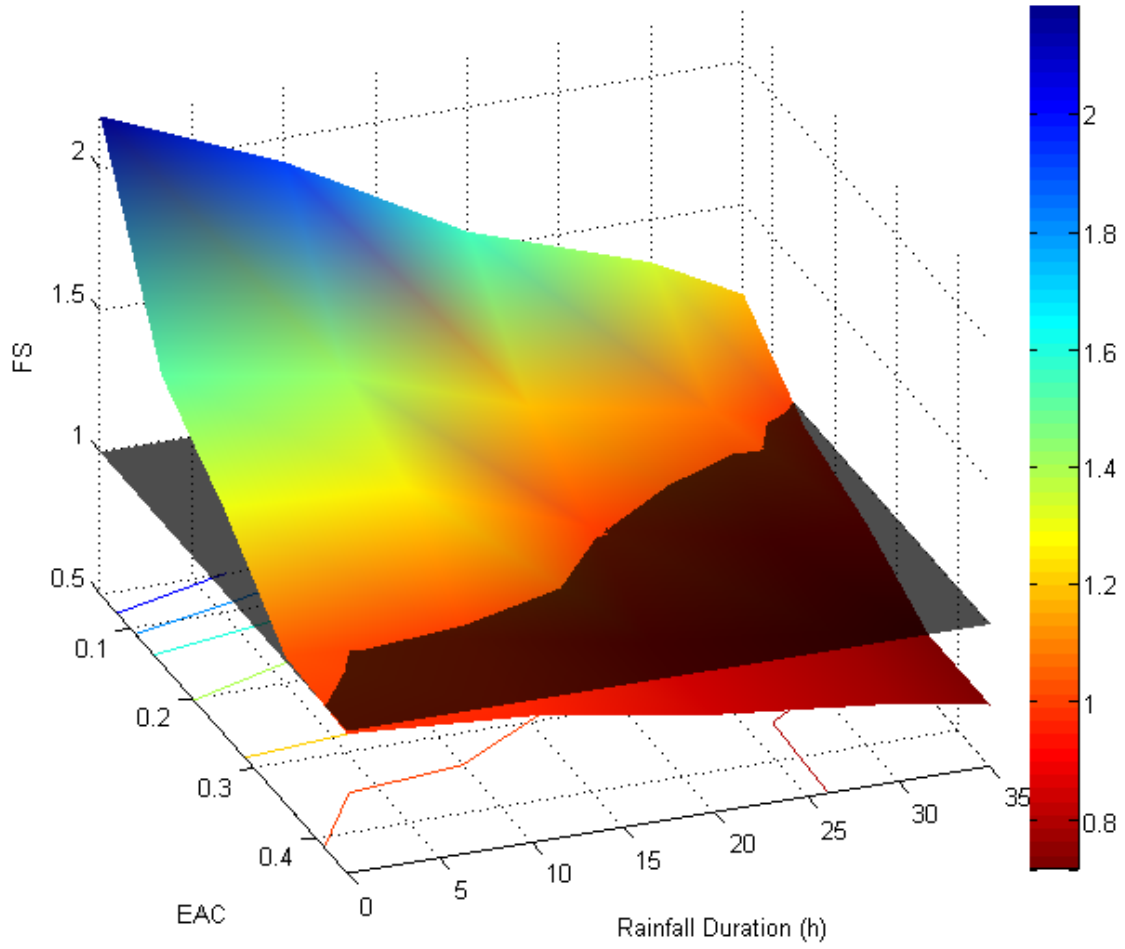

Figure 7-12. Parametric study results obtained for different EACs and rainfall durations

As can be seen in this figure, rainfall duration has a significant effect on the landslide stability. When rainfall duration is greater, landslides can potentially occur (i.e., factor of safety gets to be less than one) by earthquakes with smaller EAC. For example, a landslide can potentially occur if there would be an earthquake excitation with EAC = 0.35 after 10 hours of rainfall. In contrast, an earthquake excitation with EAC = 0.15 would be enough to trigger the landslide if this event occurred after 35 hours of rainfall.

7.6.3. Effect of Soil Saturation

In order to study the effects of soil saturation on the stability of slopes, the slope shown in Figure 7-5 is considered, and it is assumed that the depth to groundwater table is 9 m, soil cohesion and friction angles are 30 kPa, and 35 degrees, respectively. For different rainfall durations, average soil saturation above the water table and factor of safety for Ir = 1 cm/h and EAC = 0.05, 0.35, 0.65, 0.95 and 1.25 are obtained and are plotted in Figure 7-13. As expected, increasing soil saturation decreases factor of safety. Also, as can be seen, the results show that increasing earthquake acceleration coefficient decreases the effect of the soil saturation on the stability of the slope. For example, when EAC=0.05, decreasing the average degree of saturation from 31.75% to 12.43% increases the factor of safety from 2.95 to 3.21 (9% change). However, for the same change in the average degree of saturation, the factor of safety increases from 0.80 to 0.83 (4% change) when EAC=1.25.

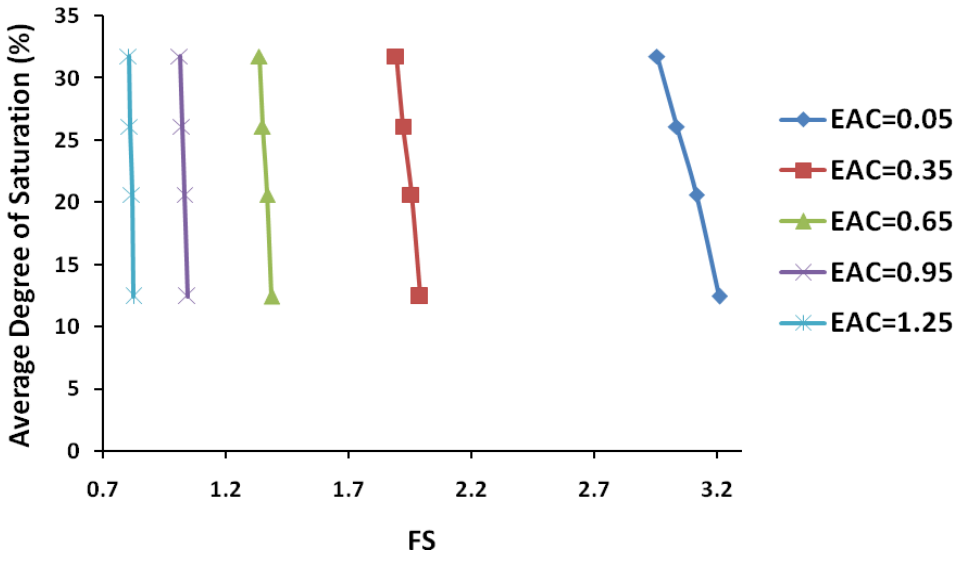

.

Figure 7-13. Results obtained for different soil saturations and EACs

7.7. Conclusions

Groundwater table position, soil strength properties and rainfall intensity are important parameters for soil stability and potential occurrence of landslides. In this study, the effect of each controlling parameter in assessing the instability of slopes under different rainfall and earthquake conditions was investigated using a newly developed combined hydrology and stability model.

It was shown that the groundwater table position affects the factor of safety regardless of the rainfall intensity or earthquake acceleration coefficient applied to the slope. The closer the groundwater table position is to the ground surface, the lower the factor of safety would be. The effect of the depth of groundwater table was shown to be more dominant than the effect of rainfall intensity on the stability of a soil slope under earthquake excitation. Furthermore, it was shown that increasing earthquake acceleration coefficient decreases the effect of the rainfall intensity.

Soil properties, including friction angle and cohesion, were shown to affect the minimum factor of safety of slopes. The smaller the soil friction angle or cohesion is, the smaller is the factor of safety. Moreover, it was shown that rainfall increases this reduction. However, compared to the rainfall intensity effect, soil friction angle and cohesion exhibited more significant effects on the factor of safety under earthquake conditions.

This study also showed that rainfall duration and soil saturation, which is a combined effect of duration and intensity, has significant effect on the landslide instability. When rainfall duration is greater, landslides can potentially occur triggered by earthquakes with smaller acceleration coefficient. In addition, if the earthquake acceleration coefficient is high enough the landslide may be initiated even without rainfall. Increasing soil

saturation decreases the factor of safety; however, increasing earthquake acceleration coefficient decreases the effect of the soil saturation on the stability of slopes.

7.8. References

Abramson L.W., Lee T.S., Sharma S., Boyce G.M. (2002) Slope stability and stabilization methods, John Wiley &Sons, Inc., 2nd Edition.

Anderson M, Holcombe L, Flory R, Renaud J-P (2008) Implementing low-cost landslide risk reduction: a pilot study in unplanned housing areas of the Caribbean. Nat Hazard 47:297–315.

Cai F., Ugai K. (2004) Numerical Analysis of Rainfall Effects on Slope Stability, International Journal of Geomechanics, 4, 69-78.

Chen H., Hawkins A. B. (2009) Relationship between earthquake disturbance, tropical rainstorms and debris movement: an overview from Taiwan, Bull EngGeol Environ, 68,161–186.

Cho S. E. and Lee S. R. (2002) Evaluation of Surficial Stability for Homogeneous Slopes Considering Rainfall Characteristics, Journal of Geotechnical and Geoenvironmental Engineering, 128(9), 756-763.

Chung J. W., Rogers J. D., Watkins C. M. (2014) Estimating severity of seismically induced landslides and lateral spreads using threshold water levels, Geomorphology 204, 31–41.

Das B. (2010) Principles of geotechnical engineering. Stamford, CT: Cengage Learning.

Fredlund D.G., Morgenstern N.R., Widger R.A. (1978) Shear strength of unsaturated soils. Canadian Geotechnical Journal, 15, 313–21.

Fredlund D. G. (2006) Unsaturated Soil Mechanics in Engineering Practice, Journal of Geotechnical and Geoenvironmental Engineering, 132(3), 86-321.

Ferentinou MD, Sakellariou M, Matziaris V, Charalambous S (2006) An introduced methodology for estimating landslide hazard for seismic and rainfall induced landslides in a geographical information system environment. In: Nadim F, Pöttler R, Einstein H, Klapperich H, Kramer S (eds) Geohazards. Lillehammer, Norway, pp 1–8.

Holcombe E, Smith S, Wright E, Anderson MG.(2012)An integrated approach for evaluating the effectiveness of landslide risk reduction in unplanned communities in the Caribbean, Nat Hazards, 61:351–385

Haverkamp R., Vauclin M., Touma J., Wierenga P., and Vachaud G. (1977) A comparison of numerical simulation models for one-dimensional infiltration, Soil Sci. Soc. Am. Journal, 41, 285-294.

Irie K., Koyama T., Nishiyama S., Yasuda Y. and Ohnishi Y. (2012) A numerical study on the effect of shear resistance on the landslide by Discontinuous Deformation Analysis (DDA), Geomechanics and Geoengineering: An International Journal, 7(1), 57–68.

Krahn J. (2004) Stability Modeling with Slope/W – An engineering methodology, Version 1.0, Geo-Slope/W International, Ltd, Calgary, Canada.

Lateh H, Anderson MG, Ahmad F. (2008) CHASM—the model to predict stability of gully walls along the east–west highway in Malaysia: a case study. Proceedings of the First World Landslide Forum. ISDR, Tokyo, Japan, pp. 340–343.

Li A.J., Lyamin A.V., Merifield R.S. (2009) Seismic rock slope stability charts based on limit analysis methods, Computers and Geotechnics 36, 135–148.

Lin G. W., Chen H., Chen Y. H., Horng M. J. (2008) Influence of typhoons and earthquakes on rainfall-induced landslides and suspended sediments discharge, Engineering Geology 97, 32–41.

Lin C. W., Liu S.H., Lee S.Y., Liu C. C. (2006) Impacts of the Chi-Chi earthquake on subsequent rainfall-induced landslides in central Taiwan, Engineering Geology 86, 87–101.

Ma C., Hu k., Tian M. (2013) Comparison of debris-flow volume and activity under different formation conditions, Nat Hazards, 67, 261–273.

Mahmood K., Ryu J. H., Kim J. M. (2013) Effect of anisotropic conductivity on suction and reliability index of unsaturated slope exposed to uniform antecedent rainfall, Landslides, 10:15–22.

Rahardjo H., Ong T., Rezaur, R., & Leong, E. (2007).Factors Controlling Instability of Homogeneous Soil Slopes under Rainfall. Journal of Geotechnical and Geoenvironmental Engineering, 133(12), 1532–1543.

Rahardjo, H., Nio, A., Leong, E., & Song, N. (2010a). Effects of Groundwater Table Position and Soil Properties on Stability of Slope during Rainfall. Journal of Geotechnical and Geoenvironmental Engineering, 136(11), 1555–1564.

Rahardjo H., Ong T. H., Rezaur R. B., Leong E. C. (2010b). Fredlund D. G., Response parameters for characterization of infiltration, Environmental Earth Sciences, 60(7), 1369-1380.

Rahimi A., Rahardjo H., Leong E.C. (2010). Effect of hydraulic properties of soil on rainfall-induced slope failure, Engineering Geology, 114(3), 135-143.

Rahimi A., Rahardjo H., Leong E. C. (2011) Effect of Antecedent Rainfall Patterns on Rainfall-Induced Slope Failure, Journal of Geotechnical and Geoenvironmental Engineering, 137:483-491.

Ray, R., Jacobs, J., and de Alba, P. (2010). Impacts of Unsaturated Zone Soil Moisture and Groundwater Table on Slope Instability. Journal of Geotechnical and Geoenvironmental Engineering, 136(10), 1448–1458.

Sakellariou M, Ferentinou M, Charalambous S (2006) An integrated tool for seismic induced landslide hazards mapping. In: Agioutantis Z, Komnitsas K (eds) First European Conference on Earthquake Engineering and Seismology. Geneva, Switzerland, pp. 1365–1375.

Shou K.J., Wu C.C., Fei L.Y., Lee J.F., Wei C.Y. (2011) Dynamic environment in the Ta-Chia River watershed after the 1999 Taiwan Chi-Chi earthquake, Geomorphology 133, 190–198.

Shukha R., Baker R. (2008) Design implications of the vertical pseudo-static coefficient in slope analysis, Computers and Geotechnics 35, 86–96.

Tang C., Zhu J., Ding J., Cui X., Chen L., Zhang J. (2011) Catastrophic debris flows triggered by a 14 August 2010 rainfall at the epicenter of the Wenchuan earthquake, Landslides 8:485–497.

Tang C., Van Asch T.W.J., Chang M., Chen G.Q., Zhao X.H., Huang X.C. (2012) Catastrophic debris flows on 13 August 2010 in the Qingping area, southwestern China: The combined effects of a strong earthquake and subsequent rainstorms, Geomorphology 139–140, 559–576.

Tang C., Zhu J., Qi X., Ding J. (2011) Landslides induced by the Wenchuan earthquake and the subsequent strong rainfall event: a case study in the Beichuan area of China. Engineering Geology 122, 22–33.

Thiebes B., Bell R., Glade T., Jäger S., Mayer J., Anderson M., Holcombe L. (2014) Integration of a limit-equilibrium model into a landslide early warning system, Landslides, DOI 10.1007/s10346-013-0416-2.

Vanapalli, S. K., Fredlund, D. G., Pufahl, D. E., and Clifton (1996) A. W. Model for the prediction of shear strength with respect to soil suction, Canadian Geotechnical Journal, 33(3), 379–392.

Van Genuchten, M. T. (1980) A closed-form equation for predicting the hydraulic conductivity of unsaturated soils. Soil Science Society of America Journal, 44,892–898.

Wasowski J., Keefer D. K., Lee C. T. (2011) Toward the next generation of research on earthquake-induced landslides: Current issues and future challenges, Engineering Geology 122, 1–8.

Wilkinson PL, Brooks SM, Anderson MG (2000) Design and application of an automated non-circular slip surface search within a combined hydrology and stability model (CHASM). Hydrol Processes 14:2003–2017.

Wilkinson PL, Anderson MG, Lloyd DM (2002a) An integrated hydrological model for rain-induced landslide prediction. Earth Surf Process Landforms 27:1285–1297.

Wilkinson PL, Anderson MG, Lloyd DM, Renaud JP (2002b) Landslide hazard and bioengineering: towards providing improved decision support through integrated numerical model development. Environ Model Softw 17:333–344.

Zhang J. , Cui P., Zhang B., Yang C. & Graeme H. M. (2010). Earthquake-induced landslide displacement attenuation models and application in probabilistic seismic landslide displacement analysis, Earthquake Engineering and Engineering Vibration, 9, 177-187.

Zhou W., Tang C., Van Asch T. W. J., Zhou C. (2014) Rainfall-triggering response patterns of post-seismic debris flows in the Wenchuan earthquake area, Nat Hazards, 70, 1417-1435.

Zhou W., Tang C. (2014) Rainfall thresholds for debris flow initiation in the Wenchuan earthquake-stricken area, southwestern China, Landslides, DOI: 10.1007/s10346-013-0421-5.

Chapter 8. Summary, Conclusions, and Recommendations

8.1. Summary

As the first part of this dissertation, a formulation of the DDA method with a new contact model has been derived and presented. In this model, disk-disk and disk-boundary contacts can be converted to point-to-line contacts. Contact formulae, including those for the normal and shear springs and the frictional force sub-matrices are derived in detail using vector analysis and the augmented Lagrangian method. The success and accuracy of the formulation are demonstrated through several examples. In this method, the number of governing equations is not increased because of the contacts. The proposed model is simple and efficient and can be easily coded into a computer program. Also, in the presented model, unlike the original disk-based DDA, there is no need to calculate coordinates of two auxiliary points in each iteration to find the reference line. The new contact model simply uses only coordinates of disk centers and their radii to obtain the reference line.

Also, in this research, a new numerical model to simulate particulate media in 3-D is presented. This model is based on the 3-D DDA for spheres and rigid boundaries. The complete formulation for stiffness and force matrices due to body forces, point loading, inertia forces, and displacement and directional constraints is presented. Moreover, a model for sphere-sphere and sphere-boundary contacts is presented. In this model, all contacts can be converted to one or more point-to-plane contacts. Using vector analysis contact formulae, including those for the normal and shear springs and the frictional force sub-matrices are derived in detail. The numerical model developed can be readily

implemented into a computer code. To verify the model, three illustrative examples are presented (central collision of spheres, sliding along an inclined plane and rotation on an inclined plane). The model results agree very well with analytical solutions. Three other more demanding test cases (billiard, funnel flow and multiple slopes) show that the proposed contact model can work well for several spheres and boundaries. Results of simulations demonstrate that the model is able to represent geometrical deformation of the granular assemblages reasonably well and can be used to efficiently carry out complex analyses.

Moreover, a new contact model for sphere-boundary edge and sphere-boundary corner contacts in 3-D DDA for modeling of particulate media is presented in this dissertation. Details of the model are given including a new algorithm to search contacts, detect the contact types and calculate contact points. Moreover, formulas for contact sub-matrices are derived. In order to reduce the computational burden, unlike the contact model presented in disk-based 2-D DDA, there is no need to calculate coordinates of auxiliary points in each iteration to find the reference plane in the proposed model. The new contact model has been implemented into a sphere-based 3-D DDA program and three examples are presented to verify its capability. The results show that the model, involving the contact searching algorithm in 3-D and formulations, successfully and correctly simulates the behavior of spheres in contact with boundaries with different situations in 3-D domain. They also show that without considering the presented contact model, the results of modeling of particulate media can be unreasonable.

Furthermore, the accuracy of the method developed under dynamic conditions is studied in this dissertation. For this purpose, a comprehensive sensitivity analysis of sliding behavior of a single disk cluster under the action of gravitational force and dynamic

loading is performed to investigate the applicability of disk-based DDA to dynamic problems (like earthquake-triggered landslides). It was shown that the agreement between disk-based DDA and analytical solution is very reasonable.

Also, in this research, for the first time, disk-based discontinuous deformation analysis (DDA) is applied to simulate a landslide triggered by an earthquake. For this purpose, the kinematic behavior of the Donghekou landslide triggered by the Wenchuan earthquake is simulated. The simulation results obtained using disk-based DDA are compared with actual data. The comparisons show that there is an acceptable agreement between the results obtained using disk-based DDA and actual data. The simulation results provided an understanding of the failure behavior of the landslide.

The final contribution of this work is to develop a new combined hydrology and slope stability method. In order to verify the model, two case studies are considered and the results obtained by the developed model are compared with actual data. Moreover, this model is used to study the impact of rainfall on instability of landslides triggered by earthquakes. For this purpose, the effect of each controlling parameter in assessing the instability of slopes under different rainfall and earthquake conditions is investigated.

8.2. Conclusions

The following conclusions emerge from this study:

- The accuracy of the contact solution depends highly on the choice of the penalty number in the existing disk-based DDA and the optimal number cannot be explicitly found a priori. These limitations can lead to significant inaccuracy and

violation of physical constraints of the problem so the simulation results may easily be affected and the results can be unreliable. As shown by the examples presented, these disadvantages are overcome by using the augmented Lagrangian method. However, if the initial penalty number is too small, many more iterations are required.

- In the case of sliding under gravitational force only, the absolute error increases at a linear rate at every time step, but the relative error decreases and more accurate results are obtained over time.

- Reducing the initial perturbation of the system during the first few time steps improves the accuracy of the computations.

- Increasing the frictional resistance increases the relative error but disk-based DDA follows the analytical results with a very good agreement and with decreasing relative error over time.

- Solutions of disk-based DDA under dynamic conditions are sensitive to time step size. Increasing time step size for a constant friction angle increases error. However, this study shows that time step size could be as high as 0.1 s to get accurate results for both velocity and displacement.

- In the first few deciseconds, a significant amount of error occurs in the solution for both velocity and displacement, but the system progresses towards an accurate solution independently of the initial error.

- Under dynamic conditions, unlike the case of sliding due to gravity only, decreasing the frictional angle increases the initial perturbation and relative errors.

- This study shows that disk-based DDA, as a practical numerical tool, can be used to simulate the post-failure behavior of landslides triggered by an earthquake.

- This study shows that the groundwater table position affects the factor of safety regardless of the rainfall intensity or earthquake acceleration coefficient applied to the slope.

- The closer the groundwater table position is to the ground surface, the lower the factor of safety would be. However, the effect of the depth of groundwater table is more dominant than the effect of the rainfall intensity on the stability of a soil slope under earthquake excitation.

- Increasing earthquake acceleration coefficient decreases the effect of the rainfall intensity.

- Soil properties, including friction angle and cohesion, affect the minimum factor of safety of slopes. The smaller the soil friction angle or cohesion is, the smaller the factor of safety. Moreover, rainfall increases this reduction. However, compared with the rainfall intensity effect, soil friction angle and cohesion have a more significant effect on the factor of safety under earthquake conditions.

- Rainfall duration has a significant effect on the landslide instability. When rainfall duration is greater, landslides can potentially occur triggered by earthquakes with smaller acceleration coefficient.

- In addition, if the earthquake acceleration coefficient is high enough the landslide may be initiated even without rainfall.

- Finally, increasing soil saturation decreases the factor of safety; however, increasing earthquake acceleration coefficient decreases the effect of the soil saturation on the stability of slopes.

8.3. Recommendation for Future Work

There exist several thematic areas where further research should be pursued and include the following:

- Consideration of different properties for individual disks in disk-based and sphere-based DDA methods will allow for the modeling of heterogeneous domains.

- Improvement of dynamic modeling in DDA using more advanced integration methods (e.g., Newmark-beta method) will increase the accuracy of the simulations.

- Implementation of pore water pressure coupling in disk-based and sphere-based DDA methods will facilitate the simulation of more realistic phenomena, such as pile penetration induced deformations, liquefaction, etc.

- Consideration of intra-cluster, above and beyond inter-cluster deformation may allow for a more realistic simulation of landslides under dynamic conditions.

- Enhancement of the combined model to handle 3D geometry and seepage faces will greatly augment its capabilities.

- Integration of the developed combined hydrology and slope stability model to large scale hydrological models will provide the opportunity to develop and employ early warning systems.